



UNIVERSITY OF BERGAMO

Department of Management, Information and Production Engineering

Doctoral Degree in Technology, Innovation and Management

XXXV Cycle

Mechanical and physical study on stainless steel alloys fabricated by metal Material Extrusion

Tutor

Prof. Gianluca Danilo D'Urso

Co-Tutor ENEA

Dr. Sergio Galvagno

Author

Mattia Carminati

PhD Candidate ID: 1035293

Academic Year 2021/2022

Acknowledgements

This thesis is part of the research activities carried out within a Ph.D. fellowship titled “Development of innovative powders, also from waste and/or recycled materials, to be used in the production of components using additive technologies” in collaboration with University of Bergamo and ENEA (the Italian National Agency for New Technologies, Energy and Sustainable Economic Development). This Ph.D. fellowship is funded by Region Lombardy.

I would like to express all my gratitude to my tutor Prof. Gianluca D’Urso, whose help and sincere support guided me during all the activities carried out in these three years.

Besides my tutor, I am deeply grateful to Prof. Mariangela Quarto, Prof. Claudio Giardini and Prof. Giancarlo Maccarini for co-authoring and contributing to improve my works, and kindly sharing their wide-ranging knowledge and skills.

Many thanks also to Dr. Sara Bocchi and Dr. Francesca Sala, estimable colleagues with whom I shared this journey.

I would like to thank Prof. Renato Redondi and all Faculty Members of the Doctoral Program in Technology, Innovation and Management of the University of Bergamo and University of Napoli Federico II.

I thank also all the UniBg laboratories people I worked with and spent my days and especially the laboratory technicians Daniele, Luca and Massimiliano, always available for any request.

A special thank to Dr. Sergio Galvagno and SSPT-PROMAS-NANO team of ENEA Portici Research Center for welcoming me and offering a substantial contribution to my work.

To my family, my mum, my dad and my brother, I am immensely grateful for your unconditional support and for the possibilities you always offered me.

To Anna, thank you for being my safe and happy place where I can really be myself.

Abstract

Industry 4.0 is revolutionizing the global manufacturing system. Among the main enabling technologies of this huge phenomenon, Additive Manufacturing represents one of the most promising and exploited, since AM makes processes more flexible, maximize customization, reduce the time to market of new products and minimize production costs for small batches. Particular attention is paid to AM technologies capable of processing metal materials owing to the significant interest of manufacturing market for this kind of materials. However, several gaps to be filled still remain due to the technologies novelty, including production costs that are still too high, especially for the production of large batches. In this context, additive technologies are less competitive than traditional processes, both because of the high cost of machinery and raw materials. Other factors include the slowness of the printing process and the high energy consumption.

In the last decade, a new Additive Manufacturing technique arose to overcome the aforementioned drawback intrinsic of the well spread metal AM technologies, especially with regards to the high purchasing cost and energy expenditure, as well as the increased safety during the process.

This newly technique, called metal Material Extrusion (ME), basically concerns the advantageous combination of the diffused Material Extrusion equipment, traditionally employed for thermoplastic materials, and metallic fine powders to realise metal finished components. This fabrication is achieved through a raw feedstock made up of metal particles evenly distributed in a polymeric matrix. This innovative multicomponent feedstock is processed by means of a multistage process, which includes the shaping, debinding and sintering phases.

Despite the promising outlook, metal Material Extrusion is still in its infancy and, thus, scarcely employed in the manufacturing sectors.

The main objective of this thesis concerns the in-depth study of metal Material Extrusion process with the final aim of expanding its knowledge and the possibilities of its application, to make it more usable in the industrial field.

This research focused on two stainless steels of great interest for different manufacturing applications and therefore widely used: AISI 316L and AISI 630. The main physical and mechanical properties of the components resulting from the multistep process were

analysed and compared to those of the relative conventional monolithic material to give a reference of the potential and countersinks of the technology.

The environmental issue developed in recent years also required an assessment of the sustainability of this technology, especially with regard to the recycling and reuse of production waste. In this perspective, a circular AM method was developed for the reuse of the defected parts collected from the shaping stage of the process to enhance the economic and sustainable competitiveness of metal Material Extrusion technology. The recycling process was developed in a joint work between the University of Bergamo and Laboratorio Nanomateriali e Dispositivi (SSPT-PROMAS-NANO) of ENEA Portici Research Center.

Contents

1	Introduction to Additive Manufacturing	1
1.1	General aspects of Additive Manufacturing	1
1.2	Additive Manufacturing Process Chain	7
1.3	Design for Additive Manufacturing (DFAM)	9
1.4	Additive Manufacturing Technologies	10
2	Metal Material Extrusion	25
2.1	Background of the technology	25
2.2	Metal ME Technology	31
2.2.1	Shaping	35
2.2.1.1	Feedstock preparation	35
2.2.1.2	Green parts printing	49
2.2.2	Debinding	59
2.2.3	Sintering	65
3	Physical and mechanical properties of sintered AISI 316L and AISI 630	71
3.1	AISI 316L	71
3.1.1	Physical Properties	72
3.1.2	Mechanical Properties	77
3.2	AISI 630	85
3.2.1	Physical Properties	88
3.2.2	Mechanical Properties	92
3.3	Research Issues	101
4	Density and shrinkage evaluation of AISI 316L parts printed via FDM process	103
4.1	Introduction	103
4.2	Materials and methods	104
4.2.1	Equipment and materials	104
4.2.2	Plan of experiments	104
4.2.3	Shrinkage and density measurement	107
4.2.4	Porosity evaluation	108
4.2.5	Data analysis	109
4.3	Results and discussion	109
4.4	Conclusion	116

5	Mechanical Characterization of AISI 316L Samples Printed Using Material Extrusion	119
5.1	Introduction	119
5.2	Materials and Methods	119
5.2.1	Equipment and material	119
5.2.2	Sample preparation	120
5.2.3	Methodology	121
5.2.3.1	Tensile test	121
5.2.3.2	Compression test	121
5.2.3.3	Charpy impact test	122
5.2.3.4	Three-point bending test	122
5.2.3.5	Rockwell hardness	123
5.2.3.6	Vickers hardness	123
5.3	Results and discussion	123
5.3.1	3.1. Tensile stress	123
5.3.2	Compression stress	126
5.3.3	Flexural strength	127
5.3.4	Absorbed energy	128
5.3.5	Hardness	130
5.4	Conclusions	131
6	On the effects of heat treatments on mechanical properties of AISI 630 parts printed via Material Extrusion	133
6.1	Introduction	133
6.2	Materials and Methods	134
6.2.1	Structural analysis	135
6.2.2	Mechanical analysis	138
6.3	Results and discussion	140
6.3.1	Structural characterization	140
6.3.2	Mechanical characterization	146
6.4	Conclusions	157
7	Recycling process of Green Parts for Metal Material Extrusion	159
7.1	Introduction	159
7.2	Materials and methods	161
7.3	Results and discussions	165

7.4	Conclusion	172
8	General conclusions	175
9	References	179
•	List of figures	193
•	List of tables	201

1 Introduction to Additive Manufacturing

1.1 General aspects of Additive Manufacturing

Additive Manufacturing (AM) is the formalized term for a series of production technologies conceived and developed since the 1980s, which involve the creation of objects by depositing layers of material one after the other. This concept derives from an evolution of the classic two-dimensional printing since parts are created by overlapping the individual sections of a predetermined thickness in a vertical direction. The American Society for Testing and Materials (ASTM) defines Additive Manufacturing technology as “the process of joining materials to make parts from 3D model data, usually layer upon layer, as opposed to subtractive manufacturing and formative manufacturing methodologies” [1].

In early days, Additive Manufacturing was exploited only for the production of prototypes due to high production costs that discouraged its massive usage in industrial contexts [2].

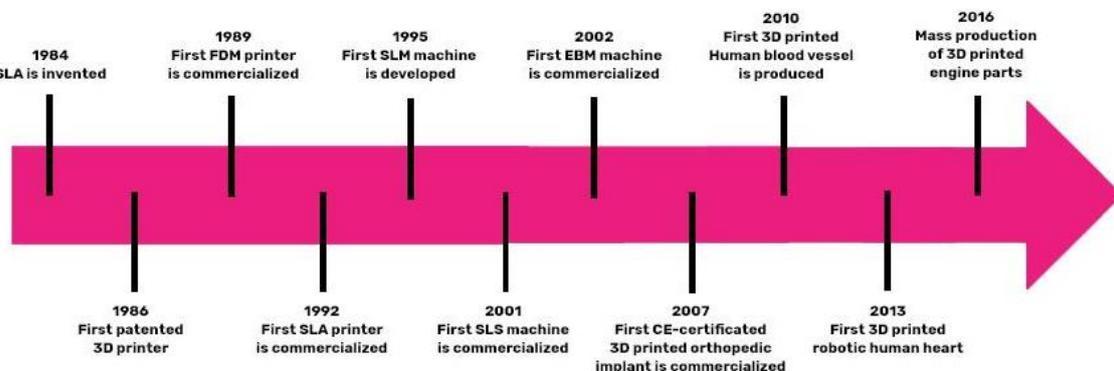


Figure 1.1: Timeline of AM technology [2].

The introduction of Additive Manufacturing dated back to the first patent of an AM machine in 1984. Chuck Hull developed and subsequently patented the first machine for Stereolithography (SLA), a technology capable of making three-dimensional objects starting from a tank containing a liquid photopolymer. In the following years, a consistent push towards the study and the development of other AM technologies led to a proper revolution in the manufacturing industrial world. In this context, existing and robust manufacturing industries grasped the potential of layer-by-layer paradigm, helping the spread of these new technologies. They were still based on the same concept of

Stereolithography but used different energy sources and raw materials broadening the range of products to be processed. In 1988, Scott Crump patented Fused Deposition Modelling (FDM) technique and founded Stratasys, a leader company in the sector. This process allows the creation of components through a layer-by-layer deposition of a thermoplastic filament, which is adequately heated and softened and extruded through a nozzle (hence the term Material Extrusion). This technology, initially conceived for prototyping, has now become the most widespread due to the low-cost equipment and the ease of use. Afterwards, Carl Deckard developed Selective Laser Sintering technique, which consists in a selective sintering of a bed of layer-by-layer polymer powder by laser beam. The introduction of this new kind of technology paved the way for Direct Metal Laser Sintering and Selective Laser Melting (SLM) in the years ahead. These precise and accurate techniques could work and manufacturing metal objects, obtaining parts with characteristics comparable to those obtainable through traditional processes. The possibility of manufacturing metal products and their increasing performances contributed to the wide and rapid growth of AM for direct production of high-performance components used in a wide range of applications. Aerospace industries need to realize extremely complex and customized aircraft components [3]; likewise, automotive, especially racing sector, is favoured by the use of customized and lighter parts, obviously with the aim of increasing the performance of the vehicles. In the medical sector, orthodontics, prosthetics, orthotics, implants, and replacement organs applications manufactured by AM technologies gained a certain level of relevance and use [4]. Also, the electronics fields [5] embraced AM technologies, especially for the production of the radio-frequency microwave and millimeter-wave devices. Besides, starting from the 2000s, printers for home use and open source systems began to spread, thus favouring continuous innovation combined with the expiration of existing patent on AM technologies developed. The Additive Manufacturing market continues to grow more and more, technologies improve, new materials can be processed and new competitors appear on the market allowing the expansion of application fields (Figure 1.2), making this technology cheaper, economically sustainable for industries and one of the enabling technologies of Industry 4.0.

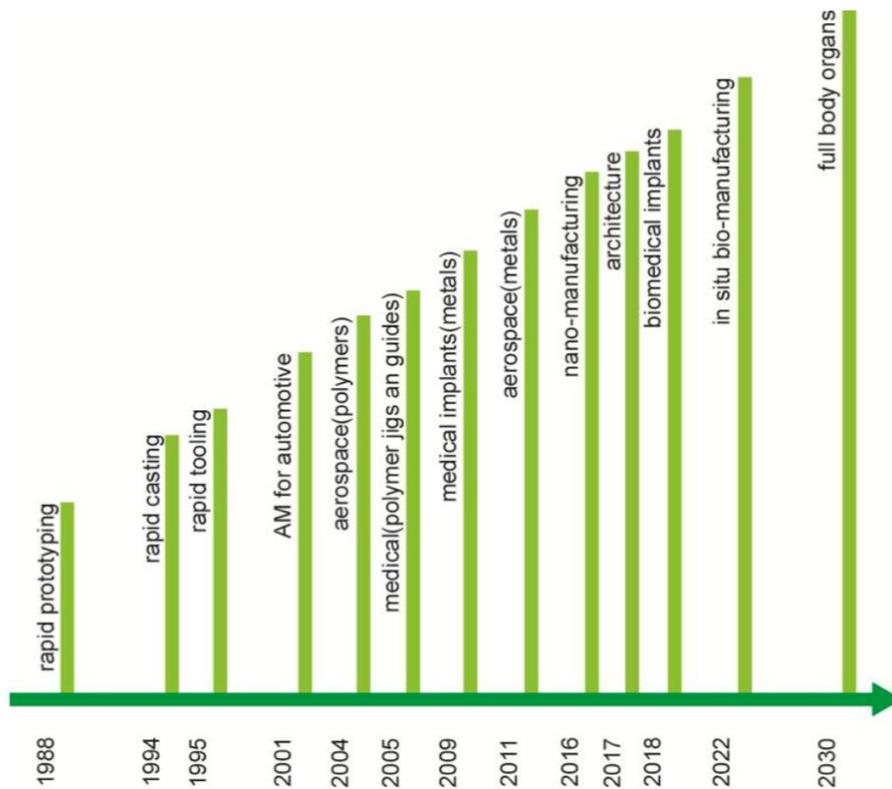


Figure 1.2 : Applications of Additive Manufacturing to the various sectors over the years [6].

To date, the amount of capital invested in AM confirms the increasing interest of industries in this revolutionary technology. Even though the staggering impact of COVID-19, it was estimated that the AM market grew from USD 12.57 billion in 2020 to USD 15.26 billion in 2021, with a projected growth up to USD 68.71 billion in 2028 at a CAGR of 24% in the 2021-2028 period [7]. This promising expansion and investments in this newly set of technologies are justified by the possibility to overcome some limitations that are typical of conventional manufacturing, thus leading to huge changes in industrial processes. Indeed, in a context characterized by rapid and continuous transformation, the concepts of personalization, differentiation and flexibility are the basis of the success of many companies, as well as essential strategic objectives revolutionizing product development and manufacturing.

Additive Manufacturing brought greater design freedom compared to subtractive and casting technologies, since traditional construction constraints (e.g., internal cavities and channels, undercuts, overhangs) are easily bypassed building layer upon layer. Furthermore, “freedom to complexity” concept is the direct cause of the constant

production costs for an AM technology. Indeed, a printed part is shape and complexity independent, since the production costs remain constant as the complexity of the geometry of the pieces varies; instead, production times and costs depend solely on the size of the piece to be made and possibly the desired qualitative characteristics. Diversely, the complexity of the objects involves costs that increase exponentially for traditional technologies, as reported in the Figure 1.3.

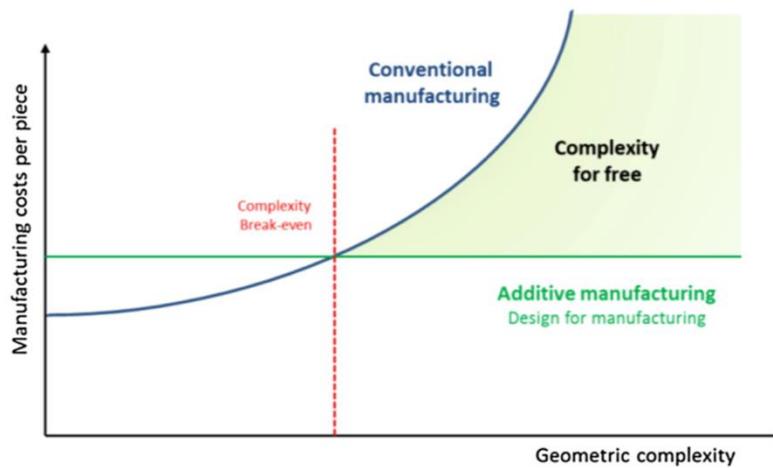


Figure 1.3: comparison between the cost of complexity for additive and traditional technologies [8].

Due to the fast production cycle and the simplicity of parts modification, it is possible to provide high levels of products customization with relatively low costs. The production process becomes very flexible and is not subject to constraints such as moulds or assembly line constraints, since it is sufficient to modify the 3D CAD file of the object and start a new printing process. Correlated to the products customization, complex parts can be produced layer by layer in a matter of hours with additional technologies. The overall cycle duration, including post-production, is typically a few days and it is shorter than conventional processes, which often require production cycles of up to several months. The design and construction phases for moulds, tools, etc. do not occur during the production cycle. The only consumable element in any AM technology is the nozzle head only for Material Extrusion and DED (not for all AM technologies), unlike conventional technologies that require moulds, tools, fixtures for clamping, equipment for the orientation of the pieces, etc. It is also worth noting that the ability to directly print

the desired geometry helps to create complex parts in a single step, thus reducing the number of assembly operations such as welding, brazing. Besides, the production costs of prototypes and small batches are much lower than traditional processes.

Other relevant advantage concerns the reduction of scraps material during the production phase compared to traditional production processes. Waste and scraps mainly derive from the support structures that must be eliminated and possibly from subsequent processing to the printing phase. The savings in terms of raw materials can be a consumption up to 25 times lower than traditional processes, a very important factor when it comes to expensive or difficult to machine alloys [9]. In addition to the reduction of waste material, a further positive environmental impact regards the ability of producing lighter components. Additive Manufacturing allows the use of dissimilar internal structures. Besides, the infill degree inside the external structure of a component can be reduced, differently from products fabricated by means of conventional technologies. Different internal structure, such as honeycomb or reticular design, provide the filling with material only where is necessary without useless structural parts, lightening considerably the component. The aerospace industry benefits from the ability to empty the infill of a component as a function of the structural constraints. A reduction in weight of a single component within an aircraft might lower the fuel consumption, leading to an environmental benefit and an economic saving.

The advantages are therefore many and for this reason additive technologies are revolutionizing a large part of the market. Furthermore, the benefits deriving from the use of additive technologies are reflected in the entire life cycle of the product, from the design phase to the market launch. The impact of additive technologies creates value throughout the entire value chain, starting from the design and production phase up to the distribution phase: the design and engineering phase is simplified and allows greater design freedom, the production phase is much more flexible and efficient on account of less production waste. Lastly, the part linked to service and logistics is also improved, since thanks to additive technologies the constraints linked to the supply chain are broken, such as the dependence on local suppliers or the need to produce only locally. Related to the supply chain, the adoption of additive productions implies some organisational changes [10]. The design and subsequent production phases require the transmission of 3D CAD part data through data networks reducing the physical movement of intermediate

inputs or final products. AM technologies could introduce the dematerialisation of the supply producing significant economic savings as it eliminates the need to physically move intermediate products [11]. AM adoption could lead to a radical change from Just-in-Time delivery strategy to a novel strategy of Just-in-Time manufacture, since warehousing and stock holding costs might be minimized, as well as the amount of capital tied up in work in progress. Besides, the enhancement of manufacturing flexibility reduces the set up times and the overall part count, changing the composition of the total inputs owing to a minimised usage of labour inputs [11].

Despite the undeniable advantages of the deployment of AM technologies, the complete diffusion of additive techniques in the market and the partial substitution of the traditional subtractive technologies are still hindered by some organizational and economic limits. As mentioned in the list of advantages, AM is competitive for the production of small batches, but when it comes to large numbers the costs become higher than traditional technologies due several factors, such as low production speeds of a single piece and, often, the inability to realize multiple objects per cycle. This causes a loss in competitiveness compared to traditional technologies which, on the other hand, can divide the production costs over numerous batches, producing more pieces at a time in an efficient manner and exploiting economies of scale. Further elements that cause the rise of production costs are the prices of raw materials, the energy consumption and any post-production costs regarding surface finishes or special treatments. Besides, there are still significant skills shortages in AM product design. In fact, a lack of know how for specific AM design disallows to capture the full potential of the technology, inhibiting a complete rethinking of the way in which the products are designed. Even from a technical point of view, different challenges and drawbacks require further research and technological developments. One of the main limitations of AM printed parts is void formation among adjacent layers with the consequent reduction of interfacial bonding between printed layers [12]. Another drawback consists of anisotropic behaviour of printed samples, which is intrinsic in the layer-by-layer matrix. Therefore, the microstructure of the material within the layers is different compared to that along their growth direction. The inherent porosity and the anisotropic behaviour of products manufactured by additive technologies affect the mechanical properties of the products themselves, leading to a general worsening compared to those of the components realized by traditional

manufacturing techniques [13]. Then, almost each product printed by means of an AM technology needs to undergo post-processing surface treatments to improve the surface finish and minimize the surface roughness. Indeed, printed parts are characterized by layer-by-layer appearance. Some applications require flat surfaces for practical aspects, e.g., aerospace and medical, and for aesthetic reasons, such as toys or jewels. Besides, the surface roughness is one of the defects and inaccuracies that creates a divergence from the design phase through Computer-aided design tool to the execution of the part [14].

1.2 Additive Manufacturing Process Chain

Over the years, plenty of additive manufacturing technique with different working principles and process parameters have been developed. However, all AM processes require the same workflow to be followed to produce physical objects. The generic 3D printing process, that move from the virtual CAD description to the physical resultant part, can then be broken down into several steps, as depicted in Figure 1.4.

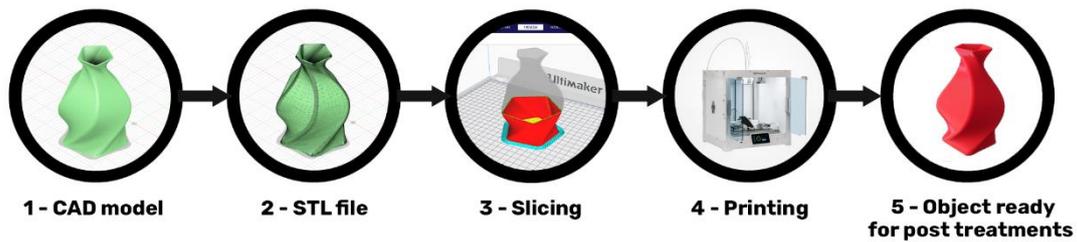


Figure 1.4: Steps of the generic 3D printing process.

The first step consists in the digital product description of the physical object and the obtainment of a 3D model that has to be produced. Such model can be designed by means of 3D CAD software or derived from an existing object with reverse engineering instruments. This model defines both geometries and parameters of the part.

A conversion from CAD format to STL format is then needed. The STL file was created in 1987 by 3D Systems Inc. when they first developed the stereolithography technique. The term STL file stands for Standard Triangulation Language and represent an unordered collection of triangle vertices and surface normal vectors, without any construction data, units, colours, materials information. A STL file creation process mainly consists in the conversion of CAD files continuous geometry into a header, small triangles, or coordinates triplet list of x, y, and z coordinates and the normal vector to the

triangles. The triangle size is determined by the shortest distance between the plane represented by the triangle and the surface it is supposed to represent. In such a way, the external surfaces of the model are approximated by a mesh of triangular elements with associated surface normal vectors. The slicing process also introduces inaccuracy since it replaces continuous contour of the CAD model with discrete stair steps forming the STL file. A more precise representation is obtained by using different sized triangles, based on the complexity of the surfaces, so that the chordal error ratio can be kept constant. However, it must be considered that the STL file will never provide an exact copy of the CAD model due to the necessary approximation of curved surfaces introducing a faceting error.

Once the STL file has been created and eventually manipulated, the next step requires the preparation for printing with its load into a slicing software. Slicing consists in the sectioning of the virtual model into the series of parallel layers, perpendicular to the building direction of layers, with which the physical object will be realized. Each slicing software is equipped with a visualization tool that allows to position the part within the working area and to change an unproper orientation of the model. Besides, scaling may be a necessary step, since the AM part requires to be slightly larger or smaller than the 3D model to account for shrinkages issues or coating processes. The generation of adhesion structures and supports for over-hanging parts represent a fundamental action for the success of the following print process. Lastly, the definition of several printing process parameters must be taken into account. This phase affects both print quality and manufacturing times. All the dissimilar information defined by the slicing software are collected into a GCODE file. Such file is then transferred to the AM machine to automatically manage the production of the component. In this phase, the process switches to the computer-controlled building phase.

In the end, printed parts are optionally subjected to a significant amount of post-processing for application purposes. In all cases, the part must be either separated from a build platform on which the part was produced or removed from excess support or surrounding material. Post-processing may involve abrasive finishing, like polishing and sandpapering, application of coatings, or chemical or thermal treatment of the part to achieve final part properties.

1.3 Design for Additive Manufacturing (DFAM)

Additive Manufacturing shares a basic principle with CNC machining technology since both processes rely on computer-based technology for the manufacturing of products. However, the primary distinction between additive and subtractive processes divided AM and CNC machining. In addition to this, design and prototyping phases play a relevant role in the fabrication of AM parts and it is based on completely different paradigms compared to CAD design for CNC machining processes. Design for manufacture (DFM) has typically comprised the tailoring of CAD designs to eliminate manufacturing difficulties and minimize manufacturing, assembly, and logistics costs. Considering these issues, the capabilities of additive manufacturing technologies provide an opportunity to review DFM to profit from the unique capabilities of these technologies. The core development of DFAM reflects the unique capabilities, which embrace the huge complexity managed and exploited by Additive Manufacturing technologies [15]. In AM, the capability to fabricate a layer is unrelated to the layer's shape, leading to virtually unlimited *shape complexity*. Besides, the absence of production constraints, that typify machining or casting processes, enables custom-designed geometries: two subsequent produced parts might have completely different shapes. *Hierarchical complexity* stands for the designs of features with shape complexity across multiple size scales, including microstructures, mesostructures, and part-scale macrostructures. The ability to simultaneously control micro and macro structures of a part by changing process parameters and CAD data completely differs AM from conventional manufacturing. *Functional complexity* ensures the direct manufacturing of fully functional assemblies and mechanisms using AM processes. Lastly, the processing of different materials point to point causes different material properties in different regions of a part. Besides, the management of *material complexity* enables changing material composition gradually or abruptly during the build process. This inherent capabilities of DFAM envision new opportunities for customization, significant improvements in product performances and lowering of overall manufacturing costs [16].

Despite the undeniable of DFAM compared to traditional DFM, a series of build-related factors should be considered during the design of a part made additively, including:

- part orientation, since an improper orientation of a part can lead to a less accurate reproduction of the original CAD data with poorer qualitative appearance due to stair-step patterning. A suitable orientation might be instead in contrast with other factors, such as the build time, the generation of additional supports.
- removal of supports, which is a manual and time consuming action that should be minimized. The contact surface between the part and the support structure presents visible marks, generating the need for clean-up and post processing finishing. In some cases, structures for the support of overhang features are necessary to avoid distortions and detachment from the build plate. Anyway, an easy-to-remove location should be preferred in order to mitigate the possibility to damage the final product and to reduce the time for the operation.
- interlocking features, which consists in the breakup of the entire design into segments that allows to fit the machine and manually assembly together, since AM machines have a finite and small build volume.

1.4 Additive Manufacturing Technologies

According to ASTM [1], the range of AM technologies can be divided into 7 different families: Vat Photo-polymerization (VAT), Material Extrusion (ME), Powder Bed Fusion (PBF), Binder Jetting (BJ), Material Jetting (MJ), Sheet Lamination (SL), Directed Energy Deposition (DED). Each of these categories comprises dissimilar distinct processes, but all of them share the principle used for the selective modelling of the layers. Indeed, all commercialized AM machines use a layer-based approach, and they differ in the materials that can be used, in the shape of the starting material, how the layers are created, and how the layers are bonded to each other. Such differences will determine factors like the accuracy of the final part, as well as material properties and mechanical properties. They will also determine factors like how quickly the part can be made, how much post-processing is required, the size of the AM machine used, and the overall cost of the machine and process.

The seven families and their working principles, along with examples and materials, are outlined in Table 1.1.

Table 1.1: AM process families, example processes and processable materials.

Process family	Working principle	Example processes	Materials
<i>VAT Photo-polymerization</i>	Light-activated polymerization selectively cures a liquid photopolymer in a vat	Stereolithography (SLA) Digital Light Processing (DLP)	UV-curable photopolymer resins
<i>Material Extrusion</i>	Material is deposited by a heated nozzle	Fused Deposition Modelling (FDM)	Polymers Metals Ceramics
<i>Powder Bed Fusion</i>	Powders are selectively fused (or melted) by a thermal energy source	Selective Laser Melting (SLM) Selective Laser Sintering (SLS) Electron Beam Melting (EBM)	Metals Polymers Ceramics
<i>Binder Jetting</i>	Powder materials are joined by a liquid binding agent that is selectively deposited	ExOne Voxeljet	Polymers Metals Sands
<i>Material Jetting</i>	Droplets of material are selectively deposited and then cured by an UV-light source	Polyjet Multi-Jet Modelling (MJM)	Polymers Waxes
<i>Sheet Lamination</i>	Sheets of material are cut and bonded one upon the other	Laminated Object Manufacture (LOM) Ultrasonic Additive Manufacturing (UAM)	Metals
<i>Directed Energy Deposition</i>	Materials are fused by focused thermal energy as they are deposited	Laser Metal Deposition (LMD) Laser Engineered Net Shaping (LENS) Direct Metal Deposition (DMD)	Metals

Vat Photo Polymerization

The Vat Photopolymerization process is the best-known Additive Manufacturing technique. It involves the use of a photo-sensitive materials, which are exposed to radiation or light in a controlled manner to photopolymerize the material. The main

elements of a photopolymer are monomers, oligomers and photo initiators (Figure 1.5). During the exposure to the selected source, the polymerization reaction occurs forming chain of polymers, which will result in a solid resin. The reaction provides that the photo initiators convert into radicals which act as catalysts for the formation of the chain between monomers and oligomers. The chain formation involves thermal and chemical processes that make this formation irreversible, since prototypes cannot be transformed into the starting liquid form [17].

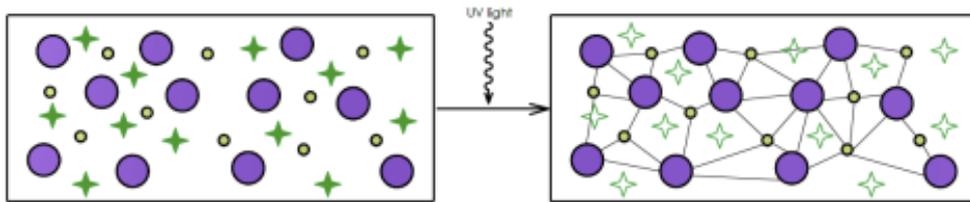


Figure 1.5: Schematic of polymerization reaction [17].

The additive process exploits the polymerization phase to complete the entire object layer by layer. As reported in Figure 1.6, the liquid photo resin is contained in a vat. The lower side of the vat is the building platform, which is lowered from the top of the resin vat downwards by the selected height of a single layer. A light or radiation cures the photo sensitive resin and once the curing process is completed, the platform is lowered or raised, depending on whether the machine uses a top-down or bottom-up process, and additional layers are built on top of the previous ones. The aid of a blade enhances the smoothing of the resin base to build the following layers. Any possible support structure should be made from the same material of the part. During post processing, the part is cleaned in a chemical solution removing wet resin. Any supports are mechanically detached from the shaped object. Lastly, the part is placed into a UV oven to complete the curing. This last step should improve the mechanical characteristics of the products [18].

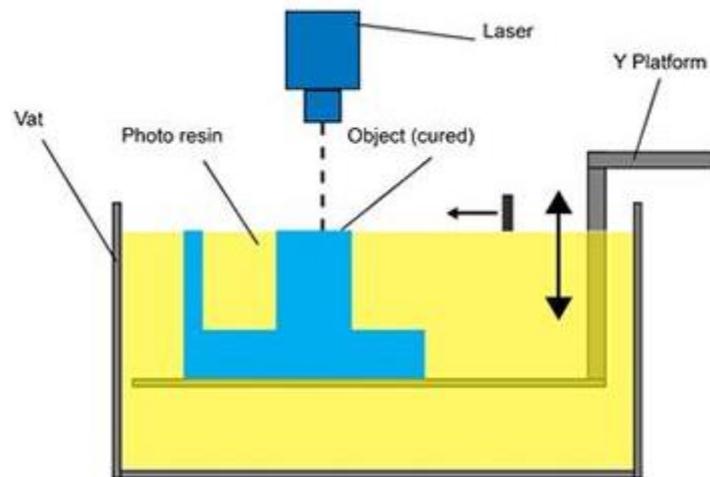


Figure 1.6: Schematic of VAT system [19].

According to the variation in curing source, the Vat Photopolymerization processes can be classified as:

- *Stereolithography (SLA)* was the first-ever introduced AM process. A laser beam is in charge of the curing process. Galvano-scanners control the laser beam trajectory, improving the part accuracy without an excessive decrease of the printing speed. The printing speed is highly correlated to curing depth and light penetration as a function of the type of resin being used.
- *Digital Light Deposition (DLP)* differs from SLA processes solely in the curing method, since a digital light projector is employed, instead of a mirror that reflects a laser source. The use of a projector implies that the DLP process is faster due to the total exposure of the single layer to the curing light. As a drawback, the part might result pixelized if the projector resolution is low.

Two of the main advantages of vat photopolymerization technology are part accuracy and surface finish. The accuracy varies from 0.025 mm to 0.05 mm per 25.4 mm of part dimension. The surface finish ranges from submicron Ra for up facing surfaces to over 100 μm Ra for tilted surfaces [17]. However, photo resins do not have the impact strength and durability required for production applications. Additionally, these materials are subjected to aging, resulting in the degradation of the already scarce mechanical properties over time.

Material Extrusion

Material Extrusion (ME) is the simplest method to produce a part additively. It was invented and patented in 1989 by Scott Crump, after the foundation of the company Stratasys. The basic principle involves the extrusion of highly viscous materials through a nozzle and its deposition layer by layer upon a building platform. Firstly, the material, generally provided in the form of filaments, is loaded in the printing machine with a continuous action. The material loading is essential to provide an input pressure for the softened material in correspondence with the heated nozzle. After the loading, the material is molten until a semisolid state to avoid the complete liquefaction. Too high temperature could lead to an excessive degradation of the polymeric material used. The extrusion phase is performed through a nozzle, which is heated by means of electrical resistances, of reduced diameter compared to the dimension of the filament. The diameter of a filament ranges within 1.75 to 3 mm, while the range of ME nozzle varies among 0.3 and 0.8 mm [20]. The dimension of the nozzle influences the width of the deposited material and the speed of the extrusion process. The next step is the deposition of the extruded material layer by layer onto the build plate. The gap between the nozzle and the print bed corresponds to the thickness of the deposited layers. Once the extrusion and deposition processes occur, the layers solidify. The gravity action and the surface tension could modify the final shape of the object. Besides, the solidification of a layer should take place after the deposition of the following layer so that the residual heat energy activates their surfaces, causing the interface bonding. ME systems are usually equipped with at least two extruders. One extruder oversees the shaping of the part with the use of building materials. The second extruder deploys a suitable material to support the shaped object (Figure 1.7). The support should be chemically or mechanically removed.

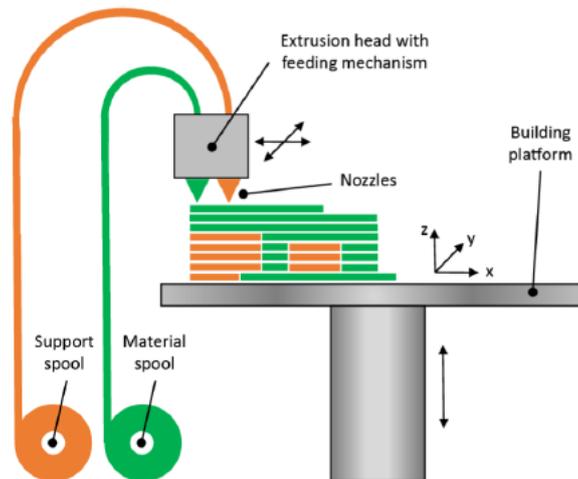


Figure 1.7: Schematic of ME system [20].

The ME technology requires very low cost equipment, especially for entry-level machines. Besides, the cost of the raw feedstock is rather low, as it works mainly with polymeric materials. The low cost of the feedstock results, however, in a negative aspect, set by the poor mechanical properties that can guarantee. Another downside of ME concerns the low surface finish of the build parts, which is extremely dependent on the material nozzle thickness.

Powder Bed Fusion

Powder Bed Fusion processes are the most wide used for the fabrication of metal components. They can be summarized in two steps. Firstly, powder material is spread in a thin layer over a bed build platform; then, an energy beam heat source selectively melts or fuses the particles. Fresh material is supplied by a hopper and spread by either a recoating blade or a powder levelling system. The process, depicted in Figure 1.8, takes place in a vacuum or inside a fully inert chamber and the steps are repeated until the part is finished.

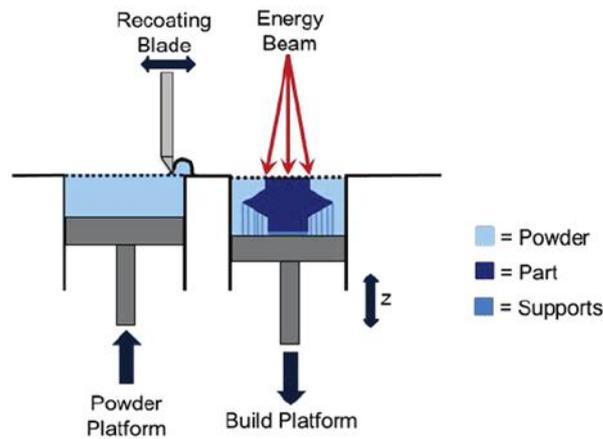


Figure 1.8: Schematic of a PBF system [21].

Generally, any weldable metal is a good candidate for PBF processing, including several types of steels, titanium alloys, nickel alloys, some aluminium alloys and cobalt-chrome alloys. PBF technologies for metal processing are:

- *Laser Powder Bed Fusion (LPBF)* employs laser beams to completely melt single-component metals and create ultra-thin layers; thus providing homogenous melt pools improves surface quality and low porosity [22].
- *Direct Metal Laser Sintering (DMLS)* is the most employed metal PBF technique. DMLS is the commercial name with which the 3D company EOS defined its patented process. Lower laser intensity is required since metallic powders are not fully melted, but final parts are characterized by higher porosity and lower surface quality compared to *Direct Metal Laser Melting (DMLM)*. Nowadays, the sintering process is performed with Yd source laser, capable to fully melt the metallic material. Since sintering allows to process materials whose components melt at different temperatures, DMLS is used only to process alloys [23].
- *Electron Beam Melting (EBM)* uses a high-energy electron beam to attain powder melting. The beam is produced by an electron gun that extracts electrons from a tungsten filament under vacuum [24]. Compared to the previous laser-based processes, EBM is faster, less energy-consuming and produces lower residual stresses, thus resulting in lower distortion of manufactured parts. However, the low diffusion in the manufacturing sectors is linked to the higher cost of the energy source.

Powder-based techniques occupy the largest share of the market since they are well developed and have been applied by both industries and academic institutions for many years. Despite its great diffusion, several issues related to heat absorption, high thermal gradients, local melting and solidification of particles, phase change and Marangoni convection [25] still need to be furtherly investigated. Another issue is represented by powder reusability, since only a small portion of the powdered material loaded into the building chamber goes into the manufactured part, thus affecting the affordability of the manufacturing process. Besides, process optimization is needed to avoid critical defects that may affect manufactured parts. Internal porosity deeply influences fatigue performances while promoting crack growth and propagation [26]. Instead balling, which occurs when the melt pool solidifies into droplets instead of layers, leads to irregular layer deposition, poor interlayer connection after fusion, low and irregular density and quality of parts [27]. Such metal AM processes operate in inert gas environments and demand high energy consumption to melt metallic powders, thus requiring high investment and maintenance costs in terms of both machinery and energy. Moreover, the exposure to small powder particles represents a serious hazard for the health of operators. Particular attention must be paid to nanosized particles that can easily enter the human body if inhaled or absorbed by skin follicles. In facts, it has been demonstrated how non-harmful compounds turn out to be toxic in the nanometric scale [28].

Binder Jetting

Binder Jetting (BJ) is the most promising additive technique in the current manufacturing scenario, due to the great combination among part accuracy, mechanical response and the overall costs of process and equipment. BJ is a technology similar to PBF. The key difference is represented by the use of a liquid binder agent to selectively join the metal powder rather than melting or fusing it by means of an energy beam. Therefore, these systems have no demand for an enclosed environment of vacuum or inert gas. The process, outlined in Figure 1.9, is suitable to produce green parts in a variety of materials including metals, ceramics, sands and polymers.

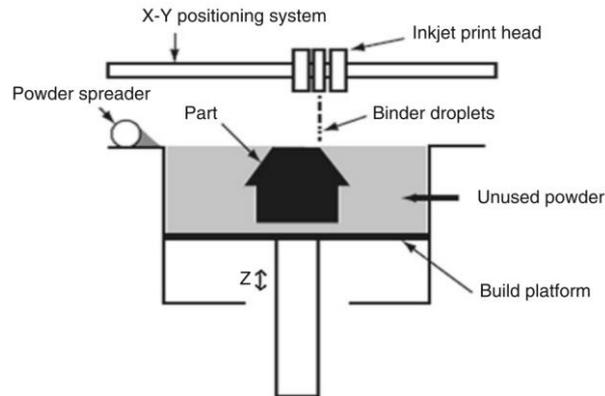


Figure 1.9: Schematic of a BJ system [16].

Once printing is complete, pieces must be freed from unsolidified powder and then cured in an oven to increase their resistance and revive colours. Metal parts also need post-processing treatments like sintering or infiltration with a low-melting-temperature metal, such as bronze. The list of metals that can be processed by BJ include stainless steels, nickel-based alloys, cobalt alloys, titanium alloys and pure copper.

As a matter of facts, this technique is well suited for the processing of optically reflective and thermally conductive metals, which can be challenging for PBF systems due to the use of energy beams. [28]. Furthermore, BJ can print more accurate objects without the need of support structures.

Material Jetting

Often compared to 2D ink jetting processes, Material Jetting (MJ) has been originally developed to print photopolymers and wax-like materials. The process comprises the use of a printhead to jet photopolymer material in the form of droplets from hundreds of tiny nozzles and build parts in a rapid, line-wise way. The material is directly cured and solidified by UV light as soon as droplets are deposited onto the build platform. Supports are often printed simultaneously and are made up of a dissolvable material. To enhance the deposition phase, the materials are heated to change the state from solid to liquid, reducing the viscosity that otherwise would not allow the outflow of the jet. A schematic of the process is shown in Figure 1.10.

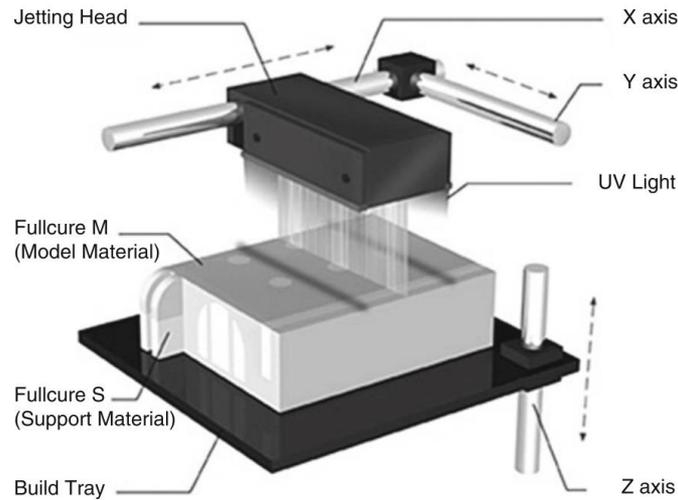


Figure 1.10: Schematic of a MJ system [16].

Due to a potentially high printing speed at low equipment and raw material cost, this technology has recently been expanded to the field of metal and ceramic processing. High accuracy can be achieved with this technique since material-jetting machines can produce parts with resolution on the order of 10 μm .

Nano Particle Jetting (NPJ), patented by XJet, uses a liquid formulation infused with metal or ceramic nanoparticles [29]. After jetting thin layers of droplets, a heating energy source inside the build envelope cause the liquid to evaporate leaving behind parts made from the building material. The resulting part still needs to be sintered in a furnace to achieve final part density. The ultra-thin resulting layers are responsible for very high-resolution parts where the layers are nearly invisible to the human eye. The downside is that many more layers are needed for a given part size as compared to other additive technologies with thicker layers. Adding more layers takes more time, justifying the employment of metal material jetting only for the production of small parts.

Sheet Lamination

Sheet Lamination represents the less widespread technique among the seven families of AM, despite Laminated Object Manufacturing (LOM) was one the first commercialized additive manufacturing technique in 1991. The layer-by-layer process is shared with all other AM methods; however, this technique requires the particular use of metal foils as feedstock, instead of powder, filaments, droplets. The foils thickness typically range from 0.07 to 0.2 mm [30]. The selected metal feedstock is rolled on the building platform and

bonded over the previous layers, using the adhesives or welding technique. The adhesion of the foils is enhanced by the heat pressure of a heated roller. A laser or mechanical cutting is performed to create the desired shape, according to the slice contour (bond-then-form). An alternative configuration could provide the cutting phase prior to the deposition and bonding process (form-then-bond) [16]. Regardless the chronological order, the process is repeated until the complete part is build. Generally, the unused material, following the cut, is left on the building platform acting as support structure. It is diced using a crosshatch pattern into smaller pieces. A post processing is necessary to remove the exceeding material and to reach an adequate surface finish.

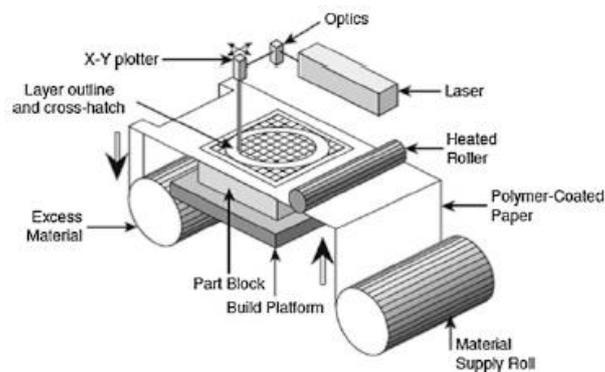


Figure 1.11: Schematic of SL system [16].

The Sheet Lamination technique could be further divided based on the adhesion mechanism among deposited layers. The LOM process involves polymeric-based adhesive to bond layer upon layer. The heated roller applies pressure on the deposited foil, melting the polymeric-based adhesive and generating a bonding between the adjacent layers. The other process is Ultrasonic Additive Manufacturing (UAM), also known as Ultrasonic Consolidation (UC). In this method, a rotating sonotrode travels along the length of a foil (typically with a thickness of 100-150 μm). The sonotrode oscillates along the rolling direction at a constant 20 kHz frequency providing ultrasonic vibration and pressure. During the movement of the digitally controlled sonotrode, the temperature of the layers increases due to frictional welding heat ensuring the bonding among the interfaces (Figure 1.12)[30].

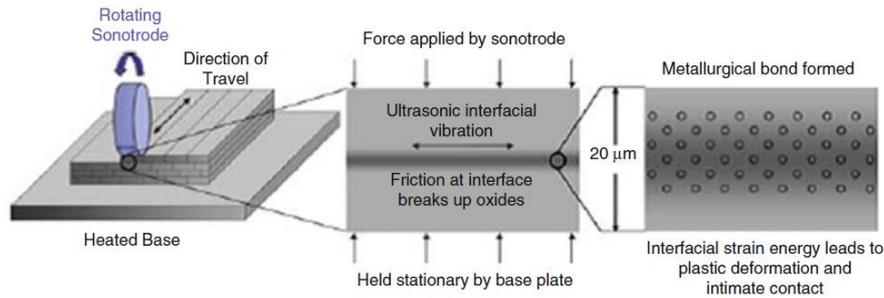


Figure 1.12: Schematic of ultrasonic consolidation [16].

The main advantages of this technologies rely on the process speed and the relative low cost of the equipment, compared to the other AM techniques that work with metallic materials. The drawbacks of SL are especially related to the microstructure of the shaped part and its mechanical properties. Large and distributed voids result from this process, mainly due to the excessive surface roughness of the foils and energy input resulting in the breaking of the previous bonds. Besides, grains are oriented end elongated along the rolling direction since metal foils are fabricated by roll lamination. Indeed, anisotropy of the mechanical response along all three axis occurs.

Directed Energy Deposition

Directed Energy Deposition (DED) technique is primarily used for the production of metal components [31], using focused thermal energy such as a laser, an electron beam or a plasma arc to completely melt material as it is deposited [32]. The feedstock material, which is provided in either powder or wire form, is pushed through a feed nozzle that also generates a protective atmosphere to prevent material oxidation. By properly overlapping the generated clads, layers are overlaid one on the other until the required geometry is produced. Both heat source and nozzle are mounted on a gantry system or robotic arm, hence the build platform can be rotated to achieve different features and eliminate the need of those support structures that are required by PBF systems. This ensures faster deposition rates, but also leads to poorer surface quality that may require additional machining. The process, shown in Figure 1.13, typically takes place in a hermetically sealed chamber filled with inert gas or in a vacuum.

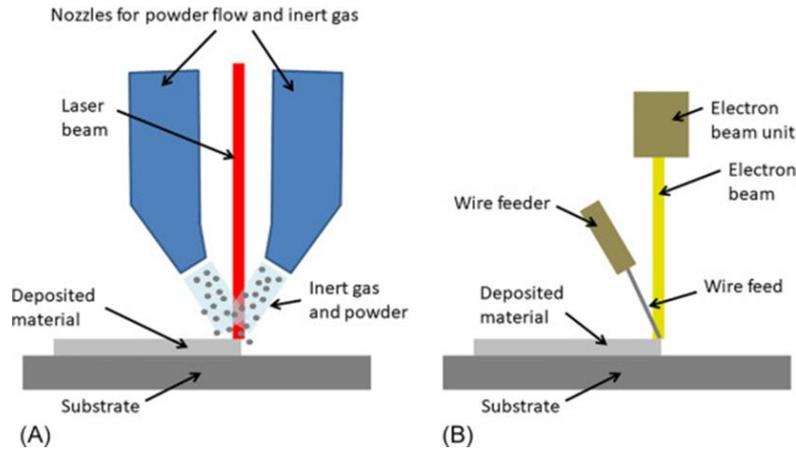


Figure 1.13: Schematics of two DED systems (A) uses laser together with powder feedstock and (B) uses electron beam and wire feedstock [33].

DED can be used to build fully dense functional parts but is mostly exploited to repair damaged parts or enhance the surface properties of already existing objects due to the absence of a powder bed.

Different metals can be processed by this technology, including tool and stainless steels, titanium alloys, nickel alloys and copper alloys. Typical DED-based processes for metals are:

- *Laser Metal Deposition (LMD)* allows for highly complex parts to be repaired with lower distortion compared to conventional welding techniques. Due to low heat input, the heat affected zone is small and the strength of material is not affected. However, the layered microstructure and residual stresses that are commonly present because of steep thermal gradients lead to anisotropy in the mechanical properties of fabricated parts.
- *Laser Engineered Net Shaping (LENS)* uses laser source to build objects layer by layer directly from metal alloys powder. The hermetically sealed chamber is filled with argon so that the oxygen and moisture levels stay very low.
- *Aerosol Jet Technology (AJT)* is a cost-effective, scalable process that enables the fabrication, enhancement and repairing of high-performance electronic and biologic devices. Electronic components such as resistors, capacitors, antennas, sensors, and thin film transistors have all been printed with AJT, eliminating the need for a separate substrate thereby reducing the size, thickness and weight of the end product [34].

- *Electron Beam Additive Manufacturing* (EBAM) is employed to produce large scale metal structures. An electron beam gun deposits metal wire feedstock to ultimately produce near-net-shape structures and parts up to 80% faster than traditional manufacturing methods [35].

Recently, also cold spray processes have drawn the attention of researchers. This kind of DED-based techniques involve material particles deposited with high kinetic energy on a substrate or already deposited coating, thus creating a successful bonding due to adiabatic shear instability or mechanical interlocking [36].

2 *Metal Material Extrusion*

2.1 Background of the technology

The introduction and development of dissimilar additive technologies within the manufacturing production chain required a leap forward in terms of production variability and containment of production costs. All this led to the study of new techniques that respect the cardinal principles of industrial productivity, but at the same time guarantee competitive structural and mechanical characteristics. In particular, the development of new techniques involved the manufacture of metal components. Among different techniques, Powder Bed and Powder Fed systems occupy the largest share of the market since they are well developed and mature. A Powder Bed System concerns the bed melting or sintering of raked powders within a working area. The main advantages is the possibility of realizing high density products, up to 99.9% of nominal density, and providing high-resolution features and allowing to produce complex and hollow parts for critical uses with final remarkable physical and mechanical properties [37]. A Powder Feed System differs from the previous one since metal powders are conveyed through a nozzle and a laser sinters a monolayer onto the build surface. This system allows to work with larger build volumes and the flexibility of the equipment also enlarges its use for repair worn or damaged components. The large amount of advantages associated with these systems makes them the most exploited types of technology for the additive manufacturing of metals. Nevertheless, the main problems shared by these two processes are high purchasing cost, high energy consumption and the need of using safety system for powder handling. The greatest cost driver is the initial investment in production equipment. Besides, further ancillary costs are required, such as sieving equipment, facility costs and post-processing equipment. Raw materials are also a relevant cost driver, as the costs of additive manufacturing materials are higher than traditional manufacturing materials by up to a factor of 8 on a weight basis [38]. Metal AM processes need to employ high-energy sources to sinter the metal powders during the manufacturing processes. This related energy expenditure clearly generates high purchasing cost and affects the sustainability of the process itself, increasing the carbon footprint, but also influences the microstructure and mechanical properties of the fabricated components. Even powder safety represents an area of concern within metal

AM, as there are many aspects of metal powder handling that pose a health and safety risk, as exposure to micrometric powders and explosions through the formation of dust clouds and ignition sources. Particular attention must be paid to nanosized particles that can easily enter the human body if inhaled or absorbed by skin follicles. In fact, it has been demonstrated how non-harmful compounds turn out to be toxic in the nanometric scale [39]. All these aspects generate the need to introduce a lower cost and safer methods of metal AM fabrication, both in the acquisition, operation and maintenance of equipment, expanding the applications even to no high value-added industries. The intensified efforts of both researchers and industries in the development of more affordable 3D printing processes to produce metal components lead to the constantly increasing presence of MJ, BJ and ME on the metal AM market. Indeed, according to [40], the metal AM market is gradually becoming more homogenized among dissimilar AM technologies, as reported in Figure 2.1.

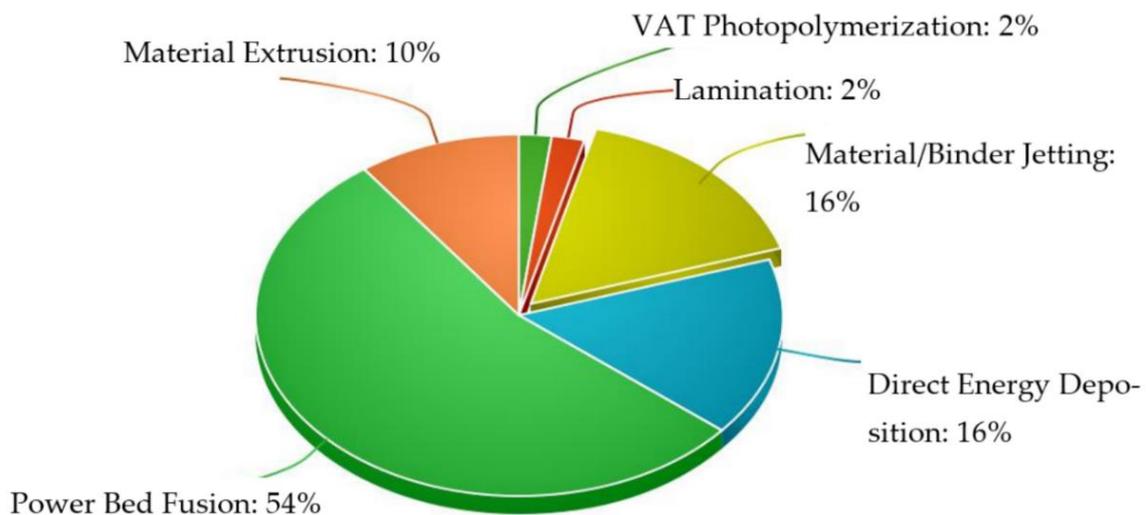


Figure 2.1: Metal AM market in 2021 [40].

Among the aforementioned rising metal AM systems, Material Extrusion (ME) is one of the most widely used AM technologies owing to its simplicity and low cost. This technique forces the extrusion material through a nozzle, which follows a predetermined path to build the component onto a build platform, layer upon layer. In the ME process, extruded materials are generally thermoplastic filaments with poor mechanical properties [41–44]. In general, parts manufactured using ME technology are excellent for prototyping and visualization purposes; however, they are rarely used for load-bearing applications owing to their lack of strength. This technical issue has limited the use of

ME in mechanical applications. Extensive research is underway to improve the mechanical properties of ME components and thereby extend the applications of this technology. Fiber-reinforced polymers have been investigated for decades owing to their tailored material properties and high specific strength. Fiberglass and carbon are the most widely used fibers in combination with a polymer matrix. The polymers hold and protect the fibers and transfer the load to the reinforcement, while fibers support the load by providing excellent resistance to the structure. A clear improvement in the ultimate tensile strength (UTS) of polymeric samples reinforced with fiberglass and carbon fibers is presented in [45,46]. Particular attention is also given to the use of filaments containing metal powders, which could improve the properties of manufactured multi-material parts compared with those of polymer composites. A few studies have been conducted on the reinforcement of polymeric filaments with metallic particles. Hwang et al. [47] stated that the tensile strength of specimens decreased with an increase in the copper and iron contents in the thermoplastic filaments, as reported in Figure 2.2.

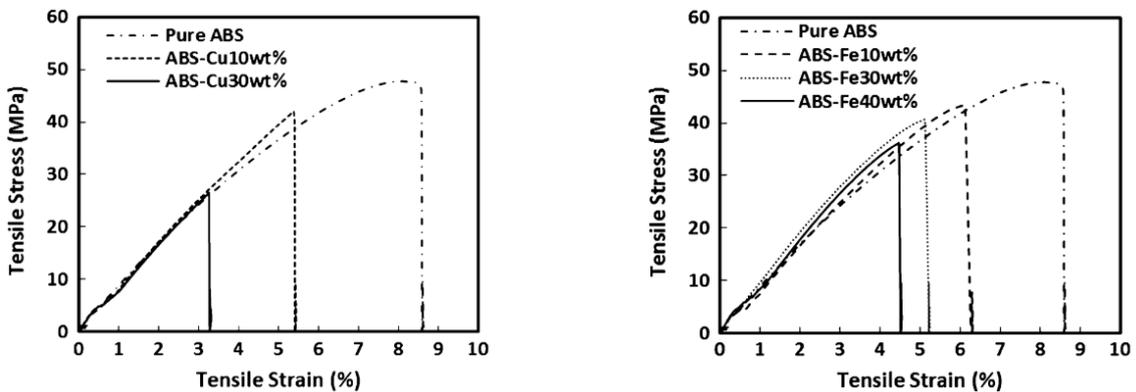


Figure 2.2: Stress – strain curves for ABS with copper particles (left) and with iron particles (right) [47].

Increasing the copper content from 10 wt.% to 30 wt.% generates a reduction of the tensile stresses from 45.7 MPa to 26.5 MPa, and the tensile strain also decreased. A similar contraction of tensile stress and strain occurred with the addition of iron particles in the polymeric matrix. A greater amount of infill particles content resulted in more numerous and larger voids, causing lower binding force between layers and disturbing the bonding force between the layers.

Likewise, Ryder et al. [48] confirmed the deterioration of the mechanical properties of samples with the addition of type 420 stainless steel particles. DSC analysis revealed the

increase of glass transition temperature of the polymer matrix up to a 15 wt.% metal particle concentration. Considering the mechanical properties, the UTS values remained relatively constant with the increase in solid loading up to 15 wt.%. Beyond this concentration threshold, the content of metal particles increased the thermal conductivity of the material and started to locally strain the glass domains and facilitate the melting phase, leading to a deterioration of the mechanical and physical properties of the samples.

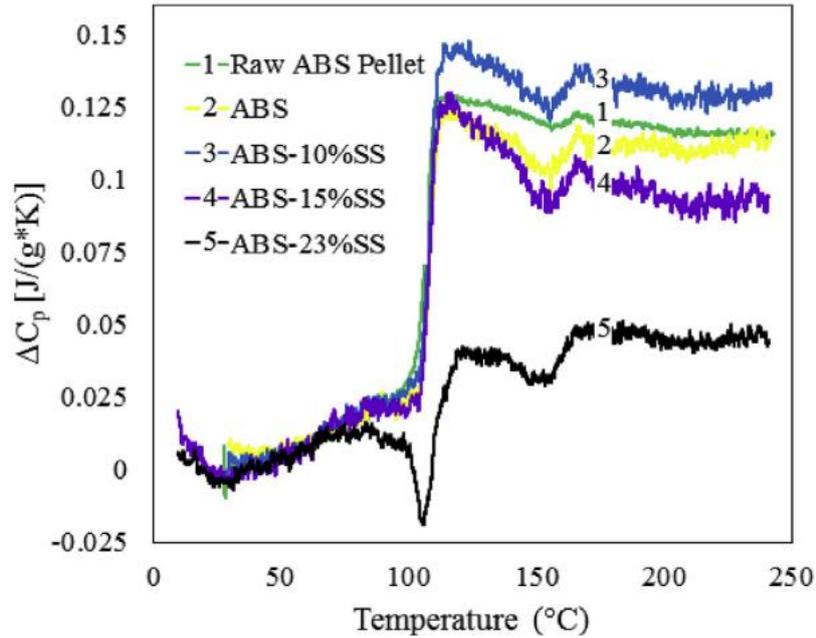


Figure 2.3: Modulated Differential Scanning Calorimetry (MDSC) results for base ABS, and ABS-SS composites [48].

In [49], an increase in the volume fraction of iron particles reduced the fracture energy. Furthermore, the authors indicated that the variations in the tensile strength and tensile elongation were strongly dependent on the size of the metal particles. Thus, a smaller particle size generated a larger tensile elongation at break but with a degradation in the tensile strength, as exhibited in Figure 2.4.

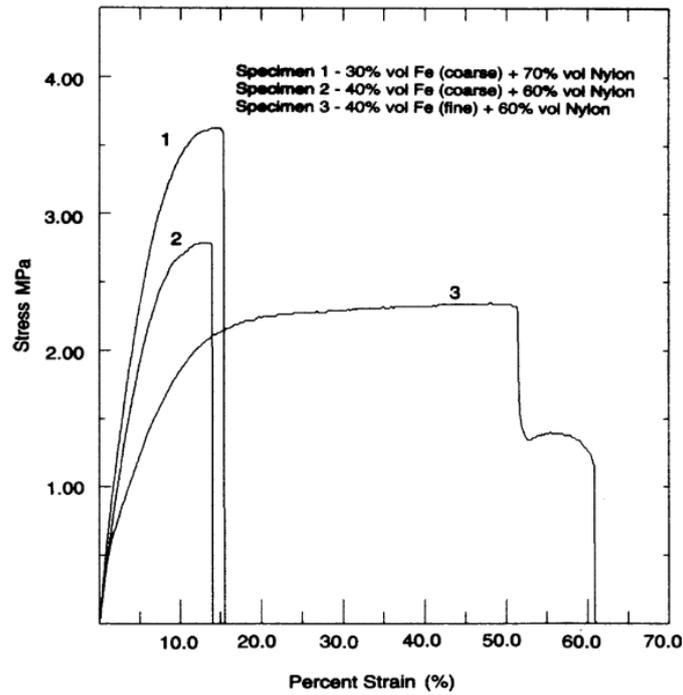


Figure 2.4: Stress – strain curves for Fe/Nylon samples with different infill compositions [49].

Polymer–metal composites reduce the mechanical performance owing to the difficulty in achieving uniform particle distribution and strong adhesion between the metal powders and polymer matrix. Poor adhesion generates large voids at the interfaces between the particles and matrix, which induce cracks upon loading. The bending behaviour of parts printed with the metal–polymer blends was not adversely affected by the separation of the filler from the polymer matrix during the test. Nabipour et al. [50] performed flexural strength tests on polyethylene–copper samples, demonstrating that the addition of metal particles increased the maximum flexural strength up to 19.41 MPa, with a reduction of flexural strain and modulus directly proportional to the increase in copper content percentage (Figure 2.5).

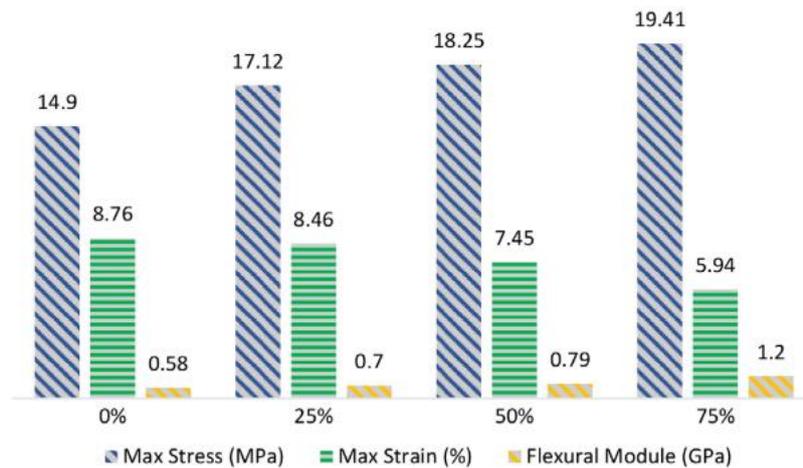


Figure 2.5: Flexural strength values for different metal contents [50].

Fafenrot et al. [51] mechanically tested Magnetic Iron/PLA and Bronzefil /PLA samples and pointed out that the mechanical properties of objects printed with metal– polymer blends were lower to parent PLA-printed objects, taking into account tensile tests and flexural tests. In Figure 2.6, the fracture surface of PLA, Magnetic Iron and Bronzefil are reported.

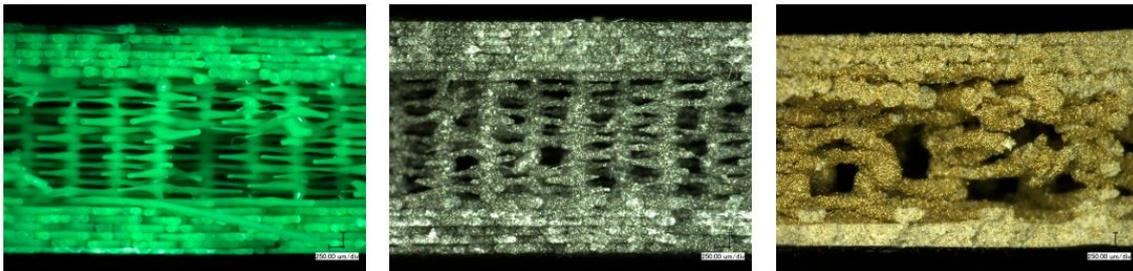


Figure 2.6: Microscopic images of specimens after tensile tests, prepared from PLA (left); Magnetic Iron (middle); and Bronzefil (right) [51].

In general, cracks were visible in the form of remarkable elongation in the infill area, while the lines in top and bottom areas were still strongly connected. Magnetic Iron and Bronzefil showed a higher irregularity of the infill lines, as compared to PLA, due to an inhomogeneous distribution of the solid content. Such inhomogeneities resulted in weaker areas, at the interface between metallic particles and polymeric matrix, suggesting the low tensile and flexural strengths measured for samples filled with solid content. Overall, the addition of metal powder within a polymeric matrix generates a reduction in the mechanical properties of the specimens when compared with those of the base polymeric material. This widespread worsening of the mechanical characteristics is also

independent of the type of thermoplastic material and solid content. Furthermore, the process parameters and the percentage of metal content are often irrelevant.

2.2 Metal ME Technology

Metal Material Extrusion (MME) is a novel variant of the traditional Material Extrusion technique, which involves the use of a multicomponent filament, made up of a polymeric matrix and metal powders evenly distributed. The basic principle of this alternative technique consists of multistep process divided in three stages. The shaping phase consists in the softening a filament, pushed through an heated nozzle, and the plotting of the softened material layer by layer according to a pre-defined path to form a coherent solid structure on a preheated platform to improve adhesion between parts and bed. The binder fraction is removed from the printed part through a debinding step using solvents and/or thermal debinding [52]. Lastly, the sintering phase provides interparticle bonding that leads to near full densification through a thermal cycle performed below the melting temperature [53]. The thermal treatment phases improve the mechanical properties of the metal components, achieving values comparable to those typical of the metal base material.

Metal ME process can be divided into three different typologies, as a function of the feeding system used. Screw based metal ME represents the most flexible system in term of material selection, since the range of different metal alloy filaments is still very narrowed. The production of rods or filaments requires special extrusion equipment to obtain feedstock with constant cross-sectional area and minimum ovality. Screw based systems use pellets as raw feedstock, which are also the starting element in Metal Injection Moulding (MIM) technology. The process relies on the rotation of the screw to transport the granulated feedstock close to the nozzle in conjunction with the heat generated by heating elements above the glass transition temperature of the polymer binder and the friction among metal particles and the screw walls. Cruz et al. developed an own screw system equipped with two band heaters, which were placed around the barrel to keep constant the temperature up to 250 °C during the plasticization process [54].

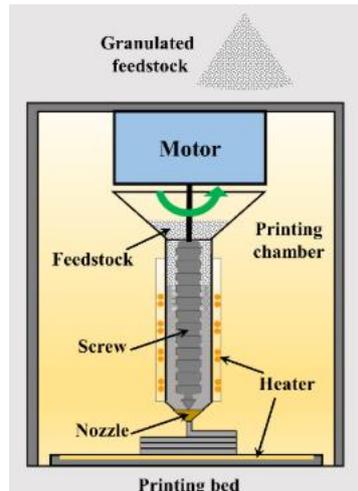


Figure 2.7: Schematic of screw-based feeding system [55].

Two main advantages feature the proposed feeding system. The feedstock can continuously be fed without any interruption due to replenishment. This leads to high productivity, since the overall printing time is reduced due to the unnecessary process stoppage during feedstock replenishment nor feedstock re-heating to the temperature required. Besides, the use of pellets as raw feedstock allows the consumption of high solid loading materials employed in MIM technique.

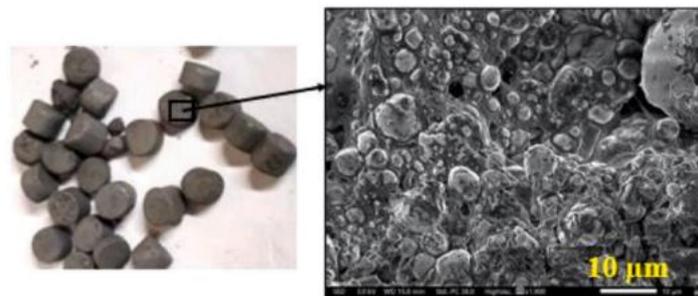


Figure 2.8: Low and high magnification of the 17-4PH stainless steel granulated feedstock [56].

The printing quality is ensured by a proper control of pellets size, since a dimension lower than 5 mm minimize defects caused by air entrapment [57]. Different authors [58,59] suggested that a size in the range of 3 to 5 mm could generate a good quality printing and an high density final part after sintering treatment. Large, granulated feedstock could generate issues during the softening phase; while granules size smaller than 3 mm could lead to the clogging of the extrusion head. The main drawback related to this system is

its stabilization, since it is difficult to maintain the material flow rate constant due to air trapped within the softened feedstock and the high viscosity of the heated pellets.

An alternative to screw-based systems is represented by plungers. A plunger-based process provides the use of circular bar feedstock, which are fit into a cartridge surrounded a heated sleeve and then fed into a plasticizing unit in charge of the softening of the material. The softened material is accumulated in a reservoir and a mechanical drive system, a plunger, drives the soft material in the melting zone.

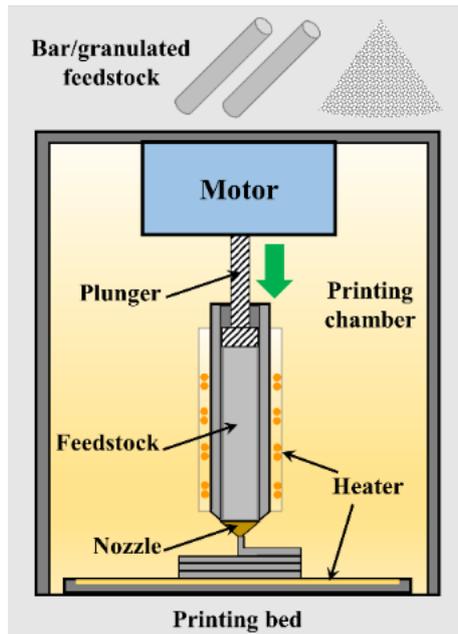


Figure 2.9: Schematic of plunger-based feeding system [55].

The main advantages concern the high material handling ability and the high solid loading content, which can be compared to MIM feedstock. Nevertheless, an additional step is required to transform the raw highly filled feedstock in circular bar feedstock. The main limitation is the time consuming print discontinuity related to the replenishment of the material. The disruption of the printing process results also in the quality deterioration of the shaped part. The solution proposed by Giberti et al. [60] consisted of a mixed system combining a screw in a plasticizer to feed the MIM feedstock and a plunger to push the feedstock through the heated nozzle (Figure 2.10). In this case, the reversing of the plunger is minimized by receiving the feedstock from the screw-based system.

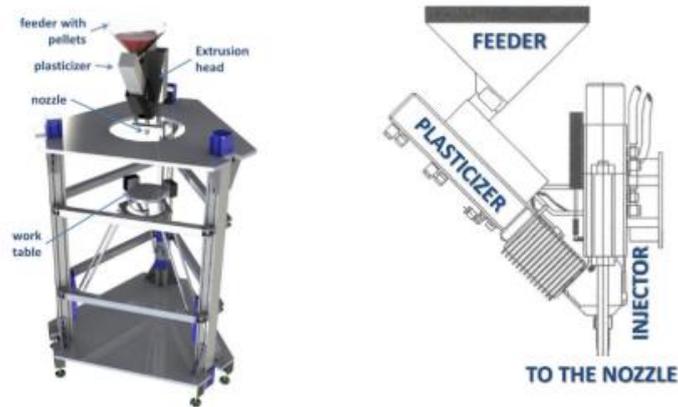


Figure 2.10: Set-up of combined plunger and filament based feeding system [60].

The most widespread feeding system is constituted by filament-based processes. A highly filled polymeric filament is fed by a transport system to the melting zone close to the heated nozzle, which oversees the extrusion process.

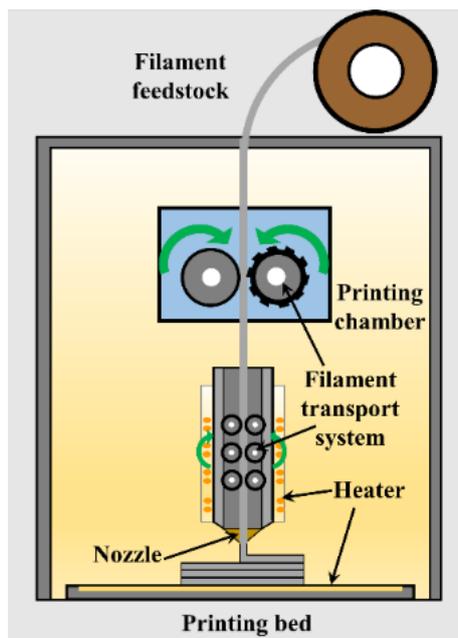


Figure 2.11: Schematic of filament-based feeding system [55].

The ease of use and safety in handling make this system the most used for extrusion-based techniques. On the other hand, the main disadvantage of this system is the need for filament production and an excellent know how for the material selection. The transport system is generally driving wheels which firstly pulls the spooled filament in the melting zone and then pushes the softened material through the nozzle. The driving wheels should be equipped with motors that generate a sufficient torque for the transport of the filament.

Besides, the wheels should have enough mechanical friction to transfer the force to the filament during its passage into the liquefier. The filament should be characterized by an appropriate level of mechanical strength to retain its shape during its transport by means of the driving wheels pushing the following softened material out of the printing head, and to avoid shearing due to the squeezing from the wheels. In addition to this requirement, the filament should also have enough flexibility to be spooled and stored on a coil facilitating the process of replenishment and extrusion into the liquefier.

2.2.1 Shaping

Shaping represents the first stage of this multi-step additive process and consists of the preparation of the required feedstock made up of polymeric blends and metal powder mixture and the printing phase of a green part by means of a ME machine. Each step of this process is essential for the successful manufacturing of the workpiece. In fact, obtaining a filament with specific physical and chemical characteristics will allow a print of excellent quality, avoiding the realization of green parts with criticalities that can not be fixed in the subsequent stages of thermal treatments of debinding and sintering.

2.2.1.1 Feedstock preparation

Most of polymeric filaments loaded with metallic particles are multi-components binder systems. The filaments containing more than 45 vol.% of metal particles become very brittle and their molten state viscosity increases considerably. The physical and mechanical properties required for extrusion are not satisfied with a single component binder and it is therefore necessary to use multicomponent polymeric binder systems.

The polymeric component of the feedstock has a great influence on the extrusion process and thus on the final properties of the sintered parts, even if the debinding step removes any traces of polymeric content inside the shaped component. The binder system is generally composed of three main binder groups. The main polymeric component is the low molecular weight element, which is the element in the largest amount in the range of 50 to 90 vol.% within the total binder system. The main binder mostly influences the extrusion process and undergoes the complete removal during the debinding treatment. The main elements in the binder system are polymers which ensure high flexibility to the filaments. Elastomers [61] and amorphous polyolefins [62] makes the feedstock flexible

enough to be spooled. Besides, the flexibility of filament can be improved by combining stiffer polymers (i.e., polyamide) and plasticizer components which can be easily dissolved during debinding. Polyacetal based components are even diffused, since it can be easily dissolved by catalytic degradation, which is the quickest debinding technique. Another crucial component within the binder mixture is the backbone. This secondary element is the higher molecular weight polymer and needs specific thermal and chemical properties to hold together the shaped part in the course of the removal of the primary binder during the first phase of the debinding process. The backbone is contained in least amount compared to the primary binder and it is removed by means of thermal degradation prior to sintering step. Since the backbone is responsible for the shape retention of the green parts, the material selected should not be susceptible to catalytic debinding and several types of polymer are suitable as secondary binder, such as Polyamide (PA [63]), Polypropylene (PP [64]) and Polyethylene (PE [65]). Lastly, a low percentage of additives in the range of 0 to 10 vol.% is added to total amount of multicomponent binder to act as surfactant and lubricant slightly modifying the properties of the feedstock. Indeed, these dispersant agents enhance the dispersion of metal powders within the binder mixture, prevent phase separation and minimize agglomeration of the filler particles. The most common used is stearic acid [66]. An optimized binder formulation is essential for the success of a green part printing, since it can affect the flexibility and the flowability of the feedstock, the superficial adhesion with the solid loading, the degradation rate during the debinding step and the porosity and final density of the sintered parts. Kukla et al. [67] evaluated the effect of three different backbones in a binder mixture, in which a thermoplastic elastomer was the main binder component. It was demonstrated the positive relationship between the improvement of modulus strength of the feedstock and the increase of backbone content in the multicomponent blend, without any deterioration of other properties, such as secant modulus and viscosity of the filament. Similarly, Cano et al. [68] studied different binder formulation considering the mechanical and rheological properties of filaments. Figure 2.12 shows the shear viscosity of the feedstock as a function of the angular frequency. It is noticeable that the single compounds (i.e., APO/No and SEBS/No) had a significantly higher complex viscosity values compared to two soluble components compounds, leading to a greater risk for nozzle clogging and a higher stiffness of the feedstock. Besides, no relevant difference

could be depicted between two different two soluble components mixture characterized by the same main binder element.

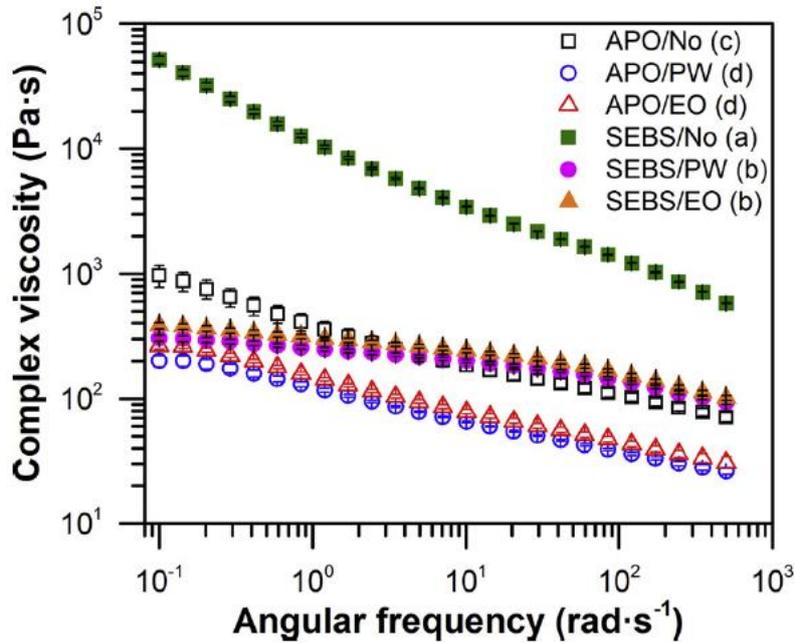


Figure 2.12: Shear viscosity as a function of the angular frequency for different binder systems measured at 150 °C [68].

Besides the viscosity, which plays a critical role in the mixture of the feedstock and the subsequent extrusion phase, the mechanical properties greatly influence the selection of binder formulation for the desired feedstock. Comparing single and double soluble components compounds, a significantly higher secant modulus (Figure 2.13C) and a higher UTS or yield stress (Figure 2.13A) was registered by adding a second soluble component, since the wax increased the crystallinity of the primary binder. Nevertheless, the corresponding strain values exhibited a worsening (Figure 2.13B) due to the poor mechanical properties of the wax, acting as defects points in the amorphous phases of the rest of the components.

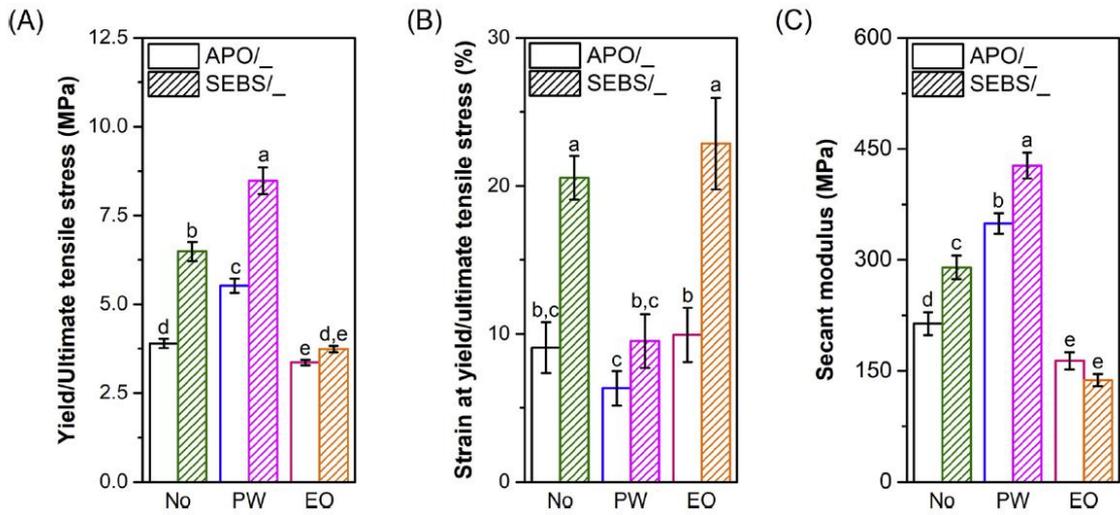


Figure 2.13: Tensile properties of filaments made up of different binders: (A) Yield or ultimate tensile stress, (B) strain at yield or at the ultimate tensile stress, and (C) secant modulus [68].

Analogous results were obtained in [69], studying the variation of a plasticizer from 0 to 100 vol.% within linear low density polyethylene as primary binder. The increase of plasticizer content reduced the viscosity of the feedstock owing to the intrinsic property of polyethylene wax used. However, the shaped component experienced a general worsening of its compressive behaviour. An optimized level of binder mixture containing 40 vol.% of plasticizer was selected to balance the rheological and mechanical properties of the feedstock.

Along with the binder formulation, the powder content, as well as its size and distribution, have a significant impact on the extrusion phase and on the final properties, both physical and mechanical, on the sintered samples following the final step of thermal treatments. To date, few alloys have been developed and commercialized, since the compatibility with multicomponent binder and debinding and sintering phases required lots of effort to expand the amount of material availability to be used with metal Material Extrusion Technique. AISI 316L and AISI 630 (17-4PH) are two main commercially widespread alloy used, followed by Ti-6Al-4V alloy and Nickel superalloys, as plotted in Figure 2.14.

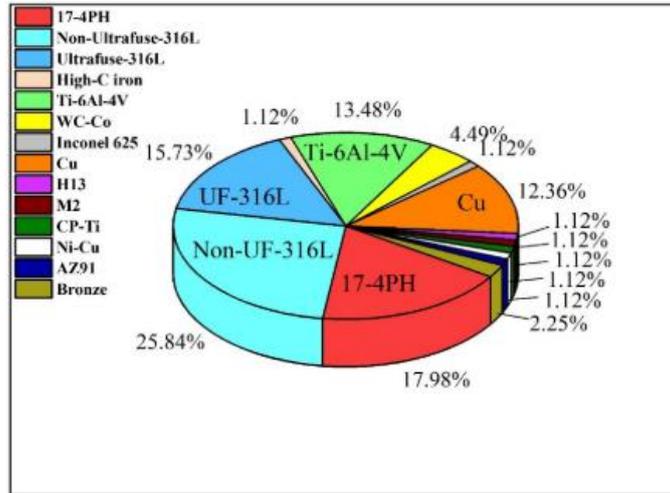


Figure 2.14: Alloys utilized to fabricate 3D parts by material extrusion additive manufacturing processes [55].

The change of powder characteristics heavily affects the mechanical and rheological properties of feedstock materials. The type of filler particles resulted to influence the processability and the tensile strength of different filaments. Kukla et al. [67] verified the viscosity and the mechanical properties of the filaments varying the powders distributed in the multicomponent compound. Since relevant chemical modifications occur, different rheologic behaviour resulted using different type of fillers. Different powders also have an influence on the mechanical properties of filament, despite all the filaments contained the same class and amount of binder formulation. The filament loaded with AISI 316L stainless steel particles exhibited the highest UTS and elongation at break. On the contrary, titanium powders generated lower value of tensile stress and flexibility, resulting in worse spooling, feeding and printability of the filament.

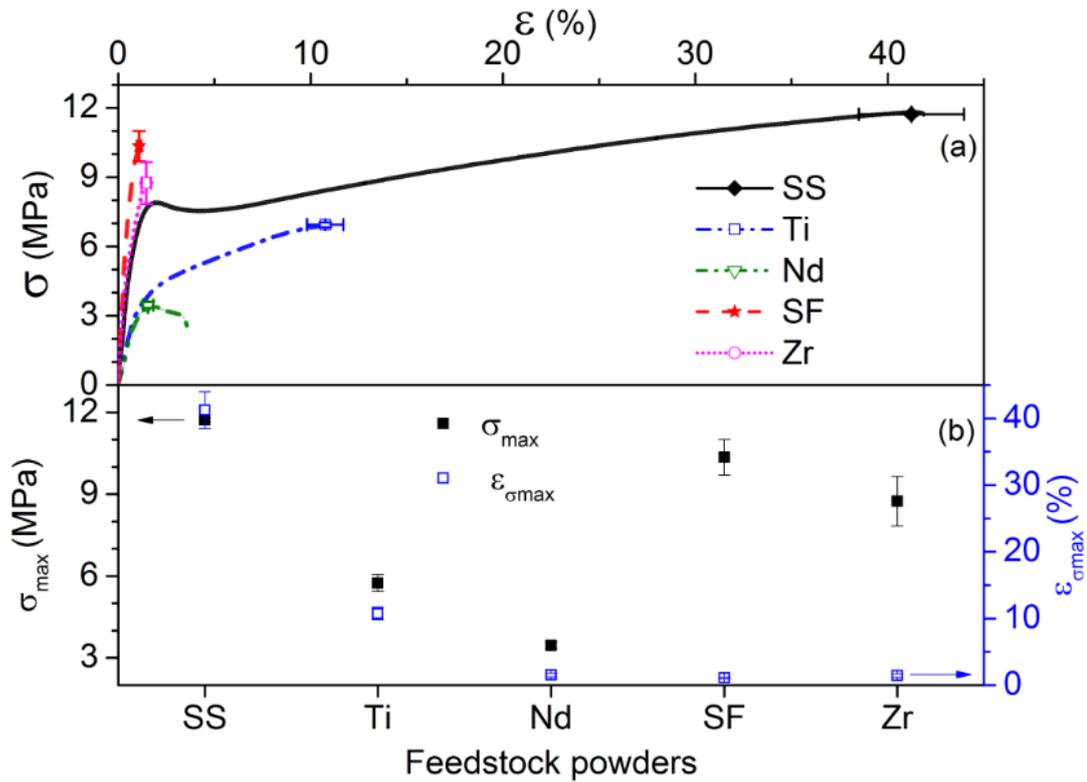


Figure 2.15: ϵ - σ curves (top) and σ_{\max} and ϵ_b (bottom) for filaments loaded with different solid loadings [67].

Besides, the morphological characteristics of the powders (e.g., size and shape) can influence the physical and mechanical properties of the feedstock materials [19]. Wu et al. [66] utilized two AISI 630 stainless steel powder with different morphology, spherical powders in the range from 3.9 to 44 μm and irregular powders in the range from 2.8 to 44 μm , stating that spherical particles are preferable due to lower viscosity compared to irregular shaped ones. Also, the influence of the powder size has been widely investigated. In [70], feedstocks containing 316L steel powder with different particle sizes were characterized in terms of viscosity and mechanical properties. Besides, also the printability of the different feedstocks was verified. Smaller particles had an average size of approximately 5.5 μm (D50), while larger particles average size was approximately 8.6 μm (D50). The increase in particle size enhanced the printability of the feedstock since the apparent viscosity decreased. Besides, a general worsening of mechanical properties of the filament occurred by rising powder dimensions, as the secant modulus decreased of 42% and the elongation at break decreased of 35%.

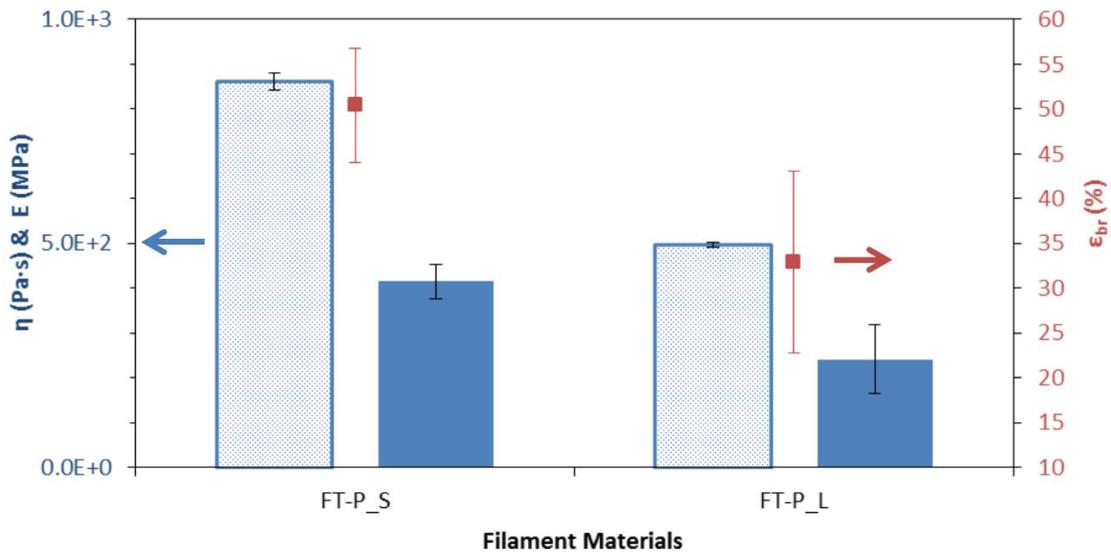


Figure 2.16: Apparent viscosity (η), secant modulus (E) and elongation at break (ϵ_{br}) for filaments with different particle sizes [70].

Similarly, Singh et al. [71] studied the effects of fine ($D_{50} = 13 \mu\text{m}$) and coarse ($D_{50} = 30 \mu\text{m}$) Ti-6Al-4V powders evenly distributed in a multi-component polymeric binder. Both type of fillers exhibited a decrease in viscosity increasing the shear rate from 20 s^{-1} to 800 s^{-1} . For all the shear rate values tested, coarse powders had a lower viscosity improving the flowability and extrusion properties of the filament. Fine powder generated an higher interparticle friction, as smaller interstitial spaces existed among the mixture [72]. Furthermore, fine powder had larger particle surface contact area between powder particles requiring a higher binder amount for uniform wetting. Lastly, the powder content plays a crucial role in the final properties of highly filled filament. Generally, the solid loading content lies in the range of 60 to 65 vol.%. Few studies analysed the effects of increasing the powder content above the target limit of 65% in volume. Giberti et al. [60] used a MIM commercial feedstock made up of AISI 630 martensitic stainless steel with a concentration of 79% in volume dispersed in water soluble polyethylene glycol and performed extrusion to evaluate the accuracy of parallel kinematics configuration. Higher solid loading provides a higher density with lower dimensional shrinkage after sintering. An excessive solid loading could lead to unprintability due to high level of viscosity of the feedstock. Gonzalez-Gutierrez et al. [73] evaluated the effect of the increase of solid loading on the mechanical properties of feedstock. Indeed, the 5 vol.% increase of AISI 316L and $\text{Fe}_{12}\text{O}_{19}\text{Sr}$ worsened the ductile behaviour of the feedstock. Despite the

brittleness of both filaments, the further addition of AISI 316L did not stopped the correct feeding and printability of the feedstocks. Diversely, the 5 vol.% of $\text{Fe}_{12}\text{O}_{19}\text{Sr}$ within the multicomponent binder required to be fed manually and the green parts resulted more fragile during the removal from the build plate. This behaviour suggested the maximum solid loading depends on the type of material, due to the diverse particle-matrix chemical interaction.

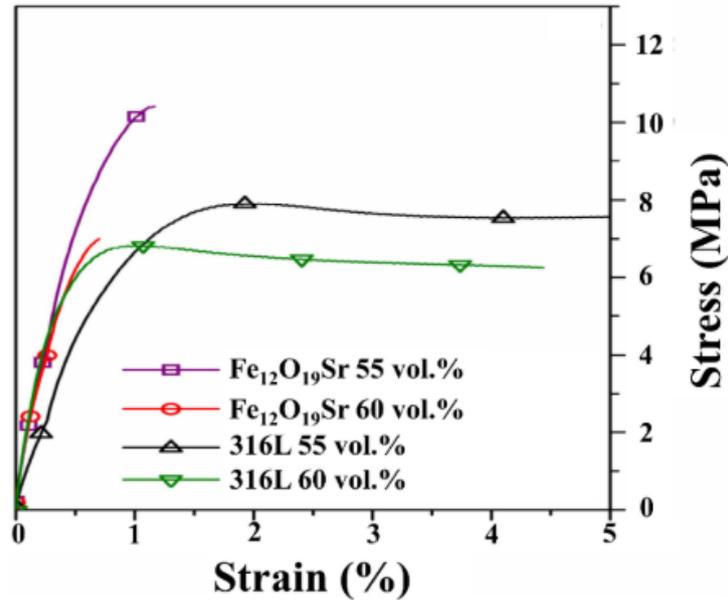


Figure 2.17: Stress – strain curves for 316L and $\text{Fe}_{12}\text{O}_{19}\text{Sr}$ 316L filaments with different solid loadings [73].

The solid loading also affects the rheological behaviour of binder mixture compound. Rane et al. [74] tested the viscosity of a filament, varying the powder content among 50, 54 and 63 vol.%. In all three cases, a very steep decrease in viscosity increasing shear rate was observed. Additionally, an increase of the solid loading within the polymeric compound deteriorated the rheologic behaviour of the feedstock, since the higher the powder content, the greater is the interparticle friction generated.

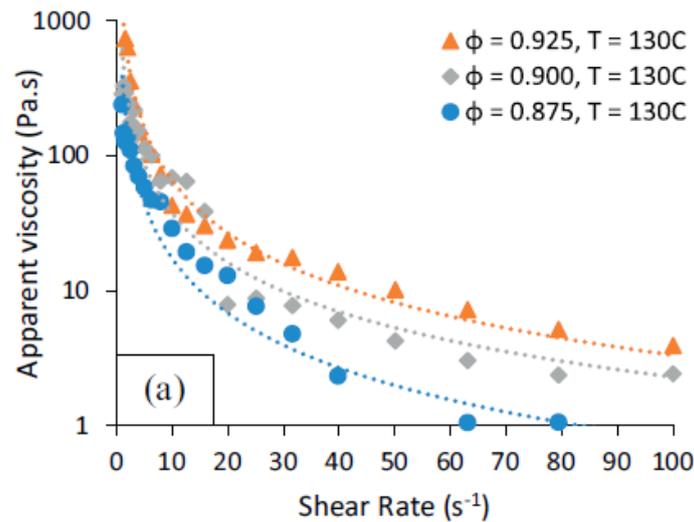


Figure 2.18: Apparent viscosity of SS316L feedstock having different solid loading [74].

The production of filaments affects their processability and printability since different properties of the filament could be modified by different extrusion processes. According to the volume production, dissimilar processes can be used: capillary rheometers [75] for small batches and single [49] or twin [76] screw extruders for larger volumes. The primary requisite for an adequate filament stands for a homogenous distribution of the metal filler within the multicomponent binder. Homogeneity helps to minimize segregation of particles or binder within the feedstock. Segregation could deteriorate the final sintered parts in terms of excessive anisotropic shrinkage or visible porosity and cracks, since a disproportionate content of binder in a small area portion could generate voids during the debinding phase that the sintering process could not densify. A possible solution to prevent segregation of binder domain or metal powder within the compound is the use of high shear mixing techniques. Abel et al. [76] compared the mechanical properties of two filaments fabricated with different mixing technique: a contra-rotating roller mixer (RM) that generated low shear forces and a high shear compounding twin screw extruder (TSE). By looking at Figure 2.19, it can be noticed that the filament compounded and produced by means of a twin screw extruder after compounding in the twin screw extruder had higher values of ultimate tensile strength and elongation at break, while its secant modulus is smaller than those of the filament produced after compounding in the roller mixer. The ductility of TSE filament enhanced its printability because the

high shear action of the twin screw extruder broke the powder agglomerates and dispersed the single metal particles.

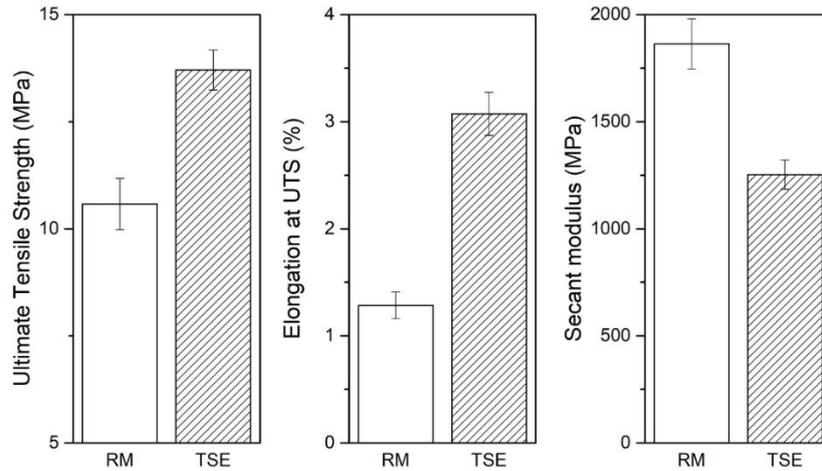


Figure 2.19: Influence on mechanical properties of feedstock fabricated with different compounding methods (RM and TSE) [76].

In addition to the homogeneous distribution of metal particles in the polymer matrix, the wire geometry is a further parameter to be considered in assessing printability of the feedstock. A constant geometry of a filament, in terms of wire diameter, positively influences the transport, the feeding and the extrusion phase of the printing process, since dimensions exceeding the target measures resulted in buckling of the filament in the extrusion head due to the excessive flow rate; while the opposite situation could lead to under-extrusion causing voids, poor bonding and geometrical inaccuracy of the sintered parts after the debinding and sintering treatments. Gutierrez and Gonzalez et al. [77] suggested that an acceptable deviation from the desired diameter is represented by the difference of 0.05 mm. The roundness of the filament may affect the printing process. The ovality is defined as the difference of the diameters in the horizontal and vertical directions. Thus, a perfect round shaped wire has no ovality since both diameters are equal. Lengauer et al. [78] fabricated an highly filled filament, which was made up of hardmetal powders (WC-10% Co) and a mixture of thermoplastic elastomer TPE as primary binder and polypropylene as backbone, by means of a capillary rheometer. The filament had a constant ovality distribution within ± 0.030 mm, which is sufficiently low to consider the filament rounded. Besides, the SEM image (Figure 2.20) confirmed the

compatibility of hardmetal particles and binder compound, resulting in an equal distribution.

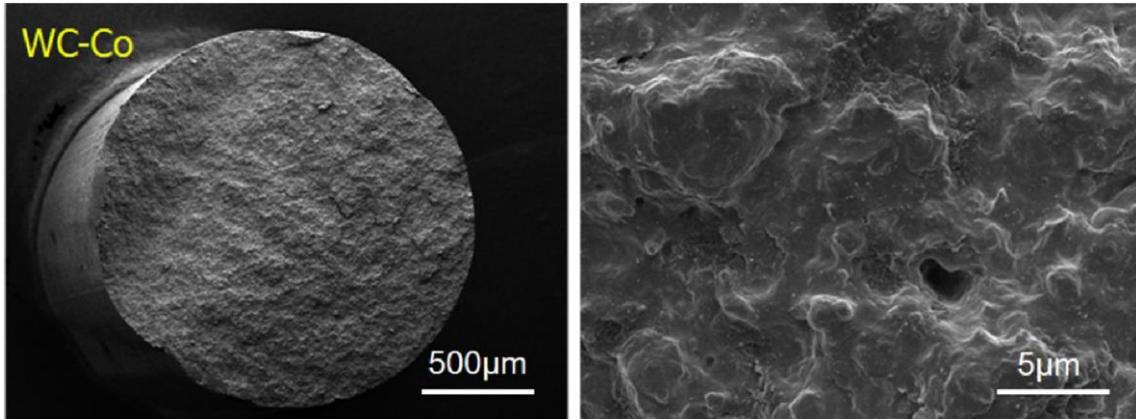


Figure 2.20; Overall view and detail of the filaments filled with hardmetal powders [78].

Other researchers [79] evaluated how any change in the extrusion temperature could affect the mechanical properties of the samples and its surface quality. It was suggested that low extrusion temperatures and medium extrusion speed ensured the best results in terms of ductility and surface quality of the filament. An extrusion temperature within the range of 155 to 160 °C conducted to the highest level of density and no break during bending test, in addition to good surface quality as shown in Figure 2.21. Besides, the ductility of the filament increased the buckling tendency of the filament worsening the printability due to nozzle clogging and cracks in the printed parts.



Figure 2.21: Extruded filaments with good and scarce surface quality [79].

Similarly, Singh et al. [75] evaluated the effects of extrusion temperature on the properties of the filament loaded with 59 vol.% coarse Ti-6Al-4V powder. The density of the filament lowered from $99.8 \pm 0.2\%$ to $91.2 \pm 0.2\%$ with the increase of temperature from

105 °C to 135 °C; while at 145 °C, the density increased to $99.9 \pm 0.1\%$. The variance of density values was consistent with the topographical observation in Figure 2.22.

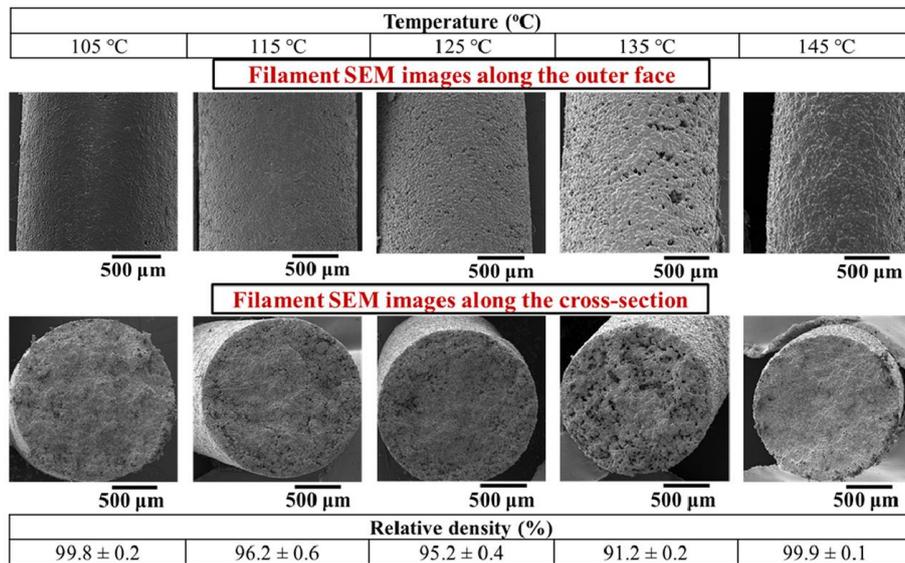


Figure 2.22: Effects of extrusion temperature on filament attributes: surface and bulk morphology and density [75].

Furthermore, the different extrusion temperatures also affected the geometry and the surface roughness of the tested filament. It is evident in the graphs plotted in Figure 2.23 that the highest temperature of 145 °C led to an excessive decrease of the wire diameter (i.e., 1.59 ± 0.09 mm) and worsened its superficial quality, since the surface roughness increased from 2.4 ± 0.04 μm at 105 °C to 6.7 ± 0.7 μm at 145 °C.

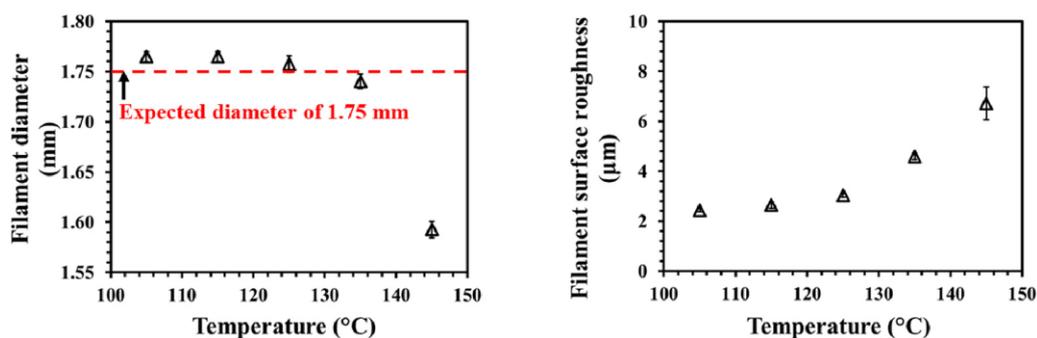


Figure 2.23: Effects of extrusion temperature on filament diameter (left) and surface roughness (right) [75].

The levels of feed rate and flow rate lead to a variance of filament properties during the extrusion process. The feed rate consists of the velocity of the extrusion and it is expressed in mm/s. Singh et al. [71] stated that the increase of feed rate required force to overcome

the pressure drop, increasing the viscosity of the feedstock. Besides, fine powders required higher force owing the higher viscosity compared to coarse powder for assessing continuous material flow.

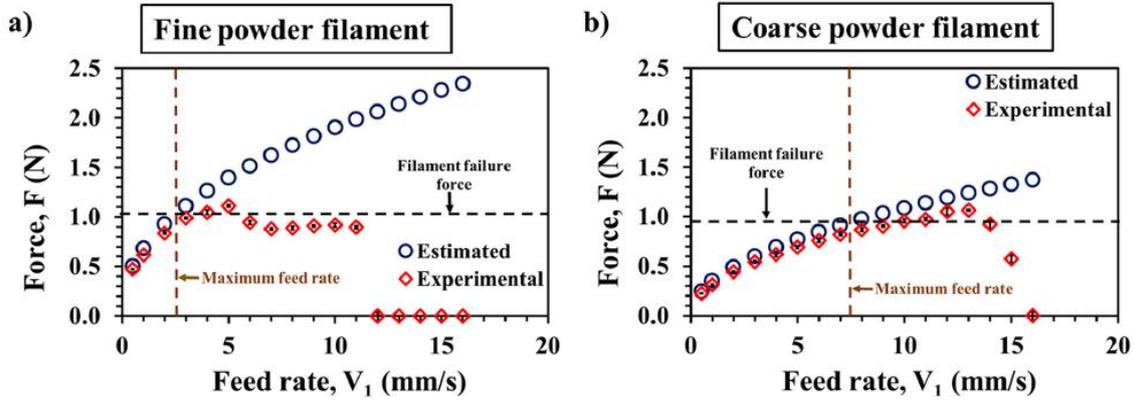


Figure 2.24: Force to overcome the pressure drop for fine powder (a) and coarse powder (b) [71]

Flow rate is the quantity of extruded feedstock coming out of an heated nozzle in the unit of time and it can be expressed as L/sec. Increasing the flow rate tend to improve the viscous behaviour of the feedstock [80]. In addition to the quantity of wire produced, the nozzle size reduced the viscosity in inverse proportion, as represented in Figure 2.25.

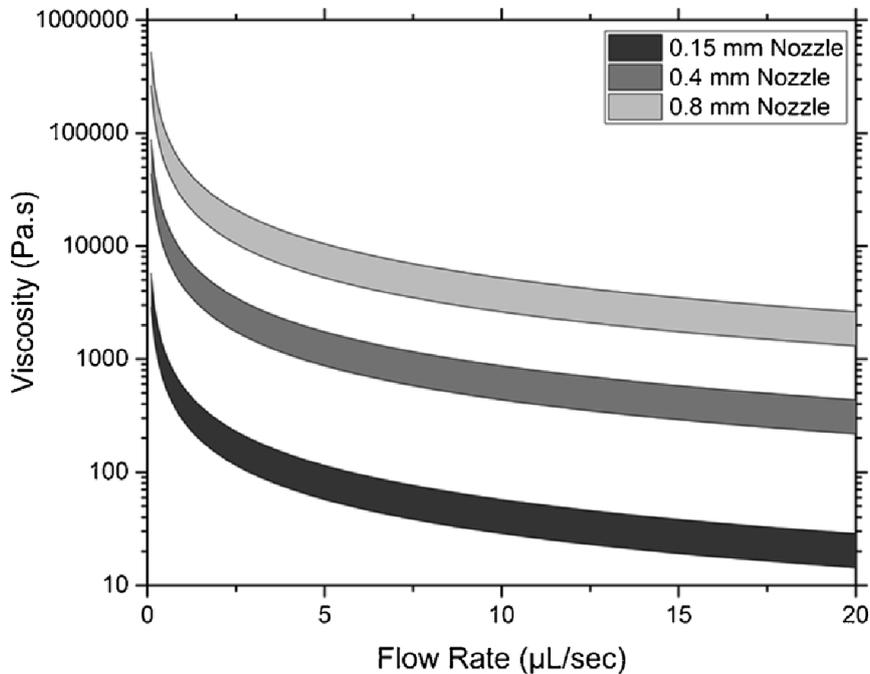


Figure 2.25: Maximum extrudable viscosity as a function of flow rate and nozzle diameter [80].

Different authors proposed various set-up of the extrusion process to improve the geometric properties of extruded filaments. As an example, conveyor belts (Figure 2.26) were placed at the end of the extruder head to transport the wire from the extrusion zone to the spooling system to minimize any distortion of the filament during the handling phase [77,80].

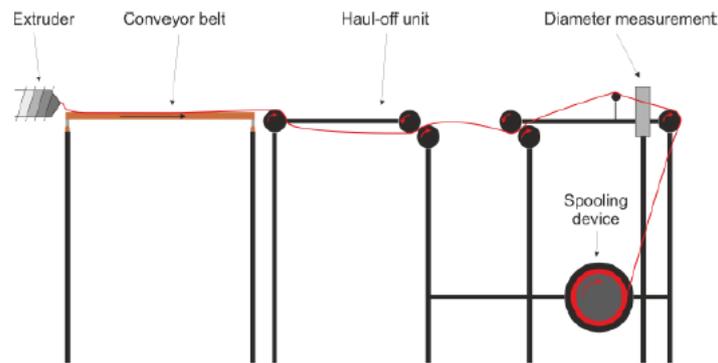


Figure 2.26: Schematic representation of filament extrusion line equipped with a conveyor belt [81].

Rane et al. [74] evaluated the effects of vertical extrusion process on the major filament characteristics. This work revealed that shrinkage rather than swelling occurred during vertical extrusion process. In particular, when the extrusion temperature was kept stable around 130 °C, no relevant difference between the two dissimilar extrusion nozzles (i.e. 0.6 and 0.9 mm) was detected. Increasing the temperature up to 140 °C, the smaller nozzle generated swelling without any compensation owing to the gravity loading. Furthermore, shrinkage of the produce filament increased for fewer solid loading (i.e., 50 vol.%), since there was a larger amount of polymeric content resulting in higher flow rate and lower viscosity. During the extrusion phase, the cooling rate was slower and the filament experienced shrinkage due to its own weight.

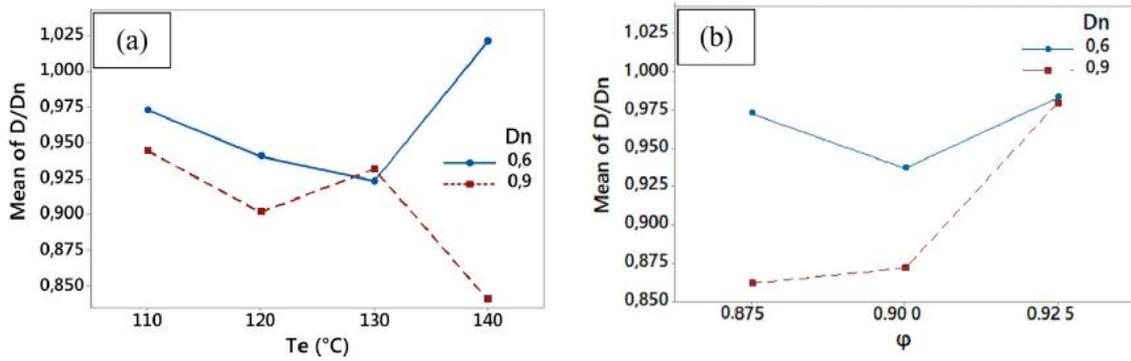


Figure 2.27: Effect of nozzle diameter and extrusion temperature (a) or solid loading (b) on diameter of vertically extruded wire [74].

During the production of the filament by means of different extrusion process, it is important to monitor the level of air trapped within the compound, since it could lead to cavities generation inside the feedstock. In Figure 2.28, cavities resulted from air entrapment during the production of the filament with a single screw extruder are visible. Cavities can cause the worsening of the mechanical properties of filaments in terms of flexibility and stiffness, compromising their printability.

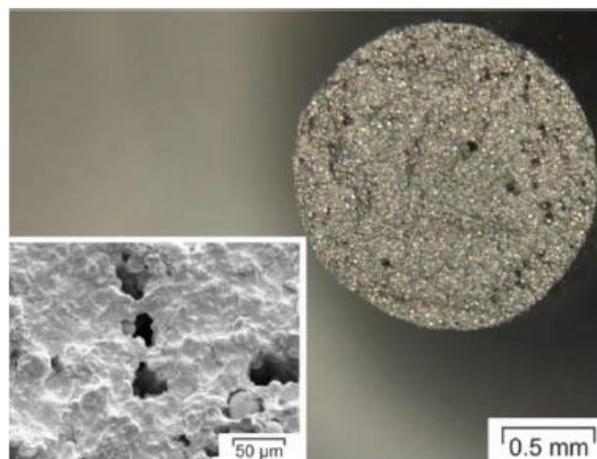


Figure 2.28: Section of a highly filled filament with visible cavities [61]

2.2.1.2 Green parts printing

The extrusion and deposition processes directly affect the result of the multistep ME technique to obtain high quality sintered parts in terms of physical and mechanical properties. Therefore, the choice and the optimization of printing process parameters influence the fabrication of green parts with desired characteristics. The achievement of specified properties of the green parts ensured proper metal parts. Although there are

several adjustable printing parameters, some of these are more critical in determining the final properties of the green parts.

Extrusion temperature represents the temperature of the extrusion nozzle, which has the task of heating and softening the filament before its deposition and it plays the most crucial role in the shaping of a green part. Any change in extrusion temperature influence the mechanical properties and the geometric accuracy of the shaped part. The nozzle temperature is directly dependent on type of binder compounded within the feedstock. Indeed, a nozzle temperature slightly above the melting point of the primary binder could successfully reduce the viscosity of the filament enhancing the deposition process. In [82], an extrusion temperature of 290 °C was selected, since the melting point of the used filament was around 220 °C. At a temperature of 270 °C, the viscosity of the feedstock was too high to allow continuous extrusion during the printing process. On the contrary, a bit higher temperature (i.e., 295 °C) resulted in unsuccessful printing trials, since it hindered a proper adhesion of new layers on the previous cooled ones.

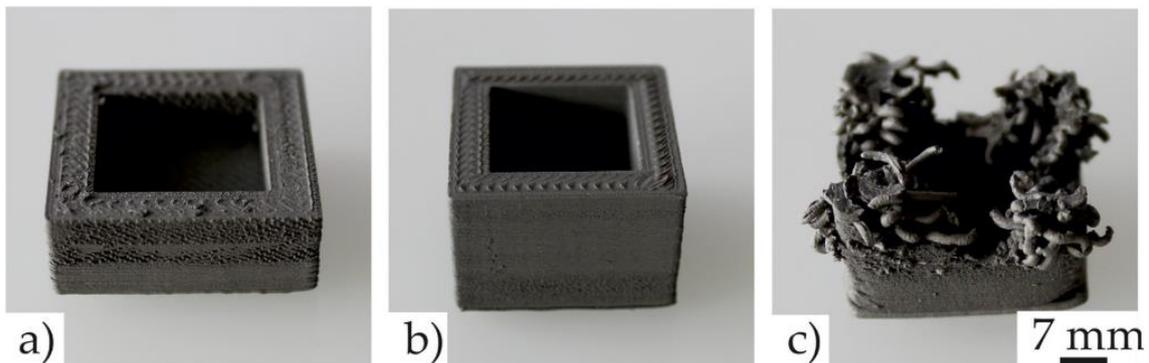


Figure 2.29: Printing Trials with nozzle temperature 270 °C (a); nozzle temperature 290 °C (b); nozzle temperature 295 °C (c) [82].

Closely connected to the extrusion temperature, the temperature of the building plate is a printing process parameter that should be considered to obtain a free defect shaped part, since an improper adhesion of the green part to the platform could lead to the detachment of the part resulting in poor-quality printed objects, likely due to shifts, warps or delaminations during the printing process. Spoerk et al. [83] suggested that a slight increase of the bed temperature above the glass transition temperature (T_g) of the primary binder enhanced the adhesion bonding between the first layer deposited and the build plate, owing to a reduction of the surface tension and a larger contact area between the printing platform and the material.

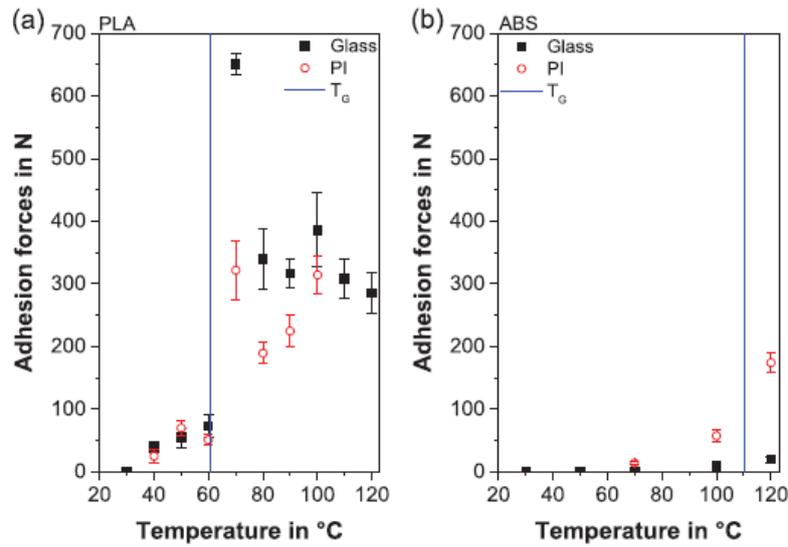


Figure 2.30: Adhesion force of printed parts varying the bed temperature [83]

The printing speed, also known as feed rate, impacts on the printability of green parts, since it affects the shape geometry and the final density of the component. Besides, the printing speed also affect the total printing time and, though, it changes the direct cost of an object. Excessive printing speed generates a critical amount of residual stresses within the build object provoking high deformation and walls distortion [84]. In [71], the relation between level of printability and feed rate was assessed. The filaments loaded with fine powder exhibited good printability up to 2 mm/s feed rate. Within the range of 2 to 4 mm/s a non uniform feedstock deposition occurred resulting in wide gaps of the structure. Above 4 mm/s, the high feed rate completely hindered the extrusion process, since no object could be printed. Diversely, a printing speed of 8 mm/s ensured a correct printing process for filaments filled with coarsed metal particles, increasing the window of feed rate for a proper printability of highly filled feedstock. The higher viscosity of fine powder caused the higher worsening of surface quality compared to coarsed powder filaments.

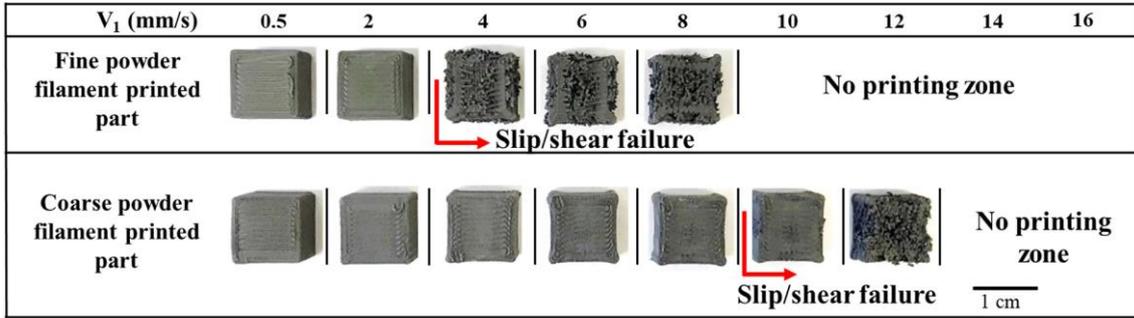


Figure 2.31: Effect of feed rate on the printed geometry as a function of the powder shape [71]

Additionally to the surface quality, the authors also investigated the relationship among the increase of feed rate, the dimensional accuracy and the mass of shaped parts. Concerning the dimensional deviation, the feed rates higher than 2 mm/s resulted in a considerable increase of the deviation from $1.7 \pm 0.3\%$ to $6.8 \pm 0.9\%$. Analogous to surface quality and dimensional accuracy, the increase of printing speed negatively affected the final mass of the green part.

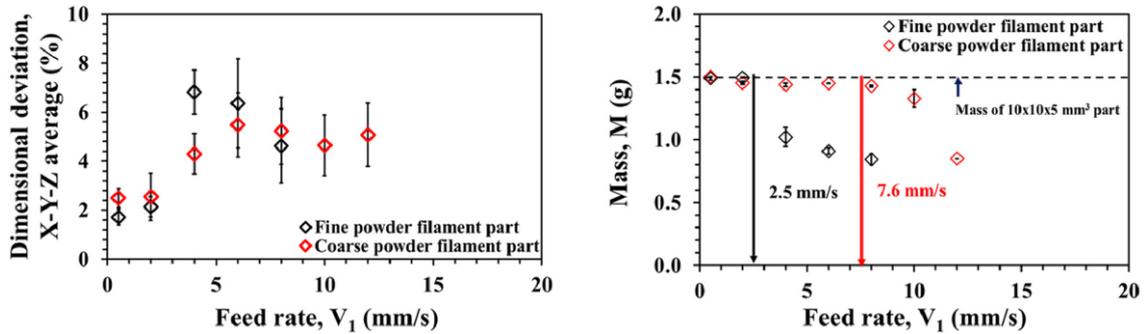


Figure 2.32: Effect of feed rate on the dimensional change with respect to the CAD file geometry (left) and printed part mass (right) [71].

In [85], the effects of various printing speed on green density and surface roughness of shaped parts were investigated. Primarily, the authors noted that the printing speed was the dominant parameters affecting the indicators compared to extrusion temperature, extrusion multiplier and layer thickness.

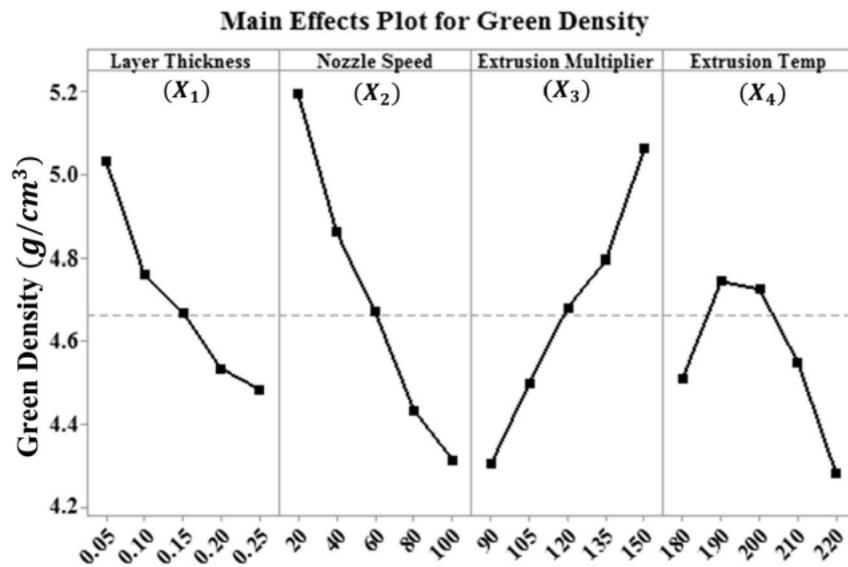


Figure 2.33: Main effects plot of green density as a function of different process parameters [85].

Additionally, the increase of printing speed from 20 to 100 mm/s drastically reduced the partial density of the green parts. Slow printing speed ensured a homogenous extrusion and deposition of the feedstock, minimizing the formation of large voids within the strands and between the consecutive layers deposited. Indeed, Figure 2.34 shows the deposited layers of parts printed with 20 and 100 mm/s. A larger amount of extrusion and printing voids can be depicted for to the samples fabricated with 100 mm/s nozzle speed.

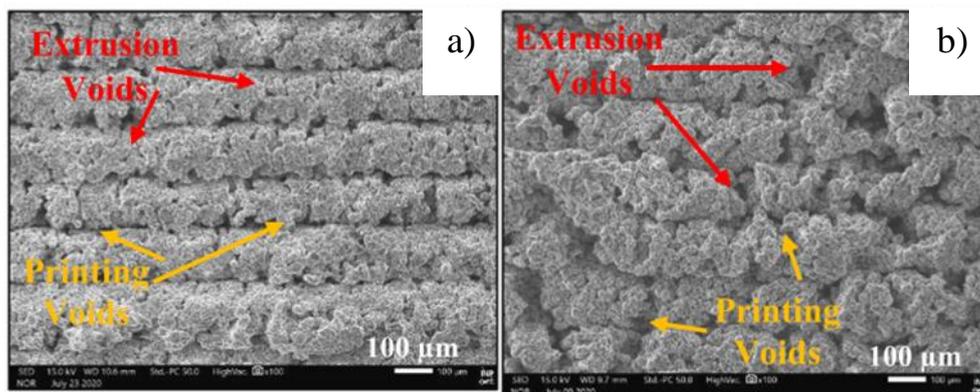


Figure 2.34: SEM images of the samples fabricated with varying nozzle speed 20 and 100 mm/s (a and b) [85].

The layer height, or layer thickness, represents the height measured along the Z axis of each layer deposited during the printing process. The height of a layer is always less than the diameter of the extruder nozzle due to technical constraints and it has an impact on

both the green density and the surface quality of the parts realized by means of ME technology. Another indicator affected by the layer height is the total printing time. Despite the total extruded material corresponds to the same amount independently of the layer thickness chosen, smaller heights increase the number of deposited layers, impacting on the route of the nozzle and slowing down the printing process.

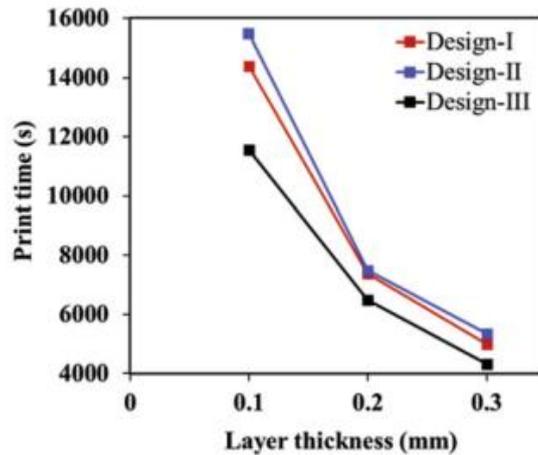


Figure 2.35: Print time with varying the layer thickness [86].

Singh et al. [85] suggested that the smaller layer thickness improved the green density of the build part, since smaller dimensions reduced the size of the printing voids between the layers and induced shrinkage of the extrusion voids due to the pressure applied for the lateral spreading of material. In Figure 2.36, it is noticeable the worsening of the surface quality of samples printed with 0.05, 0.15 and 0.25 mm layer height due to the enhance of extrusion voids within the strands and printing porosity between adjacent layers.

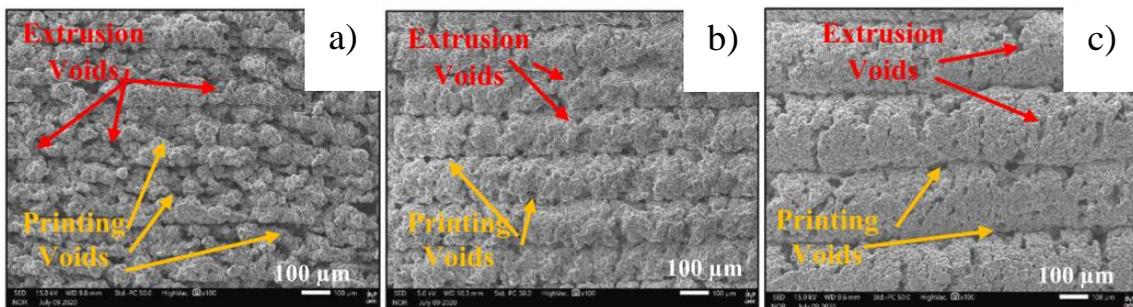


Figure 2.36: SEM images of the samples fabricated with varying layer thickness 0.05, 0.15 and 0.25 mm (a–c)[85].

Diversely, in [75], no relevant impact was detected for the increase of the layer thickness on the density and the surface roughness of the green parts. Indeed, an analysis of variance

was conducted selecting a confidence interval of 0.05. The registered p-value of the layer height following the statistical analysis were 0.4 and 0.1 for the relative density and the surface roughness, respectively.

Godec et al. [87] related the variation of the layer height as input parameter and the mechanical properties of the fabricated green parts. As evident in Figure 2.37, the increase of the layer height from 0.1 to 0.3 mm improved the tensile strength and the tensile modulus of the samples. The increase of the layer thickness reduces the number of deposited layers. The interlayers region represents the weakest area of a sample, since there is discontinuity of material between strands, a reduced cross-section due to the introduction of voids and fracture mechanic-type stress concentrations. Therefore, these issues could be reduced by decreasing the number of deposited layers and, thus, heightening the layers size.

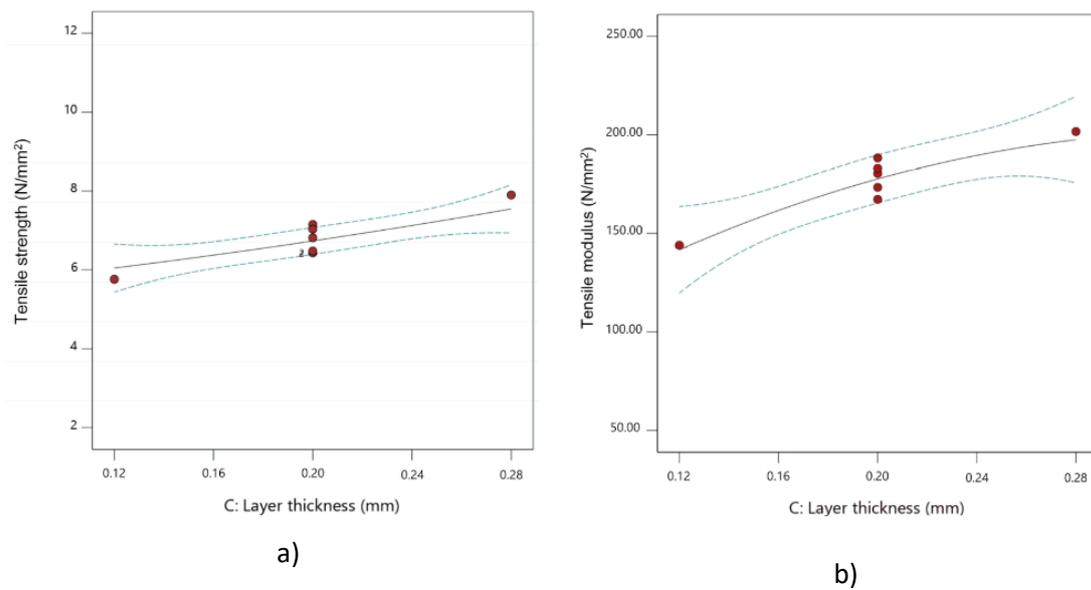


Figure 2.37: 2D graph of the influence of layer thickness on tensile strength (a) and tensile modulus (b) (flow rate multiplier 110%, extrusion temperature 235 °C) [87].

Another crucial printing process parameters is the extrusion multiplier, which controls the volumetric flow rate of the extruded feedstock. A high value of the extrusion multiplier increases the flow rate, resulting in the increase of the lateral spread of the roads and in the reduction of air gaps due to the improved adhesion of the adjacent layers. An air gap represents the distance between two adjacent and consecutive depositions, as represented in Figure 2.38. The value of can be zero, positive or negative. In the case of zero air gap, the materials deposited side by side and are slightly in contact with each

other. If the value is positive, the extruder will deposit the material at a certain distance from the previous layer, resulting in an uncompact structure. An air gap with a negative value is generated, leading to a denser structure and needs certain mechanical characteristics of the component [88].

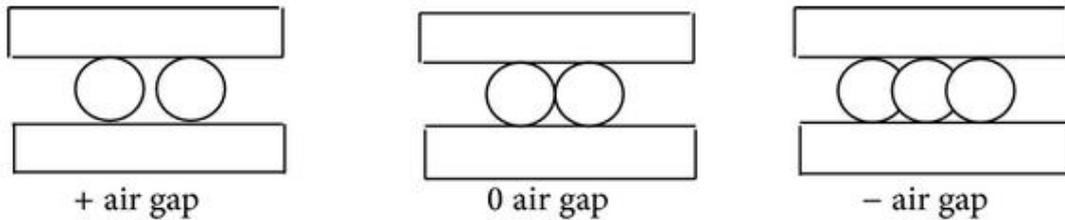


Figure 2.38: Air gap between two adjacent depositions [88].

The flow rate multiplier has a physical constraint on higher levels because the supply of excessive material through the nozzle can lead to its clogging. A clogged nozzle avoids a correct printing leading to void creation in the fabricated specimens. In [85], an improvement of the density of green parts was observed with the increase of the extrusion multiplier from 90% up to 150% (Figure 2.39).



Figure 2.39: SEM images of the samples fabricated with varying extrusion multiplier 90% and 150% (a and b) [85].

Similarly, Singh et al. [75] discovered the benefit of increasing the flow rate above 100% extrusion multiplier, which corresponds to the standard flow rate. Indeed, a 120% flow rate reduced the spacing between adjacent layers and lowered the porosity, resulting in a better green density. Besides, the extrusion multiplier emerged as the most critical factor based on ANOVA analysis.

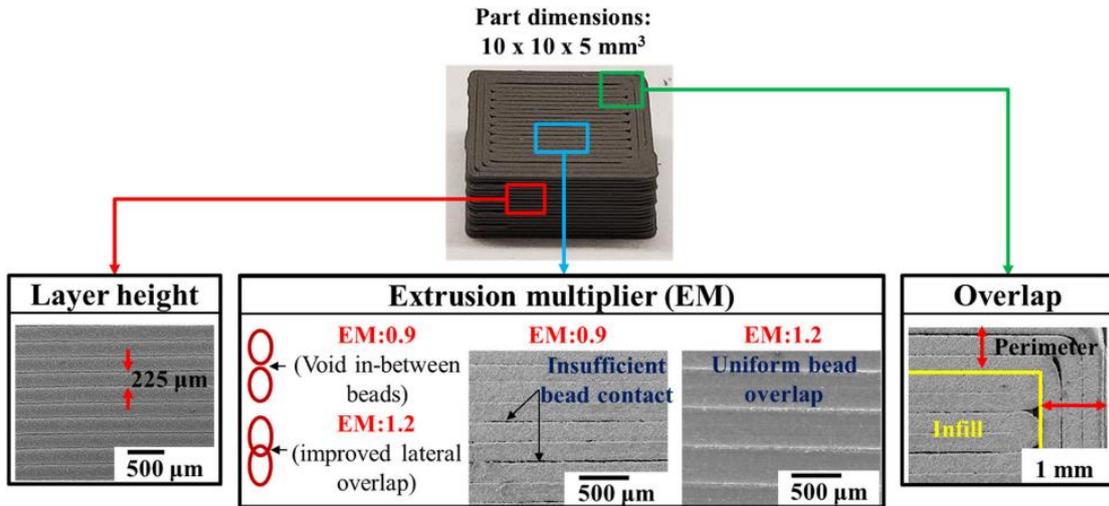


Figure 2.40: Printing parameters affecting the quality of MF3 samples. The influence of extrusion multiplier affecting the surface quality of ME samples [75].

Reducing the voids between deposited strands and the overall porosity of the structure, the flow rate multiplier parameters provided considerable benefits to the mechanical properties of green parts loaded with AISI 630 stainless steel particles [87].

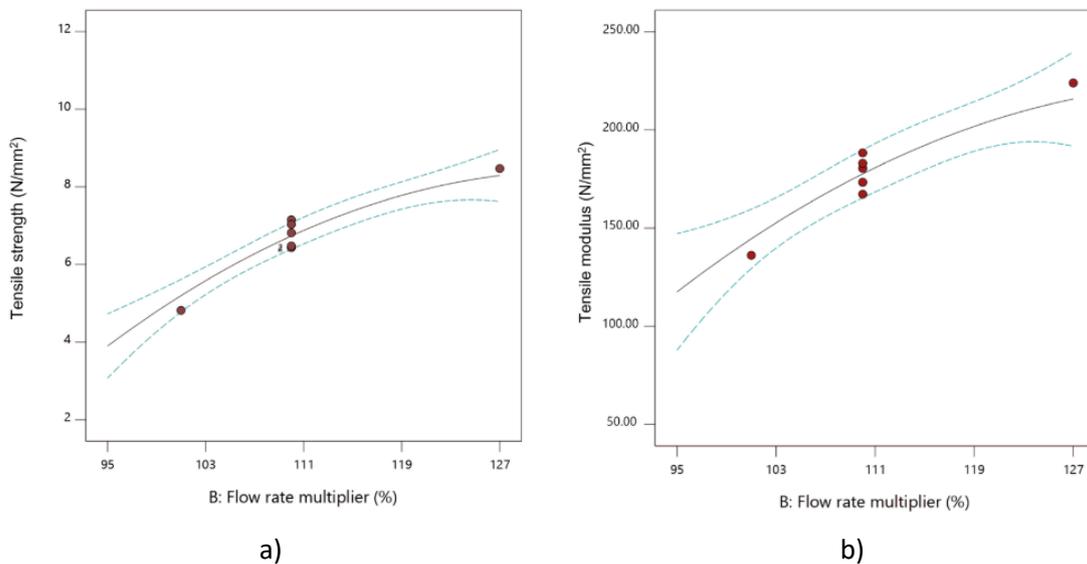


Figure 2.41: 2D graphs of the influence of flow rate multiplier on tensile strength (a) and tensile modulus (b) (extrusion temperature 235 °C, layer thickness 0.20 mm) [87].

In [61], different samples made up of AISI 630 powder distributed in thermoplastic elastomer (TPE) and a polyolefin-based backbone mixture and were printed varying the flow rate of the extrusion head. Increasing the flow rate improved the coalescence between the printed strands, ensuring the quality of the green samples, especially for the

top view. However, the authors warned for the risk of blobs appearing on the surface of a shaped part when too much material is supplied.

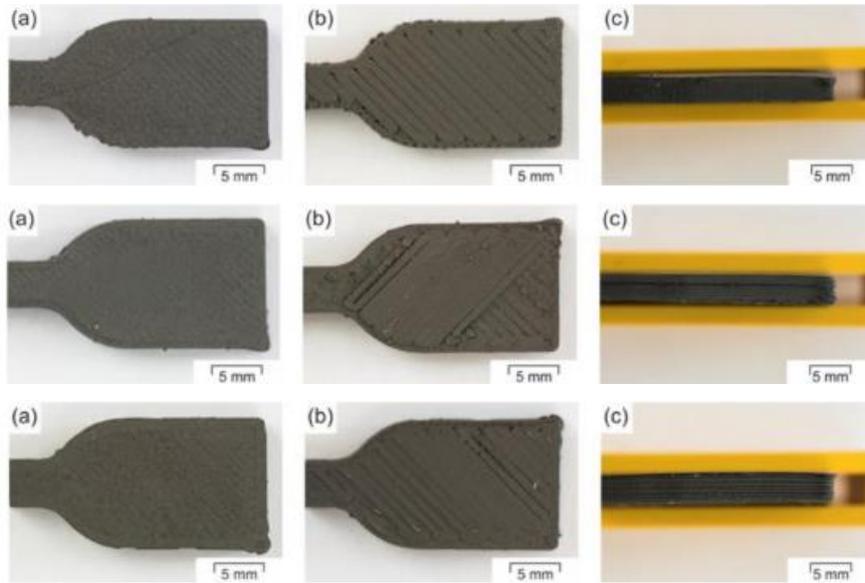


Figure 2.42: Bottom (a), top (b) and side (c) views of printed parts printed with flow rate of 100% (top), 150% (middle) and 200% (bottom) [61].

Lastly, the raster angle or raster orientation consists of the deposition direction of the material with respect to one of the horizontal axes. In Figure 2.43, the most used raster orientation is graphically represented.

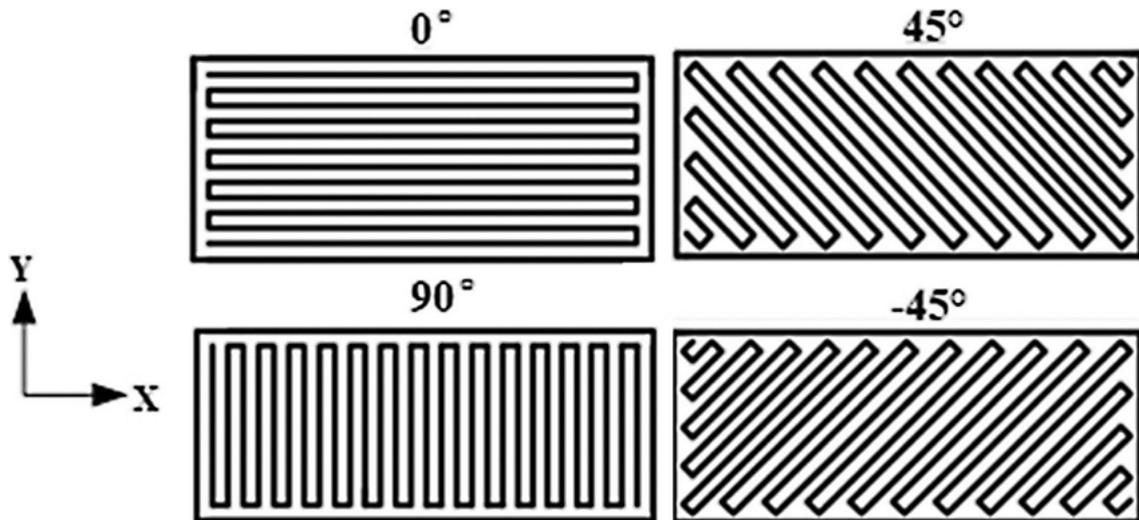


Figure 2.43: Examples of different raster angles [89].

The relative movement between the extrusion head within the XY plane and the building platform can generate different shear gradients in the nozzle, resulting in variation in

density and defect generation in shaped parts due to anisotropy. Indeed, different shear gradients in the nozzle could align the anisotropic metallic fillers within the binder compound in the direction of the flow of the feedstock out of the nozzle. The alignment along a specific direction affects the green part quality due to warping, but also the sintered part since it could be affected by an orientation dependent shrinkage. Iyer et al. [90] evaluated the effect of dissimilar printing raster patterns of 0° , 90° , and $+45^\circ/-45^\circ$ on the adhesion behaviour of the deposited layers on the build plate. The authors demonstrated that the raster orientation had an influence on the printing quality, since the raster patterns of 0° or 90° led to warping of the built parts; while warpage was avoided when the cross-hatched pattern $+45^\circ/-45^\circ$ was employed.

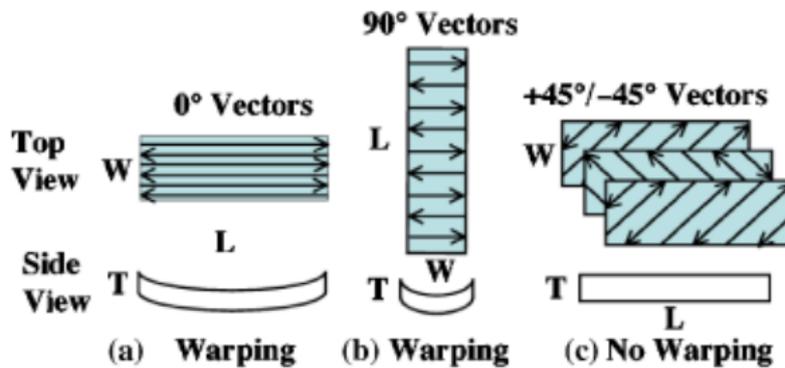


Figure 2.44: Schematic representation of warpage effects that result from: (a) 0° road vector strategy with all roads parallel, (b) 90° road vector strategy with all roads parallel, and (c) $+45^\circ/-45^\circ$ vector strategy on alternating build layers [90].

2.2.2 Debinding

The debinding process aims to remove the polymeric binder away from the green part, without disrupting the printed shape. The result consists in a so-called “brown part”, which is a skeleton of metal powders embedded in a residual polymeric matrix. This process comprises two principal steps, considering the most commonly used multi-component binder system. Firstly, a primary debinding step is applied to remove the primary binder (low molecular weight polymer), creating an interconnected pore path to enhance the removal of the backbone (high molecular weight polymer) during the second stage of the debinding [91]. A complete removal of the organic polymers should take place since a residual presence of carbon residues negatively affects the subsequent sintering process and affect the final quality of the sintered part. The backbone is a non-

degraded element which confers sufficient strength and hold the shape of the part after the removal of the first binder. This remaining element is thermally removed within a final temperature range of 450 to 600°C. The perfect range of temperature should be chosen according to the thermal degradation temperature of both binder elements. In some cases, the secondary debinding step is substituted with a pre-sintering phase in the following thermal treatment.

The debinding treatment is classifiable in 3 different techniques: thermal, solvent and catalytic [92]. The mere thermal process consists of the thermal degradation of the primary binders, which should coincide with an organic element. In this phase, the disassociation of polymers into smaller molecules or monomers, according to the type of selected polymer, and their evaporation out of the surface of the brown part occur. The chosen temperature for a proper debinding treatment should converge to the melting and degradation temperature, resulting from a thermogravimetry analysis. Besides, an evaluation of the thermal degradation speed should be also comprised in the selection of the debinding cycle. In Figure 2.45, an example of TGA curves for different polymers suitable as binder elements in air and nitrogen atmosphere is reported. Depolymerization type polymers (i.e. POM and PBMA) completed the thermal degradation in air before 300 °C with a higher degradation speed, while random type polymers, such as PP and EVA, required higher temperatures and took longer [93].

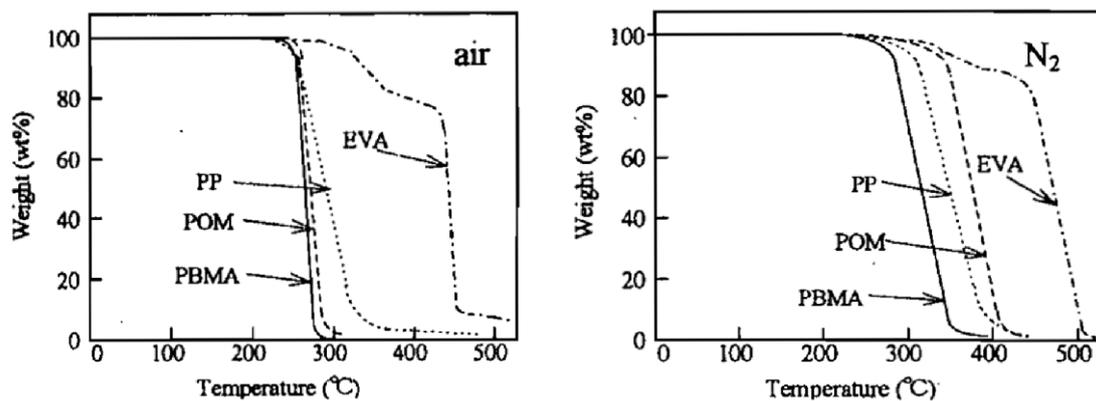


Figure 2.45: TGA curves of different polymers in air (left) and nitrogen (right) atmosphere [93].

Andersen et al. [94] performed a thermal debinding on green parts made up of PP and 316L SS powders. The cycle consisted of an increase of heating rate from 0.1 K/min to 2.0 K/min between 20 °C and 650 °C. The solution used caused an anisotropic shrinkage

along the building direction compared to solvent debound samples and generated an excessive carbon content of 0.048%, which is slightly higher compared to the specification of 0.03 wt.% carbon for 316L stainless steel. Differently, Iyer et al. [90] proposed a two-step debinding cycle. Samples were first heated to 400 °C in nitrogen atmosphere, followed by an air cycle to complete the burn out of any residual binder. The initial stage was performed in a Al₂O₃ setter bed for the wicking of the polymeric material. A very low debinding cycle was selected to prevent any possible surface damage of the part. As a consequence, the relative long thermal debinding cycle, ranging from 10 to 60 h [95], represents a relevant issue. The increase of the debinding temperature does not represent a valuable solution, since it increases the possible damage of surface bloating due to trapped vapour pressure in the core of the brown part. Over time, different solution has been added to thermal debinding to improve the efficiency of the process. The best solution was the integration of debinding and sintering in a one-step process, with the introduction of the vacuum atmosphere in the debinding step. During the process, a gas continues to flow in a chamber to remove binder vapours, which are condensed and collected within brown parts skins. After the complete removal of the binder, the sintering process could begin with the increase of the temperature. Since the physic principle still stand in thermal degradation, the debinding cycle is still very low.

Another way to remove the binder system is to immerse the green part in a liquid solvent unit. A low temperature in the range of 50 to 60°C could be used to increase the interaction between primary binders and solvents, since the temperature improves the solubility and diffusion rate of the binder. In Figure 2.46 the percentage of mass loss of 316L green parts during the solvent debinding with cyclohexane at different temperatures are plotted. Despite the selected temperature, an holding time of 12 h is required for the completion of binder extraction from the green parts. The lowest temperature (i.e. 23 °C) the total accomplishment of the debinding cycle [81].

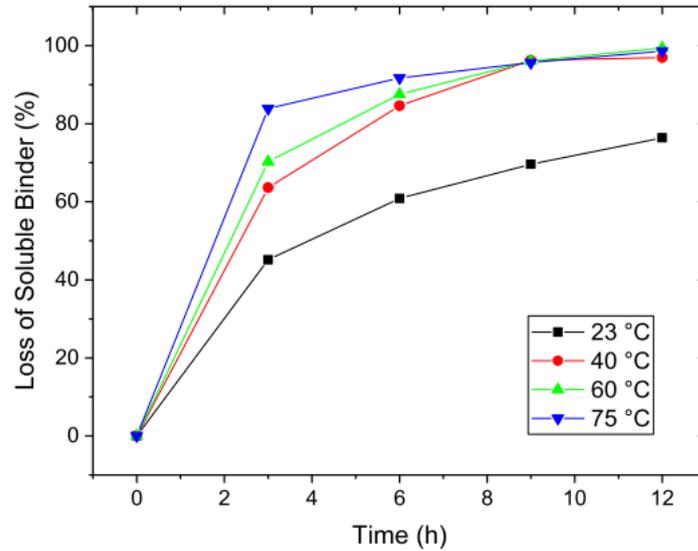


Figure 2.46: Percentage of mass loss during solvent extraction of 316L parts [81].

Higher temperatures enhance the dissolution and diffusion of binder, as well as the shape and the distribution of the metal powder in the polymeric matrix. Indeed, smaller irregular particles create more surface contact points for the binder system and smaller pores between particles, decelerating the diffusion process of the solvent. However, the selected temperature for this debinding step should not exceed the evaporation limit of the solvent used and the degradation temperature of the main polymeric component. The elimination of at least one of the polymeric components concurs with the formation of channels, which will favour the subsequent backbone burnout. The solvent debinding is strictly dependent on the green part surface to volume ratio, since the solvent liquid should reach the core of the part during its penetration [67]. The typical type of agent used in a solvent debinding is an organic compound and acetone [96] and cyclohexane [97] are the most commonly used. In addition, several studies [98,99] explored water as possible binder solvent. The main benefit of using water is the easiest handling compared to organic solvents. Polymers, which are soluble in water, should contain oxygen and nitrogen since these are hydrophilic elements. Some water soluble binders include polyethylene glycols, polyethylene oxide and polyacrylamide. The process can be accelerated by applying a heat source or a stirrer, resulting in heated [58] or agitated [100] water. This type of debinding is surely faster than thermal debinding since it takes around 6 to 10 hours. A further reduction of the total debinding time could be achieved by the combined application of solvent and thermal debinding. Catalytic debinding was firstly introduced and patented by BASF, especially for polyacetal-based binders such as

Polyoxymethylene (POM). The exposure of a green part to a catalyst with an adequate temperature enhances the decomposition of polymeric binders into monomers. The process begins at the surface of the part. As the monomers at the part surface evaporate, the creation of pore channels within the part occurs and the matrix beneath the surface is exposed to the acid vapour. This pattern intensifies the depolymerization process until the core of the structure is reached. The formation and removal of monomers decrease the total debinding time, since the small size of their molecules accelerated the rate of diffusion [101]. Besides, a capillary condensation is minimized since monomers have a high vapour pressure. This condition is also beneficial for thick part section with excellent part retention. Since it is a partial thermal process, a proper combination of temperature and catalytic concentration is fundamental in the selection of debinding rate. In general, the process is carried out below the melting point of the primary binder to avoid the formation of liquid phase and prevent the distortion of the shaped part. Besides, a low relative temperature allows a better control of the internal vapour pressure to minimize the formation and propagation of cracks within the part. Additionally, particular attention should be given to the set of temperatures also due to health risks. Polyacetal-based binders depolymerized catalytically with a direct solid to gas transition, realising formaldehyde. This gas is considered toxic and its concentration in the working environment should be kept under 20 mg/m^3 and the allowable quantity should not exceed 0.1 kg/h [102]. For this reason, the controlled catalytic debinding furnace should properly underwent a specific cycle consisting of a burn at $800 \text{ }^\circ\text{C}$ in oxidizing atmosphere to transform formaldehyde in water and carbon dioxide. [103]. The high molecular weight element should be removed with a subsequent secondary debinding or thermal debinding process, due to the fact that multicomponent binders, whose primary binder is a polyacetal based one, have a backbone polymer which does not decompose by means of a catalytic debinding.

The debinding is the crucial step for the creation of sintered parts since most of defects can be generated by inadequate process. In particular, the creation of a perfect porosity network for the removal of thermoplastic components during the debinding and/or pre sintering phases is fundamental. Bloating and surface cracking are generally caused by too high debinding rates, both during thermal and solvent processes. As evident in Figure 2.47, bloating and partial cracking are visible on the surface of the sample, which partially

underwent a binder removal cycle. The evacuation of the vapour formed during the degradation of the polymer could generate bubbles on the surface of samples when the partial pressure of the trapped vapour is higher than atmospheric pressure, especially in areas rich in polymeric binders. This results in a partial loss of the brown part shapes at superficial level [77].



Figure 2.47: Bloating and partial cracking on surface sample [77].

Similarly, in [82] surface bloating appeared on brown parts with thick walls (6 mm). The elimination of this issue, generated during debinding step, was reached with the reduction of wall thickness to 2 mm.

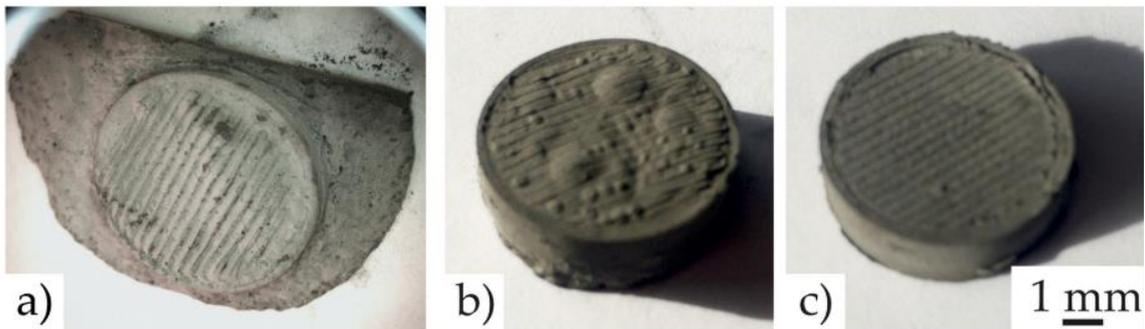


Figure 2.48: Thermal debinding of a 6mm thickness cylinder at heating rates of (a) 3 °C/min, (b) 1 °C/min and (c) 0.2 °C/min in vacuum [104].

Furthermore, large internal voids could be raised due to improper debinding rates for the removal of the binder system. In Figure 2.49, it is noticeable the relationship between the

decrease of heating rates and the closure of porosity of sintered samples with a benefit of the final relative density [105].

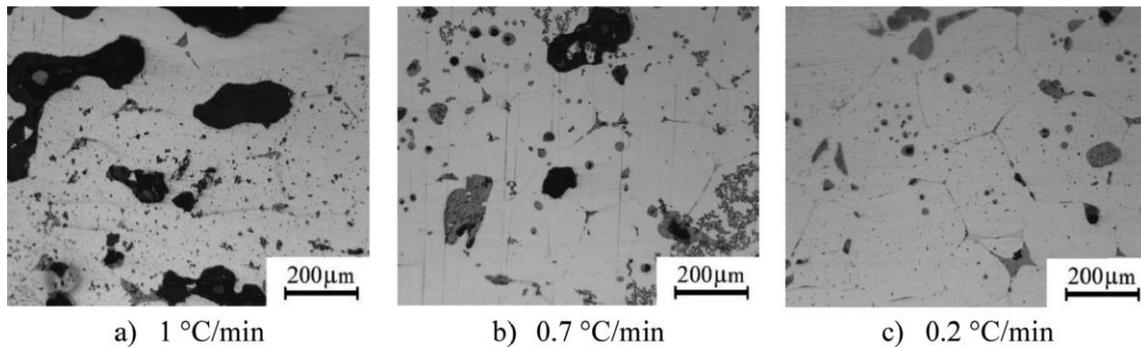


Figure 2.49: Cross section of sintered samples varying the heating rates during thermal debinding [105].

2.2.3 Sintering

Sintering consists of a heating process applied to metal powders to provide a full densification of a sample by bonding the particles into a solid. The sintering process is the fundamental stage of this multistep technology, since it ensures the proper physical and mechanical properties of metal samples. The optimal sintering conditions rely on the metallic materials used and particle size. Sintering is generally carried out within the range of 70 and 90 % of the melting temperature of the solid content [55]. Lower temperatures hinder the complete recrystallization process of the metal particles, while an excessive heating could lead to the melting point of the powders and even the swelling of the components. Nevertheless, liquid formation is a possible event during sintering cycles, but it is narrowed to less than about 15 wt.% liquid since higher amounts correspond to semi-solid casting processes.

The basic process during sintering is the atomic motion, which is triggered when the temperature exceeds one half to two thirds of the melting temperature of the powder material. Atomic motion represents a loss of surface area and surface energy during sintering cycle. During heating at low temperatures, a contact formation between particles occurs. At this stage, a weak adhesive force bonds the particles together. The increase of heat generates necks growth, which corresponds to an initial bonding at low area particles contacts due to surface diffusion [106]. Figure 2.50 explains the phenomenon of two close particles bonding.

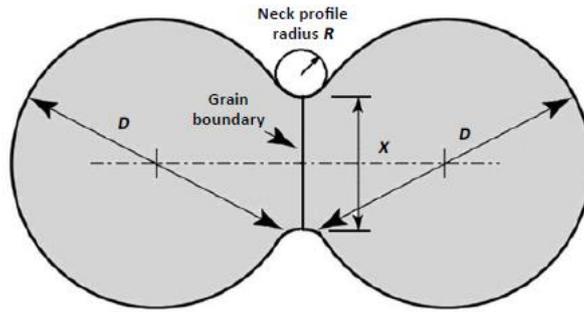


Figure 2.50: Schematic of the neck size X and the particle size D (assumed spherical) and neck saddle point curvature R during two particle sintering [106].

D represents the diameter of the spherical particles with a neck X in diameter. At the beginning of the process, the neck contour forms a concave shape opposing its radius and the circle of radius R . The smaller radius has a higher surface energy, leading to a capillary stress that induces the particles to pull together. This movement induces grain boundary formation in the neck due to random misalignment of adjacent crystals. These grain boundaries are the fundamental elements for subsequent shrinkage and densification. Indeed, the development of grain boundaries diffusion generates densification since atoms relocate into the pores from the contact plane between particles. These mechanisms enlarge the neck between particles and increase the strength of the powders. Besides, the bonding results also in shrinkage. Shrinkage enhances the progressive formation of further contacts (i.e., each particle has 5 to 6 touching particles) to bond the whole structure. Following the initial bonding, the growth of necks merge to form rounded pores and lastly the closure of the formed pores occurs, resulting in the reduction of porosity and the densification of the sintered structure [106].

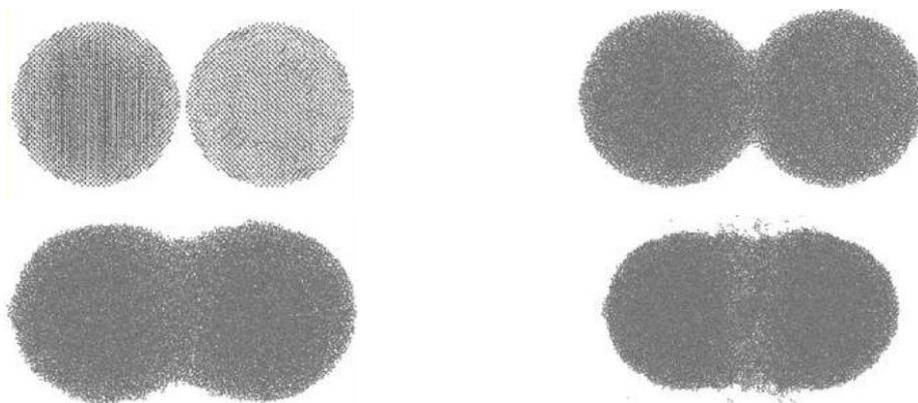


Figure 2.51: Molecular dynamics simulation of sintering process [106].

Several parameters contribute to the success of a sintering cycle, such as peak temperature, hold time, heating rate, particle size, green density and process atmosphere. The peak temperature is a dominant parameter for the control of sintering process. High temperatures reduce sintering cycle time since atomic motion is enhanced with the increase of heating. Figure 2.52 shows that the highest level of densification of 42 μm titanium powders is ensured by a temperature of 1250 °C [107].

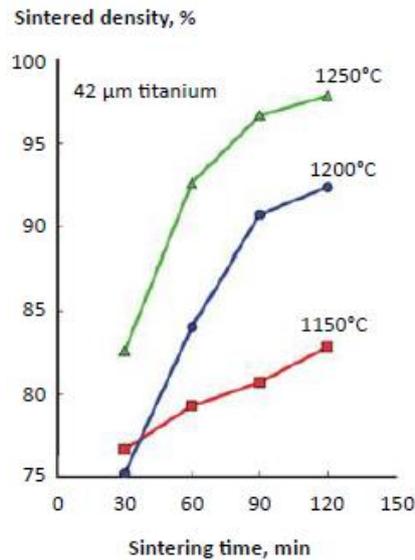


Figure 2.52: Sintered density versus hold time for 42 μm titanium powder vacuum sintered at three temperatures [107].

Prolonged hold times also contributes to the densification, despite the dominant role of temperature. Indeed, a sufficient hold time is just required to ensure uniform heating at the peak temperature. However, an uncontrolled combination of peak temperature and holding times could lead to undesirable result in terms of relative sintered density and appropriate grain size to ensure the desired mechanical properties. Indeed, high sintering temperature and hold times lead to larger grain sizes, compared to the starting ones, due to grain growth. Besides, the coarsening of pores could be enhanced owing to vacancy or gas exchange, reducing the number of pores and their surface area. Figure 2.53 demonstrates the loss of strength after 100 min of holding times, due to grain and pores coarsening [108].

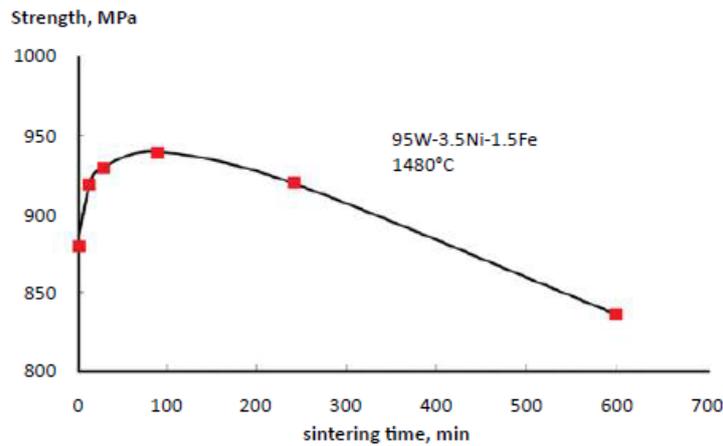


Figure 2.53: Tensile strength as a function of sintering time [108].

Besides, high heating is associated with the increase of shrinkage, while shrinkage rate is slow with increasing hold times. This evidence is confirmed by the course of the plotted curves in Figure 2.54: the first slope, corresponding to the initial heating, is high, while shrinkage rate declines during the isothermal hold. Shrinkage occurs at the necks formation due to the closure of porosities and densification of the structure and generally stands within the range of 12 to 20%.

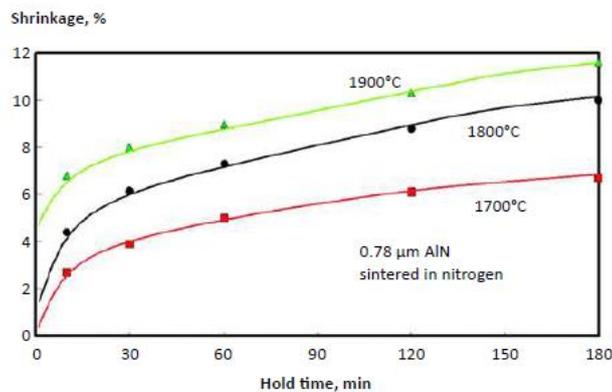


Figure 2.54: Sintering shrinkage at various time-temperature combinations [106].

Particle size influences other process parameters, since smaller particles require lower sintering temperatures and hold times. Figure 2.55 shows the negative relationship between the sintered density and the increase of particles size, because smaller powders have higher sintering stress and shorter diffusion rate enhancing the atomic motion process, which is necessary to reach the structure densification [109].

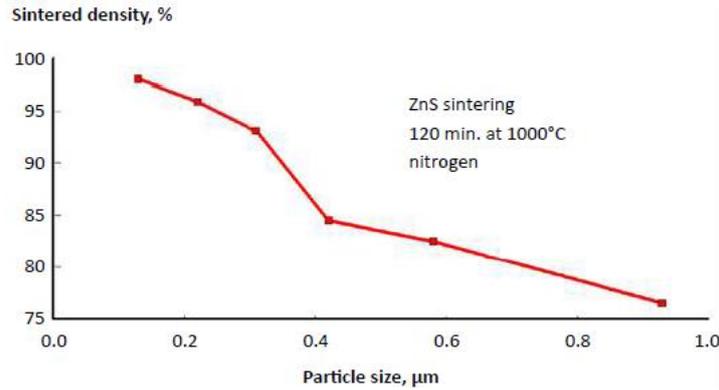


Figure 2.55: Sintered density as a function of the particle sizes [109].

Also, the density of the green parts has an impact on the sintering process. In general, the green density is enhanced by smooth. Besides, there is a linear relationship between green and sintered density: a lower green density generates a worse sintering process due to the lower amount of powder interface contacts. Indeed, it is simple to densify a high-coordination number compact in term of atomic motion. Loose particles reach about six to seven contacts; while rounded powders could generate up to twelve contacts per particles, improving the sintering cycle. [15]. In Figure 2.56 it is exhibited the correlation between the green and sintered density for 0.5 μm alumina sintered at 1650°C [110]. Below 50% of green density, it is difficult to reach satisfactory value of sintered density.

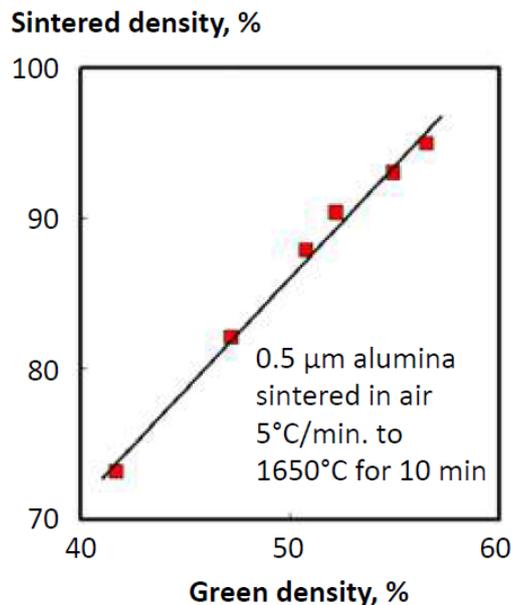


Figure 2.56: Dependency of green and sintered density for 0.5 μm alumina heated at 5°C/min. to 1650°C for a 10 min. hold in air [110].

The furnace atmosphere is another relevant sintering process parameters, which depends on material chemistry and highly influences the material properties. The most widespread furnace atmospheres are H₂, N₂, Ar and vacuum. Some alloys, such as Ti alloys, require specific atmosphere (i.e., Ar or vacuum), since they are reactive with carbon, oxygen, nitrogen and hydrogen. Even pressure could be applied during a cycle, but it increases the total time of sintering. A controlled cooling rate is necessary to ensure the proper mechanical properties of the sintered components, since during this final step occurs dissimilar phase transformation of the material [111]. A cooling phase in a protective atmosphere is preferred to avoid oxidation during sintering.

3 Physical and mechanical properties of sintered AISI 316L and AISI 630

Among a discrete variety of alloys available for the manufacture of metal AM parts by means of Material Extrusion, AISI 316L and 630 stainless steels are the most widespread material used for different final applications. The advantageous combination of chemical-physical and mechanical properties of these two stainless steels and the good ease of processing and printability contributed to the extensive research, development and production of filaments loaded with AISI 316L and AISI 630 powders by industries and academic institutions.

In this chapter a comprehensive literature review on the main achievements regarding the physical and the mechanical properties of AISI 316L and AISI 630 specimens shaped by means of metal ME will be presented. The physical properties, including the dimensional shrinkages and the final sintered density, give an account of the appearance and the dimensional accuracy of components made additively. Besides, acceptable values of shrinkage and sintered density ensure the minimization of external and internal defects of metal samples that might compromise the mechanical characteristics of the samples in exercise. Similarly, providing an adequate overview of the mechanical characterization of printed metal samples might extend their possible final applications, since mechanical properties comparable to those of the monolithic material or components fabricated by traditional manufacturing methods are a fundamental requirement for industries, especially for assembled engineering parts.

3.1 AISI 316L

AISI 316L is a chromium-nickel-molybdenum austenitic stainless steel. Austenitic stainless steels are characterised by a composition of 18% chromium, 8% nickel and carbon contents not exceeding 0.06%. The high percentage of chromium improves the resistance to corrosion and it is, therefore, essential to keep the carbon content below that threshold to prevent chromium from forming carbides by impoverishing the matrix and reducing its corrosion resistance. The typical structure of this type of steel is a cubic structure centered face [FCC] due to high content of austenitizing elements, such as nickel and this structure is maintained from high temperatures up to room temperature.

The austenitic structure does not allow the execution of tempering thermal treatments but guarantees high deformability in terms of machinability and weldability. The range of austenitic stainless steels currently on the market is distinguished by small variations in the percentages of nickel and chromium, affecting the mechanical properties and the corrosion resistance. Indeed, alloy 316L was developed to provide better corrosion resistance to alloy 304 and 304L in moderately corrosive environments [112]. The addition of molybdenum improves the overall corrosion and in particular the chloride pitting resistance. It also provides stress-to-rupture and tensile strength at elevated temperatures. In Figure 3.1 the chemical composition and the main mechanical properties of austenitic stainless steel grade 316L are reported [113].

Grade		C	Mn	Si	P	S	Cr	Mo	Ni	N
316L	Min	-	-	-	-	-	16.0	2.00	10.0	-
	Max	0.03	2.0	0.75	0.045	0.03	18.0	3.00	14.0	0.10

Grade	Tensile Str (MPa) min	Yield Str 0.2% Proof (MPa) min	Elong (% in 50 mm) min	Hardness	
				Rockwell B (HR B) max	Brinell (HB) max
316L	485	170	40	95	217

Figure 3.1: Chemical composition (top) and mechanical properties (bottom) of AISI 316L material [113].

Diffused applications for 316L stainless steel comprise component parts for exhaust manifolds, heat exchangers, jet engine, pharmaceutical and photographic equipment, valve and pump, chemical processing equipment, tanks, and evaporators. Besides, it also widely used for any parts exposed to marine environments.

3.1.1 Physical Properties

An adequate analysis of the structural and mechanical characteristics of components printed by means of metal Material Extrusion is essential to assess the potential of this newly technology.

The achievement of satisfactory level of final sintered density, as close as possible to the reference value of the relative conventional material, ensures the employment of these components in various manufacturing applications, even for critical and high value-added ones. Besides, a precise control of the volumetric shrinkage affecting the parts following the sintering process assists the design phase of the product development process. The

shrinkage of printed and sintered parts is an intrinsic issue strictly related to the multistep method; however, its prediction, also by means of simulative tools, can enhance the diffusion of the metal products shaped by ME, especially for the assembly phase.

Gong et al. [114] compared the physical properties obtained by Selective Laser Melting (SLM) and metal Material Extrusion (ME) methods. The shaping phase performed with optimized printing process parameters (i.e., layer thickness of 0.2 mm, scan speed of 60 mm/s, and extruder temperature of 235°C) ensured the fabrication of sintered parts with final density of 7.88 g/cm³, which corresponded to the 98.5% of the theoretical density of AISI 316L. Despite the satisfying level of density, a certain level of porosity was detected within the metal structure unlike the SLM process, which ensured a fully dense structure without apparent porosity. The difference of voids generation between the two additive technologies is also observable in Figure 3.2.

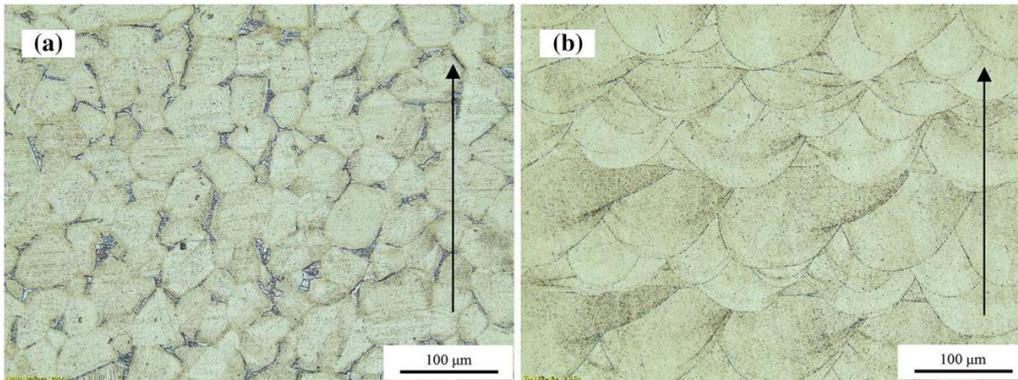


Figure 3.2: Optical microscopy of ME SS 316L microstructure (after sintering) and SLM SS 316L microstructure along the growth direction [114].

In this research, an accuracy analysis of the shrinkage behaviour on different geometric features of interest (FOI) was proposed, indicating that the calculated shrinkages along z-axis for the various FOI were on average higher than for the geometrical features in the xy plane. The author attributed the anisotropy in the shrinkage behaviour to the relevant influence of the gravity component on the metal samples during the sintering process.

Otherwise, a different cause was attributed to the anisotropic linear shrinkage of the 316L samples in [115]. They printed dog-bone specimens with three different layer directions, as reported in Figure 3.3.

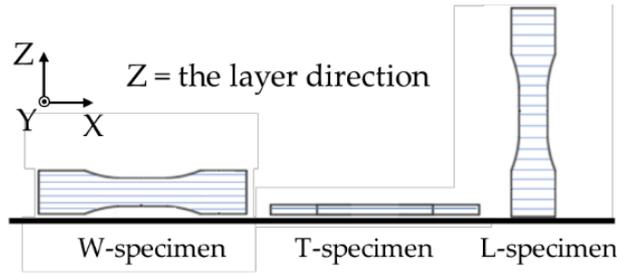


Figure 3.3: Schematic of different layer direction (W-, T-, L-specimens) [115].

Regardless of the building directions, specimens printed with the different configurations achieved similar relative density. The highest level of density was obtained by W-specimen at a layer thickness of 0.1 mm with a percentage value of 92.9%. The reference value of sintered density was consistent with the density measured in [116]. In fact, a relative density of 92.23% with 7.77% of porosity was found. This level of porosity was confirmed by the pores chain formed and uniformly distributed throughout the cross-section, which are visible in Figure 3.4. The formation of these large voids was attributed to the inefficiencies of the printing process.

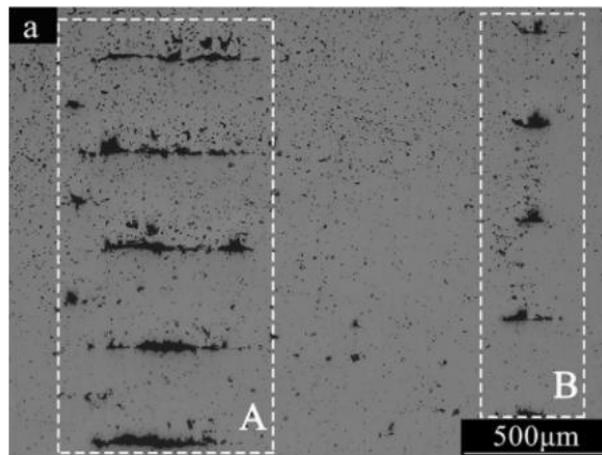


Figure 3.4: Optical microscopy of microstructure in ME 316L part [116].

The dimensional linear shrinkages exhibited notable anisotropy since the linear shrinkage was highest along the layer direction. Indeed, W-specimens had the highest shrinkage along the width direction, while T-specimens and L-specimens registered the highest shrinkage for thickness and length dimensions, respectively (Figure 3.5).

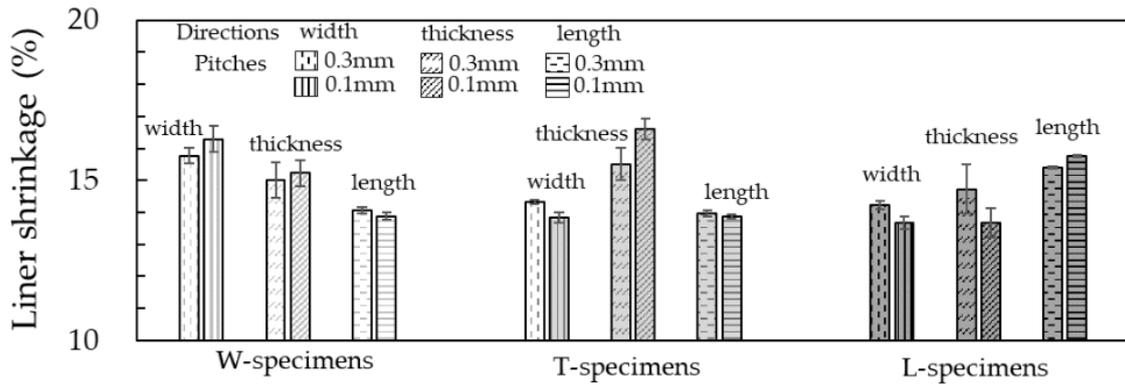


Figure 3.5: Linear shrinkage trends as a function of different layer orientation and layer thickness [115].

The green parts are characterized by oriented domain structure, which is attributed to the aggregate of the binder components. These domains were oriented perpendicularly to the building directions. The extrusion and deposition processes had a strong influence on the origin of the binder domains within the green parts. Indeed, a shear deformation of the deposited path occurred since the nozzle diameter is always greater than the layer height. Besides, the extrusion temperature higher than the melting point of the primary binder facilitated the orientation of the softened domain in the direction of the nozzle trajectory. This configuration of the metal/polymer matrix perpendicular to the layer direction increased the average metal particle distance in the building directions leading to higher dimensional linear shrinkage in the layer direction among all directions during sintering (Figure 3.6). Whenever the distance between two consecutive layers is too long, the sintering process could not succeed in the complete closure of channels, hence, the binder domain area would remain as voids. This phenomenon considerably affects the mechanical properties of sintered specimens with regard to both strength and ductility.

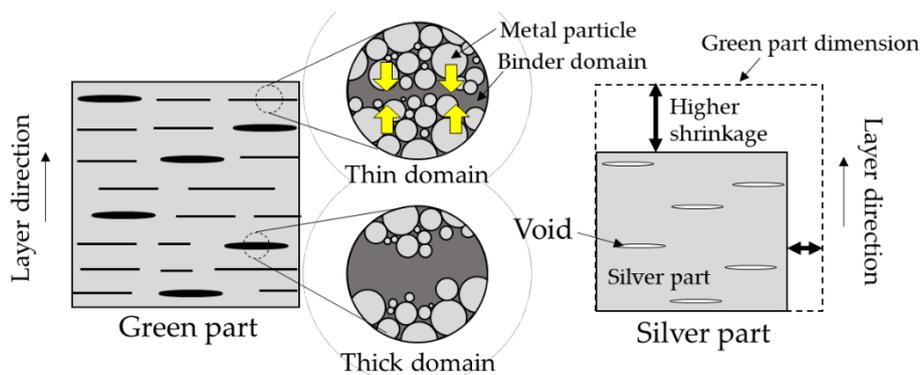


Figure 3.6: The effects of the oriented binder domain on the shrinkage and the generation of voids [115].

The reduction of the total weight of a printed component due to the decreasing of the infill percentage during the extrusion and deposition phases represents a massive advantage of the Additive Manufacturing technologies, considering the material savings for the products manufacturing. However, a variation of the infill degree affects the physical properties of sintered parts. Ait-Mansour et al. [117] revealed a negative dependency between the theoretical infill degree and the relative sintered density of the specimens. Indeed, the increase of theoretical infill level from 25% to 125% considerably improved the relative part density levels (Figure 3.7). On the contrary, varying the infill degree barely influenced the linear shrinkages within xy plane and along z direction, demonstrating that the volumetric shrinkage of metal parts printed via ME remain constant over changing the density levels.

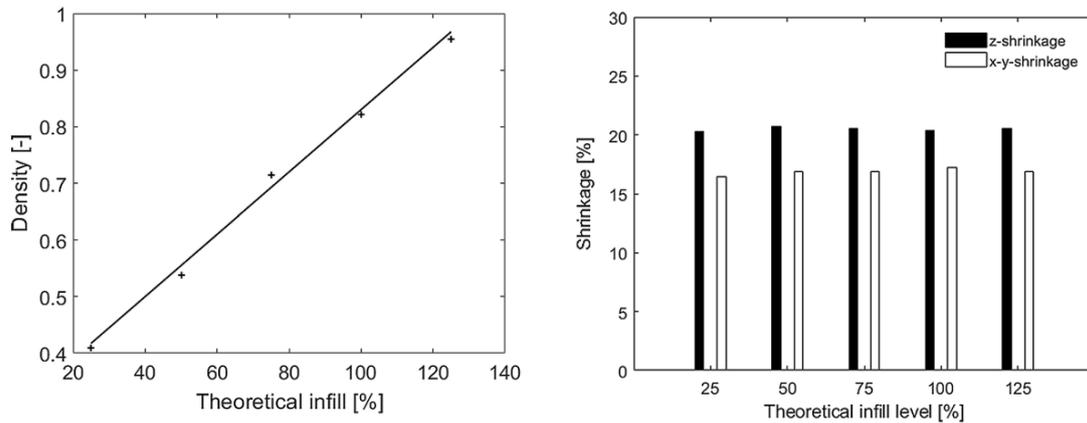


Figure 3.7: Relative part density (right) and shrinkage behaviour (left) varying theoretical infill levels [117].

The sintering phase greatly influences the final physical process of printed parts, since different sintering parameters (e.g., peak temperature and holding time) generate various levels of porosity within the structure. The overall porosity defines the final value of densification of the products. Thompson et al. [104] correlated the final density of samples and the sintering parameters used (Figure 3.8). Higher sintering temperatures led to the highest level of densification of the samples, up to the 95% of the theoretical density. Also, higher holding times improved the sintered density, since the optimal densification was reached after 120 minutes, that was the longest time selected. Longer holding times did not change the final level of sintered density but led to the grain coarsening of the microstructure.

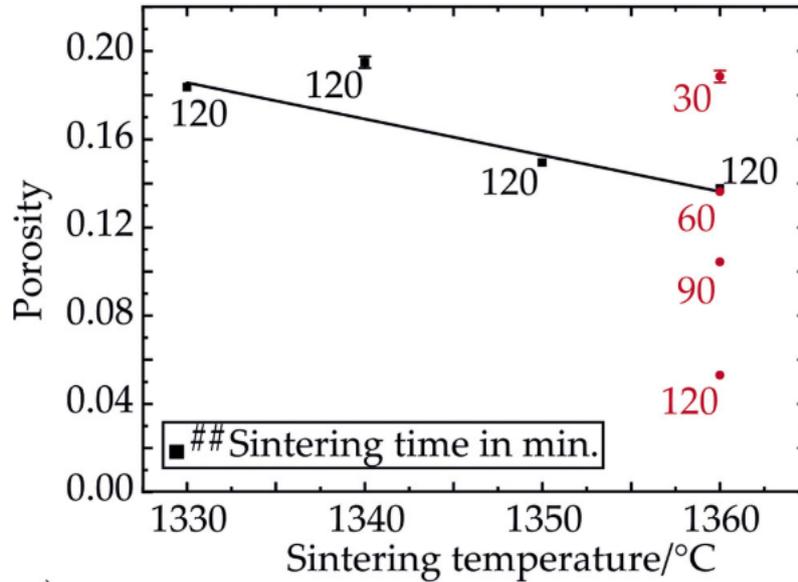


Figure 3.8: Evaluation of porosity for different sintering temperatures and times. [Black squares indicate measured porosities of sintered samples after thermal debinding at a heating rate of 0.3 °C/min. Red dots indicate measured sintered porosities after debinding at 0.2 °C/min] [104].

3.1.2 Mechanical Properties

The physical and structural properties of sintered specimens made additively differ from the conventional material, since the sintered density of parts are on average lower within the range from 2 to 8% compared to the relative parts fabricated via conventional technologies (e.g., subtractive or casting methods). The overall porosity distributed within the metal matrix plays a relevant role in the definition of the main physical properties and consequently a tight connection exists between porosity and mechanical characterization of sintered samples printed by means of ME. Indeed, the mechanical properties are negatively determined by the porosity and the layer connection, which are predominantly affected by the printing process.

Damon et al. [118] studied the relationship between overall porosity and the mechanical behaviour as a function of different deposition strategy of the softened strands. The authors selected two unidirectional patterns parallel (H-L) and perpendicular (H-P) to the load direction, building three contour strategy. In Figure 3.9a, b, c, and d, the front and top views of the gauge length for the scanning strategies are shown. Regardless of the different scan strategy, the predominance of channel-like voids as main internal defects can be detected. The measured distance of these porosity channels was 0.32 mm, on

average. Since the selected layers width was 0.4 mm and a dimensional linear shrinkage of 20% owing to the sintering step was calculated, the porosity channels could be attributed to the adhesion issues among adjacent layers during the deposition of the strands. Thus, the architecture of overall porosity is dominated by the track-induced pore channels, generated by the printing process of Material Extrusion. More pronounced pore channels are evident for the longitudinal scan strategy (H-L), while fewer channels were found for the build direction oriented 90° with respect to the load direction. Accordingly, 13 large pore channels clusters were detected for the longitudinal configuration, generating an overall porosity of 1.5%. Porosity values for H-P samples were relatively low in comparison to the other build direction with less than 0.5%, originated from 4 large pore channel clusters, as reported in Figure 3.9g, h. The shorter track length in the inner areas of the sintered specimens minimized the overall porosity, although a certain level of voids could be noticed within the metal matrix (Figure 3.9d, e).

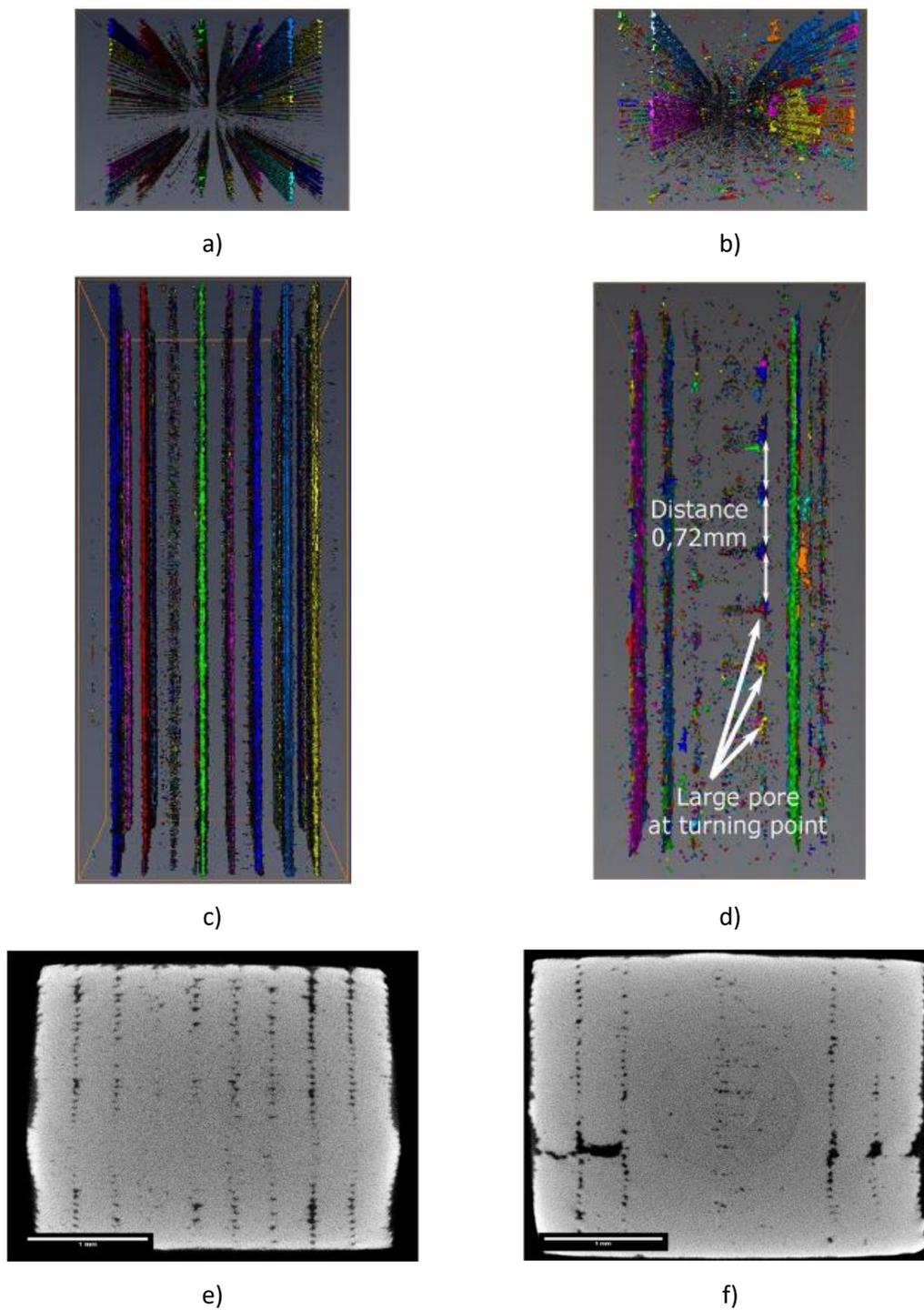


Figure 3.9: 3D porosity: front view of H-L (a) and H-P(b); top view of H-L (c) and H-P (d); CT slice of H-L sample (e)and H-P samples (f); histogram for overall porosity of H-L samples (g) and H-P samples (h) [118].

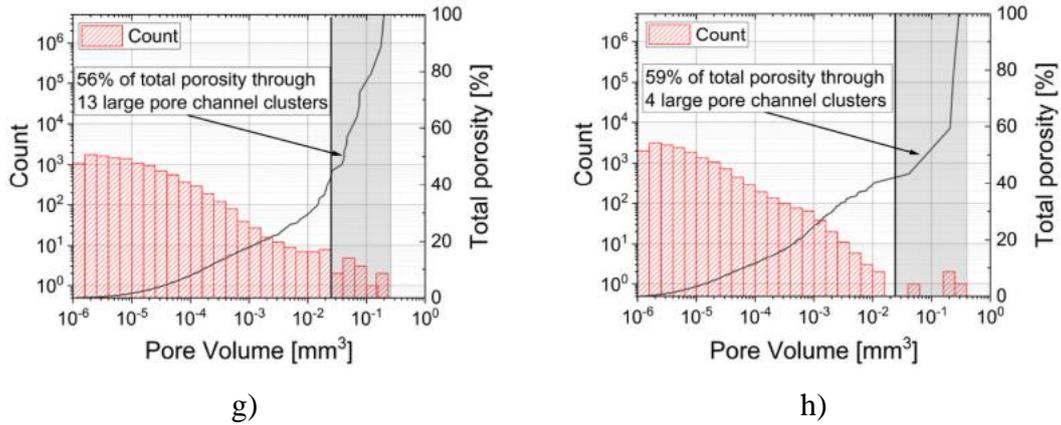


Figure 3.9: Histogram for overall porosity of H-L samples (g) and H-P samples (h) [118].

The different morphologies of channel-like voids are fundamental key point for the following mechanical characteristics of the sintered specimens. Indeed, an anisotropic behaviour of the two types of specimens was prominent as the scan strategy generating the lowest level of overall porosity ensured the best mechanical performance as for ultimate tensile strength. The authors discovered a uniform trend for the strain at break of the different samples. All configurations led to an average value of elongation at break around 35%, since this characteristic is owed to a low notch sensitivity and therefore, converging to similar ductility values of all build orientations irrespective of porosity. Different studies analysed the effects of various building orientations on the main mechanical properties of sintered samples. The components in operations could be subjected to stresses along all directions. Therefore, the knowledge of the mechanical response as a function of the loading directions could aid the diffusion of metal components printed by means of ME in the manufacturing sectors. Caminero et al. [119] stated that flat and on-edge configurations specimens exhibited the highest values of yield strength, ultimate tensile strength and elongation at fracture with very little percentage difference, lower than 3%. On the contrary, the up-right configuration induced a brittle behaviour of the specimens with lower plastic deformation compared to On-edge and Flat orientations. This finding was supported by the microstructure of the sintered specimens in the three different configurations after the tensile loading. Indeed, the elongation of grains in the load direction and the shrink in the traverse direction reflected the plastic deformation that the material underwent. Flat and on-edge specimens exhibited similar severe deformations with an average grain size after deformation of 170 ± 25 mm in length and 54 ± 11 mm in width. By contrast, the average grain size is 110 ± 20 mm in the load

direction and $70 \pm 12\text{mm}$ in width direction. In this configuration, the sintered specimens failed prematurely at a lower strength with lower plastic deformation.

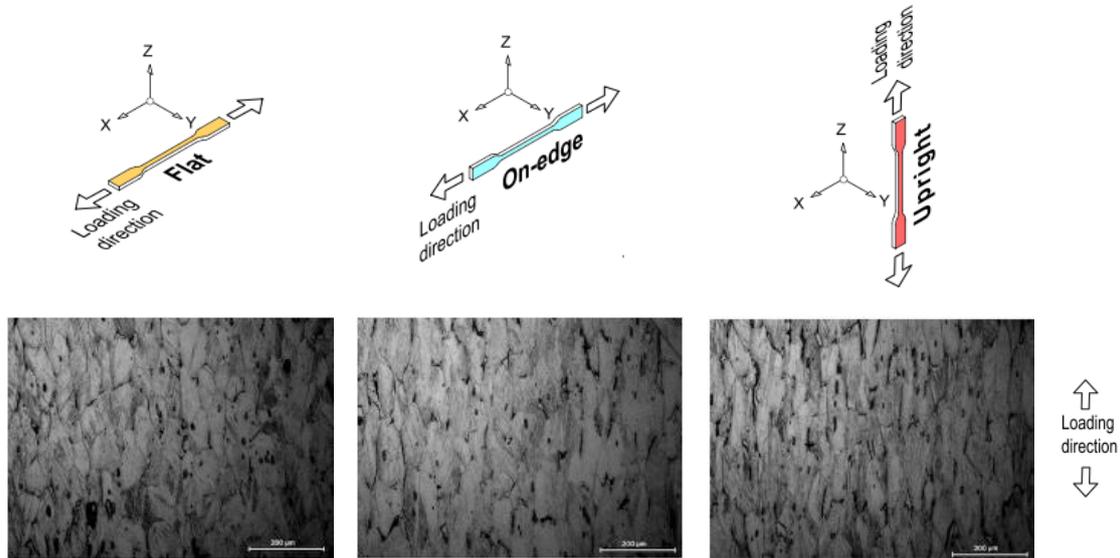


Figure 3.10: Optical micrographs of the microstructure of the sintered samples with different build orientations after uniaxial tensile stretching [119].

Similar to the previous work, Kurose et al. [115] evaluated how the building direction could affect the mechanical characteristics of sintered specimens. The flat configuration (T-specimen) ensured the highest ultimate tensile strength with 453 MPa and the highest level of ductility with a value of strain at break of 48%, followed by the on-edge configuration (W-specimen). Besides, a layer thickness of 0.1 mm generated on average the best mechanical results compared to 0.3 mm layer thickness. The upright orientation (L-specimen) showed the worst UTS and elongation at break values (Figure 3.11).

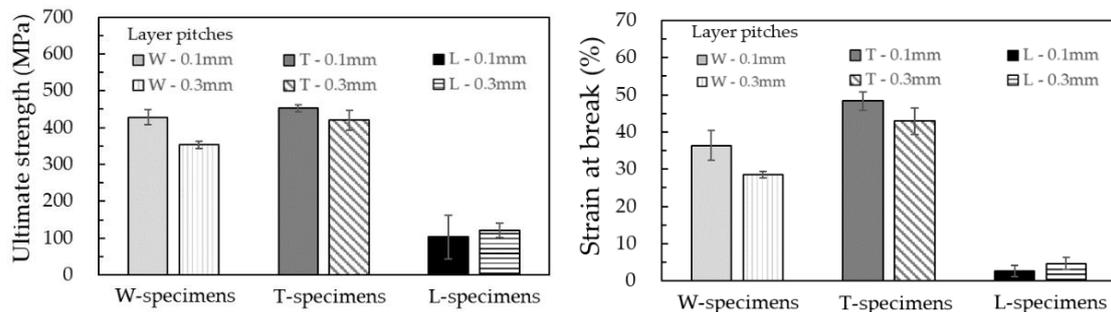


Figure 3.11: Ultimate strength (left) and strain at break (right) of the sintered parts printed in various layer directions and thicknesses [115].

The fracture surfaces of the sintered specimens confirmed the different mechanical behaviour among the three different configurations. Typical ductile fracture surfaces

characterized by dimple patterns could be observed in both W- and T-specimens. On the other hand, a smooth surface area without the presence of dimples is noticeable within most of the fracture surface of L-specimen. As demonstrated in the paragraph 3.1.1, the large number of voids in the upright orientation oriented perpendicular to the loading directions enhanced the crack initiation and the fracture propagation.

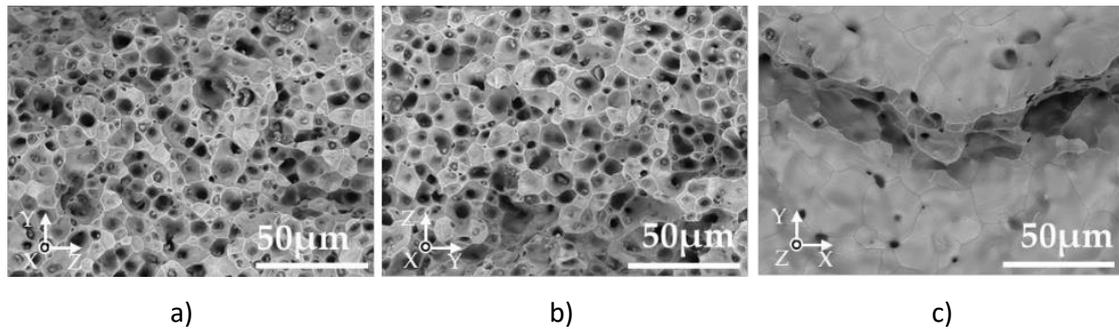


Figure 3.12: SEM micrographs of fracture surfaces after tensile tests of W-specimen (a), T-specimen (b) and L-specimen (c) printed in a layer thicknesses in 0.1 mm [115].

In [117], compressive behaviour of 316L samples was studied varying the theoretical infill percentage within the external perimeter, suggesting that compressive stress increased with the infill degrees. Indeed, comparing theoretical infill of 25 and 125%, the compressive stresses at 20% strain improved from 152.32 ± 3.73 to 667.62 ± 15.03 MPa, with a positive deviation of 77%. Yield strength did not experience a linear increase with the theoretical infill percentage, as for compressive stresses at 20% strain. The difference between 25 and 125% infill degree settled around 31%, which was a value significantly lower compared to the difference registered for the compressive stresses. The lowest levels of theoretical infills prevented the achievement of higher stress levels due to the rapid crack formation and propagation within their internal structures during the compressive loading.

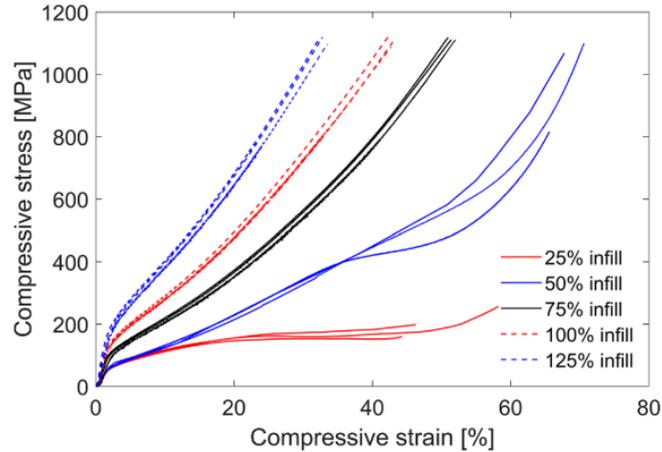


Figure 3.13: Compressive stress and strain varying infill levels [117].

AISI 316L stainless steel is not hardenable by heat treatment, as occur for precipitation hardening alloys, since the material does not undergo any phase transition in correspondence with the critical points Ac1 and Ac3. Nevertheless, work hardening considerably improves the strength and hardness of the AISI 316L products. Wang et al. [120] performed hot isostatic pressing (HIP) sintering to improve the mechanical properties of AISI 316L parts printed by means of Material Extrusion. The enhancement of tensile properties resulted from the closure of the pores owing to the HIP process. In Figure 3.14, the distributed porosity of green part, ordinary sintered sample and HIP sintered samples are plotted, showing a considerable reduction of 7.5% due to the ordinary debinding and sintering thermal treatment. Despite this improvement, horizontal pores chains were still visible along the building direction of the specimens. The application of HIP sintering led to a total amount of 0.3 vol.% of porosity.

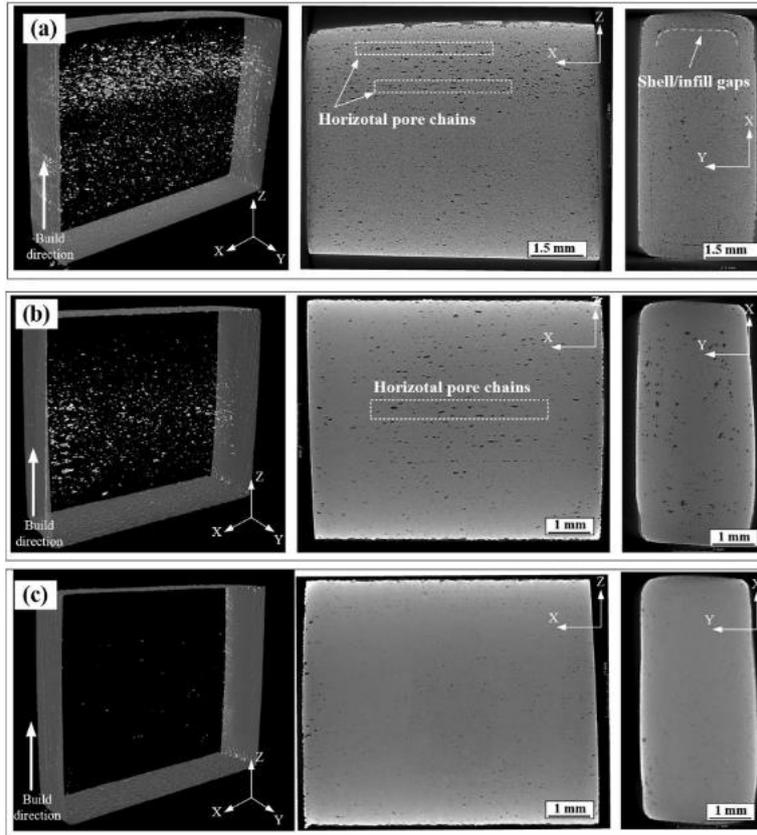


Figure 3.14: Micro CT porosity analysis (a) As-built green part, (b) Ordinary sintered part, and (c) HIP sintered part [120].

The overall reduction of voids within the internal metal matrix enhanced the ultimate tensile strength of HIP sintered samples, reaching a value of 540 MPa, which corresponds to a 35% increase as compared with ordinary sintered samples (Figure 3.15).

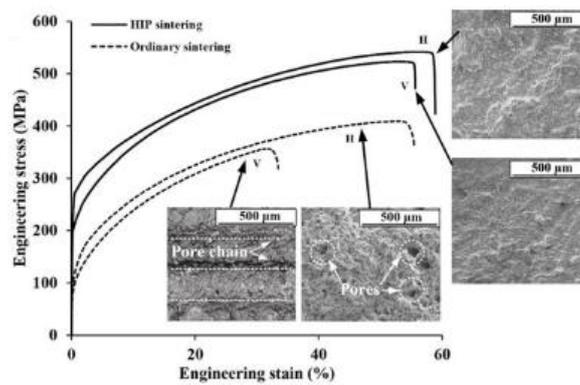


Figure 3.15: Engineering stress – strain curves for sintering and HIP sintering samples with fractography [120].

3.2 AISI 630

AISI 630 is a martensitic stainless steel. Martensitic stainless steels are similar to iron-carbon alloys that are austenitized, hardened by quenching and tempered for increased ductility and toughness. The typical structure of martensitic steel is body-centered tetragonal [BCT] providing magnetic properties. The strength obtained by heat treatment depends on the carbon content of the alloy. Increasing carbon content enhances strength but decreases ductility and toughness.

Different austenitizing elements as Molybdenum can be added to martensitic structure to improve corrosion and toughness properties. Nickel prevents the excessive free ferrite formation due to the higher chromium contents which are used to improve corrosion resistance. An excessive amount of austenitizing elements could lead to the formation of a microstructure that is not fully martensitic. AISI 630 steel are also known as 17-4PH steel, where the acronym PH (“precipitation hardening”) indicates the aging processes to which these steels can be subjected to improve certain characteristics according to the temperature at which the treatment is carried out. The precipitation hardening mechanism is a thermal treatment that allows the improvement of the mechanical properties and hardness of the steel, owing to the reduction of the motion of the dislocations present in the crystal lattice. The prevention of the dislocations movement is provided by the dispersion of precipitates in the form of nano-meter sized particles within the metal matrix. The precipitation occurs with single phase alloy at elevated temperatures, which facilitates the formation of a second phase within the matrix on cooling. The precipitation hardening mechanism consists of the three subsequent steps. Firstly, a solution heat treatment is applied at high temperatures within the range of 980° to 1065°C to allow any precipitates to dissolve or go into supersaturated solution. Following the heating, a cooling up to room temperature is performed. The cooling rate should be high enough to obtain a supersaturated solid solution. The last phase concerns the maintenance of the supersaturated solid solution for a sufficiently long time at room temperature (natural aging), or by heating the material to a temperature below the Solvus line for a few hours (artificial aging) provoking the precipitation mechanism. The supersaturated solid solution decomposes to form small precipitate clusters strengthening the material [121]. The increase of temperature enhances the tensile and yield properties up to a maximum, and then drop off dramatically. As these properties begin to decline with increasing

temperature, the elongation starts to increase, representing the so called “over-aging” condition. Over-aging occurs as the particles that caused the increase in strength continue to grow in size and they coarsen and sequentially cause a decrease in the hardness with a corresponding increase in elongation (Figure 3.16).

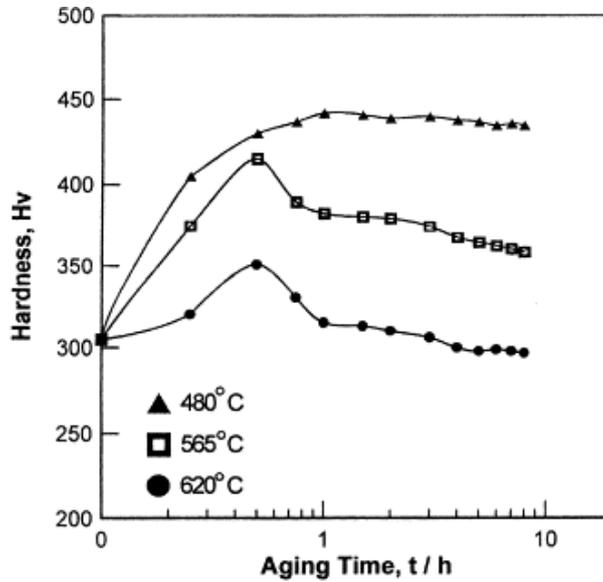


Figure 3.16: Aging time versus Vickers hardness for various temperatures [122].

Concerning AISI 630, it is a chromium-nickel-copper precipitation hardening stainless steel used for applications requiring high strength and a moderate level of corrosion resistance. The precipitation hardening mechanism for this alloy starts with the heating within the range of 1040 °C to 1066 °C, obtaining the annealed condition. The matrix structure following the solution treatment is martensitic and it is strengthened by a low temperature treatment which precipitates a copper containing phase in the alloy. The process is conducted at a temperature in the range 482°C to 621°C depending on the combination of strength and toughness desired. In Figure 3.17, the different combinations of heat treatments and the mechanical characteristics generated are reported [123].

SUMMARY OF HEAT TREATING ATI 17-4™ ALLOY				
Minimum Properties Specified in Aerospace Material Specification (AMS) 5604				
Heat Treat to Produce Martensitic Structure	Precipitation Heat Treatment to Produce Desired Strength			
	Precipitation Hardening Heat Treatment	Yield Strength psi (MPa)	Tensile Strength psi (MPa)	Hardness Rc
Solution Heat Treatment at 1950 °F (1066 °C) Condition A <i>(This is the condition furnished by ATI)</i>	900 °F (482 °C) 80 minutes Condition H 900	170,000 (1170)	190,000 (1310)	40 to 47
	925 °F (496 °C) 4 Hours Condition H 925	155,000 (1070)	170,000 (1170)	38 to 45
	1025 °F (552 °C) 4 Hours Condition H 1025	145,000 (1000)	155,000 (1070)	35 to 42
	1075 °F (579 °C) 4 Hours Condition H 1075	125,000 (860)	145,000 (1000)	33 to 39
	1100 °F (593 °C) 4 Hours Condition H 1100	115,000 (790)	140,000 (965)	32 to 38
	1150 °F (621 °C) 4 Hours Condition H 1150	105,000 (725)	135,000 (930)	28 to 37
	1400 °F (760 °C) 2 Hours + 1150 °F 4 Hours Condition H 1150-M from SA 683	75,000 (515)	115,000 (790)	26 to 36

Figure 3.17: Different aging solution and aging treatment and the resulting mechanical characteristics [123].

AISI 630 alloy is generally used in the aeronautical and aerospace, naval, chemical and petrochemical and in the energy sector for the realization of components characterized by high resistance mechanical and corrosion such as valves, shafts, bearings, turbine blades and compressors.

3.2.1 Physical Properties

The material extrusion process generated parts with final physical properties that differs from the monolithic AISI 630 material. Irregular shaped pores characterize the structure of sintered specimens lowering their final density. The voids pattern induced during the deposition process and favoured in the debinding phase might also influence the shrinkage behaviour during the sintering according to the print direction selected.

Suwanpreecha et al. [124] analysed the main structural properties of AISI 630 printed with different print orientations as a function of the voids generated within the metal matrix. Macrograph defects can be detected observing the sintered samples with flat, side and vertical layout (Figure 3.18).



Figure 3.18: Macrograph of sintered tensile specimens printed in the flat layout (top), the side layout (middle) and the vertical layout (bottom) [124].

The flat layout specimen appeared as defect free surface. The side orientation induced a slight discontinuity among layers; besides, warpage at the ends of specimens can be detected resulting from shrinkage of the polymeric binder. Unlike the previous orientation, the specimen printed with the vertical layout presented significant surface defects in terms of layers discontinuity at both grips and gauge length. Different orientation generated dissimilar voids pattern affecting the sintered density of the specimens. Considering the flat layout, triangular shaped voids characterized the metal matrix with an average area of $148 \mu\text{m}^2$, which was definitely smaller compared to the average area voids in the side layout (i.e., $443 \mu\text{m}^2$). The worse situation occurred for the specimens with the vertical layout, since incomplete fusion channels corresponding to the perimeter of the specimen infill were detectable. However, there is no significant difference in microstructure and grain size after sintering in specimens with different

specimen layouts. The dissimilarities associated with the samples orientation and the characteristics of voids generated affected also the final sintered density. The flat layout specimens, which had the lowest level of porosity, registered the highest value of density with an average value of $98.61 \pm 0.16 \text{ g/cm}^3$. On the contrary, the vertical layout provoked the worst sintered density owing to the increase of porosity and the delamination among layers.

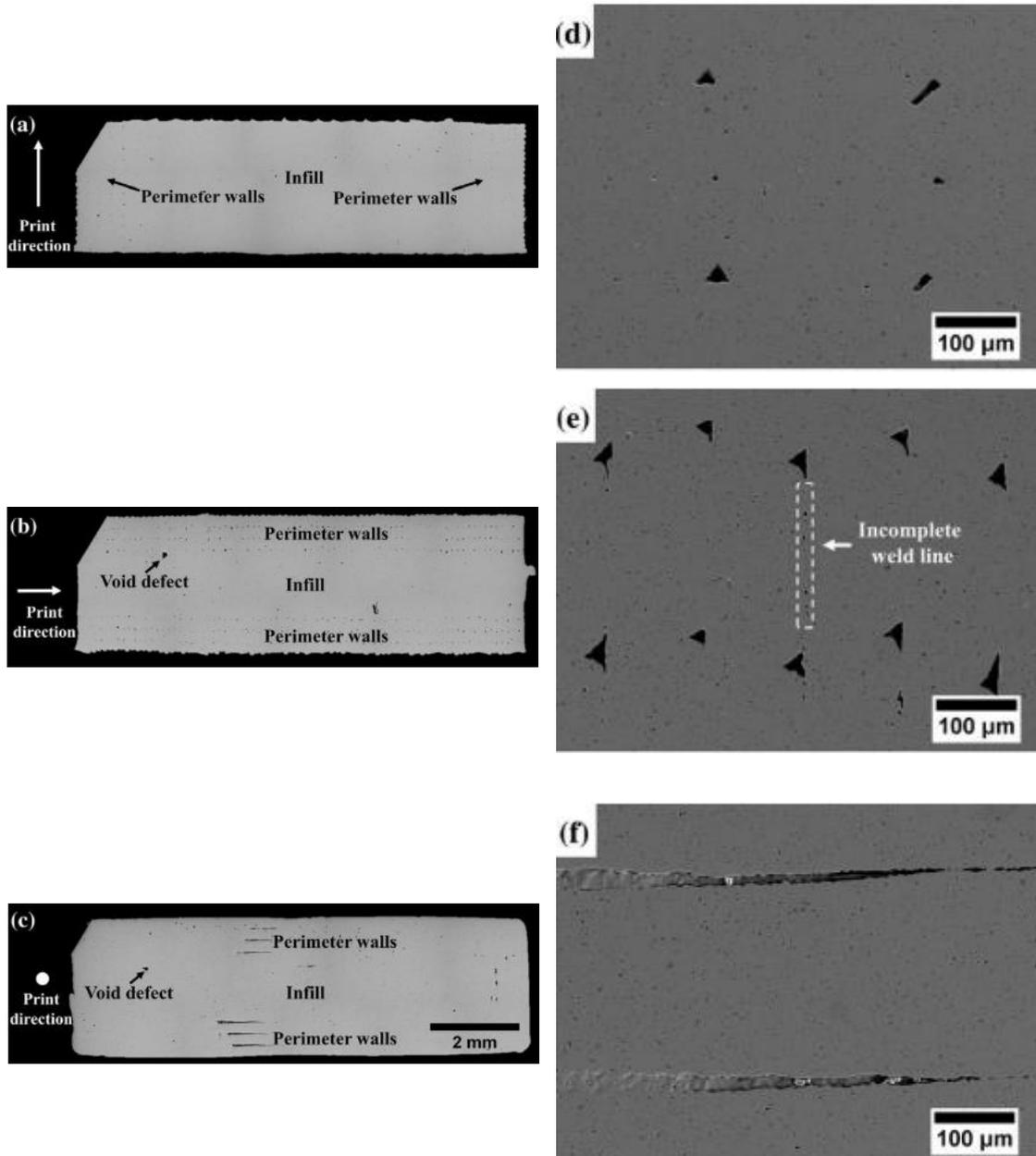


Figure 3.19: Optical macrographs of sintered specimens in the flat layout (a), the side layout (b), the vertical layout (c); SEM micrographs, focusing on the voids between perimeter wall area of sintered tensile specimens printed in the flat layout (d), the side layout (e), and the vertical layout (f) [124].

In a similar research [125], the authors evaluated the shrinkage behaviour by varying the layer directions of the specimens with respect to the building directions. Despite the orientation of the specimens, the authors confirmed the anisotropic tendency of the shrinkage. Besides, the highest value of linear shrinkage always occurred in the layer direction than in other directions, as shown in Figure 3.20.

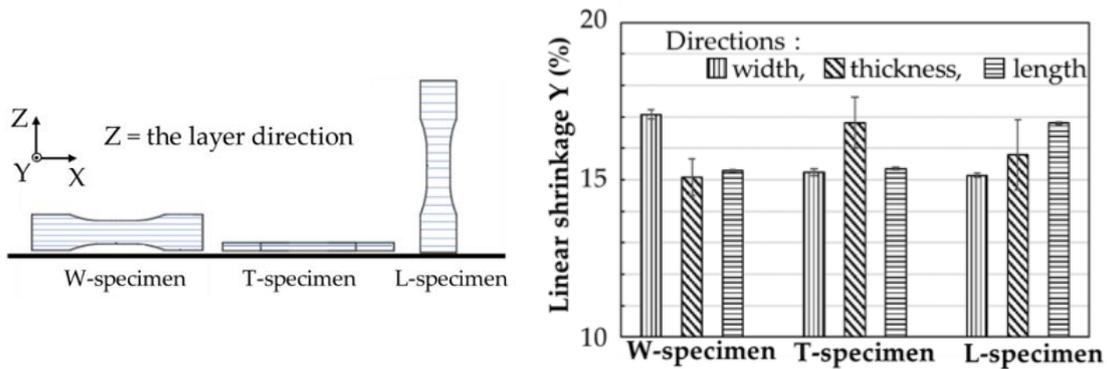


Figure 3.20: Linear shrinkage of the sintered specimens printed in various layer directions [125].

The anisotropy of the linear shrinkage is attributable to the extrusion and deposition process. Indeed, the binder domain was oriented parallel to the nozzle-moving direction (perpendicular to the building direction) since the deposited material was deformed by shearing between the moving nozzle and the previous layer. The large voids formed during the debinding process could not be closed by the sintering phase. As a result, the sintered specimens exhibited pores patterns perpendicular to the building direction, increasing the linear shrinkage in that direction. In Figure 3.21 it is noticeable the voids formed by the debinding of large organic binder domains and remained in the sintered L-specimens.

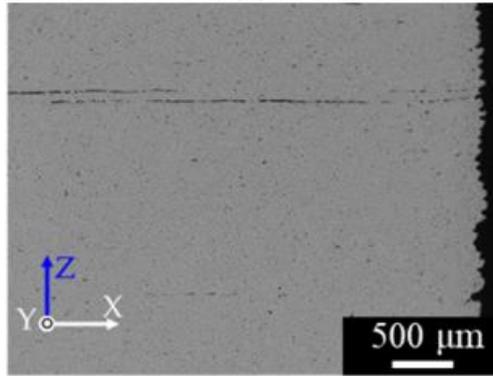


Figure 3.21: SEM micrographs of cross-sections of the as-sintered specimens observed perpendicular to the thicknesses of the L-specimen [125].

The solution and aging treatments affect the final physical properties and the microstructure of AISI 630 ME samples. The relative sintered densities improved by the application of heat treatments with the exception of specimens printed on the flat side in [125] (Figure 3.22).

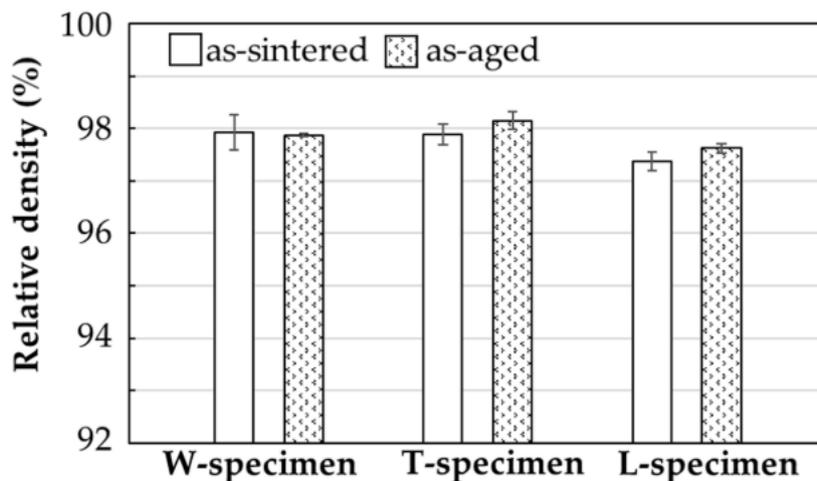


Figure 3.22: Relative densities of the sintered and aged specimens printed in various layer directions [125].

Condruz et al. [126] conducted a microstructural analysis with the combination of SEM images and EDS to denote any difference between the phases presented in as-printed and as-aged specimens. As exhibited in Figure 3.23, in the as-printed state were observed martensite and ferrite. The solution treatment favoured the formation of retained austenite at the grain boundaries. Lastly a difference of microstructure was detected in the as aged, since ferrite phases were encountered along with austenite at the grain boundaries, in

addition to martensite, which is the characterizing phase of AISI 630 material in quenched and tempered state.

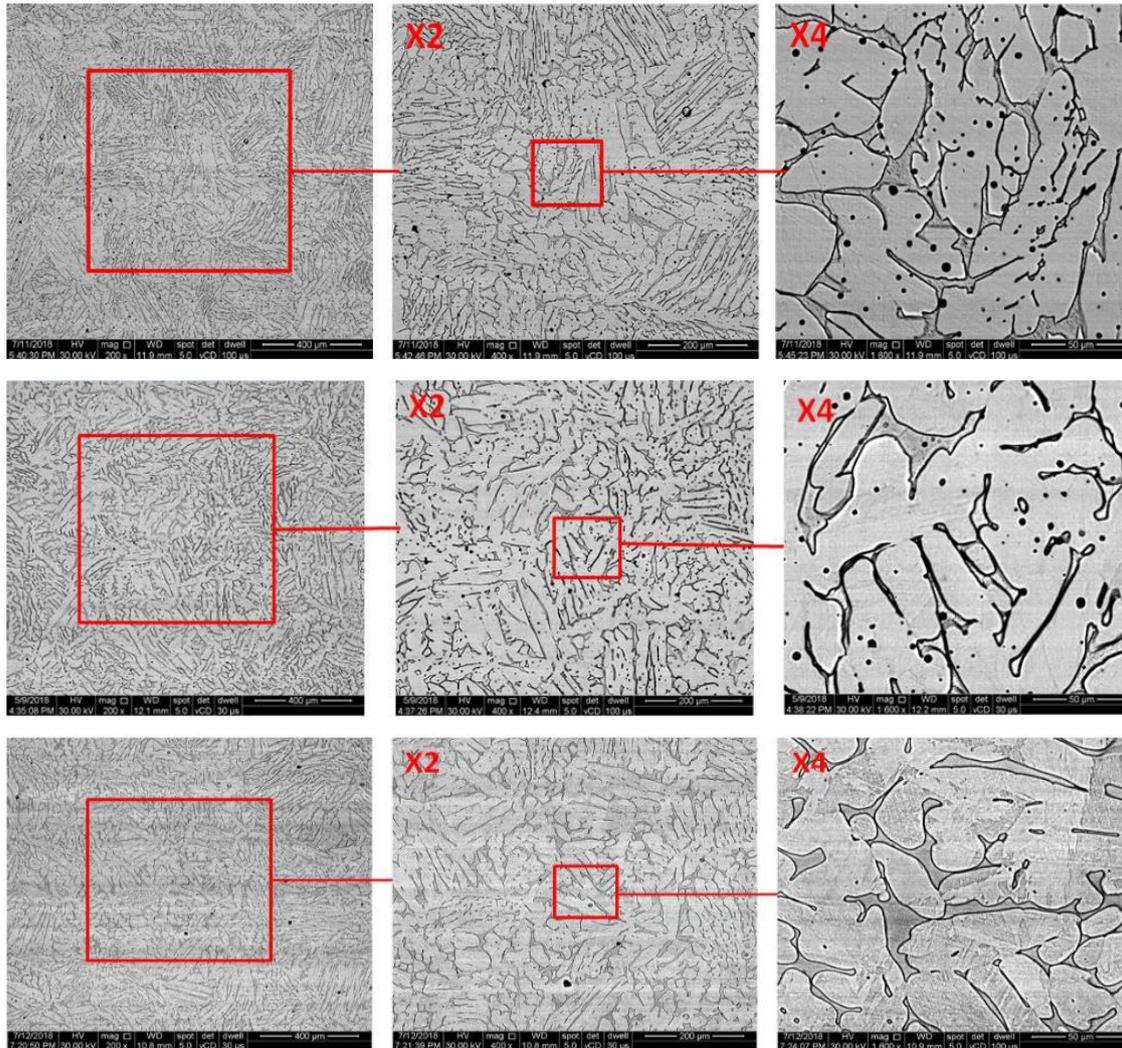


Figure 3.23: SEM image of AISI 630 sintered (top), quenched (middle) and aged (bottom) specimens [126].

3.2.2 Mechanical Properties

As reported in the previous section regarding the mechanical characterization of 316L ME specimens, ME process combined with subsequent debinding and sintering thermal treatments worsened the mechanical properties of AISI 630 specimens. Gonzalez-Gutierrez et al. [127] tested sintered dog-bone specimens with an average porosity of 4% to assess the relative tensile properties. The ultimate tensile stress (UTS) was lower than 34% compared to the value of the monolithic AISI 630. A smaller deviation from the bulk material was detected for the elongation at break.

Henry et al. [128] assessed the tensile behaviour of AISI 630 ME specimens as a function of dissimilar building orientation by means of a Digital Image Correlation (DIC) analysis. The highest value of UTS was registered for the specimens printed on xy plane. This configuration also ensured the maximum axial strain in comparison to on-edge and upright directions, as reported in figure. In all three cases (i.e., flat, on-edge and upright build orientations) the material failure arose in the gauge section at a location of axial strain concentration aligned perpendicular to the loading direction [128].

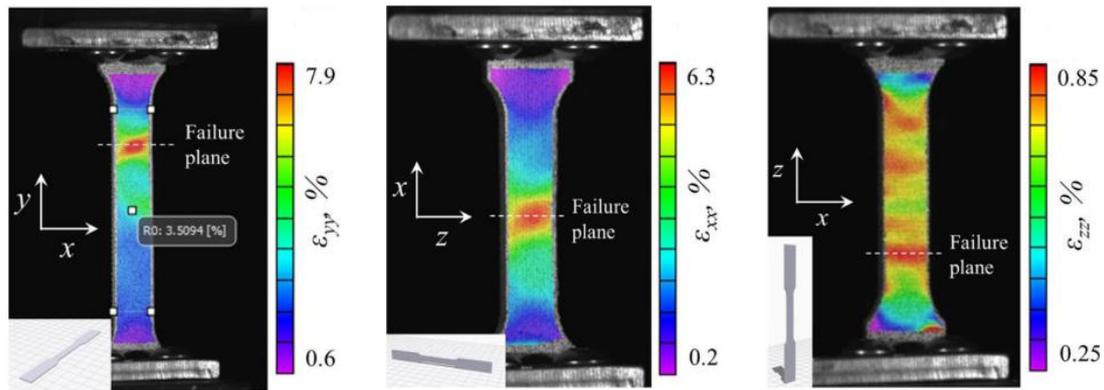


Figure 3.24: Axial strain field data for different loading conditions [128].

In [129], the bending behaviour of specimens made additively varying the build orientation was studied. The sintered specimens printed with flat and on-edge orientations exhibited a ductile behaviour compared to upright ones, which exhibited very limited plasticity with the lowest flexural strength and strain to failure, due to incomplete weld between two adjacent layers resulting in delamination and discontinuity issues. The flexural strength of the flat orientation is 22% and 92% higher than the on-edge and upright orientations, respectively. However, the on-edge orientation provides higher flexural strain to failure.

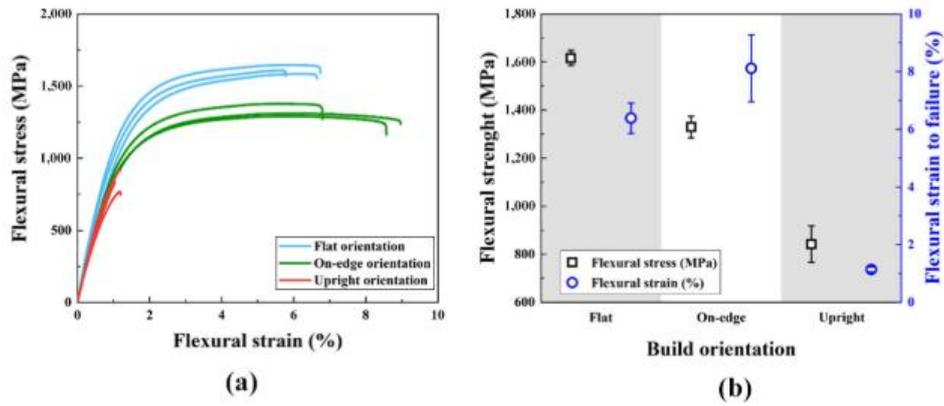


Figure 3.25: Flexural stress – strain curves varying build orientations (a); average flexural strength and strain to failure varying build orientations (b) [129].

This behaviour reflected the correlation between the voids positioning within the metal matrix and the loading direction. Indeed, the orientation of the voids in the on-edge layout induced the vertical printed layers to overflow up – layer sliding upwards, resulting in a considerable deformed specimen with a curve trapezoidal shape owing to the Poisson’s effect [130]. The Poisson’s effect generates a tensile stress state in the upper half and a compressive stress state in the bottom side. Both tensile and compressive stresses increase further away from the neutral axis (i.e., the center line of the specimen). Consequently, the sides of the specimen tend to laterally expand in the upper half and laterally shrink in the lower half. The sliding upwards of the layers provided a greater overwhelming effect on the on-edge specimens, leading to a higher bending strain with a lower bending strength compared to the flat orientation (Figure 3.26).

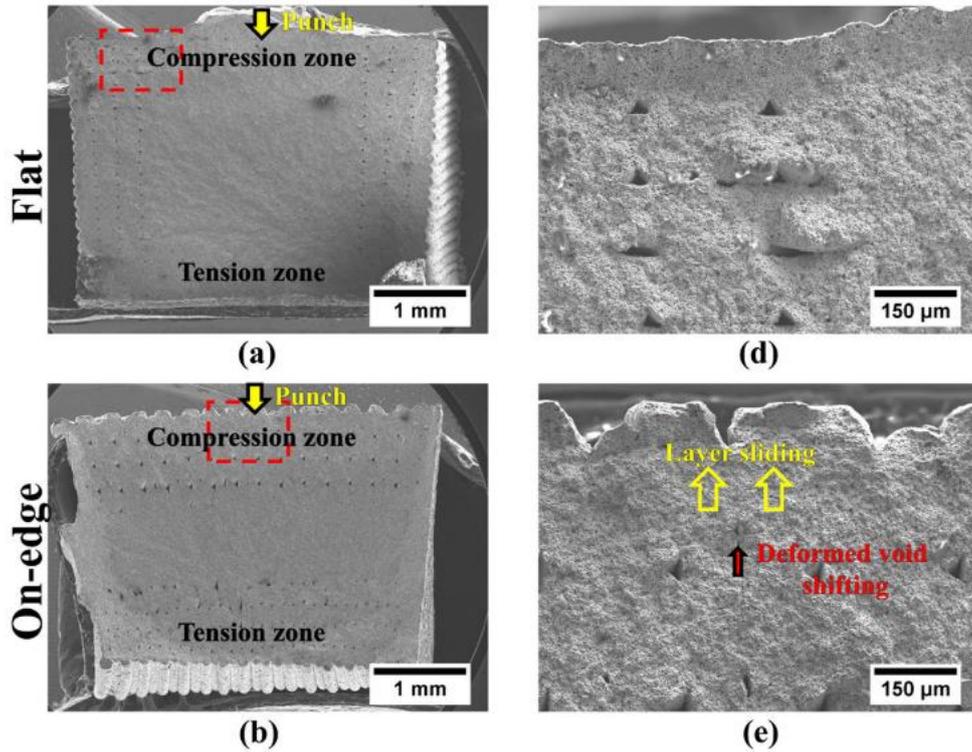


Figure 3.26: Fracture surface of sintered samples at low magnification with flat (a) and on-edge (b) orientations; high magnification of the fracture surface with flat (d) and on-edge (e) orientations corresponding to the red-dashed boxes [129].

Akindi et al. [131] studied the effects of printing angles variation on the tensile properties of sintered samples. The authors suggested the use of orientation angles within the range of 0° to 10° to achieve significant results in terms of tensile strength and ductility. The voids in the sintered specimens were oriented perpendicularly to the layer direction, despite the part orientation selected. However, the voids had a different orientation regarding the tensile direction for specimens printed with 0° and 90° with respect to the building platform. Indeed, the voids were oriented parallel to the tensile direction in the specimens with orientation angle of 0° , but perpendicular to the tensile direction in the samples with 90° printing angle. The voids in the second configuration were sensitive crack sites and the origin of fracture, lowering the values of UTS and elongation at break. Specimens printed at 0° to the build plate experienced an average of 947.26 MPa of ultimate tensile strength and 2.98% of elongation at break, while specimens printed at 90° showed a decrease of tensile strength close to 50% and almost 4 times lower elongation at break, compared to specimens flat printed. Besides, less anisotropic trend was detectable for yield strength of specimens printed with different orientation angles.

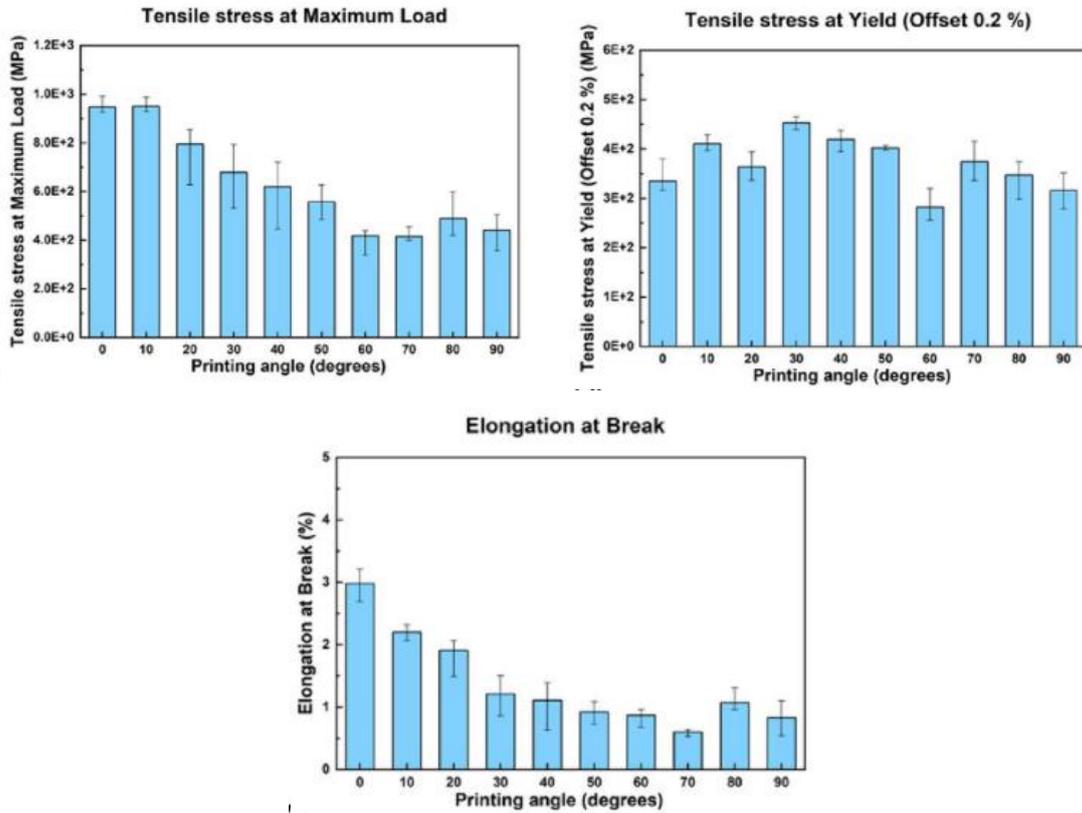


Figure 3.27: Tensile stress at maximum load, tensile stress at yield and elongation at break histograms as a function of different printing angles [131].

A correlation between the mechanical properties as a function of the printing angles and the voids formation within the specimens was detected by the authors. As evident in Figure 3.28, at 0° printing angle the pores had a triangular shape with a relatively small areas and they were spatially separated from each other. With the increase of printing angles, the voids shapes changed into line or rectangular and became spatially connected reducing the effective cross section of the specimens and providing sites for crack initiation.

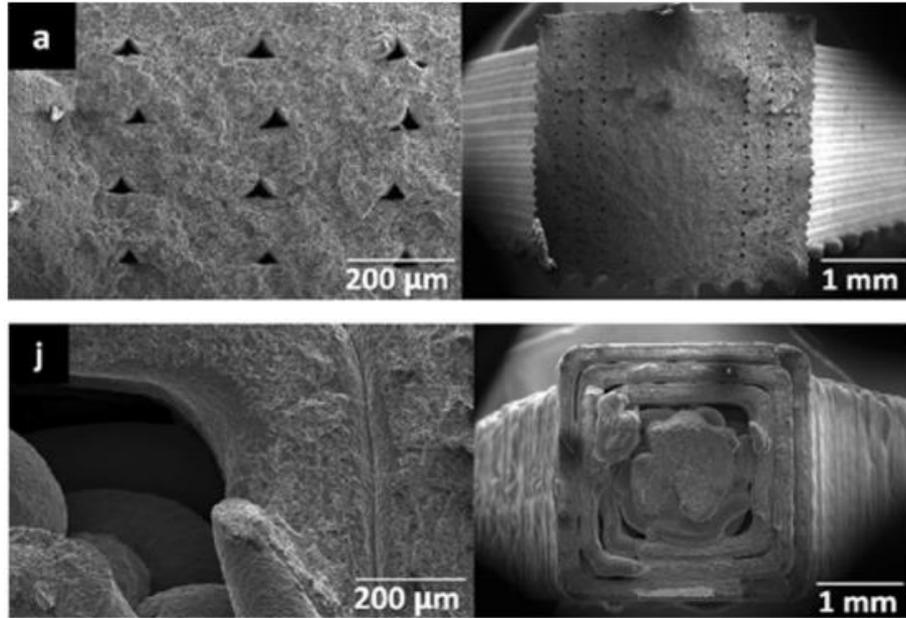


Figure 3.28: Cross section view of the fracture surface without undergoing tensile test at 0° (a) and 90° (j) printing angles [131].

The use of post-sintering heat treatment to improve the mechanical characteristic of the sintered parts is gaining significant attention. Indeed, the artificial aging after solution treatment was proved to enhance the mechanical properties in terms of strength due to the generation of refined ϵ -Cu precipitates with a size of 5–10 nm [132]. The formation of nanoscale Cu precipitates within the martensite structure prevents dislocation movements strengthening the tensile strength of AISI 630 specimens manufactured by material extrusion method. In [125], the authors proved the advantages of the precipitation aging mechanism for the tensile strength of the material regardless the build orientation selected for the specimens. Diversely, the artificial aging worsened the ductility of the specimens with a deviation of almost 40% compared to the bulk material for the aged specimens flat printed (Figure 3.29).

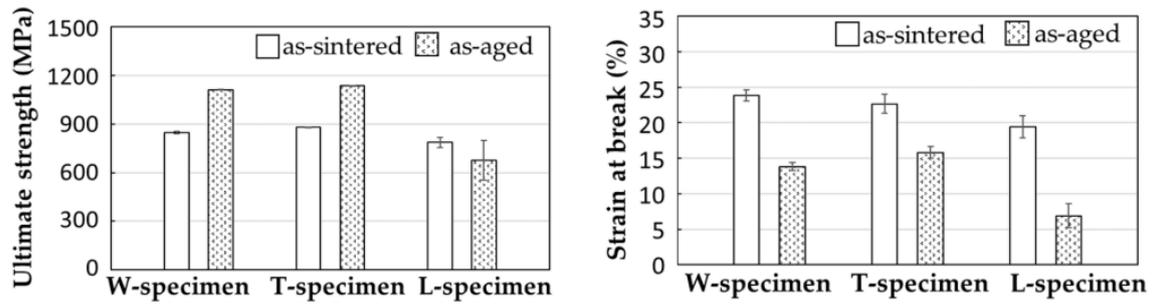


Figure 3.29: Ultimate strength and strain at break of the sintered and aged specimens printed in various layer directions [125].

Bouaziz et al. [133] confirmed the enhancement of the tensile properties of heat treated AISI 630 samples by 16%. Indeed, the H900 treatment improved the ultimate net section strength from 700 to 825 MPa, without any significant reduction of the ductile property of heat treated specimens. In this research the effects of H900 heat treatment on the surface roughness of samples was inspected. The artificial aging slightly deteriorated the surface roughness with an increase of R_a from $4.1 \pm 0.3 \mu\text{m}$ to $4.6 \pm 0.1 \mu\text{m}$ (Figure 3.30). The negligible worsening of surface roughness did not affect the mechanical properties of H900 samples.

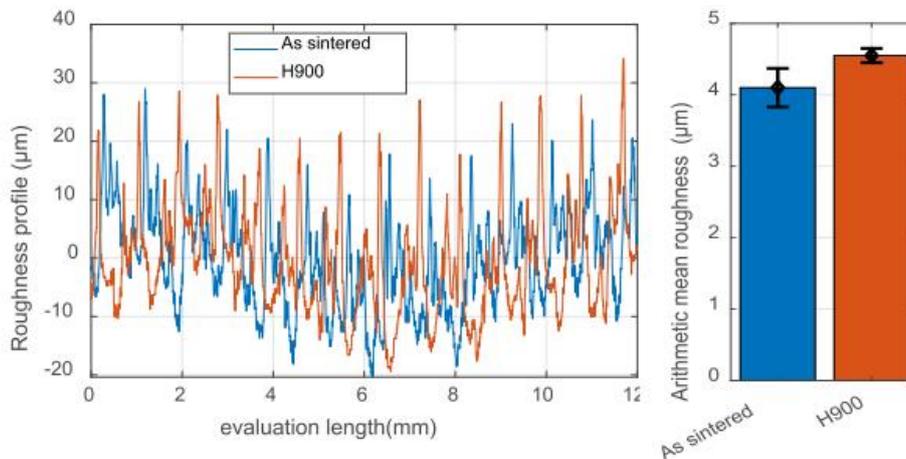


Figure 3.30: Roughness profiles and corresponding arithmetic mean roughness (R_a) of sintered and H900 treated samples [133].

Similarly to precipitation hardening treatments, Chemkhi et al. [134] applied surface mechanical post treatment (SMAT) to improve surface and mechanical properties of AISI 630 samples fabricated by means of material extrusion technique. Surface Mechanical Attrition Treatment provides the vibration of metal spheres using a high frequency ultrasonic generator. The vibration of spherical balls induces hardening on the surface induced by plastic deformation, as illustrated in Figure 3.31.

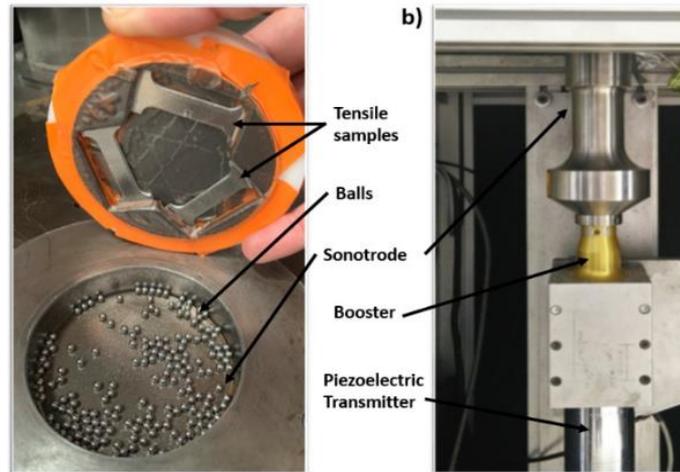


Figure 3.31: Schematic of SMAT set-up [134].

The attrition between spherical balls and the samples surfaces considerably reduced the surface roughness. Indeed, a reduction of almost 90% was calculated both for Ra and Rt surface roughness parameters. Since rough profiles of metal ME samples induce stress concentration and become sites for crack initiation, the reduction of peaks and valleys on the surface gave benefit also to the mechanical properties of the printed specimens. As shown in Figure 3.32, the net section stresses for equal engineering strain were higher for mechanically post treated samples, with a maximum value of 774 MPa. However, SMAT slightly reduced the final elongation of the treated samples.

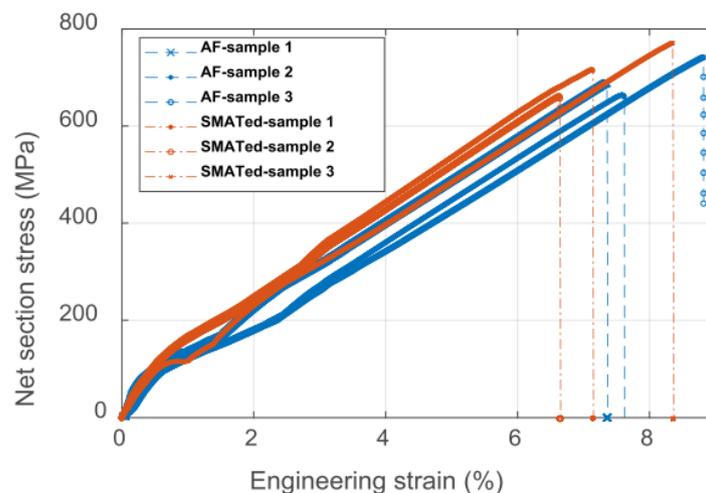


Figure 3.32: Net section stress – engineering strain curves of sintered and SMAT specimens [134].

3.3 Research Issues

This work aims to study and assess a newly Additive Manufacturing technology from the physical and mechanical point of view and study in deep the applicability of metal Material Extrusion technique in the manufacturing industries. This work was jointly developed within the collaboration between University of Bergamo and ENEA Portici Research Center.

Metal Material Extrusion is a multistep technique that comprises different processes including debinding and sintering thermal treatments. In literature, many efforts have been made to establish a relationship between debinding and sintering processes and the physical characterization of the metal parts. In addition to post shaping treatments, the dependency of the solid loading and the final sintered density has been extensively reviewed. Indeed, the process considered implies the loading of metal powder in a binder compound, which is extruded by means of printing machine traditionally born for polymeric materials.

The first objective of this work covers, thus, the analysis of how different combinations of printing process parameters affect the physical properties of AISI 316L samples manufactured by means of metal ME. In particular, the effort focuses on the optimization of the process parameters to achieve the highest relative density of the metal samples, compared to the conventional density of the relative material. Besides, also the response of the dimensional linear shrinkages to the variation in the printing process has been widely analysed. Lastly, a porosity evaluation was carried out on samples printed with different process parameters to estimate the dependency between the extrusion and deposition phases and the set of defects generated in the shaping step.

Once it has been established the combination of printing process parameters that maximize the final density of sintered samples, an overall mechanical characterization of metal ME samples was conducted. The optimized combination was used to print the test samples and AISI 316L was selected due to its interesting combination of mechanical and corrosive properties. These characteristics allow a large use of AISI 316L in different manufacturing sectors. For this reason, thorough knowledge of the mechanical response of ME components made up of with this alloy is essential to expand its application beyond the mere prototyping phase. Tensile tests, compression tests, Charpy impact tests, Rockwell B and Vickers hardness tests were performed. Besides, an X-ray diffraction

analysis was conducted to assess the crystallographic structure of the ME 316L samples compared to that of the monolithic material.

In this research, another metal alloy was considered to verify the technical feasibility of the technology analysed. AISI 630, also commercially known as 17-4PH, is a precipitation hardening stainless steel. This martensitic stainless steel is well diffused in dissimilar manufacturing sectors, since thermal treatments considerably improve the mechanical response to applied loads. This section provides a comprehensive structural characterization to establish the combination of process parameters ensuring the highest relative density compared to the conventional one. This analysis was carried out by means of a Taguchi DoE and a statistical analysis. Based on the physical properties outlined, specimens for dissimilar mechanical tests were printed with the optimized combination of printing process parameters. In literature, little knowledge about the effects of different solution and aging treatments on metal specimens obtained via Material Extrusion technique is available. To fill this gap, sintered samples were subjected to H900 (peak-aged) and H1150 (over-aged) thermal treatments and, subsequently, to tensile, compressive, bending and Vickers hardness tests. One of the most important goals of this research was the evaluation of the mechanical properties of sintered samples following post sintering thermal treatments compared to those of the monolithic material.

The physical and mechanical characterization of sintered ME samples made up of AISI 316L and 630 proved that this newly technique represents a valid and robust alternative to more spread and used metal AM technologies, such as Powder Bed Fusion or Direct Energy Deposition. However, metal ME is still immature from a process perspective generating a considerable amount of defects within the green parts. Defected green parts result in scraps, which represent an environmental and economic waste. The negative impact of internal and superficial defects could undermine the economic advantage of metal ME technique with respect to traditional metal AM technology to produce metal components. To minimize this possibility, a recycling methodology was proposed for reusing scraped green parts to produce a new highly filled filament. Furthermore, a preliminary analysis was provided to evaluate the technical effectiveness of the proposed method. A comparison among the filaments, the green parts and the sintered parts realized with commercial and recycled feedstock was provided. This contribution represents a novelty, since any similar work was available in literature.

4 Density and shrinkage evaluation of AISI 316L parts printed via FDM process

This chapter is derived from the article “Quarto, M.; Carminati, M.; D’Urso, G (2021). Density and shrinkage evaluation of AISI 316L parts printed via FDM process. Materials and Manufacturing Processes”.

DOI: 10.1080/10426914.2021.1905830.

I am immensely grateful to the support received from my co-authors. I am responsible for all the changes in this chapter with respect to the published version.

4.1 Introduction

As reported in the previous chapters, the development and the spread of metal Material Extrusion technique necessary involves the study and the analysis of the main relevant indicators of the physical properties of sintered samples.

The literature review illustrated in paragraph 3.1.1 showed the correlation among different printing orientation (i.e., flat, on edge and upright) and dissimilar sintering conditions in terms of peak temperatures and holding times with final sintered density and dimensional linear shrinkages. However, few studies concentrated the effort on the interaction between the printing process, consisting of the extrusion and deposition phase, and the physical properties of specimens resulting following the debinding and sintering steps.

In this chapter, some of the main relevant parameters of metal ME printing process were analysed by means of an analysis of variance (ANOVA) to verify their possible influence on the physical and dimensional response of the produced parts. This study aims to identify which factors affect the final AM products in terms of shrinkage percentage along X, Y and Z directions and bulk density (ρ_{Bulk}).

Moreover, the optimal process parameters combination assuring a density value as close as possible to the traditional material were identified. The experimental tests were carried out on prisms printed with a low-cost 3D printer and using a metal-polymer composite filament. Once it is defined if the selected process parameters affect in some way the indicators, it is possible to identify the specific values of the shrinkage useful to oversizing CAD models.

In the same way, it is possible to set-up the process parameters in order to obtain a satisfactory density. The novelty of this work is related to the possibility to produce parts for non-critical environment with high value added by means of a low-cost equipment.

4.2 Materials and methods

4.2.1 Equipment and materials

The test samples were fabricated by means of an Ultimaker S5 printer, using a filament with a diameter of 2.85 mm provided by BASF and called Ultrafuse 316L. It is an innovative metal filament made up of 316L austenitic stainless-steel powder (90 wt%), characterized by high ductility and corrosion resistance, and polyoxymethylene (POM), polyolefin, which allows for easy printing. The direct drive extruder of the printer was equipped with a hardened steel nozzle CC0.6 (supplied by Ultimaker) with a diameter of 0.6 mm. Its main properties are reported in Figure 4.1a, where they are compared to those of monolithic AISI 316L. Once the samples were printed, the main polymer content (primary binder, i.e., polyoxymethylene) was removed from the so-called green-part through a catalytic debinding process at 120 °C, obtaining the brown-part, consisting of pure metal particles and a residual binder (backbone). The brown-part was characterized by the same volume and a reduction in mass with respect to the green-part. The subsequent sintering process at temperatures immediately below the melting temperature of the metal allowed to remove the secondary binder from the brown-part and to sinter the metal particles, so filling the cavities left by the binder. The sintering cycle consisted in two ramps at high temperatures with two different holding times which allow to reach the final physical and mechanical characteristics of the parts, generating a volume reduction described by the shrinkage percentages. Further details could not be provided since the post-shaping processes instructions are confidential. The material reaches its final properties in terms of hardness, strength and ductility after the sintering phase. These treatments were performed by an external company.

4.2.2 Plan of experiments

The geometry chosen for the samples is very simple (prism as it is possible to see in Figure 4.1c), since, at this stage of the study, the analysis was focused on the identification

of the main behavior of this material and the ability of a commercial 3D printer to print composite materials producing metal parts with a simple and low-cost technology. The experimental campaign was conducted on the base of a 2^4 full factorial design of experiments (DoE) varying the nozzle temperature (T_{nozzle}), the infill type (In), the print speed (s) and the layer thickness (h) on 2 levels (low and high). 4 repetitions were considered for each combination of the process parameters. The infill density was set at a constant level of 100%, since the aim of the experimental campaign was to achieve a final ρ_{Bulk} of the specimens as close as possible to the value of technical datasheet of AISI 316L. A bed temperature of 100 °C was applied to enhance the bonding of the first layer and to avoid the warpage of the samples. The dimensional (shrinkage) and physical properties (density) of the fabricated samples were measured to identify if and how they are related to the printing process parameters. The levels of the different factors were chosen on the base of the following considerations. The nozzle temperature (T_{nozzle}) is a critical parameter that affects the success of the extrusion process. T_{nozzle} above the melting point of binders is recommended to reduce the viscosity of the filament and to enable the extrusion. In represents the trajectory of the nozzle while filling the internal volume of the parts. Table 4.1 shows the 2^4 factorial plan displaying the combination of process parameters for each sample. Figure 4.1b shows the two types of infill pattern used to produce the layers of samples. s refers to the speed of the extruder movement and h represents the height of the single deposited layer. This last parameter affects the quality of the parts along the growth direction (Z). The low and high levels of each considered parameter were selected by means of preliminary tests aimed at defining a technological window in which it was possible to print the selected material. Their values are reported in Figure 4.1a.

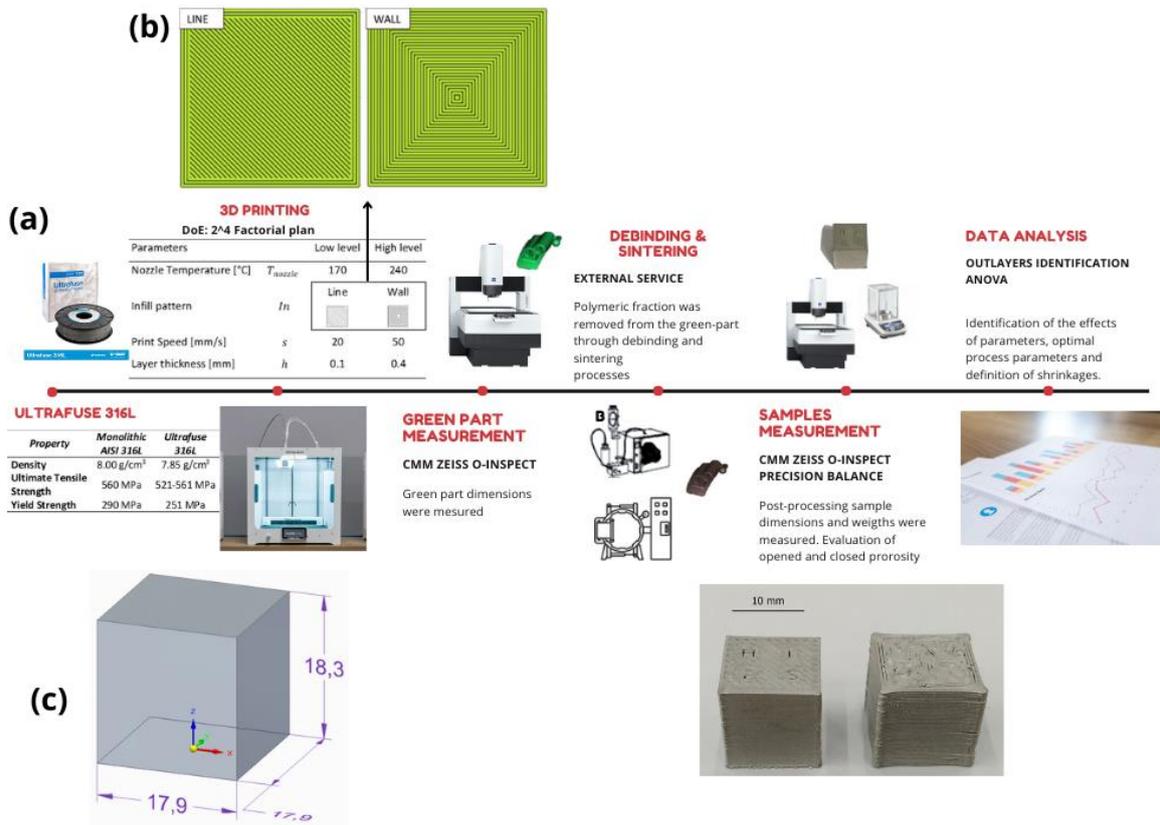


Figure 4.1: Details about process and methodology and different aspects of samples printed with different set of process parameters (in particular layer thickness).

Table 4.1: Design of experiments: sample identification and process parameters combinations.

Samples	T_{nozzle}	In	s	h
1 – 17 – 33 – 49	170	Line	20	0.1
2 – 18 – 34 – 50	240	Line	20	0.1
3 – 19 – 35 – 51	170	Wall	20	0.1
4 – 20 – 36 – 52	240	Wall	20	0.1
5 – 21 – 37 – 53	170	Line	50	0.1
6 – 22 – 38 – 54	240	Line	50	0.1
7 – 23 – 39 – 55	170	Wall	50	0.1
8 – 24 – 40 – 56	240	Wall	50	0.1
9 – 25 – 41 – 57	170	Line	20	0.4
10 – 26 – 42 – 58	240	Line	20	0.4
11 – 27 – 43 – 59	170	Wall	20	0.4
12 – 28 – 44 – 60	240	Wall	20	0.4
13 – 29 – 45 – 61	170	Line	50	0.4
14 – 30 – 46 – 62	240	Line	50	0.4
15 – 31 – 47 – 63	170	Wall	50	0.4
16 – 32 – 48 – 64	240	Wall	50	0.4

4.2.3 Shrinkage and density measurement

The printed samples were measured by a CMM (Zeiss O-Inspect) obtaining values along X, Y, and Z – directions. The measurements were performed both for green-parts and for samples after debinding and sintering processes. In this way, it was possible to calculate the dimensions and the volume of the samples before and after the thermal treatments. The measurements were performed in an automatic way using a touching probe. Once all

the plans were scanned by the probe, the software estimated the distance between the reconstructed plans and the sample volume. The measurements were repeated three times to ensure the accuracy of the procedure and to avoid random errors in measurements (positioning errors, movement of samples on the CMM). Then, the average values were used as reference values for the analysis.

The shrinkage due to the debinding and sintering processes was calculated as the percentage dimension reduction along the three directions according to Eq. (1).

$$Shrinkage_i = \frac{(D_{gp_i} - D_{pp_i}) \cdot 100}{D_{gp_i}} \quad (1)$$

Where i indicates the dimension (X, Y, Z), D_{gp} and D_{pp} refer to the dimension of the green-part and the post-processing parts respectively.

The bulk density (ρ_{bulk}) was calculated only for the samples obtained after thermal processes as the ratio between the weight and the volume of the sample (2). In particular, the theoretical volume (V_{theo}) is related to the volume of the sample after thermal treatments calculated using the dimensions estimated through the CMM and w indicates the post processing weight measured using a precision balance.

$$\rho_{bulk} = \frac{w[g]}{V_{theo}[cm^3]} \quad (2)$$

4.2.4 Porosity evaluation

The metal ME process can produce parts characterized by the presence of porosity into the internal structure; for this reason, the bulk density was compared with the density of monolithic AISI 316L ($\rho_{AISI} = 8 \text{ g/cm}^3$) and the amount of opened and closed porosity were estimated through a method based on the evaluation of liquid penetration.

The sample was first weighed in air (m_1) before being immersed in a wetting liquid (1-butanol) for 24 h to fill open porosity. Then, the sample was taken out of the solvent and its surface was quickly swabbed before weighing it in air (m_2 , corresponds to m_1 with the addition of the mass of solvent contained in the open pores). Knowing the density of the solvent (ρ_{fluid}) and combining these weights, the opened porosity fraction (op - (3)) and closed porosity fraction (cp - (4)) of the sample were given.

$$op = \frac{m_2 - m_1}{\rho_{fluid}} \quad (3)$$

$$cp = V_{theo} - \frac{m_1}{\rho_{AISI}} - op \quad (4)$$

4.2.5 Data analysis

Before applying the analysis of variance (ANOVA), a pre-treatment of the data was carried out for identifying possible outlier values. The interquartile range (IRQ) criterion was used and, in particular, it was considered as outlier a value that is more than 1.5 times the interquartile range away from the top or bottom of the box. The analysis was carried out by means of a Matlab code. Once the outliers were identified and displayed by the boxplots, they were eliminated from the dataset considered for the ANOVA. A boxplot for each indicator was generated showing information about the median, the lower and upper quartiles and the outliers. The ANOVA was carried out to identify a possible influence of selected process parameters on the final indicators previously described (shrinkage along three dimensions and bulk density) and a confidence interval equal to 95% was considered.

4.3 Results and discussion

The outlier analysis identified 2 outliers for the shrinkage along the X-axis and 3 along the Y-axis. These data were deleted from the dataset. The boxplots of the measured sample characteristics in terms of shrinkage and density are reported in Figure 4.2, where it is easy to pinpointed the outliers in terms of sample number (Table 4.1).

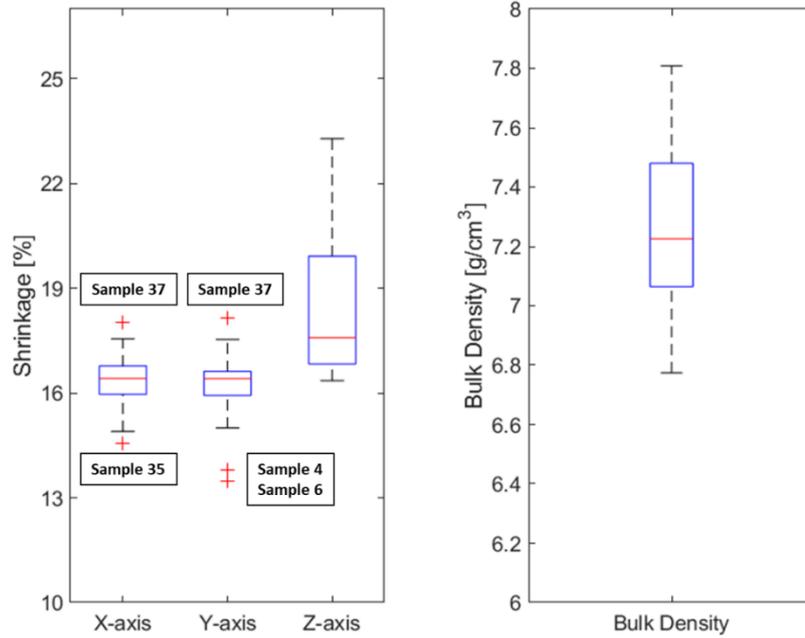


Figure 4.2: Boxplot for shrinkages and bulk density outliers identification.

In Figure 4.3 the plots for the shrinkages along the axis and the bulk density are reported. It is possible to compare the experimental results with the nominal shrinkages and bulk density values defined in the technical sheets (BASF and monolithic AISI 316L, respectively). The black dots represent the mean values of the shrinkage estimated using the three measures collected for each sample. In general, it is possible to observe that the standard deviations of the data are very small indicating that the results of each group of measures are close. Regarding the shrinkage along X and Y-axis, the results assume a very similar trend; in both cases, the data are placed close to the nominal shrinkage. Different behavior can be observed for the shrinkage along Z-axis. In this case, the deviation from the nominal values is higher and it is possible to observe a relation with the set of applied parameters. Considering the bulk density of the post-processing samples (Figure 4.3), it is possible to note that the densities reached during the process are included in a range between 6.7 and 7.8 g/cm³.

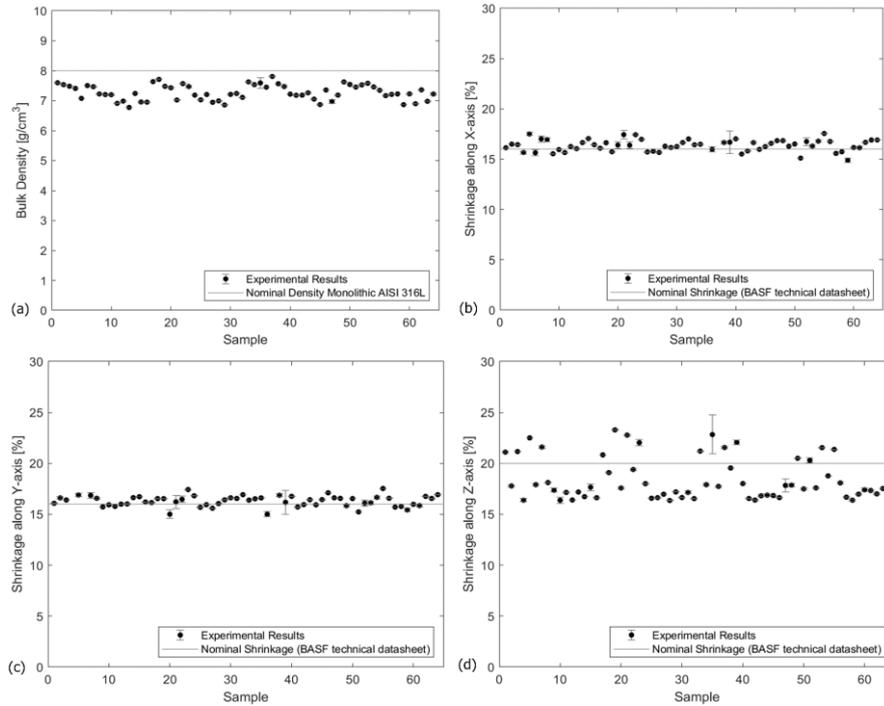


Figure 4.3: Errorbar of bulk density and shrinkages.

The analysis of variance was performed to identify a possible influence of the process parameters on the main characteristics of the post-processing samples. The analysis was conducted considering the dataset obtained by eliminating the outliers. The residuals demonstrated, in all cases, to be normally distributed and randomly scattered with an average value near to zero. Table 4.2 summaries the p-values obtained after the ANOVA. It is possible to observe that the single parameters affect, in each case in a different way, the indicators, while only few 3-way interactions affect the indicators. In particular, the bulk density is affected by In , s and h . In this case, the T_{nozzle} , as a single parameter, does not affect the results, but it plays an important role from the interaction point of view, especially as regards its interaction with the infill type and the layer thickness. For the shrinkages, it is clear that each direction is influenced in a different way; in general, speed is the factor that affects all shrinkage directions, but, while shrinkage along X direction shows an effect derived from layer thickness, the shrinkage along Z direction shows also an effect due to the T_{nozzle} . Indeed, the temperature of the nozzle affects the adhesion of the layers along the growth direction. The objective of the AM process should be to obtain the highest possible bulk density, close to the monolithic AISI 316L (8 g/cm³). The main effects plot (Figure 4.4a) shows the parameters combination satisfying

this requirement: In = Line infill, s = 20 mm/s and h = 0.1 mm. This is also confirmed by the graph reported in Figure 4.4b, where it is possible to observe that the greatest bulk density was obtained for the process parameters combination indicated above (red circle), regardless of the T_{nozzle} value.

Table 4.2: ANOVA p-values.

	p-value			
	Bulk Density	X-Shrinkage	Y-Shrinkage	Z-Shrinkage
T_{nozzle}	0.0790	0.2860	0.4310	0.0000
In	0.0030	0.0830	0.9890	0.8050
s	0.0050	0.0000	0.0000	0.0010
h	0.0000	0.0010	0.0590	0.0000
2-way interaction				
$T_{nozzle} \cdot In$	0.0060	0.6250	0.0010	0.0550
$T_{nozzle} \cdot s$	0.1200	0.0070	0.4050	0.8430
$T_{nozzle} \cdot h$	0.0030	0.0930	0.0420	0.0000
$In \cdot s$	0.2500	0.0110	0.0130	0.2950
$In \cdot h$	0.3940	0.0330	0.1620	0.0580
$s \cdot h$	0.0580	0.7550	0.6810	0.3340
3-way interaction				
$T_{nozzle} \cdot In \cdot s$	0.0040	0.6410	0.8370	0.3760
$T_{nozzle} \cdot In \cdot h$	0.8250	0.2510	0.0770	0.0450
$T_{nozzle} \cdot s \cdot h$	0.1210	0.0760	0.9360	0.4810
$In \cdot s \cdot h$	0.2150	0.2000	0.0290	0.1500
$T_{nozzle} \cdot In \cdot s \cdot h$	0.9870	0.1840	0.0840	0.2160

Figure 4.4b and 4.5 show the average values of bulk density and shrinkages (average and standard deviation of the 4 runs), as function of the process parameters combination. In all cases, the low standard deviations show the stability and repeatability of the process. The shrinkages along X, Y and Z directions obtained through the experimental campaign were compared with the values declared in the technical datasheet. Figure 4.5a and b show that shrinkage percentage along X and Y-axis are closer to the nominal value declared. Moreover, it is possible to observe a near-perfect overlap of the trends of shrinkage along X and Y-axis. This means that X and Y directions are characterized by a very similar behavior. On the contrary, the shrinkage along Z-axis shows a greater dispersion (Figure 4.5c). Furthermore, samples with 0.4 mm of layer thickness show a similar trend lower than the nominal value (~16.90%), while samples with a layer thickness equal to 0.1 mm clearly show an effect due to the interaction of the layer thickness with the nozzle temperature. In particular, the samples obtained with the lowest temperature have a higher shrinkage along Z-axis with respect to those realized with the highest temperature. These evidences are confirmed by the p-value reported in Table 4.2.

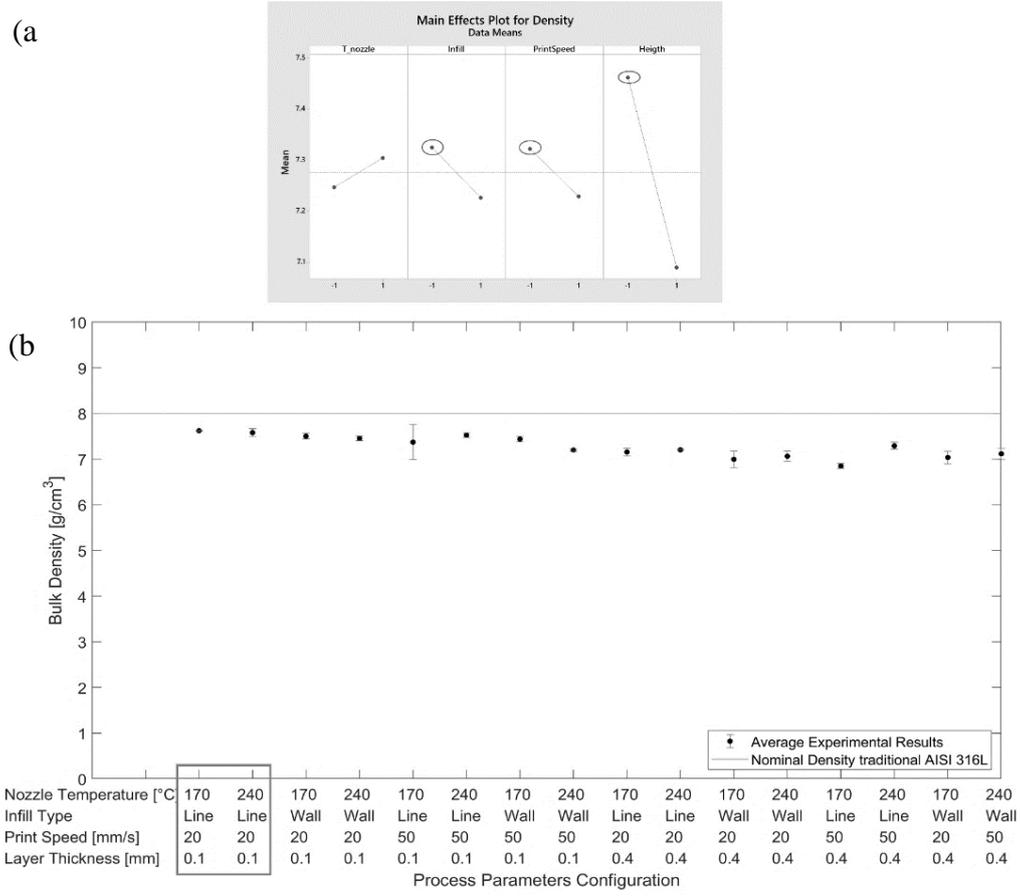


Figure 4.4: Main effects plot for bulk density (a) and aggregate data (b) as a function of process parameters.

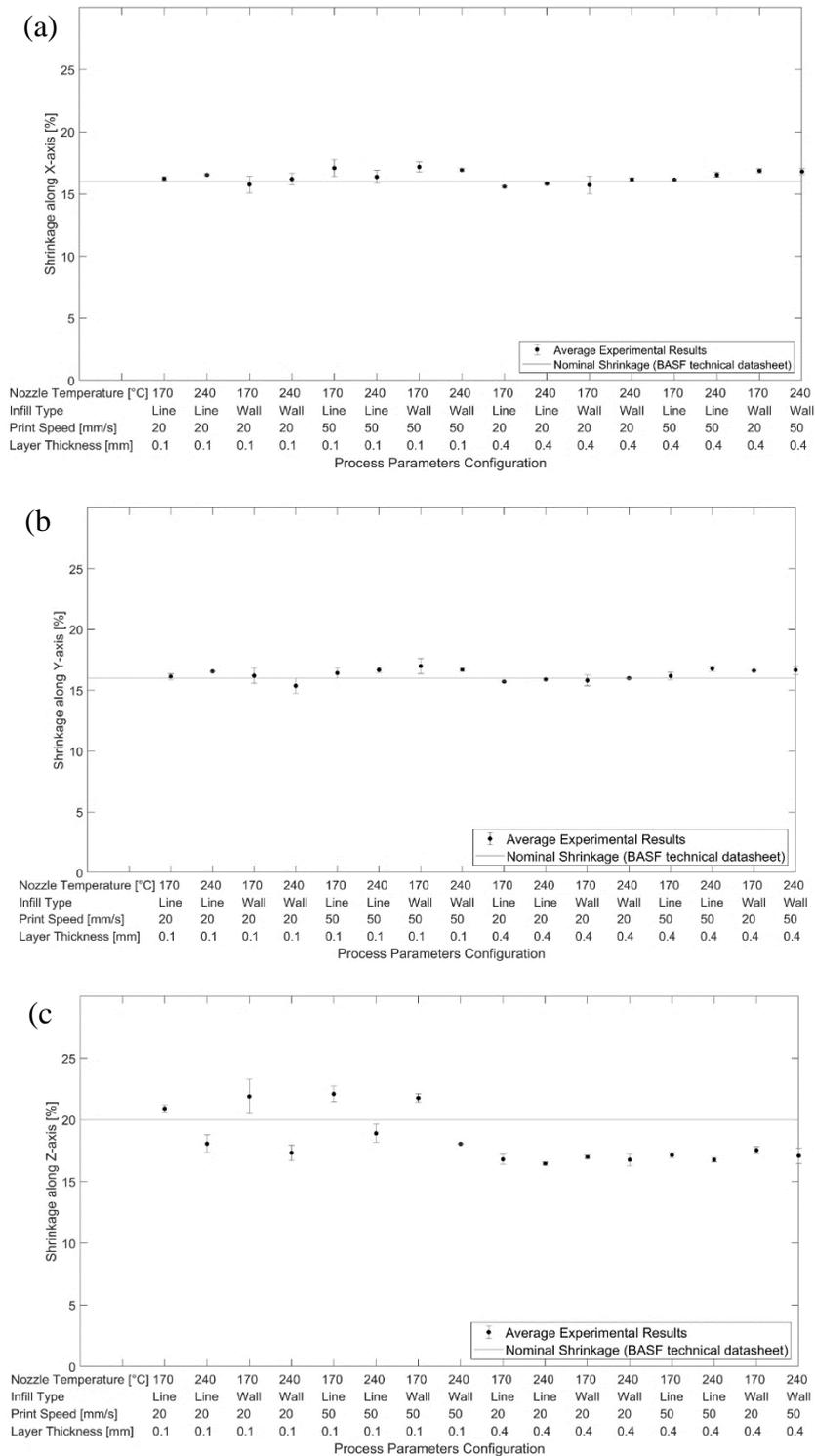


Figure 4.5: Aggregate data of shrinkage along X-axis (a) and Y-axis (b) and Z-axis (c) as a function of process parameters.

The percentage of the porosities was estimated to set the real density and the structure of the material. The percentages of the volume of opened and closed porosity were evaluated

as a function of the theoretical volume estimated through a CMM. This analysis was performed for the samples produced with the optimal process parameters and the samples characterized by the lowest bulk density, allowing to identify any different behavior of the distribution of metal particles. Differences in the structures are evident (Figure 4.6): the samples with the worst bulk density show a higher percentage of opened porosity, indicating a not optimal layer adhesion and imperfection on the external surfaces. On the contrary, the percentage of closed porosities is similar for all the analyzed samples. To be precise, the differences between the samples printed with optimal parameters is very small, showing an opened porosity percentage equal to 2.41% and 2.72% for T_{nozzle} equal to 240°C and 170°C respectively. Therefore, this result allows to define the application of low temperature of the nozzle as a better solution.

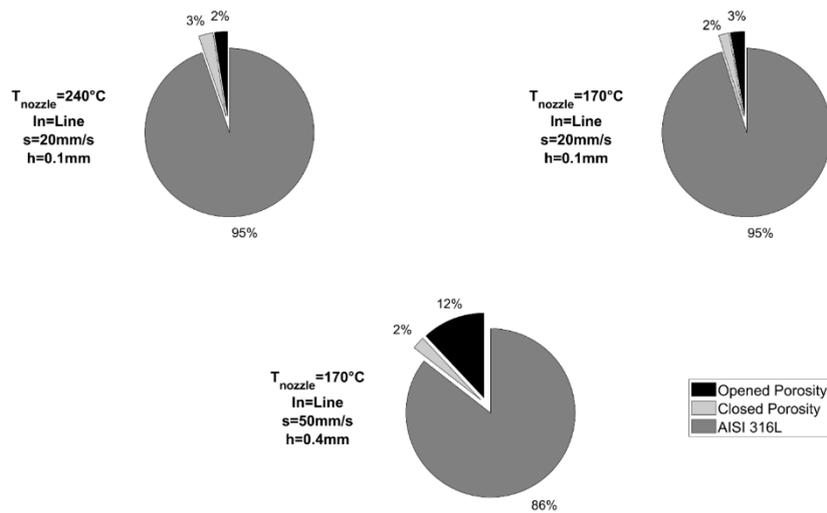


Figure 4.6: Pie-chart of ratio between percentages of AISI 316, open porosity and closed porosity volume.

4.4 Conclusion

This study introduced the application of Ultrafuse 316L filament on a low-cost FDM machine. The conducted experiments pointed out that the bulk density of the final parts is affected by the process parameters. In specific, a printing process characterized by infill line pattern, s 20 mm/s and h 0.1 mm generated the best results in terms of nominal density. Conversely, nozzle temperature showed no influence on nominal density of samples. It was also found that shrinkage along X and Y directions has a similar behaviour

(about 16.40%) after the thermal treatment, while the effects due to the debinding and sintering processes was more critical along the Z-axis in terms of both shrinkage value and scatter. This is mainly due to the effect of the layer thickness and to the interaction between the temperature and the infill type. The optimal parameters combination allowed to obtain a shrinkage equal to 20%. In particular, the best combination was found for a line infill, layer thickness equal to 0.1 mm and a print speed equal to 20 mm/s. Considering these characteristics, it is possible to claim that the use of a metal filament in ME process is a promising way of making non-critical metal AM parts and deserves further investigations, also thanks to its cost-efficiency. In particular, it was shown that it is possible to convert a commercial FDM printer, typically used for polymeric materials, in a printer for metal filament by simply changing the printer nozzle (nozzle with a higher wear resistance is needed). This may represent a sustainable solution both for the economical aspect and for the simplicity of production of parts having complex geometry.

5 Mechanical Characterization of AISI 316L Samples Printed Using Material Extrusion

This chapter is derived from the article “Carminati, M.; Quarto, M.; D’Urso, G.; Giardini, C.; Maccarini, G. Mechanical Characterization of AISI 316L Samples Printed Using Material Extrusion. *Appl. Sci.* 2022, 12, 1433”.

DOI: 10.3390/app12031433.

I am immensely grateful to the support received from my co-authors. I am responsible for all the changes in this chapter with respect to the published version.

5.1 Introduction

Based on the results obtained in the chapter 4, specimens for the mechanical tests were printed using the optimized combination of printing process parameters that ensured the highest level of apparent density. Indeed, the overall porosity distributed in the metal matrix is the main cause for the deterioration of the mechanical properties of components made additively compared to the those of the conventional material.

In the present work, an overall technical feasibility of debinded and sintered specimens was provided in comparison with the monolithic AISI 316L material to expand the technical feasibility of this promising ME alternative for the manufacture of components requiring good mechanical characteristics utilizing low-cost equipment.

Tensile, compressive, Charpy impact, three point bending, Rockwell and Vickers hardness tests were carried out and the mechanical response of metal samples to different types of loading were assessed.

5.2 Materials and Methods

5.2.1 Equipment and material

The testing samples were fabricated using a ME polymeric machine Ultimaker 5S, equipped with a direct drive extruder with a hardened steel nozzle CC0.6 of diameter 0.6 mm, which was the smallest nozzle diameter limiting the clogging problem. A filament with a diameter of 2.85 mm, provided by BASF (Ultrafuse 316L), was used. This is an innovative filament, which is made up of 316L austenitic stainless-steel powders (90 wt%), evenly distributed in a polymeric matrix composed of polyoxymethylene (POM)

and polyolefin. The immobilization of the metal particles and the uniform distribution of the metal within the binder matrix allows for safe and simple handling. The parts are built up layer upon layer from a moldable material, with the polymer content of the filament acting as a binder. The main polymer content (primary binder) was removed from the so-called green part through a catalytic and thermal debinding process at 120°C with HNO₃ (concentration 98%). The result of this process is the brown part, which consists of pure metal particles and a residual binder (secondary binder). The brown part is characterized by the same volume and a loss of mass compared to that of the green part. The subsequent sintering process removes the secondary binder from the as-built part and causes metal particle coalescence. The sintering cycle was performed in argon atmosphere and consisted of three thermal ramps:

- room temperature – 5 °C/min – 600 °C, holding time 1 hour;
- 600 °C – 5 °C/min – 1380°C, holding time 3 hours;
- 1380 °C – furnace cooling - room temperature.

5.2.2 Sample preparation

The sample geometry was established based on international standards applicable to the mechanical tests to be performed. To date, there are no specific standards that regulate the mechanical tests of samples obtained by AM; test procedures were defined according to the guidelines presented in ASTM F3122-14 [135]. This standard serves as a guide to existing standards or variations of existing standards that may be applicable to determine the specific mechanical properties of materials made with metal AM processes. All the specimens were oversized because of the shrinkage expected to occur during the debinding and sintering processes. In particular, based on a previous study [136], the specimens were oversized by 16% along the X-and Y-axes, and 20% along the Z-axis (growth direction).

All samples were printed using the same process parameters, which were defined through a preliminary study based on a 24 factorial plan [136]. In this investigation, the nozzle temperature (T_{nozzle}), infill type (In), print speed (s), and layer thickness (h) were set for investigating how the printing parameters affect the density. It was decided to maximize the density for identifying the printing parameters that generate a bulk density as close as

possible to that of monolithic stainless steel. This is the first characteristic that allows to evaluate the possibility of using this production technique for printing non-critical metal components. The effects of the process parameters and their interactions were investigated, in a previous work [136], using analysis of variance software. The optimal combination of the process parameters that ensured the highest level of bulk density of metal specimens (i.e., 95%) is shown in Table 5.1. Five samples were printed for each mechanical test.

Table 5.1: Optimized process parameters combination.

<i>Nozzle temperature</i>	<i>Infill type</i>	<i>Printing speed</i>	<i>Layer thickness</i>	<i>Infill density</i>	<i>Build orientation</i>
170 °C	Line 	20 mm/s	0.1 mm	100%	Flat

5.2.3 Methodology

5.2.3.1 Tensile test

According to ASTM F3122-14, the procedure outlined in the test method ISO 6892-1:2020 [137] defines the guidelines for tension testing to determine the yield and tensile strengths of material under various conditions. These procedures can be applied to components made additively. Tensile tests (five samples) were conducted using a Galdabini testing machine with a 50 kN load cell. The tests were conducted orthogonally to the growth direction of the layers under speed control (0.09 mm/s).

5.2.3.2 Compression test

ASTM F3122-14 designates Test Methods E9:2019 [138] as the basic method for uniaxial compression testing of metallic samples. These standards are applicable to specimens made additively, except for thin sheets. Compression tests (five samples) were conducted using a hydraulic press BRT with a 1000 kN load cell. The tests were conducted in a parallel direction with respect to the growth of the layers under speed control (0.01 mm/s).

Two bearing blocks with a Vickers hardness of 1,450 HV were used. A layer of Teflon with a thickness of 0.075 mm was applied to both bearing blocks to minimize the friction between the elements.

5.2.3.3 Charpy impact test

According to ASTM F3122-14, ISO 148-1:2016 [139] includes guidelines on pendulum impact tests for determining the energy absorbed in an impact test of metallic samples fabricated using AM techniques. Five samples were tested using a Tinius Olsen Charpy pendulum. The dimensions of the metallic samples are reported in Figure 5.1.

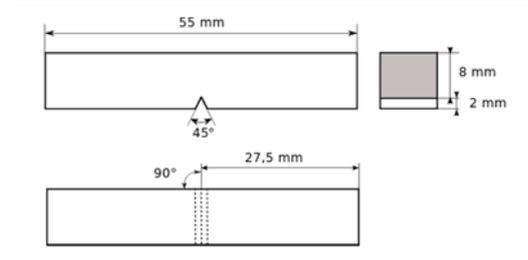


Figure 5.1: Dimensions of Charpy impact samples.

5.2.3.4 Three-point bending test

According to ASTM F3122-14, ISO 7438:2020 [140] includes plastic deformation methods to evaluate a material's bending strength and limit of elasticity under bending conditions. These standards are also applicable to metal-based additive-manufactured parts. Three-point bending tests (five samples) were performed using a Galdabini testing machine with a 50 kN load cell. The bending tests were conducted with two supports spaced 42 mm away from the center. The rate of displacement was set to 0.8 mm/s, as indicated in the standard. The procedure was performed until the physical bending limit of each specimen was reached. This physical limit is strictly related to the selected clamping system and the distance between the supports. This configuration produced U-shaped specimens, as depicted in Figure 5.2.



Figure 5.2: U-bend sample.

5.2.3.5 Rockwell hardness

ASTM F3122-14 specifies ISO 6508-1:2016 [141] as a standard for the Rockwell hardness (HRB) of additive-manufactured parts. A cubic sample was sectioned along the growth direction; on the internal section of the sample, a 3×3 line grid was drawn, following the instructions of ISO 6508-1. The procedure was repeated for three different samples to obtain 27 uniformly spaced indentations, by means of an A-200 Galileo hardness tester.

5.2.3.6 Vickers hardness

The same procedure followed for the Rockwell tests was used for the Vickers hardness tests, as specified in ISO 6507-1:2018 [142], according to ASTM F3122-14. The indentations were performed using a microhardness tester UHL – VHMT.

5.3 Results and discussion

5.3.1 3.1. Tensile stress

The tensile properties of the specimens, such as the yield strength (σ_{f02}), UTS, and elongation at break, are presented in Table 5.2. The results of the tests indicated that the ME samples exhibited poorer mechanical properties than those of the samples made of monolithic AISI 316 L. Specifically, the average value of the yield strength (141.9 ± 14.1 MPa) was lower by 17% compared to that of the monolithic material. The average value of UTS (426.6 ± 23.7 MPa) was lower than that of the monolithic material by

approximately 12%. These results could be attributed to the larger equiaxed grains and full austenitic structure after the sintering phase [52,115]. Regarding the elongation at break, the percentage values were close to those of the monolithic AISI 316L. The inherent porosity of the sample generated by this AM technique [136], particularly the open one, could deteriorate the ductility of the ME specimens owing to local stress concentrations.

Table 5.2. Tensile properties of 316L AM samples.

	$\sigma_{0.2}$ (MPa)	UTS (MPa)	Elongation at break (%)
Sample 1	161.3	464.1	41%
Sample 2	125.0	407.3	37%
Sample 3	134.6	405.9	32%
Sample 4	132.9	409.0	32%
Sample 5	155.7	445.2	38%
AISI316L [143]	170	485	60%

To provide a wider context of the tensile properties of stainless steel 316L samples realized with ME, a comparison among tensile values collected in different works was reported in Table 5.3. On average, the obtained yield and tensile strength resulted slightly lower than the other values presented; conversely, the ductility set the highest level compared to the values available in literature.

Table 5.3: Comparison of tensile properties among 316L specimens fabricated by means of ME technique.

Source	$\sigma_{0.2}$ (MPa)	UTS (MPa)	Elongation at break (%)
This work	141.9 ± 14.1	426.6 ± 23.7	36.4 ± 3.15
Ait-Mansour et al. [117]	140.77 ± 6.97	311.81 ± 39.96	12.48 ± 2.81
Gong et al. [114]	167	465	31
Liu et al. [116]	194 ± 19	441 ± 27	29.5 ± 3.8
Rosnitschek et al. [144]	-	296 ± 78	32 ± 16
Damon et al. [118]	155	500	32
AISI 316L [143]	170	485	60

The tensile curves, represented in Figure 5.3a, show a similar trend, demonstrating the repeatability of the printing process. However, the difference in UTS and elongation at break among the samples suggests a significant presence of defects (voids and residual stress as a result of thermal processes). No significant necking phenomenon was observed during the tests.

Figure 5.3b depicts the failure modes of the specimens. Three samples exhibited fractures inside the useful length, indicated by two blue lines near the edge of the samples. In contrast, samples 3 and 4 show fractures near the fillet radius, which is a critical stress intensity zone.

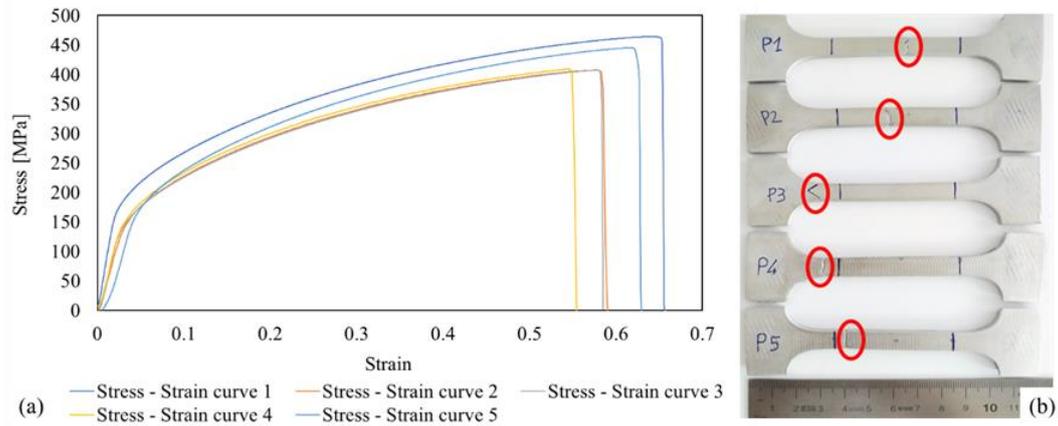


Figure 5.3: Tensile stress-strain curves (a); fracture positions of the samples (b).

5.3.2 Compression stress

The stress–stroke graphs of the compression tests are shown in Figure 5.4. The near-perfect overlap of the compressive curves proves the stability and repeatability of the tests. In general, for monolithic materials, the absolute values of the tensile and compressive stresses are almost symmetric with respect to the yielding behavior of metals. This condition is also present for ME 316L specimens, as the compressive and tensile yield strength values were approximately 150 MPa.

In addition, the compression load seems to guarantee an improvement in the compressive stress values of the samples. The average compressive stress of the ME 316L specimens was 54% lower than that of the tested bulk sample at 1 mm stroke, whereas the average compressive stress value exhibited a deviation of 26% from the value of the bulk specimen at 8 mm stroke.

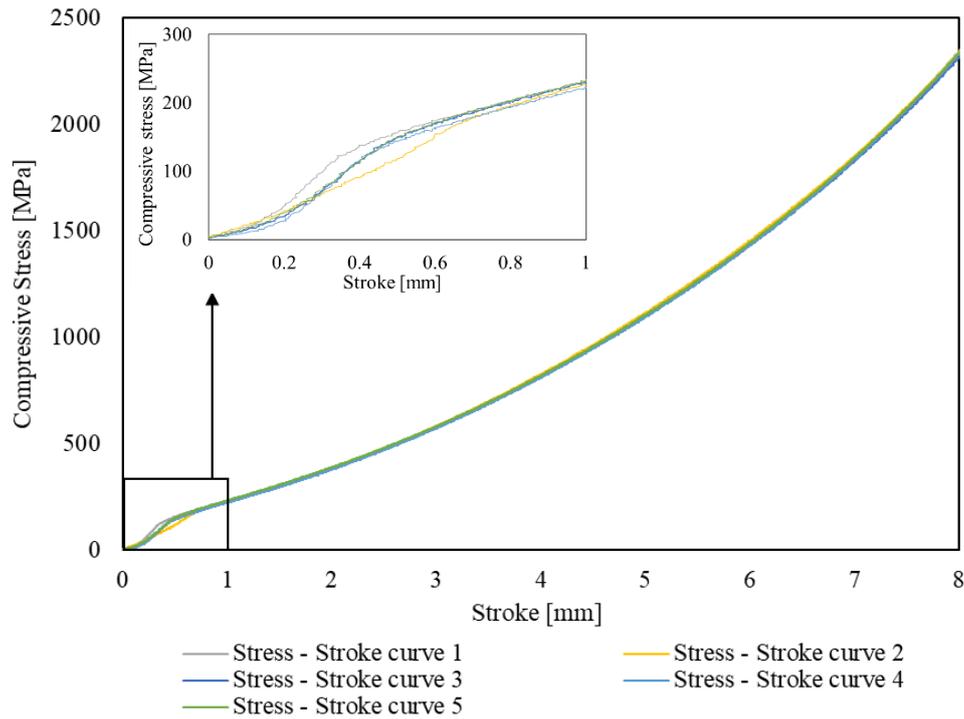


Figure 5.4: Compressive stress–stroke curves.

5.3.3 Flexural strength

The three-point bending stress–stroke curves are plotted in Figure 5.5. Bending tests produce tensile stress on the convex side of the specimens above the neutral axis and compressive stress on the concave side of the specimens below the neutral axis. Flexural strength is the maximum stress in the outermost fiber. The average value of the flexural strength was 795 ± 27 MPa, and the average value of the flexural strain was approximately 44% with a standard deviation of 1.4. The flexural strength values depend on the type of tests performed and the structural characteristics of the samples printed using the ME technique. During the bending test, the maximum stress was mainly concentrated in a small region above the neutral axis. The metal ME process and further thermal treatments generate an intrinsic percentage of porosity in the specimens, which are highly sensitive to the defect content. Because the gauge area of the samples is limited, for example, compared to the gauge area of tensile specimens, the statistical probability of finding open and closed porosities in the samples is small.

Furthermore, the bending curves show a similar trend, confirming the repeatability of the process, and all the maximum stress values were registered at approximately 12 mm of

deflection of the specimens under bending load. All the samples exhibited a complete deformation without the presence of cracks in the area subjected to tensile loading.

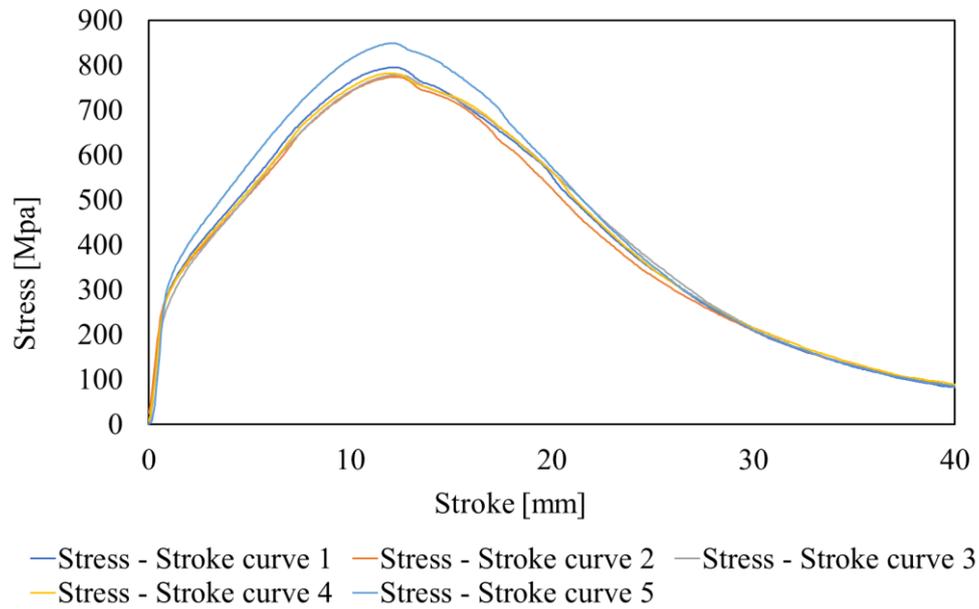


Figure 5.5: Bending stress-stroke curves.

5.3.4 Absorbed energy

The absorbed energy values of the V-notched specimens are presented in Table 5.4. The average value ($54.6 \text{ J} \pm 8.01$) is almost half that of AISI 316L, suggesting the brittleness of the metal specimens printed using the ME technique.

Additionally, samples 2 and 5 underwent a complete fracture (Figure 5.6a), whereas the other specimens exhibited a partial fracture (Figure 5.6b).

Table 5.4: Absorbed energy values of samples.

	Absorbed Energy (J)
Sample 1	62.5
Sample 2	58.5
Sample 3	42.0
Sample 4	48.5
Sample 5	61.5
Monolithic AISI316L	103 [145]

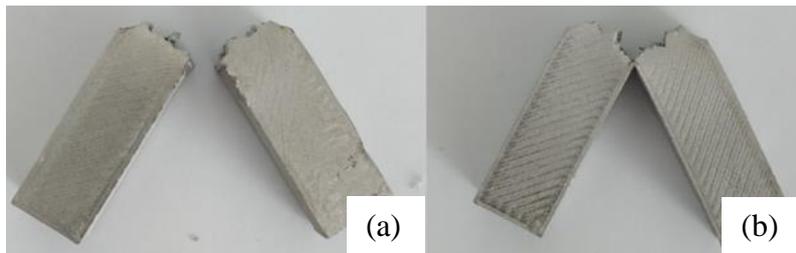


Figure 5.6: Samples with complete fracture (a), samples with partial fracture (b).

The brittleness of the metal ME samples can be attributed to two main causes. As reported in [136], 5% of porosity could reduce the ductility of the samples. Moreover, the X-ray diffraction (XRD) analysis (Figure 5.7) indicated the presence of austenite and δ -ferrite phases. The portion of austenite represents a metallurgical characteristic of the material because AISI 316L is an austenitic stainless steel, which is composed of a single stable austenitic phase at 20° C owing to the presence of nickel. In contrast, the existence of the δ -ferrite phase is merely an effect of the thermal history of the samples produced by the ME process and subsequent sintering. The formation of the δ -ferrite phase occurred immediately below 1,400 °C. The temperature during the extrusion process reached close to 240 °C, whereas that during the sintering cycle reached close to the temperature window of stable delta ferrite and was compatible with its formation.

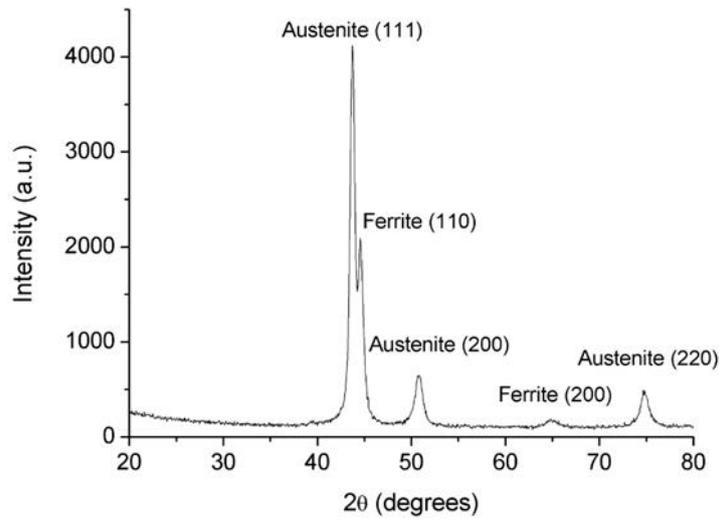


Figure 5.7: XRD patterns of the ME 316L stainless steel.

During the cooling process, the primary δ -ferrite solidifies within the metal matrix, and the transformation of δ to γ ferrite may occur. Because this transformation is a diffusion-controlled process, the fast cooling rate in the sintering cycle (uncontrolled cooling from 1,380 °C to room temperature) does not guarantee a sufficiently long time for the completion of the transformation [146]; thus, exceeding portions of δ -ferrite may be retained in the austenitic matrix of specimens at room temperature. The non-equilibrium cooling phase results in the retention of δ -ferrite at the subgrain boundaries [147]. This phenomenon may significantly decrease the strength and ductility and increase the stiffness of the metal ME samples.

5.3.5 Hardness

Figure 5.8 depicts values of Rockwell B and Vickers hardness respectively, depending on their positions on the drawn grid. The average Rockwell B hardness value was approximately 55 ± 4 HRB, which is lower than that of the monolithic AISI 316L (80 HRB [145]), with a deviation of 32%. Regarding the Vickers hardness, the average value (132.2 ± 3.8 HV) was approximately 15% lower with respect to the value of the monolithic AISI 316L (155 HV [145]).

It is reasonable to assume that the difference between the percentage deviations (32% vs. 15%) depends on the correlation between the sample porosity and test methodologies. The Vickers hardness test concentrates the stress on the surface of the specimen, with a limited influence on thickness, leaving a shallow indentation with reduced dimensions,

compared to the indentation made during the Rockwell hardness test. Consequently, the Rockwell hardness test is more affected by the presence of porosities, even if they are not outcropped on the surface, as the larger size of the indenter and greater load applied, lead to a greater probability of intercepting non-emerging porosities compared to the probability of finding porosities in the indentations of the Vickers hardness test. Furthermore, the uniform distribution of the hardness values, both Rockwell B and Vickers, along the growth direction may suggest the homogeneity of the material.

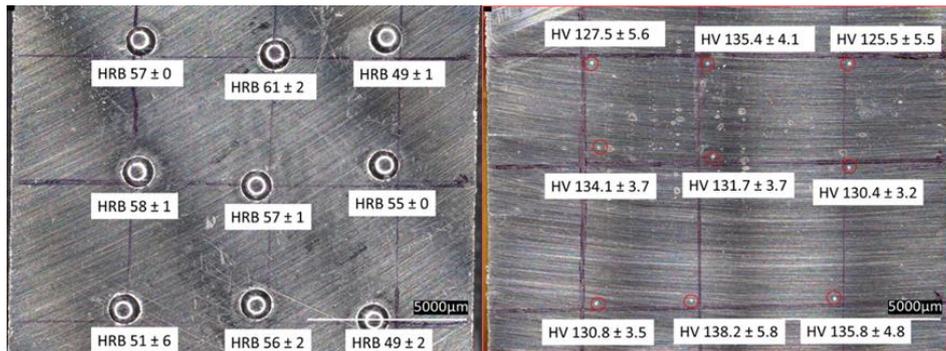


Figure 5.8: Rockwell B Hardness (left) and Vickers hardness (right) values in their relative positions within the sample.

5.4 Conclusions

This study presents an overview of the main mechanical characterization tests performed on debinded and sintered samples fabricated by means of an innovative metal-polymer feedstock on a low-cost ME machine. Specimens for mechanical characterization were printed using the optimal combination of process parameters for obtaining the highest bulk density compared with that of the monolithic material.

Tensile specimens printed via the ME technique exhibited lower values of yield strength and UTS compared to those of the monolithic material. In particular, the yielding behavior exhibited the worst load values. The compression action on the specimens enhanced the average stress value in direct proportion to the increase in displacement. The bending samples exhibited no cracks or deformations on the surface subjected to a tension load. An XRD analysis showed the abnormal presence of δ -ferrite in the austenitic matrix, which may explain the brittleness of the metal specimens observed during the Charpy impact tests. Both Rockwell B and Vickers hardness tests verified the homogeneous behavior of the material along the growth direction of the layers. In general, the conducted

experiments indicated that the ME 316L samples had poorer mechanical performances compared to those of monolithic materials. However, all the tests performed demonstrated excellent repeatability of this AM process.

Metal extrusion is a prospective cost-effective technique that avoids powder handling and reduces the carbon footprint compared to traditional metal additive manufacturing technologies. Despite the promising advantages, the considerable presence of porosity and the necessary improvement of the mechanical properties narrow the industrial applications of this technique to non-critical metallic parts with high added value, including tanks for dyeing machines and pipeline for chemical industry due to the high resistance to corrosion. The biocompatibility of the material ensures its use for food and medical applications and the possibility to produce complex shaped parts extends its applications also for heat exchanger and heat sink.

6 The enhancement of the mechanical properties via post-heat treatments of AISI 630 parts printed with Material Extrusion

This chapter is derived from the article “Carminati, M.; D’Urso, G.; Giardini, The enhancement of mechanical properties via post-heat treatments of AISI 630 parts printed with material extrusion. *Prog Addit Manuf* (2023)”.

DOI: 10.1007/s40964-023-00401-2

I am immensely grateful to the support received from my co-authors. I am responsible for all the changes in this chapter with respect to the submitted version.

6.1 Introduction

As reported in 3.2.2, AISI 630 is a precipitation hardening stainless steel and it is an alloys of interest for different manufacturing applications due to the possibility of performing thermal treatments to modify the microstructure of the material and, thus, the mechanical properties of manufactured components. In particular, H900 and H1150 are the two most diffused thermal treatments since a relevant enhancement of strength and ductility could be reached, respectively.

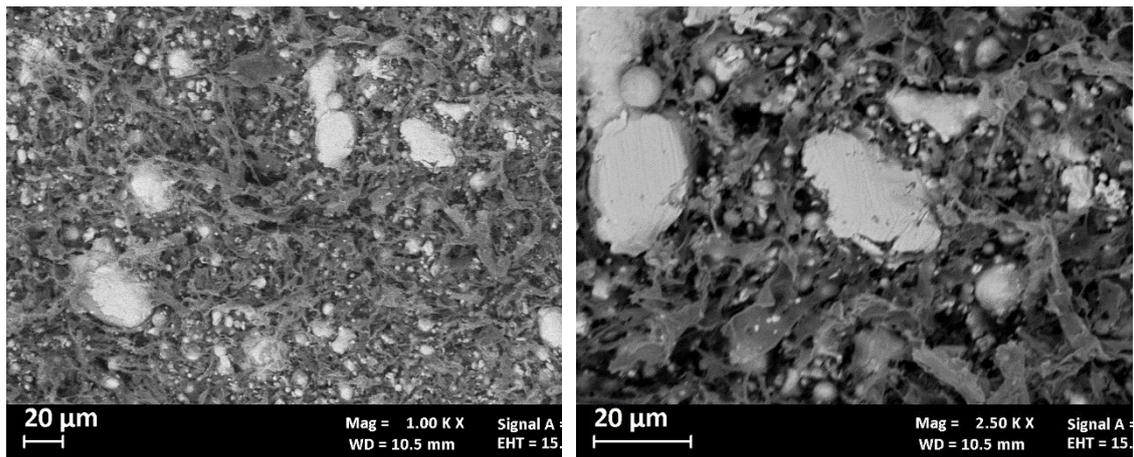
Despite the number of papers studying metal ME is increasing, an assertive response of the mechanical properties of AISI 630 martensitic stainless steel after tempering remains unclear, since the effects of dissimilar heat treatments on different mechanical characteristics, including compression and bending strength, are missing.

In the present work, an overall technical feasibility of the metal ME technique was provided to expand its industrial applications to non-critical metallic parts with high added value. A preliminary structural analysis was conducted to establish any possible influence of the main process parameters on the physical and dimensional response of the AISI 630 parts produced by means of the mentioned technology. The optimized combination of process parameters ensuring the lowest level of inherent porosity was selected to perform a subsequent mechanical characterization. The effects of aging treatments on the main mechanical properties of AISI 630 ME samples were investigated with a comprehensive comparison with those of the monolithic material. In particular, H900 and H1150 heat treatments were performed on metal samples and different

mechanical tests, comprising tensile, compressive, bending and Vickers hardness, were carried out.

6.2 Materials and Methods

The test samples were fabricated by means of a FDM 3D printer Ultimaker 5S (Ultimaker B.V., Utrecht, NL), equipped with a CC hardened steel nozzle having a diameter of 0.6 mm. The machine extruded an innovative 2.85 mm filament made up of AISI 630 martensitic stainless steel powder (90 wt.%), provided by BASF, equally distributed in a polymeric matrix composed of polyoxymethylene (POM) and polyolefin. In Figure 6.1a, the cross section of the filament shows good homogeneity of the metal powders with the dimensions in the range of 2 and 25 μm , embedded in the polymeric binder. The geometry of the powders could be not defined since both rounded and irregular shapes of the metal particles could be detected (Figure 6.1b).



(a)

(b)

Figure 6.1: SEM images of the cross section of the filament: 1000X (a), 2500X (b).

After the printing process, thermal treatments were required. The main polymeric content (primary binder) was removed from the green parts with the aid of a catalytic debinding process at 120 °C, resulting in a brown part, consisting of metal particles and a residual polymeric backbone. The subsequent sintering process removed the secondary binder and caused coalescence of the metal particles. At the end of the thermal treatments, the part has undergone a volume reduction due to shrinkage. The sintering cycle was performed in Argon atmosphere and consisted of three thermal ramps, as reported in Table 6.1:

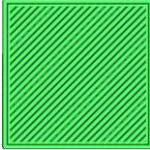
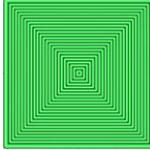
Table 6.1: Ramps of the sintering cycle.

	Initial temperature	Final temperature	Ramp rate	Holding time
Ramp 1	Room temperature	600 °C	5 °C/min	1 hour
Ramp 2	600 °C	1380 °C	5 °C/min	3 hours
Ramp 3	1380 °C	Room temperature	Furnace cooling	-

6.2.1 Structural analysis

A cube with a side of 10 mm was the chosen geometry of the test samples for the structural analysis. The experimental design was based on a Taguchi L16 orthogonal array. The factors taken into consideration were the main process parameters of the ME technique, i.e., the nozzle temperature (T_{nozzle}), the infill pattern (In), the print speed (s), the layer height (h) and the infill density (d), varied on two levels. The low and high levels of each parameter were selected by means of a preliminary windows process tests to verify the actual printing process of the selected material and the values are reported in Table 6.2. 4 repetitions were considered for each combination of the process parameters.

Table 6.2: Levels of the process parameters

Parameters		Low level	High level
Nozzle Temperature [°C]	T_{nozzle}	170	240
Infill Pattern	In	Line	Wall
			
Print Speed [mm/s]	s	15	50
Layer Height [mm]	h	0.1	0.4
Infill Density [%]		100	125
	d		

Nozzle temperatures (T_{nozzle}) above the melting point of the primary binder (i.e., 165 °C) were chosen to minimize the viscosity of the filament and to ease the extrusion process. *Line* pattern and *Wall* pattern were chosen as trajectories of the nozzle while filling the infill volume within the structure. The *Line* pattern consists of lines printed in one direction and tilted by 45° degrees each layer. The *Wall* pattern is constituted of concentric walls entirely filling the samples. s refers to the speed of the extruder movement. h represents the height of each single layer and affects the quality of the parts along the growth directions. d corresponds to the density of infill, i.e., the distance of the infill lines. An infill density higher than 100% leads to a partial overlap of the deposited strand. A bed temperature of 100 °C was set to enhance the adhesion and to prevent the detachment of the first deposited layer from the building platform. Table 6.3 shows the Taguchi L16 plan displaying the combination of process parameters for each sample.

Table 6.3: Taguchi Design of experiments: sample identification and process parameters combinations.

Combination	Samples	Tnozzle	In	s	h	d
1	1 – 17 – 33 – 49	170	Line	15	0.1	100
2	2 – 18 – 34 – 50	170	Line	15	0.4	125
3	3 – 19 – 35 – 51	170	Line	50	0.1	125
4	4 – 20 – 36 – 52	170	Line	50	0.4	100
5	5 – 21 – 37 – 53	170	Wall	15	0.1	125
6	6 – 22 – 38 – 54	170	Wall	15	0.4	100
7	7 – 23 – 39 – 55	170	Wall	50	0.1	100
8	8 – 24 – 40 – 56	170	Wall	50	0.4	125
9	9 – 25 – 41 – 57	240	Line	15	0.1	125
10	10 – 26 – 42 – 58	240	Line	15	0.4	100
11	11 – 27 – 43 – 59	240	Line	50	0.1	100
12	12 – 28 – 44 – 60	240	Line	50	0.4	125
13	13 – 29 – 45 – 61	240	Wall	15	0.1	100
14	14 – 30 – 46 – 62	240	Wall	15	0.4	125
15	15 – 31 – 47 – 63	240	Wall	50	0.1	125
16	16 – 32 – 48 – 64	240	Wall	50	0.4	100

The green parts and the debinded and sintered samples were measured by a Coordinate Measuring Machine (CMM) Zeiss O-Inspect along X, Y and Z directions. The measurements were performed using a vertical touching probe, repeating the automatic path three times for each plan of the sample to obtain average values for the dimensional analysis. The described procedure ensured the accuracy of the methodology and avoided random errors in measurement. The shrinkage of the area within XY plan and the

shrinkage along Z axis were calculated as the percentage dimension reduction along the reference directions, according to Eq. 1:

$$Shrinkage_i = \frac{(Dgp_i - Dsp_i) \cdot 100}{Dgp_i} \quad \text{Eq. 1}$$

Where i indicates the dimension (area within XY plan, Z axis), Dgp_i is the dimension of the green parts and Dsp_i is the dimension of the sintered parts.

The apparent density (ρ_{app}) of sintered samples was calculated as the ratio between the post processing weight (w), measured using a precision balance, and the geometrical volume (V_{geo}), estimated through the CMM, as reported in Eq. 2

$$\rho_{app} = \frac{w [mg]}{V_{geo} [mm^3]} \quad \text{Eq. 2}$$

An Analysis of Variance (ANOVA) was applied to the sampled measures to study the eventual effect of the chosen process parameters on the dimensional shrinkages and apparent density, selecting a 95% confidence interval. In order to delete possible outlier values from the dataset, a Matlab code was created to execute a pre-treatment of the collected data by means of the interquartile range (IRQ) criterion.

6.2.2 Mechanical analysis

The apparent porosity corresponds to porous defects that are formed unintentionally in the well-prepared structure and/or at the unetched surface of the additively manufactured material [148]. This attribute represents an enormous issue related to the fabrication of parts by means of ME technology. Indeed, both opened and closed porosity may influence the mechanical properties of sintered samples, lowering the structural utilization of metal ME parts [149]. Therefore, the specimens used for the mechanical characterization were printed using the process parameters combination corresponding to the maximum of the apparent density as resulted from the previous structural analysis.

For each mechanical test, 9 samples were fabricated: 3 samples were mechanically tested as sintered (AS-IS samples). The remaining ones were formerly subjected to solution followed by water quenching and aging treatments followed by air cooling. Different studies verified the influence of the application of the solution treatment prior to tempering on parts made additively [128,134]. Both yield and ultimate tensile strengths receive an improvement from solution and aging post treatment; on the contrary, aged samples without any pre-treatment solution experienced a general worsening of

mechanical properties. The solution treatment prior to aging is very important since it almost fully prevents the austenite reversion in the martensitic matrix and enhances the strength of printed samples. In fact, aging on an as-fabricated sample generates a gradual reintroduction of austenite by the reversion of martensite, generally attributed to the chemical stabilization by the diffusion of constituents to form precipitates toward lath boundaries.

In Table 6.4, the temperatures and the holding times for H900 (peak aged) and H1150 (over aged) conditions are reported. Three specimens were tested under each condition to ensure repeatability.

Table 6.4: Solution and aging treatments.

	Solution treatment		Aging treatment	
	T [°C]	t [min]	T [°C]	t [min]
H900	1040±5	60±5	482±5	60±5
H1150	1040±5	60±5	621±5	240±15

The tensile tests were performed according to procedure outlined in test method ISO 6892-1:2020 [137], using a Galdabini testing machine with a 50 kN load cell under speed control (0.09 mm/s). The tests were conducted orthogonally to the growth direction of the layers, according to different works investigated in literature [115,125].

The compression tests (Test Methods E9:2019 [138]) were conducted in a parallel direction with respect to the growth of the layers under speed control (0.01 mm/s), using a hydraulic press BRT with a 1000 kN load cell. A layer of Teflon with a thickness of 0.075 mm was used to minimize the friction between the specimen and the dies.

The three-point bending tests were performed using a Galdabini testing machine with a 50 kN load cell. Two support spaced 42 mm away from the center and 0.8 mm/s as rate of displacement were selected, as indicated in the standard ISO 7438:2020 [140]. The procedure was executed until the complete fractures of the samples.

Vickers Hardness tests were conducted sectioning the cubic samples along the growth direction of the layers and executing the tests on a 3 × 3 line grid (9 indentations) on the sections of each sample, in accordance to ISO 6507-1:2018 [142]. The procedure was

repeated for three different samples to obtain 27 indentations for each condition by means of a hardness tester UHL–VHMT.

The internal structure of the metal samples, both as sintered and heat treated, were analyzed. The cross sections of sintered and tempered samples were polished up to 0.05 μm with alumina suspension and etched by Marble solution (50 mL H_2O , 10 g CuSO_4 , 50 mL HCl). The chemically etched surfaces were observed using a digital microscope (Keyence VHX-7000). The fracture surfaces were examined by scanning electron microscopy (Zeiss EVO 40) at room temperature.

6.3 Results and discussion

6.3.1 Structural characterization

The structural analysis was carried out to identify any possible influence of the printing process parameters on the physical and dimensional indicators of the sintered parts, with particular attention to the parameters combination maximizing the apparent density of the samples.

3 outliers for the shrinkage within XY plan were identified, while no outliers were found for shrinkage along Z axis and density. The boxplots of the measured sample characteristics in terms of shrinkage and density are reported in Figure 6.2.

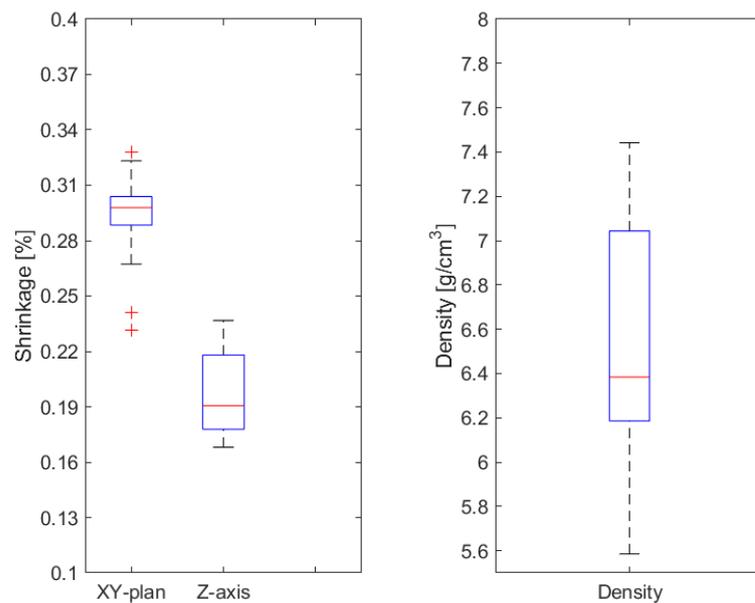


Figure 6.2: Boxplot for shrinkages and apparent density outliers identification.

After removing the outliers, an analysis of variance was performed to define any influence of the process parameters on the main indicators of structural properties of sintered samples. Analyzing p-values obtained by the ANOVA (Table 6.5), it can be stated that the apparent density is affected by all parameters, except for the nozzle temperature. Even for the 2-way interaction, *Tnozzle* does not play an important role on the apparent density. Conversely, all shrinkage directions are affected by the temperature of the nozzle, both for 1-way and 2-way interactions. Also, *h* parameter influences shrinkage along XY plan and Z axis. Lastly, the interactions nozzle temperature-print speed and nozzle temperature-layer height have a strong influence on both shrinkages.

Table 6.5: ANOVA p-values.

	p-value		
	Apparent Density	Planar Shrinkage	Z-Shrinkage
T_{nozzle}	0.889	0.007	0.000
In	0.000	0.000	0.465
s	0.009	0.378	0.570
h	0.000	0.000	0.000
d	0.000	0.089	0.025
2-way interaction			
$T_{nozzle} \cdot In$	0.036	0.000	0.182
$T_{nozzle} \cdot s$	0.696	0.001	0.000
$T_{nozzle} \cdot h$	0.123	0.000	0.000
$T_{nozzle} \cdot d$	0.712	0.482	0.026
$In \cdot s$	0.018	0.944	0.947
$In \cdot h$	0.001	0.671	0.573
$In \cdot d$	0.000	0.007	0.063
$s \cdot h$	0.002	0.887	0.066
$s \cdot d$	0.395	0.059	0.341
$h \cdot d$	0.315	0.197	0.759

Figure 6.3Figure 6.4 show the average values of apparent density and shrinkages (average and standard deviation of the 4 runs), as function of the 16 combinations of process parameters. For each plot, a comparison among the experimental results and the nominal values of shrinkages and density, defined in BASF technical datasheet and International Standards, respectively, is feasible (red line and blue line). In accordance with ANOVA

results, Figure 6.3 confirms that *In* Line infill, *s* 15 mm/s, *h* 0.1 mm and *d* 125% was the combination of process parameters that maximize the density of sintered parts, as also reported by the main effect plot (Figure 6.5a), with an average value of 7.4 g/cm³. The mentioned optimal process parameters combination generated 29.8% and 19.5 % shrinkages along XY plan and Z axis, respectively, which are the closest values compared to the nominal shrinkages reported in the technical datasheet. Furthermore, shrinkage values within XY plan settled around the nominal value of shrinkages. Different conclusion could be drawn for the shrinkage along Z-axis. It's clearly noticeable a spread variability of the shrinkage values around the blue line in Figure 6.4b. Lastly, planar shrinkages and shrinkages along Z axis exhibited a similar trend, related especially to the *h* parameters, since on average samples printed with 0.1 mm layer height incurred higher shrinkage (i.e. greater than nominal shrinkages) compared to those characterized by *h* equal to 0.4 mm. This evidence is also confirmed by the main effects plots (Figure 6.5b, c) since the influence of the process parameter on both dimensional shrinkages can be noticed.

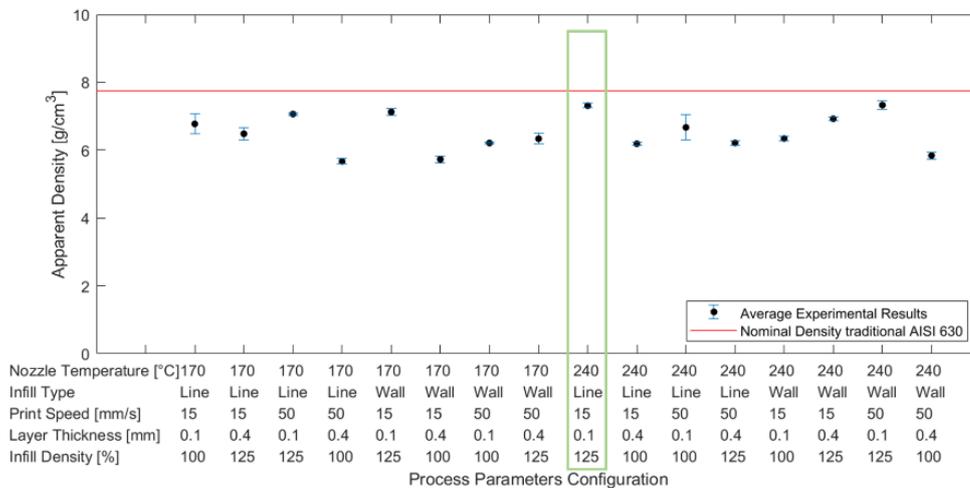


Figure 6.3: Average values of apparent density as a function of the process parameters combination.

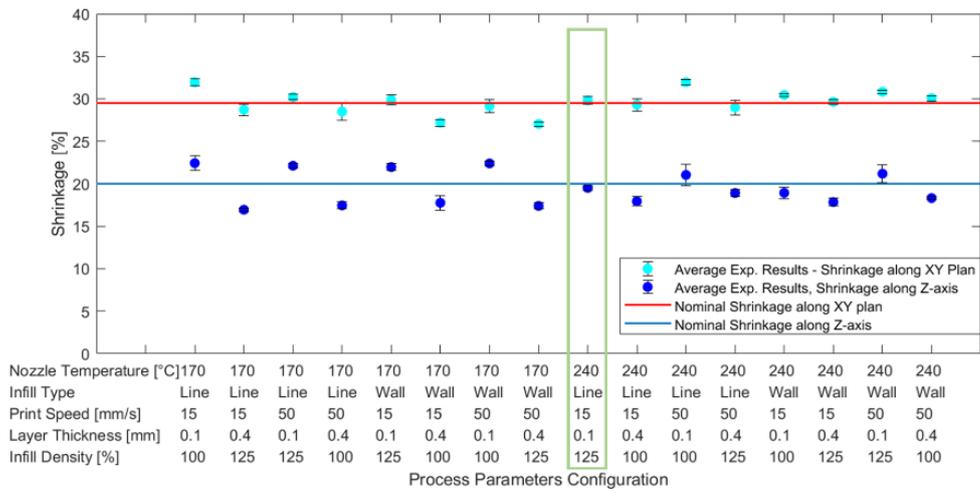
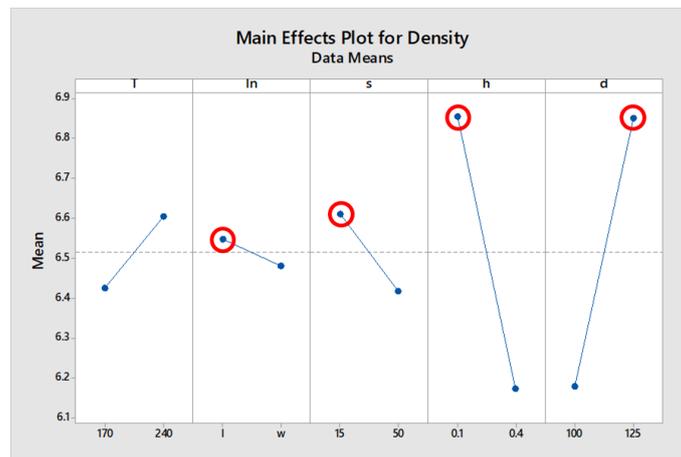
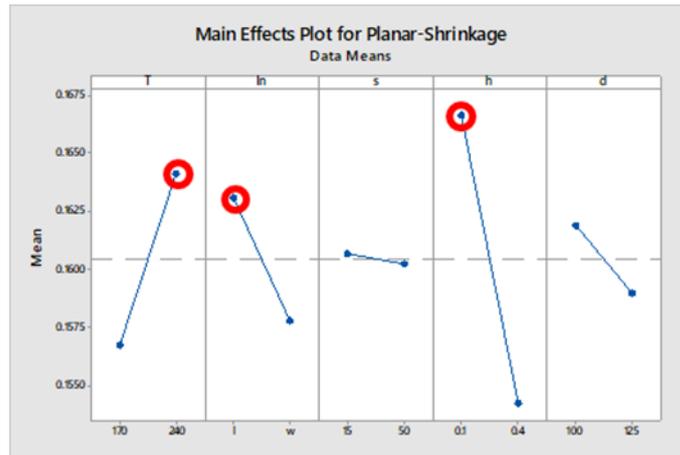


Figure 6.4: Average values of dimensional shrinkages as a function of the process parameters combination.

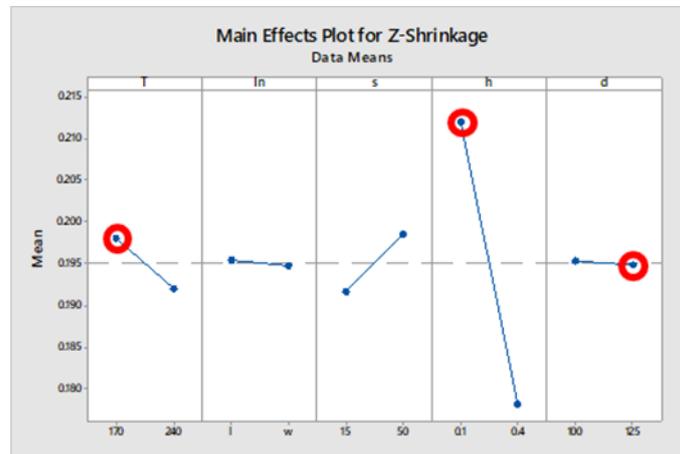


(a)

Figure 6.5: Main effects plots for density (a).



(b)



(c)

Figure 6.5: Main effects plots for planar shrinkage (b) and Z shrinkage (c).

Concerning the repeatability of the process, the residuals of the final indicators of the structural analysis are reported in Figure 6.6. The plots demonstrate the random distribution of the points with an almost constant variance, especially for the apparent density and planar shrinkage, ensuring the reproducibility of metal parts printed via ME.

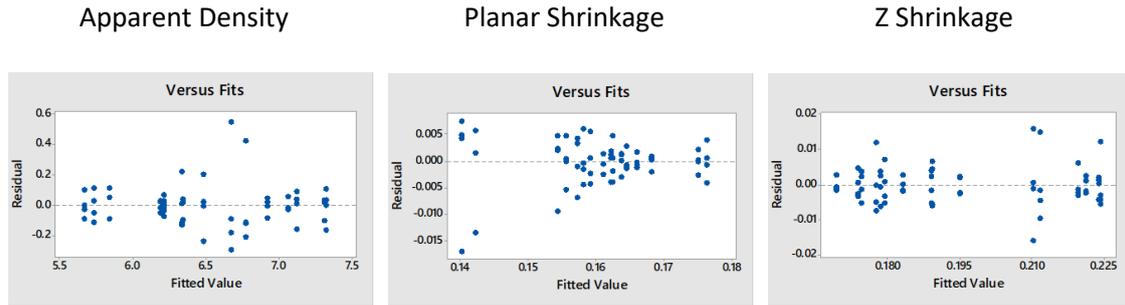


Figure 6.6: Residuals versus fits plots for apparent density, planar shrinkage and Z shrinkage.

6.3.2 Mechanical characterization

The characterization of AISI 630 ME samples was carried out using process parameters that allow to maximize the apparent density of the sintered samples. Figure 6.7 exhibits two different types of porosity, which are distinctive of the metal ME technique. Indeed, the first class of porosity is a matrix of spherical pores with micrometric dimensions, uniformly distributed. The debinding process enhances the binder leakage, creating large voids in the samples. The sintering step promotes just a partial closure of voids, leaving micro porosity in the metal matrix. The second class of porosity is generated by the deposition process. Irregularly shaped pores form patterns at the interfacial region between deposited layers, that the sintering treatment can barely interfere. Moreover, this type of porosity is characterized by pores of greater dimensions compared to those of the first class.

Both type of porosity adversely affect the mechanical properties of sintered metal parts; namely, spherical pores lower the stiffness while the irregular ones reduce the mechanical strength of specimens [150]. Therefore, the reduction of porosity maximizing the apparent density represents a relevant milestone to expand the industrial application of the aforementioned technique.

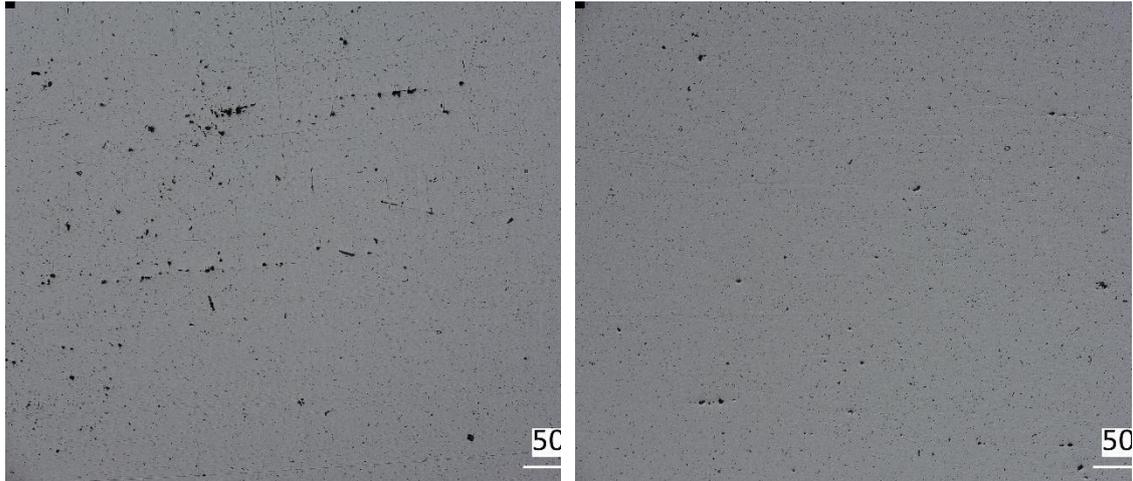


Figure 6.7: Cross section XY plan X100 (left), Cross section YZ plan X100 (right).

Heat treatments on ME samples is a possible solution to enhance the mechanical characteristics of AISI 630 material, by means of the precipitation hardening phenomenon.

The monolithic AISI 630 is characterized by a predominantly martensitic microstructure with occasional presence of δ -ferrite in the form of stringers. The sintered samples revealed an uncompleted microstructure transformation, since sintering and subsequent uncontrolled cooling phase from 1380 °C to room temperature promoted the unconventional formation of austenite grains, detectable through its typical grain boundaries structures (Figure 6.8a). Besides, an initial transformation from austenite to martensite occurred and the presence of δ -ferrite characterized the microstructure as a minor constituent, as shown in Figure 6.8b.

After aging treatments, the microstructure of the samples changed. A prior solution treatment and the following tempering at 482 °C transformed the previous AS-IS structure into near fully martensite block structure within the prior austenite grain boundaries and along the packet boundaries (Figure 6.8c). Lastly, Figure 6.8d shows a completely lath martensite structure and still well noticeable δ -ferrite elements, characterized by irregular shapes.

The microstructures of each heat treatment condition reveal rounded pores, as a consequence of the high temperatures used and partial interparticle bonding during the sintering process.

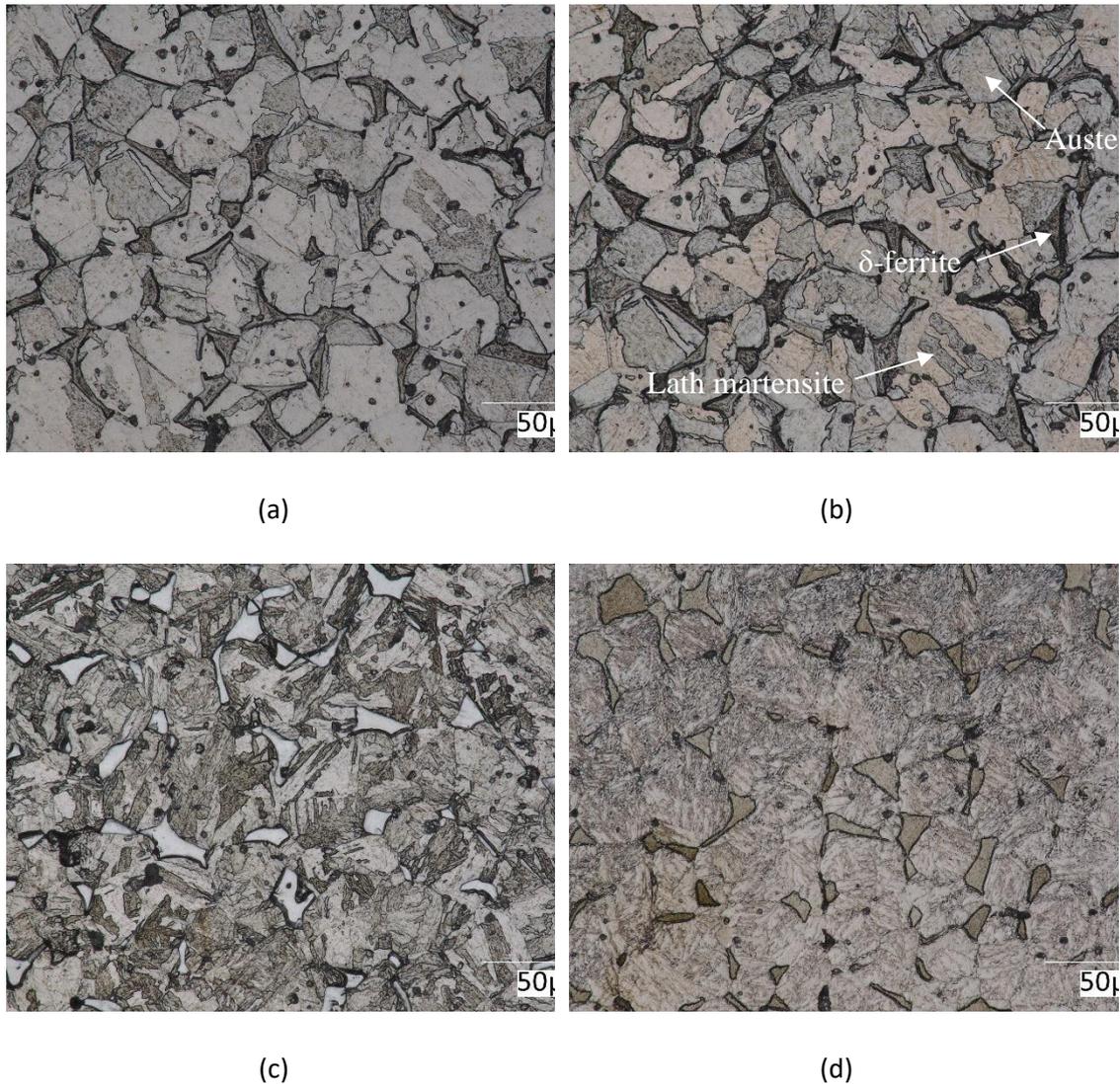


Figure 6.8: Digital-microscope micrographs of the cross-sections along building directions of samples AS-IS (a,b), H900 (c) and H1150 (d).

Figure 6.9 plots the tensile properties of specimens, such as yield strength, UTS and elongation at break, for the different heat treatment conditions comparing sintered and monolithic samples. The AS-IS samples exhibited average yield strength and UTS of 768 ± 5 MPa and 887 ± 9 MPa, respectively. After solution and aging treatment, the strength of H900 samples improved to 1028 ± 80 MPa and 1124 ± 49 MPa, with an increase of 16% and 12% respectively compared to AS-IS samples. The precipitation of nanoscale spherical Cu and secondary carbides rich in Cr along the packet boundaries limits the dislocation motion due to tempering, resulting in a considerable enhancement of material strength. On the contrary, H1150 samples experienced a worsening of yield strength and ultimate tensile strength, on average. At higher aging condition, grain boundaries become

thicker and the coarsening of Cu precipitates promotes the formation of clusters with a consequence reduction of the coherency within the martensitic matrix. Regarding the elongation at break, a growing trend for the ME samples is visible: it is evident how it is directly dependent on the increase of time and temperature of the heat treatments undergone.

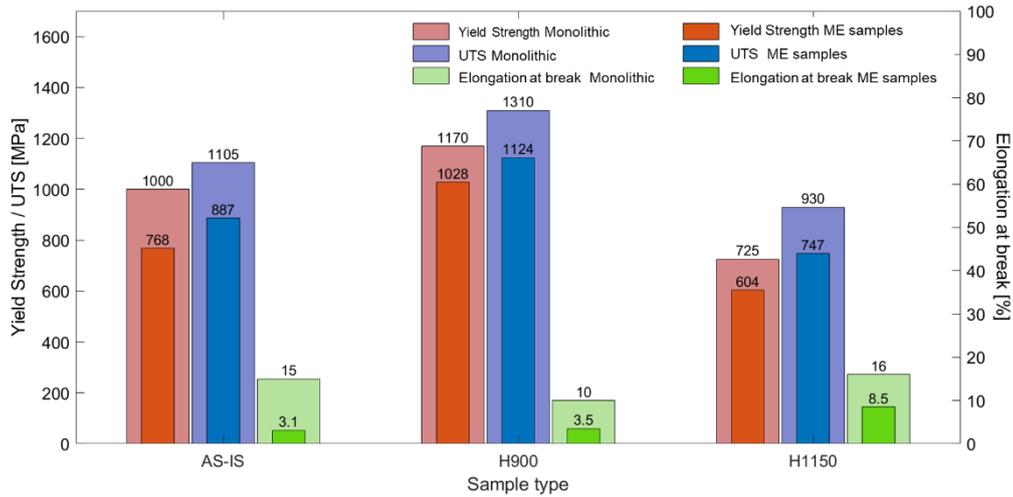


Figure 6.9: Tensile properties of AISI 630 ME samples

By comparing the values of mechanical characteristics for monolithic AISI 630 with the sintered samples ones (Figure 6.10) it is evident how the AS-IS samples represented the worst case for all the tensile properties analysed. In particular, the elongation at break value diverged of almost 80% from the monolithic material. The H900 aging treatment was found to be the best solution to approach the yield strength and UTS of the monolithic AISI 630.

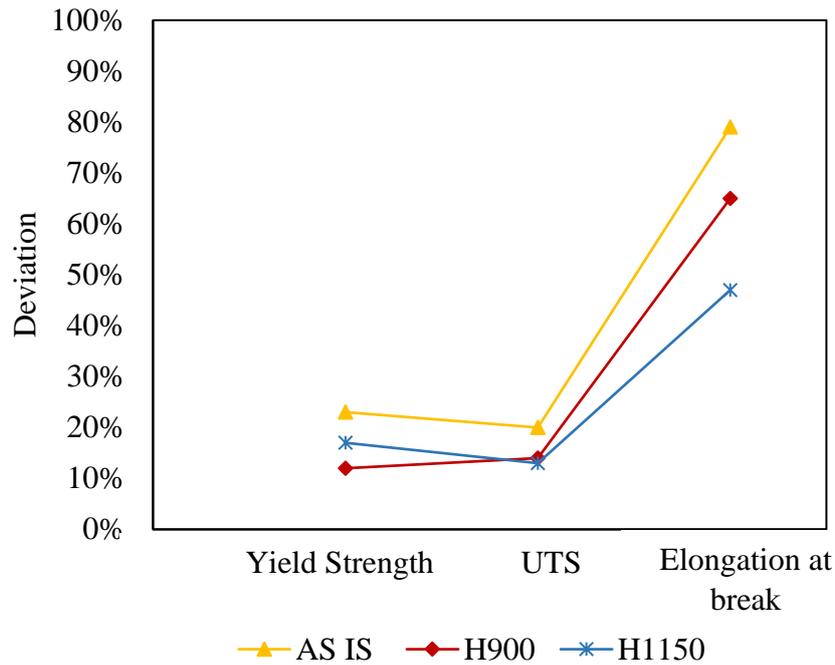


Figure 6.10: Deviation of tensile properties of ME samples in the different conditions from the relative monolithic material

To assess the tension behaviour of ME sintered samples, the fracture surfaces of the sintered and aged specimens after the tensile loads were observed by optical microscopy and scanning electron microscopy. Despite the differences in total elongation and strength, all three types of samples showed a similar fracture behaviour. Figure 6.11a, b highlight the presence of voids and porosities evenly distributed in fracture surfaces of both samples. In addition, more pronounced layers could be depicted suggesting a consistent layer separation. This evidence was well confirmed by the gaps between separated layers shown in Figure 6.11c. The tensile load applied during the tests enhanced the issue of poor adhesion between layers during the deposition process. SEM analysis shows the predominant existence of dimple structures in correspondence with the zones of the layers. Dimple patterns, which were formed through the initiation and coalescence of micro-voids, typify ductile fracture patterns (Figure 6.11d). A clear transition in the interlayers zones from highly populated smaller dimples area to smooth areas can be observed in Figure 6.11e. The separated layers, clearly delineated in Figure 6.11c, were characterized by brittle fracture patterns with deep cleavage, which were likely caused by higher concentration of irregular voids. These results indicate that specimens in all three conditions failed in a more brittle manner, with more limited plastic deformation than the

corresponding monolithic samples, as demonstrated by the higher levels of yield ratio (y_s/UTS).

A large number of spherical inclusions with a particle size of approximately $5\ \mu\text{m}$ were found. According to EDS compositional analysis, the spherical particles are SiO_2 . During the atomization process to fabricate spherical metal powders, up to 1 mass% silicon is often added to prevent oxidation by forming a thin silica films that cover metal powders [132]. The high temperature of the sintering process evolved the films into spherical particles, as it can be observed in the dimples of fractured surfaces (Figure 6.11f).

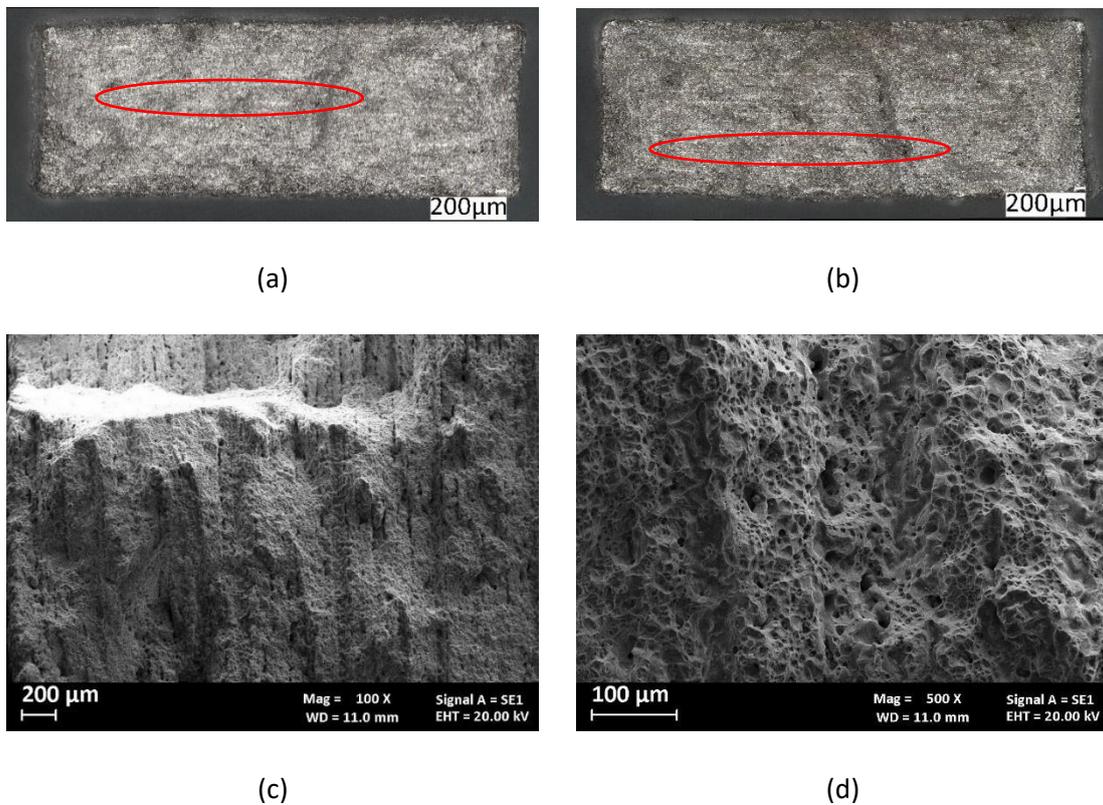
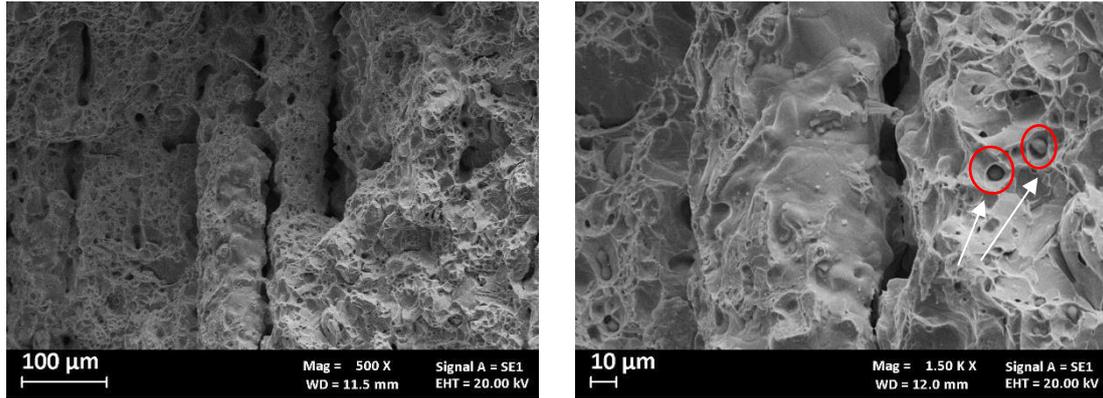


Figure 6.11: Optical and SEM analysis of fracture surfaces at different magnifications: (a,b) 40 X, (c) 100 X, (d) 500 X.



(e)

(f)

Figure 6.11: Optical and SEM analysis of fracture surfaces at different magnifications: (e) 500 X, (f) 1500 X.

The average compressive stress–strain curves of each tested conditions are shown in Figure 6.12. It is noticeable a clear disomogeneity among curves, represented by H900 samples. Indeed, the average value of compressive stress at 50% strain for H900 samples set at 2690 ± 29 MPa. On the contrary, a near perfect overlap between the two other clusters exists (AS-IS and H1150 samples). This evidence suggests the considerable improvement of the formability for sintered samples after the H900 heat treatment.

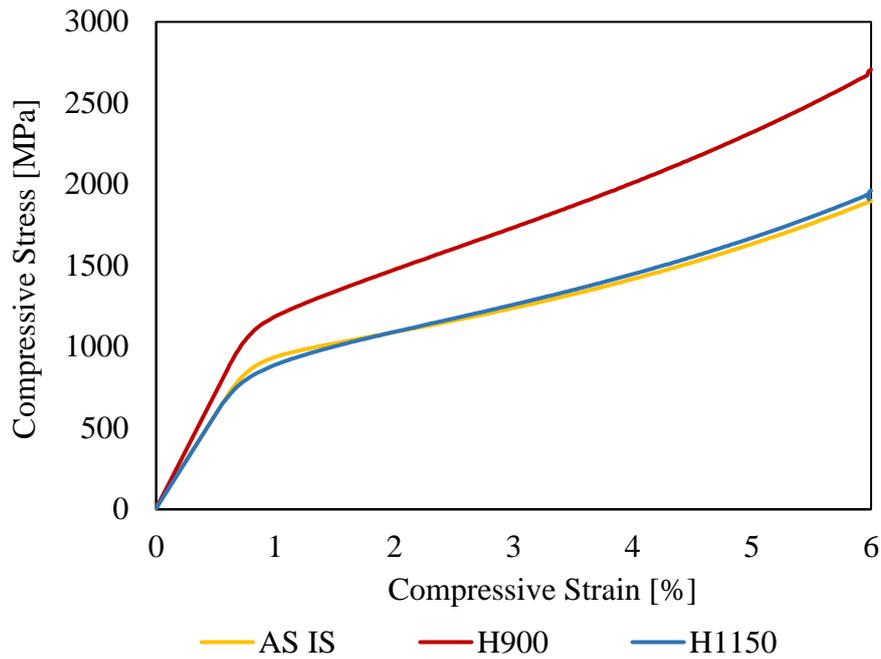


Figure 6.12: Compressive stress-stroke curves.

While monolithic metallic materials are characterized by an homogenous plasticity response and symmetric compressive and tensile yield strengths, asymmetry occurs for porous materials [150]. All the AISI 630 sintered samples exhibited a slight asymmetry, as compressive yield strength values are higher than tensile yield strength on average with a pronounced tensile-compressive asymmetry (TCA) for H900 samples, as reported in Table 6.6. The negative role of inherent porosity in specimens made additively does not represent a key factor in compressive loads [151]. The obtained results show how the nature of the compressive loads tends to close the pores and solidifies the defective areas as long as the porosity is minimal. In contrast, under tensile loading, the pores begin to coalesce and expand leading to failure.

Table 6.6: Tensile and compressive yield strength values.

	Tensile Yield Strength	Compressive Yield Strength	TCA
AS IS	768±5	815±25	5%
H900	1028±80	1120±29	8%
H1150	604±41	645±24	6%

The average three-point bending stress–strain curves of each tested conditions are plotted in

Figure 6.13. Three distinctable curves are noticeable and a similar tendency between tensile and bending properties could be outlined in relation to the thermal treatments. The AS-IS samples registered an average flexural strength of 1827 ± 18 MPa. The H900 treatment led to a rise of the average flexural strength up to 2212 ± 75 MPa. Comparing the aforementioned values, an enhancement by 17% was generated due to tempering at 480 °C. Aging to the H1150 resulted in the over-aged condition characterized by a lowering of the flexural strength (1691 ± 88 MPa). The flexural strain values exhibited a different behaviour. The peak-aging treatment generated a slightly reduction in percentage from 4.5% for AS-IS samples to 4.1%. An identical value of flexural strain (i.e., 8.6%) was obtained for H1150 samples, compared to the tensile property reported in Figure 6.9.

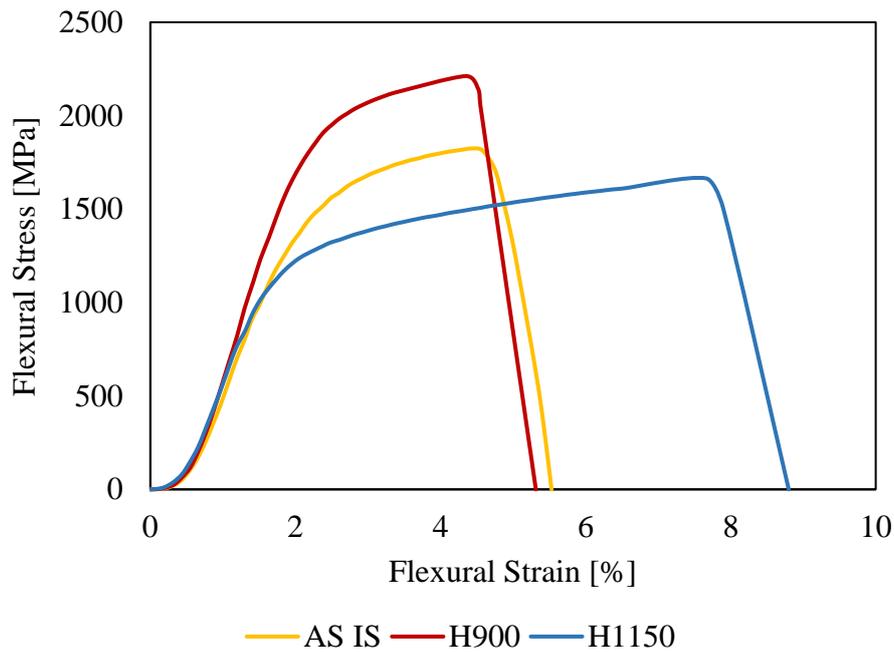


Figure 6.13: Bending curves.

All the tested samples underwent a complete fracture, regardless of the heat treatment experienced. Three-point bending tests produce tensile and compressive stresses on the convex and concave side of the specimens above the neutral axis, respectively. The formation of the cracks occurs in the convex side of all samples and a rapid propagation along the width of specimens was detectable for AS-IS and H1150 samples (Figure 6.14). H900 samples behaved differently, since the formation and the propagation phases of the crack are indistinguishable and any significant deformation occurs.



Figure 6.14: Bending test phases for the H1150 specimen.

Figure 6.15 depicts the values of Vickers hardness depending on the thermal treatment, as the average of the results collected from the indentation within the 3x3 line grids. A clear leverage of the peak-aging treatment is detectable with an average value of 397 ± 7 HV, with respect to the average value registered for the as sintered condition. Comparing the average hardness values of metal ME samples to those of monolithic material, a

further improvement of H900 and H1150 treatments on additive specimens are noticeable, since the difference with the relative monolithic value decreases from 11% for the AS-IS samples to 4.8% and 8.6%, respectively for peak and over-aged samples. Furthermore, a uniform distribution of the Vickers value along the growth direction of the layers may signify the homogeneity of the material, both in as sintered and aged state.

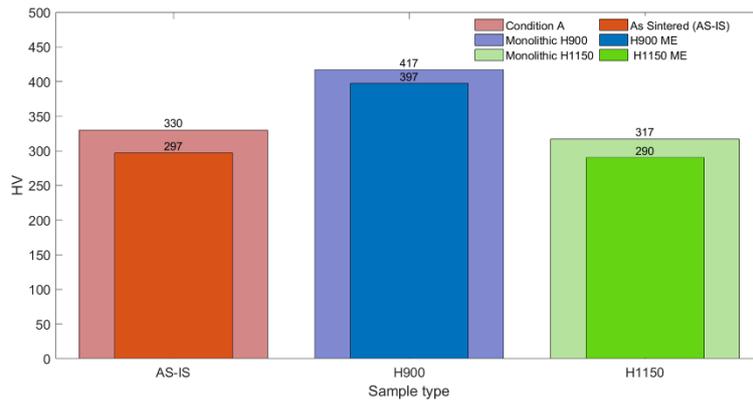


Figure 6.15: Vickers hardness values.

In order to characterize the level of repeatability for the mechanical of metal samples, the coefficient of variation was calculated and used as a comparison metric. This coefficient is the ratio of the standard deviation to the mean for all analyzed samples. The coefficients of variation of AS IS, H900 and H1150 samples for each mechanical tests are highlighted in Table 6.7. In general, limited values were registered for all different covered conditions, ensuring the reproducibility of the different mechanical tests on metal samples manufactured by Material Extrusion. A maximum of 0.043 was registered for the H900 samples tested by means of a tensile test. Concerning the compressive test, an upwards trend is detected with a minimum value of 0.002 for the sintered samples and a peak value (0.036) associated to H1150 samples. The same behaviour depicted for compressive test are also evident for the flexural values, as the lowest value (0.010) was registered for the AS IS samples and 0.05 was the highest values for the H1150 specimens. The increase of holding time and treatment temperature enhanced the coefficients of the variation, with a subsequent low control of the repeatability of the compressive and bending specimens. Then, the coefficients of variation for Vickers hardness tests result to be the steadiest, also due to the uniformity of the test performed.

Table 6.7: Coefficients of variation of AS IS, H900 and H1150 samples for each mechanical tests.

	Condition state		
	AS IS	H900	H1150
Tensile test	0.010	0.043	0.019
Compressive test	0.002	0.011	0.037
Bending test	0.010	0.034	0.052
Vickers hardness test	0.025	0.019	0.019

6.4 Conclusions

In the present research, a comprehensive evaluation of AISI 630 samples fabricated by means of metal material extrusion techniques was assessed, leading to the following key results:

- (1) The best combination of printing process parameters (*In Line*, s 15 mm/s, h 0.1 mm, d 125%) ensured a 95% of apparent density compared to the bulk material, with a mean value of 7.4 g/cm³. Besides, this combination generates the dimensional shrinkages closest to those defined in the technical datasheet.
- (2) The mechanical tests proved the benefit derived from the heat treatment H900. Yield Strength, UTS and hardness improved significantly without any detriment of the ductility compared to the as sintered samples. Higher aging time and temperature led to an increase in the ductility of the specimens, observable both in elongation at break and flexural strain average values. All the specimens exhibited a slight TC asymmetry, regardless of the specific thermal condition.
- (3) Solution and aging treatment on sintered samples reduced the deviation with respect to the corresponding values of tempered monolithic ones in terms of strength, ductility and hardness. The microstructure of AS-IS significantly differed from traditional martensite and δ -ferrite structure, since the presence of typical austenitic grains was detectable. Tempered samples approached the structure of respective monolithic structure, though.

- (4) The optical and SEM observations of the fractured surfaces revealed the interruption of ductile behaviour of material with smooth area in correspondence of the areas between different layers, suggesting the brittle failure for samples of all three conditions. The microstructure also included spherical SiO₂ inclusions with particle size of 5 μm.

Metal material extrusion is a promising cost effective technology that may overcome the considerable entry barriers related to traditional Powder Bed and Powder Fed systems, such as high purchasing costs, relevant carbon footprint and needs for safety requirements. The use of this technique combined with subsequent solution and aging treatment on precipitation hardening alloy could extend its application even to high value-added products requiring good mechanical properties, with the major advantage of the lower production costs.

7 Recycling process of Green Parts for Metal Material Extrusion

This chapter is derived from the combined work between University of Bergamo and ENEA Portici research center.

I am immensely grateful to the support received from my co-authors. I am responsible for everything written in this chapter.

7.1 Introduction

On basis of the results achieved in chapters 4, 5 and 6, this multi-step additive technique represents a considerable alternative to traditional metal additive manufacturing technologies, due to the remarkable advantages. However, its novelty implies the generation of a considerable amount of defects during the printing process. High value-added applications need for certain quality characteristics, in terms of surface roughness and geometrical properties. Owing to the amount of process parameters combinations, dissimilar Material Extrusion process faults can badly affect the quality of green parts, since the occurrence of typical part defects may occur. One of the most harmful defects is the warpage of the printed parts, which results in bad first layer adhesion and a consequent lift of the corner of the printed object from the build platform. The primary cause is the immediate change between the extrusion and the ambient temperature, leading to an uneven plastic shrinkage [152]. Another issue strictly connected to the temperature is the delamination within the part: thermal gradients, which result from the deposition of the hot melt on a previously deposited partially printed cool part, as well as different convective cooling rates within the build environment can generate stresses resulting in delamination of roads from one another or even cracking of parts [153]. Besides, the nozzle clogging phenomenon occurs especially with high filler contents materials. The clogged nozzle precludes a correct material flow and intermittent deposition leads to a print failure through significant changes in the volume [154]. Overhang structures of the printed parts require support elements, which could be mechanically removed from the final element. The removal action could cause damage to the part if the support material is fused too tightly [155]. In addition to the listed defects narrowed to the deposition phase, there are plenty of issue related to the print quality of the final parts, concerning dimensional accuracy, resolution and surface roughness [155], which might be critical for visual models, fit and assembly and for tooling applications,

as well as in the manufacture of finished parts. In general, all these defects and print quality issues are quite visible for the operator in charge of the deposition process and the subsequent debinding and sintering phases are useless, since in most cases the defectology can only worsen. These kinds of green parts represent scrap that needs to be managed. An accurate handling of the wasted green parts could arise this novel ME technique in terms of sustainability, both environmental and economical. In this context, there are three methodology that might be pursued to prevent and manage the generation of scrap from metal material extrusion process, which might be categorized in process monitoring, material recycling and scraps reuse. In the first case, preventive actions are taken to monitor qualitative uncertainties and to provide in-situ correction reducing costs due to rejection, since anomalies in printing are detected almost immediately after they occur. In [156], a comprehensive review about the different sensor technology groups for process monitoring was presented, including 2D vision with camera [157], temperature monitoring with thermal cameras [158], vibration monitoring with accelerometers [159] and 3D vision with structured light [160] and laser triangulation [161]. All these groups were combined with analytical models and artificial intelligence tools. Process monitoring mitigates the defects generation, while recycling is a possible solution at the time that green parts are already scrap. Since the raw feedstock for this technology consists of dissimilar elements (i.e., polymers, metals, additives, etc.), a controlled multiphase process for the green parts disposal is necessary. In particular, a proper equipment for the separation of dissimilar material is required, such as filters for metallic powders, that need to be disposed in special collection centres for the management of fine metallic particles. Besides, the polymeric content necessitates to be removed chemically or thermally. In the first case, the solvent used for the chemical separation needs to be collected and filtered; if the separation is carried out by thermal processes, a controlled atmosphere furnace is required, since the release of fumes is extremely dangerous for the safety of the operators [92]. Lastly, the reuse of the wasted green parts is the third way forward to manage the scraps generated by metal material extrusion. This operation comprises the collection and the remanufacturing of scraps to produce recycled filaments as new feedstock to be used in metal ME. To the best authors' knowledge, there is no paper dealing with the reuse of green parts for the sustainability of MME technology.

In this work developed in cooperation between University of Bergamo and ENEA Portici research center, a preliminary evaluation of a circular methodology for the reuse of wasted green parts has been proposed. A comparison between virgin and recycled filaments is proposed to assess any effects of the filament extrusion process on the raw feedstock, considering both polymeric contents and solid loadings. Subsequently, a structural and mechanical evaluations of the secondary metallic samples (recycled ones) were proposed in terms of apparent density, microstructure and Vickers hardness and compared to properties of virgin sintered samples. The novelty of this work is related to the possibility to reuse green parts, considered scraps, to extrude a new filament to be used for metal material extrusion process with economical and sustainable advantages and without any deterioration of physical and mechanical properties of the secondary final parts.

7.2 Materials and methods

The virgin feedstock is the mixture of 316L stainless steel water-atomised powders (90 wt.%), evenly distributed in a polymeric matrix made up of polyoxymethylene (POM) as primary binder, polyolefin as backbone and additives. The immobilization of the metal particles eases the handling of the filament and the uniform distribution of the metal within the binder matrix allows a homogenous shrinkage of the printed part during debinding and sintering phase.

The proposed methodology consists of reusing green parts with apparent defects and it is composed by different stages, as illustrated in Figure 7.1.

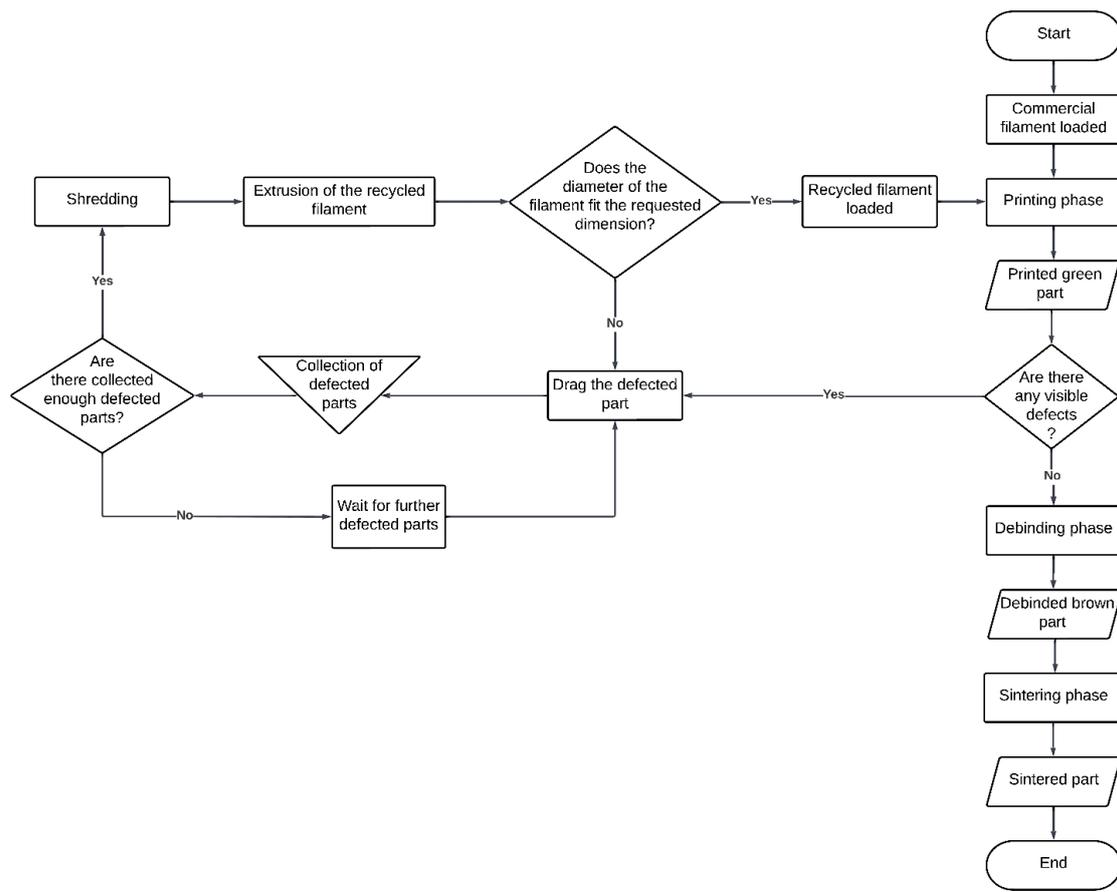


Figure 7.1: Flow chart of the recycling methodology.

The first action involves the recognition of an apparent defects within a printed green part. Warpage and delamination issues due to wrong temperature render a green part unusable, since the subsequent thermal treatments do not resolve these geometric distortions. Besides, an inappropriate temperature of the printing bed combined with bad adhesion systems, such as adhesive sheets or glue stick applied, cause a complete detachment of the printed samples from the working area blocking the building process. Lastly, the removal of the support breakaway material can damage the product. Any of the mentioned situations transforms a printed green part into a scrap. In the second phase all the green parts with visible defects were collected to reach a kilogram of wasted material. Then, the collected material was shredded by means of a commercial grinder, until the size of the granulated feedstock reached the range from 3 to 5 mm to obtain stability during extrusion process minimizing air entrapment, which may generate defects in the production of a filament [57]. Prior to the extrusion phase, the granulated material was also dried in a vacuum furnace at 100°C for 60 mins in order to reduce the moisture

contained in the material [162] and to adequately prepare the granulated feedstock. Extrusion then occurred once thoroughly dry. The extrusion of the granulated scraps was enabled by means of a commercial machine, composed by a filament extruder and a spooler. The extrusion process parameters are reported in Table 7.1.

Table 7.1: Process parameters of filament extruder and spooler.

Nozzle temperature	Nozzle diameter	Gearmotor speed	Puller speed	Fan
200 °C	2.85 mm	3 rpm	0.8 m/min	OFF

It was selected a nozzle temperature higher than the melting point of the primary binder (i.e., polyoxymethylene) to reduce the viscosity of the feedstock and to facilitate the extrusion phase. The fan was switched off to ensure a better control and stability of the extrusion of the filament. The extrusion process continued until the diameter of the filament reached a diameter of 1.7 ± 0.05 mm. A systematic control of the constant filament thickness was guaranteed, since the spooler was equipped with a filament diameter controller that automatically calibrate the extrusion. The filament portions, which did not comply with the specified tolerance, were collected and manually shredded before being inserted again in the hooper.

After the recycling process for extending damaged green parts lifecycle, the secondary filament was extruded by means of a desktop 3D printer to obtain simple prismatic green parts, since the aim of this work is the assessment of a newly circular fabrication method. The last step concerns a catalytic debinding process with HNO_3 (concentration 98%) at 120 °C removed the primary binder from the green parts, resulting in a brown part, consisting of metal particles and a residual polymeric backbone. The subsequent sintering process at temperatures immediately below the melting point of the metal content removed the secondary binder and caused metal particle coalescence. The sintering cycle was performed in argon atmosphere and consisted of three thermal ramps, as reported in Table 7.2.

Table 7.2: Ramps of the sintering cycle.

	Initial temperature	Final temperature	Ramp rate	Holding time
Ramp 1	Room temperature	600 °C	5 °C/min	1 hour
Ramp 2	600 °C	1380 °C	5 °C/min	3 hours
Ramp 3	1380 °C	Room temperature	Furnace cooling	-

The virgin and recycled filaments were analysed by means of thermogravimetric (TG) analysis (Netzsch STA 449 F3 Jupiter). The TG analysis were conducted in N₂ atmosphere according to the thermal cycle reported in Table 7.3. An holding time of one hour at the temperature of 320°C was chosen to evaluate the degradation behaviour of POM [93], since it is the only binder component known in the filament composition.

Table 7.3: Cycle for thermogravimetric analysis.

	Initial temperature	Final temperature	Ramp rate	Holding time
Ramp 1	30 °C	320 °C	10 °C/min	-
Ramp 2	320 °C	320 °C	5 °C/min	60 min
Ramp 3	320 °C	900 °C	10 °C/min	-

The internal structures of the primary and secondary filaments, green parts and sintered parts were analysed by means of a digital microscope (Keyence VHX-7000). Besides, the cross sections of the filaments were also observed by means of scanning electron microscope (Zeiss EVO 40). The particle size distributions of the metallic powders were estimated through image analysis of 15 SEM images for both filaments with the support of an image processing program. The cross section of sintered samples perpendicular to the building direction were polished up to 0.05 µm with alumina suspension and etched by Kalling II solution (2g CuCl₂, 40 ml HCl, 40 ml Ethanol). The chemically etched

surfaces were observed using a digital microscope to analyse the microstructure and grain size. The densities of the secondary green and sintered parts were measured by pycnometer method.

Lastly, to ensure a preliminary mechanical characterization of the samples, Vickers Hardness tests were conducted sectioning three samples along the growth direction of the layers. Sequentially, a 3×3 line grids on the sections of each sample was drawn in accordance to ISO 6507-1:2018 [142]. The tests were performed by means of a hardness tester UHL–VHMT.

7.3 Results and discussions

The TG analysis conducted on commercial and recycled polymeric filaments loaded with AISI 316L stainless steel powders gave the results graphically plotted in Figure 7.2. The evident gap in the vertical stroke of the curves is a direct graphical consequence of the holding time applied to the analysis at 320 °C. The thermogravimetric curves show an almost perfect overlap for the first portion of the curves, indicating an identical degradation behaviour of the primary binder (i.e., polyoxymethylene), contained in the filaments. Diversely, the mass loss of POM in the recycled filament is higher than that in the commercial one, with a difference of 0.6%. The melting point of polyoxymethylene is around 165 °C, while the recycling method was carried out at 200°C. Performing the extrusion phase at temperatures higher than the melting point of the primary binder led to a change in the final binder content of the recycled filament, with a total mass loss assessed around 10.4%, that is 0.6% higher compared to the commercial filament. The difference of the mass loss of polymeric content in both type of filaments precisely corresponds to the discrepancy of POM degradation in commercial and recycled filaments. Then, the slopes in the second portion of the curves corresponds to the degradation phase of the backbone element. This change of slopes started around 420°C, which corresponds to the degradation temperature of polypropylene (PP) [163]. It can be noticed the symmetricity of the slopes in the second portion of both curves and a similar mass loss of PP around 0.9%.

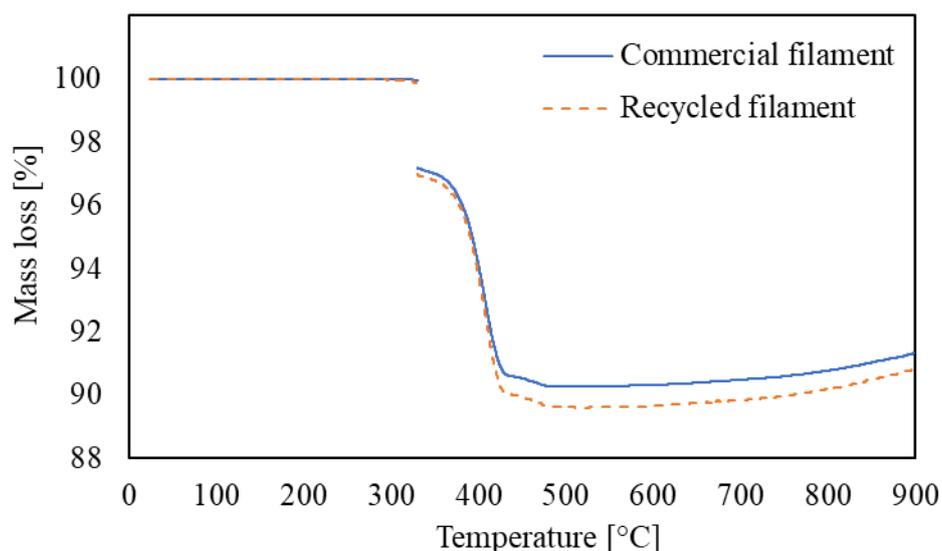


Figure 7.2: TGA curves for commercial (blue line) and recycled (orange dashed line) filaments.

The cross sections of the commercial and recycled filaments were reported in Figure 7.3a and b. Concerning the virgin filament, a perfect round shape can be observed; while, the recycled filament presents an irregular shape. After SEM analysis, the dark spots detectable in the cross sections of the filaments were confirmed as binder components in the form of segregates. It is possible to observe a lower amount of dark spots within the recycled filament, due to the higher mass loss of POM in this kind of feedstock, in accordance with the TG analysis. In Figure 7.3c and d, representative SEM images of the 316L powders dispersed in the polymeric content are provided, showing a proper spherical morphology of the particles in both the considered filaments. Besides, the size distribution of the metal powders distributed in the polymeric matrix of the commercial and recycled filament are mentioned in Table 7.4. The average size of particles involved in MME is lower compared to those of the traditional metal AM technologies, such as Laser Powder Bed Fusion and Direct Energy Deposition, since a decrease in their size ensures an enhancement of the flowability during the extrusion phase of the filament. Concerning the recycling method, it seemed to slightly affect the particle size distribution in the commercial and recycled filaments, especially in D10 and D90 distribution. It is possible to notice that the median diameters of the particle number size distribution D50 were almost identical, since the difference in average sizes settled around 2%. However, the detectable growth in deviations of the average distribution of smaller and larger

particles (i.e., D10 and D90) could be directly attributable to the recycling process. Indeed, this type of recycling process is characterized by the synergy between mechanical behaviour of metal powder during shredding and extrusion process and the heat input. The thermal component is generated by both the friction between material-material and material-equipment during shredding phase and from the heat contribution of the external source in extrusion phase. Despite that, the thermal transition during the shredding and extrusion steps could not lead to any dimensional change of powders, given that the temperature experienced during the filament extrusion process was definitely lower than the sintering window of the AISI 316L stainless steel. Therefore, the deviations in D10 and D90 distributions were ascribed to the mechanical component of the recycling process. In particular, the higher values of almost 10% of D10 distribution in the recycled filament compared to the commercial filament suggest a possible loss of very fine particles during shredding and extrusion operations. An explanation of this loss can be linked to the volatility of these smallest and lighter particles, which can disperse during mixing. On the contrary, a reduction in the D90 distribution of particles was detected in the case of recycled filament compared to the commercial one, as they are more easily involved in the cutting action experienced during the shredding phase.

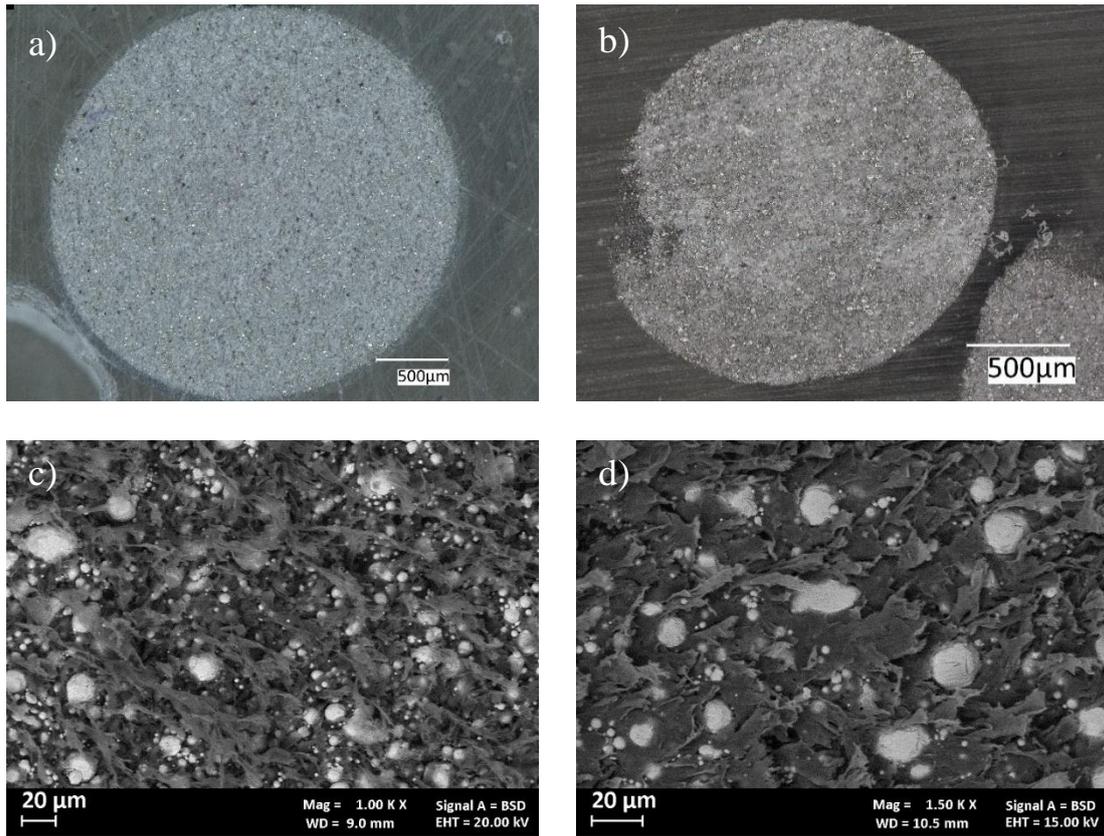


Figure 7.3: Cross sectional micrographs of commercial (a) and recycled (b) filaments; SEM micrographs of commercial (c) and recycled (d) filaments.

Table 7.4: Particle size distribution of commercial and recycled filaments.

	Commercial filament	Recycled filament	Deviation
D ₁₀	3.735 µm	4.108 µm	9.1 %
D ₅₀	11.364 µm	11.643 µm	2.4 %
D ₉₀	21.616 µm	18.964 µm	-14.0 %

The measured densities for primary and secondary green parts were 4.07 and 4.33 g/cm³, respectively. The difference of 0.26 g/cm³ was a direct consequence of the polymeric content breakdown during the extrusion phase of the recycled filament. This result hints lower volumetric shrinkage for secondary metallic components compared to samples obtained by commercial feedstocks.

A qualitative analysis of primary and secondary green parts was conducted in Figure 7.4. The specimens fabricated with the recycled filaments presented a larger content of voids within the deposited loads, both in vertical and side views. Again, a lower content of polymeric binder caused a decrease in the secondary green parts quality, visible with voids and jagged surfaces.

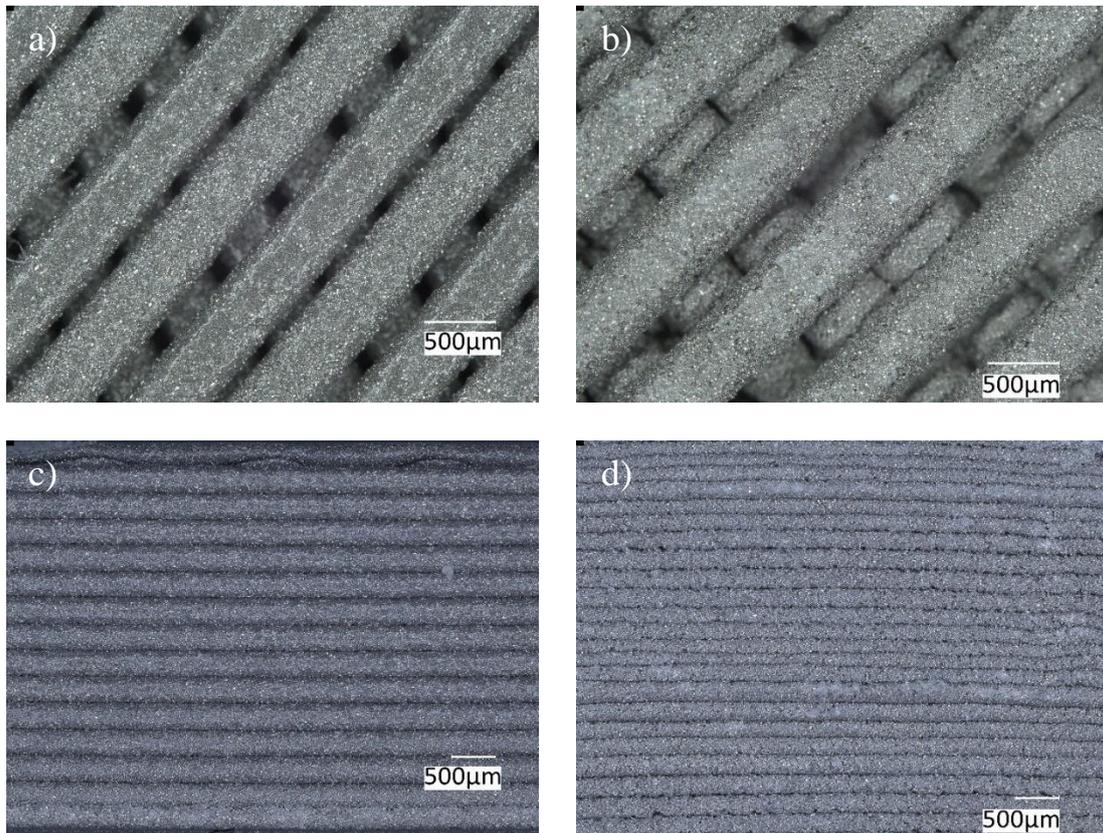


Figure 7.4: Optical micrographs of the Top view of primary (a) and secondary (b) green parts; optical micrographs of the Side view of primary (c) and secondary (d) green parts.

The recycled metal samples exhibited an apparent density of 7.52 g/cm^3 , which corresponds to the 94% of the density of monolithic AISI 316L. A comparison among density value of the samples obtained using recycled and commercial feedstocks and the percentage value in comparison to the monolithic material are reported in Table 7.5. From the comparison among the density value found in literature, the proposed methodology ensured promising results in terms of final physical properties of the secondary metal samples fabricated, since no clear difference can be detected from the matching.

Table 7.5: Comparison of apparent density among 316L specimens fabricated by means of the MME technique.

	Apparent density	Relative density
This work	7.52 g/cm ³	94%
Quarto et al. [136]	7.58 g/cm ³	95%
Liu et al. [116]	7.36 g/cm ³	92.2%
Gong et al. [114]	7.85 g/cm ³	98.5%
Kurose et al. [115]	7.43 g/cm ³	92.9%
Ait-Mansour et al. [117]	7.63 g/cm ³	95.4%

The microstructures of primary and secondary sintered parts are reported in Figure 7.5a and b. No dissimilarities were detectable between the two microstructures, since both type of samples underwent the same sintering conditions. Indeed, the sintering phase is the most influential process for the final microstructure of the metal components realized by means of multi-step MME technique. In general, the proposed microstructures were primarily composed by equiaxed austenite grains with an average size in the range of 30 and 60 μm and limited pores, which can be observed within the austenitic structure. The specific thermal process of this technique modified the microstructure of ME 316L samples, since the high temperature of sintering promoted the coarsening of the grain size. Monolithic 316L microstructure comprises austenitic grain with lower dimension. Besides, the presence of twin boundaries and a relevant amount of δ -ferrite along the grain boundaries seemingly opposed to fully austenitic phase when processed by conventional manufacturing methods. The twin crystal structures can be recognized by parallel bands with different contrast. The boundaries separating the twins have a very low energy per unit area and therefore, the twin-boundaries tend to be flat, becoming a preferential site for crack initiation. The δ -ferrite resulted from high temperature and subsequent fast cooling rate in the sintering cycle since a sufficient period was not achieved for the completion of the phase transformation from δ to γ ferrite. Thus, exceeding presence of δ -ferrite was retained in the austenitic matrix, as also confirmed by an XRD analysis performed in a previous work [164]. Additionally, the presence of δ -

ferrite was promoted by ferrite former, such as silicon. According to EDS compositional analysis, SiO₂ inclusions were found in both primary and secondary sintered samples. During the atomization process to fabricate spherical metal powders, a limited percentage of silicon is often added to prevent oxidation by forming a thin silica films that cover metal powders [132]. Lastly, no preferential orientation of the grains could be found, suggesting an independency of MME sintered samples from the building direction of the deposited layers.

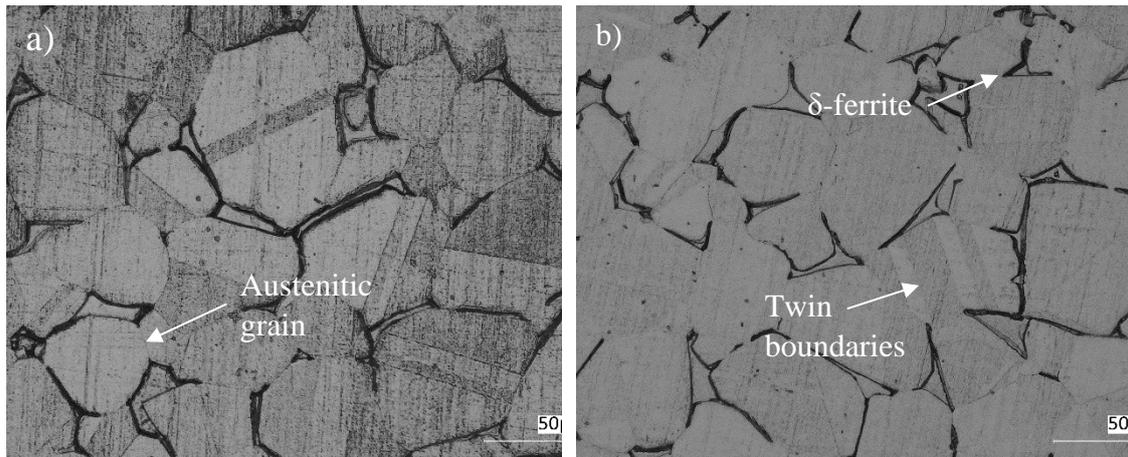


Figure 7.5: Digital-microscope micrographs of etched cross-section of primary (a) and secondary (b) sintered samples along building directions of samples.

Considering the preliminary mechanical characterization, the average Vickers hardness value was 138.1 ± 5.1 HV, which was approximately 11% lower with respect to the monolithic AISI 316L. Matching the aforementioned value with the Vickers hardness of sintered parts obtained from AISI 316L commercial feedstocks (Table 7.6), a significant hardness value was experienced. Besides, it can be noticed that this mechanical property is nominally the same similar to the sintered density, which is almost independent of the recycled state of the metal samples considered. This is expected as density is generally a proper indication of the mechanical properties of porous material, such as samples fabricated by means of MME technique. These evidences could suggest the possibility to register even considerable mechanical properties concerning dissimilar tests performed, such as tensile, compressive and bending tests and it is partially confirmed by the estimated value of UTS obtained from the conversion tables, reported in the right column of Table 7.6. Lastly, the low value of standard deviation guaranteed the uniform

distribution of the Vickers hardness values along the growth direction, suggesting the homogeneity of the material.

Table 7.6: Comparison of Vickers hardness values among 316L specimens fabricated by means of the MME technique.

	Vickers Hardness	Other scales	UTS
This work	138.1 ± 5.1 HV		445 MPa
Carminati et al. [164]	132.2 ± 3.8 HV		425 MPa
Gong et al. [165]	105.9 HV	60 HRB	335 MPa
Liu et al. [116]	145.2 ± 6.7 HV		335 MPa
AISI 316L (MatWeb, n.d.)	155 HV		465 MPa

7.4 Conclusion

This study introduced a preliminary recycling methodology for the reuse of defected green parts for MME technique. The proposed recycling methodology concerned the development of a recycled filament to manufacture metal samples starting from scraped green parts collected following the development of defects due to printing process issues. The TGA demonstrated a partial influence of the filament extrusion process, since a higher mass loss for the recycled filament occurred in comparison to the commercial filament. The recycling method did slightly affect the metallic particles size distribution, narrowing the distribution span in the recycled filament. As a consequence of the binder content breakdown, the secondary green parts exhibited a density of 0.26 g/cm³ higher than the primary green part. The effects of the recycled feedstock on the apparent density, microstructure and hardness of secondary sintered parts were also investigated and directly compared to the available reference of the primary sintered parts. The apparent density seemed not to be influenced by the use of recycled filament, since a significant value of 7.52 g/cm³ was achieved, which is on average when compared to apparent density reached with MME technique. Consequently, the microstructure and the mechanical properties of secondary sintered parts are nominally constant since the recycled method only affected the polymeric content of the filament. Any difference could be noticed in the microstructure of primary and secondary sintered parts; instead,

samples printed by means of metal material extrusion remarkably differed from monolithic material in terms of microstructure, since coarsening of austenitic grains, twin boundaries and δ -ferrite phase prevailed. Vickers hardness value settled around 138.1 ± 5.1 HV, ensuring a great reliability of the mechanical response of sintered parts fabricated with recycled filament with respect to primary sintered samples.

The proposed methodology marked a new milestone in the development of MME technology, since the preliminary structural and mechanical assessment of sintered parts manufactured with a recycled metal polymer filament was proved. The closed loop process enhanced the environmental and economical benefits of this technique, compared to traditional metal AM technology, such as Laser Powder Bed Fusion and Direct Energy Deposition. Further improvements are required to boost the diffusion of this recycling process. The volumetric shrinkage needs to be assessed to guarantee the geometric accuracy of the final products. Besides, further mechanical tests are necessary to validate the preliminary mechanical characterization performed. Lastly, the verification of any possible of properties degradation, both structural and mechanical, should be pursued with the increase of number of reuse cycles.

8 *General conclusions*

Metal Material Extrusion is an attractive alternative to traditional metal Additive Manufacturing technology for the fabrication of metal components. The advantages concern the use of low cost equipment and the low budget necessary for the raw feedstock. Besides, the raw feedstock is typically supplied in the form of filaments, which considerably increase the safety in handling compared to volatile and micrometric powder. Lastly, this newly method is less energy-intensive with respect to other additive technologies producing metal products. Regardless of the remarkable advantages, the technology requires extensive studies and analysis to minimize its drawbacks and defects, especially in terms of physical and mechanical properties. The complete evaluation of the multi-process, including shaping, debinding and sintering phases as well as any subsequent thermal processes, is very important for the industries, since it allows to spread this interesting technology for dissimilar fields throughout the optimization of the process parameters to obtain the best performances in terms of process and product characteristics.

In the first section of this research, an extensive physical analysis on 316L samples fabricated via ME was conducted. The objective was to investigate the possible influence of some relevant ME printing parameters on dimensional shrinkage and bulk density of the sintered samples on the basis of a statistical analysis. The best combination of process parameters resulted from the conducted analysis (i.e., Lines as infill pattern, extrusion speed set to 20 mm/s and 0.1 mm as layer thickness) ensured the achievement of an apparent density equal to 95% of that of the monolithic 316L. Besides, this combination generated less than 3% of open porosity, which is the most critical defect of a component made additively. The open porosity is an outcropping defect that significantly undermines the mechanical response to the tensile and compressive loads applied in comparison with the close porosity.

The study also outlined the anisotropic dimensional shrinkage of metal parts following the sintering process, since the shrinkage along Z axis was 25% greater than X and Y shrinkages.

After the structural assessment of sintered parts, an overall mechanical characterization was provided by performing tensile tests, compression tests, bending tests, Charpy impact tests, Rockwell B and Vickers hardness tests. A mechanical evaluation of ME 316L

samples was necessary to frame the functional perspective of the metal components for different manufacturing areas, especially for critical uses and high value-added applications. 316L ME specimens registered lower values in terms of strength, stiffness, resilience and ductility compared to those of the monolithic AISI 316L. The deterioration of the mechanical properties was attributed to the 5% of porosity within the metal matrix and to the presence of δ -ferrite phase retained in the austenitic structure. Besides, the hardness tests demonstrated the homogeneity of the material since the hardness value were distributed uniformly along the growth directions of the layers.

Once the completion of both physical and mechanical characterization of 316L samples, the attention shifted to another relevant stainless steel from an industrial point of view. AISI 630 is a martensitic stainless steel which could be hardened following solution and aging treatments. Different thermal treatments induce dissimilar mechanical properties as for strength and ductility. The study demonstrated that solution and aging treatments enhanced the mechanical characteristics of AISI 630 ME samples reducing the differences with respect to the corresponding values of tempered monolithic ones. In particular, the peak-aged treatment (H900) ensured the highest yield and ultimate tensile strength. Over-aged treatment (H1150) led to an improvement of the ductile behaviour of the specimens, compared to the sintered ones. In general, the sintered samples unexposed to any post thermal treatments exhibited the worst mechanical properties. Besides, SEM observation revealed a common fracture behaviour, which occurs to the interface between two adjacent layers, regardless of the conditions of the samples exposing one of the main issues related to the deposition phase of Material Extrusion.

Lastly, the analysis focused on the sustainable aspects of metal ME technique. As a novel technology, metal ME generates scraps, due to still existing process inefficiencies, which increase the total costs of fabrication and undermine its economic competitiveness. The circular economy of a newly additive process has been assessed with a focus on the reuse and the remanufacture of wasted products. Particularly, the reuse of defective green parts of metal ME technique was investigated to assess a circular manufacture of metallic parts. A filament was fabricated starting from scrapped green parts as raw feedstocks with a commercial extrusion system to print secondary green parts. A comparison between commercial and recycled filaments was carried out. Besides, the polymeric content was studied by means of macrographic and thermogravimetric analysis, while a particle size

distribution analysis was proposed to evaluate any change in metal powders sizes. The recycled feedstock did not influence the sintered density of secondary specimens, even because any difference between the microstructure of primary and secondary sintered parts occurred.

Furthermore, preliminary mechanical evaluations of the secondary metallic samples were proposed suggesting the technical feasibility of the proposed circular fabrication process. Further steps will involve the study and the development of new deposition strategies to minimize the overall porosity generated within the polymer/metal matrix during the printing process. Besides, the fatigue behaviour of metal samples fabricated by means of this innovative additive technique represents a topic of interest that requires in-depth analysis.

9 References

1. ISO/ASTM 52900:2021; Additive manufacturing - General principles - Fundamentals and vocabulary. *ASTM Int.* 2021.
2. Lipson, Hod; Kurman, M. Fabricated : the new world of 3D printing; *John Wiley and Sons, Ed.*; Indianapolis, **2013**;
3. Khorasani, M.; Ghasemi, A.H.; Rolfe, B.; Gibson, I. Additive manufacturing a powerful tool for the aerospace industry. *Rapid Prototyp. J.* **2022**, *28*, 87–100, doi:10.1108/RPJ-01-2021-0009.
4. Yan, Q.; Dong, H.; Su, J.; Han, J.; Song, B.; Wei, Q.; Shi, Y. A Review of 3D Printing Technology for Medical Applications. *Engineering* **2018**, *4*, 729–742, doi:10.1016/j.eng.2018.07.021.
5. Lu, B.H.; Lan, H.B.; Liu, H.Z. Additive manufacturing frontier: 3D printing electronics. *Opto-Electronic Adv.* **2018**, *1*, 1–10, doi:10.29026/oea.2018.170004.
6. Tromans Graham *Developments in Rapid Casting*; Wiley, **2003**;
7. 3D Printing Trend Report 2022. **2022**, 1–23.
8. Kirchheim, A.; Dennig, H.; Zumofen, L. Industrializing Additive Manufacturing - Proceedings of Additive Manufacturing in Products and Applications - AMPA2017. *Ind. Addit. Manuf. - Proc. Addit. Manuf. Prod. Appl. - AMPA2017* **2018**, doi:10.1007/978-3-319-66866-6.
9. EPMA Introduction to additive manufacturing technology, a guide for designers and engineers. *Eur. Powder Metall. Assoc.* **2019**, 28–34.
10. Tuck, C.; Hague, R.; Burns, N. Rapid manufacturing: Impact on supply chain methodologies and practice. *Int. J. Serv. Oper. Manag.* **2007**, *3*, 1–22, doi:10.1504/IJSOM.2007.011459.
11. John Foran. Taking Power: On the Origin of Third World Revolutions; 1st ed.; *Cambridge University Press*: Cambridge, **2005**;
12. Wang, X.; Jiang, M.; Zhou, Z.; Gou, J.; Hui, D. 3D printing of polymer matrix composites: A review and prospective. *Compos. Part B Eng.* **2017**, *110*, 442–458, doi:10.1016/j.compositesb.2016.11.034.
13. Mühler, T.; Gomes, C.M.; Heinrich, J.; Günster, J. Slurry-based additive manufacturing of ceramics. *Int. J. Appl. Ceram. Technol.* **2015**, *12*, 18–25, doi:10.1111/ijac.12113.
14. Oropallo, W.; Piegl, L.A. Ten challenges in 3D printing. *Eng. Comput.* **2016**, *32*, 135–148, doi:10.1007/s00366-015-0407-0.
15. Doubrovski, Z.; Verlinden, J.C.; Geraedts, J.M.P. Optimal Design for Additive Manufacturing: Opportunities and Challenges 2011, 635–646.
16. Gibson, Ian; Rosen, David; Stucker, B. *Additive Manufacturing Technologies*; Second.; Springer, 2019; ISBN 9781493921126.

17. Pagac, M.; Hajnys, J.; Ma, Q.P.; Jancar, L.; Jansa, J.; Stefek, P.; Mesicek, J. A review of vat photopolymerization technology: Materials, applications, challenges, and future trends of 3d printing. *Polymers*. **2021**, *13*, 1–20, doi:10.3390/polym13040598.
18. Garcia, E.A.; Ayranci, C.; Qureshi, A.J. Material property-manufacturing process optimization for form 2 VAT-photo polymerization 3D printers. *J. Manuf. Mater. Process.* **2020**, *4*, doi:10.3390/jmmp4010012.
19. Ransikarbum, K.; Pitakaso, R.; Kim, N. A decision-support model for additive manufacturing scheduling using an integrative analytic hierarchy process and multi-objective optimization. *Appl. Sci.* **2020**, *10*, doi:10.3390/app10155159.
20. Calignano, F.; Manfredi, D.; Ambrosio, E.P.; Biamino, S.; Lombardi, M.; Atzeni, E.; Salmi, A.; Minetola, P.; Iuliano, L.; Fino, P. Overview on additive manufacturing technologies. *Proc. IEEE* **2017**, *105*, 593–612, doi:10.1109/JPROC.2016.2625098.
21. Moylan, S.; Whinton, E.; Lane, B.; Slotwinski, J. Infrared thermography for laser-based powder bed fusion additive manufacturing processes. *AIP Conf. Proc.* **2014**, *1581* 33, 1191–1196, doi:10.1063/1.4864956.
22. Yap, C.Y.; Chua, C.K.; Dong, Z.L.; Liu, Z.H.; Zhang, D.Q.; Loh, L.E.; Sing, S.L. Review of selective laser melting: Materials and applications. *Appl. Phys. Rev.* **2015**, *2*, doi:10.1063/1.4935926.
23. Delgado, J.; Ciurana, J.; Rodríguez, C.A. Influence of process parameters on part quality and mechanical properties for DMLS and SLM with iron-based materials. *Int. J. Adv. Manuf. Technol.* **2012**, *60*, 601–610, doi:10.1007/s00170-011-3643-5.
24. Körner, C. Additive manufacturing of metallic components by selective electron beam melting - A review. *Int. Mater. Rev.* **2016**, *61*, 361–377, doi:10.1080/09506608.2016.1176289.
25. Bauereiß, A.; Scharowsky, T.; Körner, C. Defect generation and propagation mechanism during additive manufacturing by selective beam melting. *J. Mater. Process. Technol.* **2014**, *214*, 2522–2528, doi:10.1016/j.jmatprotec.2014.05.002.
26. Edwards, P.; O’Conner, A.; Ramulu, M. Electron beam additive manufacturing of titanium components: Properties and performance. *J. Manuf. Sci. Eng.* **2013**, *135*, 1–7, doi:10.1115/1.4025773.
27. Kruth, J.P.; Froyen, L.; Van Vaerenbergh, J.; Mercelis, P.; Rombouts, M.; Lauwers, B. Selective laser melting of iron-based powder. *J. Mater. Process. Technol.* **2004**, *149*, 616–622, doi:10.1016/j.jmatprotec.2003.11.051.
28. Mellin, P.; Jönsson, C.; Åkermo, M.; Fernberg, P.; Nordenberg, E.; Brodin, H.; Strondl, A. Nano-sized by-products from metal 3D printing, composite manufacturing and fabric production. *J. Clean. Prod.* **2016**, *139*, 1224–1233, doi:10.1016/j.jclepro.2016.08.141.
29. Elliott, A.; Alsalihi, S.; Merriman, A.L.; Basti, M.M. Infiltration of nanoparticles into porous binder jet printed parts. *Am. J. Eng. Appl. Sci.* **2016**, *9*, 128–133,

- doi:10.3844/ajeassp.2016.128.133.
30. Zhang, Y.; Jarosinski, W.; Jung, Y.G.; Zhang, J. *Additive manufacturing processes and equipment*; Elsevier Inc., **2018**; ISBN 9780128121559.
 31. Bento, J.B.; Lopez, A.; Pires, I.; Quintino, L.; Santos, T.G. Non-destructive testing for wire + arc additive manufacturing of aluminium parts. *Addit. Manuf.* **2019**, *29*, 100782, doi:10.1016/j.addma.2019.100782.
 32. Dass, A.; Moridi, A. State of the Art in Directed Energy Deposition : From. *Coatings* **2019**, *9*, 1–26.
 33. Sing, S.L.; Tey, C.F.; Tan, J.H.K.; Huang, S.; Yeong, W.Y. *3D printing of metals in rapid prototyping of biomaterials: Techniques in additive manufacturing*; Second Edi.; Elsevier Ltd., 2019; ISBN 9780081026632.
 34. Optomec Aerosol Jet Technology Available online: <https://optomec.com/printed-electronics/aerosol-jet-technology> (accessed on Sep 2, 2022).
 35. Sciaky Make Metal Parts Faster & Cheaper with EBAM® Metal 3D Printing Technology Available online: <https://www.sciaky.com/additive-manufacturing/electron-beam-additive-manufacturing-technology> (accessed on Sep 2, 2022).
 36. Petráčková, K.; Kondás, J.; Guagliano, M. Mechanical Performance of Cold-Sprayed A357 Aluminum Alloy Coatings for Repair and Additive Manufacturing. *J. Therm. Spray Technol.* **2017**, *26*, 1888–1897, doi:10.1007/s11666-017-0643-5.
 37. Frazier, W.E. Metal additive manufacturing: A review. *J. Mater. Eng. Perform.* **2014**, *23*, 1917–1928, doi:10.1007/s11665-014-0958-z.
 38. Bauer, J.; Systems, P.; Malone, P. Cost Estimating Challenges in Additive Manufacturing. *ICEAA Conference* **2015**, 1–8.
 39. Arrizubieta, J. I; Ukar, O.; Ostolaza, M.; Mugica, A. Study of the Environmental Implications of Using Its Handling. *Metals.* **2020**, *10*, 261.
 40. Vafadar, A.; Guzzomi, F.; Rassau, A.; Hayward, K. Advances in metal additive manufacturing: A review of common processes, industrial applications, and current challenges. *Appl. Sci.* **2021**, *11*, 1–33, doi:10.3390/app11031213.
 41. Brischetto, S.; Torre, R. Tensile and compressive behavior in the experimental tests for pla specimens produced via fused deposition modelling technique. *J. Compos. Sci.* **2020**, *4*, doi:10.3390/jcs4030140.
 42. Syrlybayev, D.; Zharylkassyn, B.; Seisekulova, A.; Akhmetov, M.; Perveen, A.; Talamona, D. Optimisation of strength properties of FDM printed parts—A critical review. *Polymers.* **2021**, *13*, doi:10.3390/polym13101587.
 43. Özen, A.; Auhl, D.; Völlmecke, C.; Kiendl, J.; Abali, B.E. Optimization of manufacturing parameters and tensile specimen geometry for fused deposition modeling (Fdm) 3d-printed petg. *Materials.* **2021**, *14*, doi:10.3390/ma14102556.
 44. Chalgham, A.; Ehrmann, A.; Wickenkamp, I. Mechanical properties of FDM

- printed PLA parts before and after thermal treatment. *Polymers*. **2021**, *13*, doi:10.3390/polym13081239.
45. Agarwal, K.; Kuchipudi, S.K.; Girard, B. Mechanical properties of fiber reinforced polymer composites: A comparative study of conventional and additive manufacturing methods. *J. Compos. Mater.* **2018**, *Vol. 52(23)*, 3173–3181, doi:10.1177/0021998318762297.
 46. Der Klift, F. Van; Koga, Y.; Todoroki, A.; Ueda, M.; Hirano, Y.; Matsuzaki, R. 3D Printing of Continuous Carbon Fibre Reinforced Thermo-Plastic (CFRTP) Tensile Test Specimens. *Open J. Compos. Mater.* **2016**, *06*, 18–27, doi:10.4236/ojcm.2016.61003.
 47. Hwang, S.; Reyes, E.I.; Moon, K.; Rumpf, R.C.; Kim, N.S. Thermo-mechanical Characterization of Metal/Polymer Composite Filaments and Printing Parameter Study for Fused Deposition Modeling in the 3D Printing Process. *J. Electron. Mater.* **2015**, *44*, 771–777, doi:10.1007/s11664-014-3425-6.
 48. Ryder, M.A.; Lados, D.A.; Iannacchione, G.S.; Peterson, A.M. Fabrication and properties of novel polymer-metal composites using fused deposition modeling. *Compos. Sci. Technol.* **2018**, *158*, 43–50, doi:10.1016/j.compscitech.2018.01.049.
 49. Masood, S.H.; Song, W.Q. Development of new metal/polymer materials for rapid tooling using Fused deposition modelling. *Mater. Des.* **2004**, *25*, 587–594, doi:10.1016/j.matdes.2004.02.009.
 50. Napibour, M.; Akhouni, B.; Saed, A.B. Manufacturing of polymer / metal composites by fused deposition modeling process with polyethylene. **2019**, *48717*, 1–9, doi:10.1002/app.48717.
 51. Fafenrot, S.; Grimmelsmann, N.; Wortmann, M.; Ehrmann, A. Three-dimensional (3D) printing of polymer-metal hybrid materials by fused deposition modeling. *Materials*. **2017**, *10*, doi:10.3390/ma10101199.
 52. Oliveira, R.V.B.; Soldi, V.; Fredel, M.C.; Pires, A.T.N. Ceramic injection moulding: Influence of specimen dimensions and temperature on solvent debinding kinetics. *J. Mater. Process. Technol.* **2005**, *160*, 213–220, doi:10.1016/j.jmatprotec.2004.06.008.
 53. Gonzalez-Gutierrez, J.; Beulke, G.; Emri, I. Powder Injection Molding of Metal and Ceramic Parts. *Some Crit. Issues Inject. Molding* **2012**, doi:10.5772/38070.
 54. Cruz, N.; Santos, L.; Vasco, J.; Barreiros, F.M. Binder System for Fused Deposition of Metals. In Proceedings of the Proceedings of the Euro PM2013; Gothenburg, **2013**; pp. 79–84.
 55. Suwanprecha, C.; Manonukul, A. A Review on Material Extrusion Additive Manufacturing of Metal and How It Compares with Metal Injection Moulding. *Metals*. **2022**, *12*, 429, doi:10.3390/met12030429.
 56. Singh, G.; Missiaen, J.M.; Bouvard, D.; Chaix, J.M. Additive manufacturing of 17–4 PH steel using metal injection molding feedstock: Analysis of 3D extrusion printing, debinding and sintering. *Addit. Manuf.* **2021**, *47*,

doi:10.1016/j.addma.2021.102287.

57. Bellini, A.; Shor, L.; Guceri, S.I. New developments in fused deposition modeling of ceramics. *Rapid Prototyp. J.* **2005**, *11*, 214–220, doi:10.1108/13552540510612901.
58. Singh, G.; Missiaen, J.M.; Bouvard, D.; Chaix, J.M. Copper additive manufacturing using MIM feedstock: adjustment of printing, debinding, and sintering parameters for processing dense and defectless parts. *Int. J. Adv. Manuf. Technol.* **2021**, *115*, 449–462, doi:10.1007/s00170-021-07188-y.
59. Clemens Lieberwirth; Arne Harder; Hermann Seitz Extrusion Based Additive Manufacturing of Metal Parts. *J. Mech. Eng. Autom.* **2017**, *7*, 79–83, doi:10.17265/2159-5275/2017.02.004.
60. Giberti, H.; Strano, M.; Annoni, M. An innovative machine for Fused Deposition Modeling of metals and advanced ceramics. *MATEC Web Conf.* **2016**, *43*, doi:10.1051/matecont/20164303003.
61. Gonzalez-Gutierrez, J.; Guráñ, R.; Spoerk, M.; Holzer, C.; Godec, D.; Kukla, C. 3D printing conditions determination for feedstock used in fused filament fabrication (FFF) of 17-4PH stainless steel parts. *Metallurgija* **2018**, *57*, 117–120.
62. McNulty, T.F.; Mohammadi, F.; Bandyopadhyay, A.; Shanefield, D.J.; Danforth, S.C.; Safari, A. Development of a binder formulation for fused deposition of ceramics. *Rapid Prototyp. J.* **1998**, *4*, 144–150, doi:10.1108/13552549810239012.
63. Manonukul, A.; Songkuea, S.; Moonchaleanporn, P.; Tange, M. Effect of weld line positions on the tensile deformation of two-component metal injection moulding. *Int. J. Miner. Metall. Mater.* **2017**, *24*, 1384–1393, doi:10.1007/s12613-017-1531-1.
64. Huang, M.S.; Hsu, H.C. Effect of backbone polymer on properties of 316L stainless steel MIM compact. *J. Mater. Process. Technol.* **2009**, *209*, 5527–5535, doi:10.1016/j.jmatprotec.2009.05.011.
65. Heaney, D.F.; Mueller, T.W.; Davies, P.A. Mechanical properties of metal injection moulded 316L stainless steel using both prealloy and master alloy techniques. *Powder Metall.* **2004**, *47*, 367–373, doi:10.1179/003258904225020855.
66. Wu, G.; Langrana, N.A.; Sadanji, R.; Danforth, S. Solid freeform fabrication of metal components using fused deposition of metals. *Mater. Des.* **2002**, *23*, 97–105, doi:10.1016/s0261-3069(01)00079-6.
67. Kukla, C.; Gonzalez-Gutierrez, J.; Cano, S.C.; Holzer, C. Fused Filament Fabrication (FFF) of PIM Feedstocks. In Proceedings of the VI CONGRESO NACIONAL DE PULVIMETALURGIA Y I CONGRESO IBEROAMERICANO DE PULVIMETALURGIA; Ciudad Real, Spain, **2017**; p. 6.
68. Cano, S.; Gonzalez-Gutierrez, J.; Sapkota, J.; Spoerk, M.; Arbeiter, F.; Schuschnigg, S.; Holzer, C.; Kukla, C. Additive manufacturing of zirconia parts by fused filament fabrication and solvent debinding: Selection of binder

- formulation. *Addit. Manuf.* **2019**, 26, 117–128, doi:10.1016/j.addma.2019.01.001.
69. Bhat, V.V.; Geetha, K.; Das, R.N.; Gurumoorthy, B.; Umarji, A.M. Characterization of Polyolefin-Aluminacompounded mix for FDC processing. In Proceedings of the Proceedings of the Solid Freeform Fabrication Symposium; Austin, TX, USA, **2000**.
 70. Kukla, C.; Gonzalez-Gutierrez, J.; Duretek, I.; Schuschnigg, S.; Holzer, C. Effect of particle size on the properties of highly-filled polymers for fused filament fabrication. *AIP Conf. Proc.* **2017**, 1914, 2–6, doi:10.1063/1.5016795.
 71. Singh, P.; Balla, V.K.; Tofangchi, A.; Atre, S. V.; Kate, K.H. Printability studies of Ti-6Al-4V by metal fused filament fabrication (MF3). *Int. J. Refract. Met. Hard Mater.* **2020**, 91, 105249, doi:10.1016/j.ijrmhm.2020.105249.
 72. Jamaludin, K.R.; Muhamad, N.; Rahman, M.N.A.; Amin, S.Y.M.; Ismail, M.H.; Murtadhahadi Particle Size and Injection Temperature Effect on the injection Molding of SS316L Powder. *J. Mech. Eng.* **2008**, 5, 59–71.
 73. Gonzalez-Gutierrez, J.; Duretek, I.; Holzer, C.; Arbeiter, F.; Kukla, C. Filler Content and Properties of Highly Filled Filaments for Fused Filament Fabrication of Magnets. In Proceedings of the Proceedings of the ANTEC 2017; Society of Plastics Engineers, Ed.; Anaheim, CA, USA, **2017**; pp. 1–4.
 74. Rane, K.; Di Landro, L.; Strano, M. Processability of SS316L powder - binder mixtures for vertical extrusion and deposition on table tests. *Powder Technol.* **2019**, 345, 553–562, doi:10.1016/j.powtec.2019.01.010.
 75. Singh, P.; Balla, V.K.; Atre, S. V.; German, R.M.; Kate, K.H. Factors affecting properties of Ti-6Al-4V alloy additive manufactured by metal fused filament fabrication. *Powder Technol.* **2021**, 386, 9–19, doi:10.1016/j.powtec.2021.03.026.
 76. Abel, J.; Scheithauer, U.; Janics, T.; Hampel, S.; Cano, S.; Müller-Köhn, A.; Günther, A.; Kukla, C.; Moritz, T. Fused filament fabrication (FFF) of metal-ceramic components. *J. Vis. Exp.* **2019**, 2019, 1–13, doi:10.3791/57693.
 77. Gonzalez-Gutierrez, J.; Godec, D.; Kukla, C.; Schlauf, T.; Burkhardt, C.; Holzer, C. Shaping , Debinding and Sintering of Steel Components Via Fused Filament Fabrication. *16th Int. Sci. Conf. Prod. Eng. - CIM2017* **2017**.
 78. Lengauer, W.; Duretek, I.; Fürst, M.; Schwarz, V.; Gonzalez-Gutierrez, J.; Schuschnigg, S.; Kukla, C.; Kitzmantel, M.; Neubauer, E.; Lieberwirth, C.; et al. Fabrication and properties of extrusion-based 3D-printed hardmetal and cermet components. *Int. J. Refract. Met. Hard Mater.* **2019**, 82, 141–149, doi:10.1016/j.ijrmhm.2019.04.011.
 79. Riecker, S.; Hein, S.B.; Studnitzky, T.; Andersen, O.; Kieback, B. 3D printing of metal parts by means of fused filament fabrication - A non beam-based approach. *Proc. Euro PM 2017 Int. Powder Metall. Congr. Exhib.* **2017**.
 80. Fallon, J.J.; McKnight, S.H.; Bortner, M.J. Highly loaded fiber filled polymers for material extrusion: A review of current understanding. *Addit. Manuf.* **2019**, 30, 100810, doi:10.1016/j.addma.2019.100810.

81. Gonzalez-Gutierrez, J.; Godec, D.; Kukla, C.; Schlauf, T.; Burkhardt, C.; Holzer Gonzalez-Gutierrez, C.J.; Leoben, M.; Glöckel-Straße, O.; Ass Godec, L.D.; Kukla, mont C.; et al. Shaping, Debinding and Sintering of Steel Components via Fused Filament Fabrication. *16 th Int. Sci. Conf. Prod. Eng.* **2017**, 8–10.
82. Thompson, Y.; Gonzalez-Gutierrez, J.; Kukla, C.; Felfer, P. Fused filament fabrication, debinding and sintering as a low cost additive manufacturing method of 316L stainless steel. *Addit. Manuf.* **2019**, 30, 100861, doi:10.1016/j.addma.2019.100861.
83. Spoerk, M.; Gonzalez-Gutierrez, J.; Sapkota, J.; Schuschnigg, S.; Holzer, C. Effect of the printing bed temperature on the adhesion of parts produced by fused filament fabrication. *Plast. Rubber Compos.* **2018**, 47, 17–24, doi:10.1080/14658011.2017.1399531.
84. Solomon, I.J.; Sevel, P.; Gunasekaran, J. A review on the various processing parameters in FDM. *Mater. Today Proc.* **2020**, 37, 509–514, doi:10.1016/j.matpr.2020.05.484.
85. Singh, G.; Missiaen, J.M.; Bouvard, D.; Chaix, J.M. Copper extrusion 3D printing using metal injection moulding feedstock: Analysis of process parameters for green density and surface roughness optimization. *Addit. Manuf.* **2021**, 38, 101778, doi:10.1016/j.addma.2020.101778.
86. Shaikh, M.Q.; Lavertu, P.Y.; Kate, K.H.; Atre, S. V. Process Sensitivity and Significant Parameters Investigation in Metal Fused Filament Fabrication of Ti-6Al-4V. *J. Mater. Eng. Perform.* **2021**, 30, 5118–5134, doi:10.1007/s11665-021-05666-8.
87. Godec, D.; Cano, S.; Holzer, C. Optimization-of-the-3D-printing-parameters-for-tensile-properties-of-specimens-produced-by-fused-filament-fabrication-of-174PH-stainless-steel2020MaterialsOpen-Access.pdf. **2020**.
88. Onwubolu, G.C.; Rayegani, F. Characterization and Optimization of Mechanical Properties of ABS Parts Manufactured by the Fused Deposition Modelling Process. *Int. J. Manuf. Eng.* **2014**, 2014, 1–13, doi:10.1155/2014/598531.
89. Liu, Z.; Lei, Q.; Xing, S. Mechanical characteristics of wood, ceramic, metal and carbon fiber-based PLA composites fabricated by FDM. *J. Mater. Res. Technol.* **2019**, 8, 3743–3753, doi:10.1016/j.jmrt.2019.06.034.
90. Iyer, S.; Mcintosh, J.; Bandyopadhyay, A.; Langrana, N.; Safari, A.; Danforth, S.C.; Clancy, R.B.; Gasdaska, C.; Whalen, P.J. Microstructural characterization and mechanical properties of Si₃N₄ formed by fused deposition of ceramics. *Int. J. Appl. Ceram. Technol.* **2008**, 5, 127–137, doi:10.1111/j.1744-7402.2008.02193.x.
91. Gonzalez-Gutierrez, J.; Cano, S.; Schuschnigg, S.; Kukla, C.; Sapkota, J.; Holzer, C. Additive manufacturing of metallic and ceramic components by the material extrusion of highly-filled polymers: A review and future perspectives. *Materials.* **2018**, 11, doi:10.3390/ma11050840.
92. Gonzalez-Gutierrez, J.; Beulke, G.; Emri, I. Powder Injection Molding of Metal

- and Ceramic Parts. *Some Crit. Issues Inject. Molding* **2012**, doi:10.5772/38070.
93. Kankawa, Y. Effects of polymer decomposition behavior on thermal debinding process in metal injection molding. *Mater. Manuf. Process.* **1997**, *12*, 681–690, doi:10.1080/10426919708935175.
 94. Andersen, O.; Riecker, S.; Studnitzky, T.; Hein, S.; Lohse, U.; Kieback, B. Manufacturing and properties of metal parts made by fused filament fabrication. *Euro PM 2018 Congr. Exhib.* **2020**.
 95. Dos Santos, M.A., Neivock, M.P., Maliska, A.M., Klein, A.N. & Muzart, J.L.R. Plasma debinding and pre-sintering of injected parts. *Mater. Res.* **2004**, *7*, 505–511.
 96. Zhang, Y.; Bai, S.; Riede, M.; Garratt, E.; Roch, A. A comprehensive study on fused filament fabrication of Ti-6Al-4V structures. *Addit. Manuf.* **2020**, *34*, 101256, doi:10.1016/j.addma.2020.101256.
 97. Burkhardt, C.; Freigassner, P.; Weber, O.; Imgrund, P.; Hampel, S. Fused filament fabrication (FFF) of 316L green parts for the MIM process. *World PM 2016 Congr. Exhib.* **2016**, *1*.
 98. Singh, G.; Missiaen, J.M.; Bouvard, D.; Chaix, J.M. Additive manufacturing of 17–4 PH steel using metal injection molding feedstock: Analysis of 3D extrusion printing, debinding and sintering. *Addit. Manuf.* **2021**, *47*, 102287, doi:10.1016/j.addma.2021.102287.
 99. Singh, G.; Missiaen, J.M.; Bouvard, D.; Chaix, J.M. Copper extrusion 3D printing using metal injection moulding feedstock: Analysis of process parameters for green density and surface roughness optimization. *Addit. Manuf.* **2021**, *38*, 101778, doi:10.1016/j.addma.2020.101778.
 100. Rane, K.; Cataldo, S.; Parenti, P.; Sbaglia, L.; Mussi, V.; Annoni, M.; Giberti, H.; Strano, M. Rapid production of hollow SS316 profiles by extrusion based additive manufacturing. *AIP Conf. Proc.* **2018**, *1960*, doi:10.1063/1.5035006.
 101. Clemens, F. Thermoplastic Extrusion for Ceramic Bodies BT - Extrusion in Ceramics. In; Händle, F., Ed.; Springer Berlin Heidelberg: Berlin, Heidelberg, **2007**; pp. 295–311 ISBN 978-3-540-27102-4.
 102. Goyer, N.; Bégin, D.; Beaudry, C.; Bouchard, M.; Carrier, G.; Lavoué, J.; Noisel, N.; Gérin, M. *Prevention guide - Formaldehyde in the workplace*; **2006**; ISBN 9782896310685.
 103. Torralba, J.M.; Hidalgo, J.; Jiménez-Morales, A. Powder injection moulding: Processing of small parts of complex shape. *Int. J. Microstruct. Mater. Prop.* **2013**, *8*, 87–96, doi:10.1504/IJMMP.2013.052648.
 104. Thompson, Y.; Gonzalez-gutierrez, J.; Kukla, C.; Felfer, P. Fused filament fabrication, debinding and sintering as a low cost additive manufacturing method of 316L stainless steel. *Addit. Manuf.* **2019**, *30*, 100861, doi:10.1016/j.addma.2019.100861.
 105. Mousapour, M.; Salmi, M.; Klemettinen, L.; Partanen, J. Feasibility study of

- producing multi-metal parts by Fused Filament Fabrication (FFF) technique. *J. Manuf. Process.* **2021**, *67*, 438–446, doi:10.1016/j.jmapro.2021.05.021.
106. German Rand *Metal AM.* **2021**, pp. 127–139.
 107. R. F. Wang, R.F.; Wu, Y. X.; Zhou, X.; Tang, A.C. Debinding and Sintering Processes for Injection Molded Pure Titanium. *Powder Metall. Technol.* **2006**, *24*, 83–93.
 108. A. Bose, I. Otsuka, T. Yoshida, H.; Toyoshima Metal Injection Molding of Ultrafine 316L Stainless Steel Powders. *Adv. Powder Metall. Part. Mater.* **2007**.
 109. R. M. German *Sintering: From Empirical Observations to Scientific Principles*; Elsevier: Oxford, UK, **2014**; ISBN 9780124016828.
 110. G. J. Shu, K. S. Hwang, Y.T.P. Improvements in Sintered Density and Dimensional Stability of Powder Injection Molded 316L Compacts by Adjusting the Alloying Composition. *Acta Mater.* **2006**, *54*, 1335–1342.
 111. Boljanovic, V. Powder metallurgy. In *Metal Shaping Processes: Casting and Molding, Particulate Processing, Deformation Processes, Metal Removal*; Industrial Press Inc.: New York, USA, **2010**; pp. 75–106 ISBN 9780831 133801.
 112. COMPANY, S.S. Specification Sheet : Alloy 316 / 316L. **2014**, 9–11.
 113. Stainless Steel - Grade 316L - Properties , Fabrication and Applications (UNS S31603). **2004**, 2–5.
 114. Gong, H.; Snelling, D.; Kardel, K.; Carrano, A. Comparison of Stainless Steel 316L Parts Made by FDM- and SLM-Based Additive Manufacturing Processes. *Jom* **2019**, *71*, 880–885, doi:10.1007/s11837-018-3207-3.
 115. Kurose, T.; Abe, Y.; Santos, M.V.A.; Kanaya, Y.; Ishigami, A.; Tanaka, S.; Ito, H. Influence of the Layer Directions on the Properties of 316L Stainless Steel Parts Fabricated through Fused Deposition of Metals. *Materials* **2020**, *13*(11), 2493, doi: 10.3390/ma13112493.
 116. Liu, B.; Wang, Y.; Lin, Z.; Zhang, T. Creating metal parts by Fused Deposition Modeling and Sintering. *Mater. Lett.* **2020**, *263*, 127252, doi:10.1016/j.matlet.2019.127252.
 117. Ait-Mansour, I.; Kretschmar, N.; Chekurov, S.; Salmi, M.; Rech, J. Design-dependent shrinkage compensation modeling and mechanical property targeting of metal FFF. *Prog. Addit. Manuf.* **2020**, *5*, 51–57, doi:10.1007/s40964-020-00124-8.
 118. Damon, J.; Dietrich, S.; Gorantla, S.; Popp, U.; Okolo, B.; Schulze, V. Process porosity and mechanical performance of fused filament fabricated 316L stainless steel. *Rapid Prototyp. J.* **2019**, *25*, 1319–1327, doi:10.1108/RPJ-01-2019-0002.
 119. Caminero, M.Á.; Romero, A.; Chacón, J.M.; Núñez, P.J.; García-Plaza, E.; Rodríguez, G.P. Additive manufacturing of 316L stainless-steel structures using fused filament fabrication technology: mechanical and geometric properties. *Rapid Prototyp. J.* **2021**, *27*, 583–591, doi:10.1108/RPJ-06-2020-0120.

120. Wang, Y.; Zhang, L.; Li, X.; Yan, Z. On hot isostatic pressing sintering of fused filament fabricated 316L stainless steel – Evaluation of microstructure , porosity , and tensile properties. *Mater. Lett.* **2021**, *296*, 129854, doi:10.1016/j.matlet.2021.129854.
121. Ömer Faruk MURATHAN Heat Treatment and Surface Hardening of Materials - Heat Treatment of 17-4 PH Stainless Steel.
122. Gratton, A. Comparison of Mechanical , Metallurgical Properties of 17-4PH Stainless Steel between Direct Metal Laser Sintering (DMLS) and Traditional Manufacturing Methods. *Proc. Natl. Conf. Undergrad. Res.* **2012**, 423–431.
123. ATI 17-4TM Precipitation Hardening Stainless Steel. **2016**, *1*, 1–7.
124. Suwanpreecha, C.; Seensattayawong, P.; Vadhanakovint, V.; Manonukul, A. Influence of Specimen Layout on 17-4PH (AISI 630) Alloys Fabricated by Low-Cost Additive Manufacturing. *Metall. Mater. Trans. A Phys. Metall. Mater. Sci.* **2021**, *52*, 1999–2009, doi:10.1007/s11661-021-06211-x.
125. Abe, Y.; Kurose, T.; Santos, M.V.A.; Kanaya, Y.; Ishigami, A.; Tanaka, S.; Ito, H. Effect of layer directions on internal structures and tensile properties of 17-4ph stainless steel parts fabricated by fused deposition of metals. *Materials.* **2021**, *14*, 1–12, doi:10.3390/ma14020243.
126. Condruz, M.R.; Paraschiv, A.; Puscasu, C. Heat Treatment Influence on Hardness and Microstructure of Adam Manufactured 17-4 Ph. *Turbo* **2018**, *V*, 4–11.
127. Gonzalez-Gutierrez, J.; Arbeiter, F.; Schlauf, T.; Kukla, C.; Holzer, C. Tensile properties of sintered 17-4PH stainless steel fabricated by material extrusion additive manufacturing. *Mater. Lett.* **2019**, *248*, 165–168, doi:10.1016/j.matlet.2019.04.024.
128. Henry, T.C.; Morales, M.A.; Cole, D.P.; Shumeyko, C.M.; Riddick, J.C. Mechanical behavior of 17-4 PH stainless steel processed by atomic diffusion additive manufacturing. *Int. J. Adv. Manuf. Technol.* **2021**, *114*, 2103–2114, doi:10.1007/s00170-021-06785-1.
129. Suwanpreecha, C.; Manonukul, A. On the build orientation effect in as-printed and as-sintered bending properties of 17-4PH alloy fabricated by metal fused filament fabrication. **2022**, *6*, 1076–1085, doi:10.1108/RPJ-07-2021-0174.
130. Ponnusamy, P.; Masood, S.H.; Ruan, D.; Palanisamy, S.; Rahman Rashid, R.A.; Mohamed, O.A. Mechanical performance of selective laser melted 17-4 PH stainless steel under compressive loading. *Solid Free. Fabr. 2017 Proc. 28th Annu. Int. Solid Free. Fabr. Symp. - An Addit. Manuf. Conf. SFF 2017* **2020**, 321–331.
131. Alkindi, T.; Alyammahi, M.; Susantyoko, R.A.; Atatreh, S.; Dewa, R.; Electricity, D. The effect of varying specimens ' printing angles to the bed surface on the tensile strength of 3D - printed 17 - 4PH stainless - steels via metal FFF additive manufacturing. *MRS Commun.* **2021**, *11*, 310–316, doi:10.1557/s43579-021-00040-0.
132. Chung, C.Y.; Tzeng, Y.C. Effects of aging treatment on the precipitation behavior

- of ϵ -Cu phase and mechanical properties of metal injection molding 17-4PH stainless steel. *Mater. Lett.* **2019**, *237*, 228–231, doi:10.1016/j.matlet.2018.11.107.
133. Bouaziz, M.A.; Djouda, J.M.; Chemkhi, M.; Rambaudon, M.; Kauffmann, J.; Hild, F. Heat treatment effect on 17-4PH stainless steel manufactured by Atomic Diffusion Additive Manufacturing (ADAM). *Procedia CIRP* **2021**, *104*, 935–938, doi:10.1016/j.procir.2021.11.157.
 134. Chemkhi, M.; Djouda, J.M.; Bouaziz, M.A.; Kauffmann, J.; Hild, F.; Reiraint, D. Effects of Mechanical Post-Treatments on Additive Manufactured 17-4PH Stainless Steel Produced by Bound Powder Extrusion. *Procedia CIRP* **2021**, *104*, 957–961, doi:10.1016/j.procir.2021.11.161.
 135. ASTM F3122-14. *ASTM Int.* **2014**, *10.04*, 6.
 136. Quarto, M.; Carminati, M.; D'Urso, G. Density and shrinkage evaluation of AISI 316L parts printed via FDM process. *Mater. Manuf. Process.* **2021**, 1–9, doi:10.1080/10426914.2021.1905830.
 137. ISO 6892-1:2020. *Int. Stand.* **2020**.
 138. ASTM E9:2019 - Standard Test Methods of Compression Testing of Metallic Materials at Room Temperature. *ASTM Int.* **2019**, *03.01*.
 139. ISO 148 - 1:2016 - Metallic materials - Charpy pendulum impact test. *Int. Stand.* **2016**.
 140. ISO 7438:2020 - Metallic materials - Bend test. *Int. Stand.* **2020**.
 141. ISO 6508-1:2016 - Metallic materials - Rockwell hardness test method. *Int. Stand.* **2016**.
 142. ISO 6507-1:2018 - Metallic materials - Vickers hardness test method. *Int. Stand.* **2018**.
 143. ASTM A666 - 15: Standard Specification for Annealed or Cold-Worked Austenitic Stainless Steel Sheet, Strip, Plate, and Flat Bar. *Int. Stand.* **2016**.
 144. Rosnitschek, T.; Tremmel, S.; Seefeldt, A.; Alber-Laukant, B.; Neumeyer, T.; Altstädt, V. Correlations of geometry and infill degree of extrusion additively manufactured 316L stainless steel components. *Materials.* **2021**, *14*, doi:10.3390/ma14185173.
 145. MatWeb Available online: <http://www.matweb.com/search/DataSheet.aspx?MatGUID=a2d0107bf958442e9f8db6dc9933fe31>.
 146. Dadfar, M.; Fathi, M.H.; Karimzadeh, F.; Dadfar, M.R.; Saatchi, A. Effect of TIG welding on corrosion behavior of 316L stainless steel. *Mater. Lett.* **2007**, *61*, 2343–2346, doi:10.1016/j.matlet.2006.09.008.
 147. Ziętała, M.; Durejko, T.; Polański, M.; Kuncze, I.; Płociński, T.; Zieliński, W.; Łazińska, M.; Stępniewski, W.; Czujko, T.; Kurzydłowski, K.J.; et al. The microstructure, mechanical properties and corrosion resistance of 316 L stainless

- steel fabricated using laser engineered net shaping. *Mater. Sci. Eng. A* **2016**, *677*, 1–10, doi:10.1016/j.msea.2016.09.028.
148. Martínez-Frutos, J.; Allaire, G.; Dapogny, C.; Periago, F. Structural optimization under internal porosity constraints using topological derivatives. *Comput. Methods Appl. Mech. Eng.* **2019**, *345*, 1–25, doi:10.1016/j.cma.2018.10.036.
 149. Al-Maharma, A.Y.; Patil, S.P.; Markert, B. Effects of porosity on the mechanical properties of additively manufactured components: a critical review. *Mater. Res. Express* **2020**, *7*, doi:10.1088/2053-1591/abcc5d.
 150. Campbell, J.E.; Thompson, R.P.; Dean, J.; Clyne, T.W. Comparison between stress-strain plots obtained from indentation plastometry, based on residual indent profiles, and from uniaxial testing. *Acta Mater.* **2019**, *168*, 87–99, doi:10.1016/j.actamat.2019.02.006.
 151. Sert, E.; Hitzler, L.; Hafenstein, S.; Merkel, M.; Werner, E.; Öchsner, A. Tensile and compressive behaviour of additively manufactured AlSi10Mg samples. *Prog. Addit. Manuf.* **2020**, *5*, 305–313, doi:10.1007/s40964-020-00131-9.
 152. Turner, B.N.; Gold, S.A. A review of melt extrusion additive manufacturing processes: II. Materials, dimensional accuracy, and surface roughness. *Rapid Prototyp. J.* **2015**, *21*, 250–261, doi:10.1108/RPJ-02-2013-0017.
 153. Jagenteufel, R.; Hofstaetter, T.; Kamleitner, F.; B. Pedersen, D.; Tosello, G.; N. Hansen, H. Rheology of high melt strength polypropylene for additive manufacturing. *Adv. Mater. Lett.* **2017**, *8*, 712–716, doi:10.5185/amlett.2017.1450.
 154. Beran, T.; Mulholland, T.; Henning, F.; Rudolph, N.; Osswald, T.A. Nozzle clogging factors during fused filament fabrication of spherical particle filled polymers. *Addit. Manuf.* **2018**, *23*, 206–214, doi:10.1016/j.addma.2018.08.009.
 155. Loh, G.H.; Pei, E.; Gonzalez-Gutierrez, J.; Monzón, M. An overview of material extrusion troubleshooting. *Appl. Sci.* **2020**, *10*, doi:10.3390/app10144776.
 156. Oleff, A.; Küster, B.; Stonis, M.; Overmeyer, L. Process monitoring for material extrusion additive manufacturing: a state-of-the-art review. *Prog. Addit. Manuf.* **2021**, *6*, 705–730, doi:10.1007/s40964-021-00192-4.
 157. Zhang, Z.; Fidan, I. Failure detection of fused filament fabrication via deep learning. *Solid Free. Fabr. 2019 Proc. 30th Annu. Int. Solid Free. Fabr. Symp. - An Addit. Manuf. Conf. SFF 2019* **2019**, 2156–2164.
 158. Choo, K.; Friedrich, B.; Daugherty, T.; Schmidt, A.; Patterson, C.; Abraham, M.A.; Conner, B.; Rogers, K.; Cortes, P.; MacDonald, E. Heat retention modeling of large area additive manufacturing. *Addit. Manuf.* **2019**, *28*, 325–332, doi:10.1016/j.addma.2019.04.014.
 159. Tlegenov, Y.; Hong, G.S.; Lu, W.F. Nozzle condition monitoring in 3D printing. *Robot. Comput. Integr. Manuf.* **2018**, *54*, 45–55, doi:10.1016/j.rcim.2018.05.010.
 160. Ye, Z.; Liu, C.; Tian, W.; Kan, C. A deep learning approach for the identification of small process shifts in additive manufacturing using 3D point clouds. **2020**, *48*,

770–775, doi:10.1016/j.promfg.2020.05.112.

161. Lin, W.; Shen, H.; Fu, J.; Wu, S. Online quality monitoring in material extrusion additive manufacturing processes based on laser scanning technology. *Precis. Eng.* **2019**, *60*, 76–84, doi:10.1016/j.precisioneng.2019.06.004.
162. Brammer, J.G.; Bridgwater, A. V. The influence of feedstock drying on the performance and economics of a biomass gasifier - Engine CHP system. *Biomass and Bioenergy* **2002**, *22*, 271–281, doi:10.1016/S0961-9534(02)00003-X.
163. Aboulkas, A.; El harfi, K.; El Bouadili, A. Thermal degradation behaviors of polyethylene and polypropylene. Part I: Pyrolysis kinetics and mechanisms. *Energy Convers. Manag.* **2010**, *51*, 1363–1369, doi:10.1016/j.enconman.2009.12.017.
164. Carminati, M.; Quarto, M.; D'urso, G.; Giardini, C.; Maccarini, G. Mechanical Characterization of AISI 316L Samples Printed Using Material Extrusion. *Appl. Sci.* **2022**, *12*, doi:10.3390/app12031433.
165. Gong, H.; Crater, C.; Ordonez, A.; Ward, C.; Waller, M.; Ginn, C. Material Properties and Shrinkage of 3D Printing Parts using Ultrafuse Stainless Steel 316LX Filament. *MATEC Web Conf.* **2018**, *249*, 1–5, doi:10.1051/mateconf/201824901001.

• *List of figures*

Figure 1.1: Timeline of AM technology [2].	1
Figure 1.2 : Applications of Additive Manufacturing to the various sectors over the years [6].	3
Figure 1.3: comparison between the cost of complexity for additive and traditional technologies [8].	4
Figure 1.4: Steps of the generic 3D printing process.	7
Figure 1.5: Schematic of polymerization reaction [17].	12
Figure 1.6: Schematic of VAT system [19].	13
Figure 1.7: Schematic of ME system [20].	15
Figure 1.8: Schematic of a PBF system [21].	16
Figure 1.9: Schematic of a BJ system [16].	18
Figure 1.10: Schematic of a MJ system [16].	19
Figure 1.11: Schematic of SL system [16].	20
Figure 1.12: Schematic of ultrasonic consolidation [16].	21
Figure 1.13: Schematics of two DED systems (A) uses laser together with powder feedstock and (B) uses electron beam and wire feedstock [33].	22
Figure 2.1: Metal AM market in 2021 [40].	26
Figure 2.2: Stress – strain curves for ABS with copper particles (left) and with iron particles (right) [47].	27
Figure 2.3: Modulated Differential Scanning Calorimetry (MDSC) results for base ABS, and ABS-SS composites [48].	28
Figure 2.4: Stress – strain curves for Fe/Nylon samples with different infill compositions [49].	29
Figure 2.5: Flexural strength values for different metal contents [50].	30
Figure 2.6: Microscopic images of specimens after tensile tests, prepared from PLA (left); Magnetic Iron (middle); and Bronzefil (right) [51].	30
Figure 2.7: Schematic of screw-based feeding system [55].	32
Figure 2.8: Low and high magnification of the 17-4PH stainless steel granulated feedstock [56].	32
Figure 2.9: Schematic of plunger-based feeding system [55].	33
Figure 2.10: Set-up of combined plunger and filament based feeding system [60].	34

Figure 2.11: Schematic of filament-based feeding system [55].	34
Figure 2.12: Shear viscosity as a function of the angular frequency for different binder systems measured at 150 °C [68].	37
Figure 2.13: Tensile properties of filaments made up of different binders: (A) Yield or ultimate tensile stress, (B) strain at yield or at the ultimate tensile stress, and (C) secant modulus [68].	38
Figure 2.14: Alloys utilised to fabricate 3D parts by material extrusion additive manufacturing processes [55].	39
Figure 2.15: ϵ - σ curves (top) and σ_{\max} and ϵ_b (bottom) for filaments loaded with different solid loadings [67].	40
Figure 2.16: Apparent viscosity (η), secant modulus (E) and elongation at break (ϵ_{br}) for filaments with different particle sizes [70].	41
Figure 2.17: Stress – strain curves for 316L and Fe ₁₂ O ₁₉ Sr 316L filaments with different solid loadings [73].	42
Figure 2.18: Apparent viscosity of SS316L feedstock having different solid loading [74].	43
Figure 2.19: Influence on mechanical properties of feedstock fabricated with different compounding methods (RM and TSE) [76].	44
Figure 2.20; Overall view and detail of the filaments filled with hardmetal powders [78].	45
Figure 2.21: Extruded filaments with good and scarce surface quality [79].	45
Figure 2.22: Effects of extrusion temperature on filament attributes: surface and bulk morphology and density [75].	46
Figure 2.23: Effects of extrusion temperature on filament diameter (left) and surface roughness (right) [75].	46
Figure 2.24: Force to overcome the pressure drop for fine powder (a) and coarse powder (b) [71]	47
Figure 2.25: Maximum extrudable viscosity as a function of flow rate and nozzle diameter [80].	47
Figure 2.26: Schematic representation of filament extrusion line equipped with a conveyor belt [81].	48

Figure 2.27: Effect of nozzle diameter and extrusion temperature (a) or solid loading (b) on diameter of vertically extruded wire [74].	49
Figure 2.28: Section of a highly filled filament with visible cavities [61]	49
Figure 2.29: Printing Trials with nozzle temperature 270 °C (a); nozzle temperature 290 °C (b); nozzle temperature 295 °C (c) [82].	50
Figure 2.30: Adhesion force of printed parts varying the bed temperature [83]	51
Figure 2.31: Effect of feed rate on the printed geometry as a function of the powder shape [71]	52
Figure 2.32: Effect of feed rate on the dimensional change with respect to the CAD file geometry (left) and printed part mass (right) [71].	52
Figure 2.33: Main effects plot of green density as a function of different process parameters [85].	53
Figure 2.34: SEM images of the samples fabricated with varying nozzle speed 20 and 100 mm/s (a and b) [85].	53
Figure 2.35: Print time with varying the layer thickness [86].	54
Figure 2.36: SEM images of the samples fabricated with varying layer thickness 0.05, 0.15 and 0.25 mm (a–c)[85].	54
Figure 2.37: 2D graph of the influence of layer thickness on tensile strength (a) and tensile modulus (b) (flow rate multiplier 110%, extrusion temperature 235 °C) [87].	55
Figure 2.38: Air gap between two adjacent depositions [88].	56
Figure 2.39: SEM images of the samples fabricated with varying extrusion multiplier 90% and 150% (a and b) [85].	56
Figure 2.40: Printing parameters affecting the quality of MF3 samples. The influence of extrusion multiplier affecting the surface quality of ME samples [75].	57
Figure 2.41: 2D graphs of the influence of flow rate multiplier on tensile strength (a) and tensile modulus (b) (extrusion temperature 235 °C, layer thickness 0.20 mm) [87].	57
Figure 2.42: Bottom (a), top (b) and side (c) views of printed parts printed with flow rate of 100% (top), 150% (middle) and 200% (bottom) [61].	58
Figure 2.43: Examples of different raster angles [89].	58
Figure 2.44: Schematic representation of warpage effects that result from: (a) 0° road vector strategy with all roads parallel, (b) 90° road vector strategy with all roads parallel, and (c) +45°/-45° vector strategy on alternating build layers [90].	59

Figure 2.45: TGA curves of different polymers in air (left) and nitrogen (right) atmosphere [93].	60
Figure 2.46: Percentage of mass loss during solvent extraction of 316L parts [81].	62
Figure 2.47: Bloating and partial cracking on surface sample [77].	64
Figure 2.48: Thermal debinding of a 6mm thickness cylinder at heating rates of (a) 3 °C/min, (b) 1 °C/min and (c) 0.2 °C/min in vacuum [104].	64
Figure 2.49: Cross section of sintered samples varying the heating rates during thermal debinding [105].	65
Figure 2.50: Schematic of the neck size X and the particle size D (assumed spherical) and neck saddle point curvature R during two particle sintering [106].	66
Figure 2.51: Molecular dynamics simulation of sintering process [106].	66
Figure 2.52: Sintered density versus hold time for 42 μm titanium powder vacuum sintered at three temperatures [107].	67
Figure 2.53: Tensile strength as a function of sintering time [108].	68
Figure 2.54: Sintering shrinkage at various time-temperature combinations [106].	68
Figure 2.55: Sintered density as a function of the particle sizes [109].	69
Figure 2.56: Dependency of green and sintered density for 0.5 μm alumina heated at 5°C/min. to 1650°C for a 10 min. hold in air [110].	69
Figure 3.1: Chemical composition (top) and mechanical properties (bottom) of AISI 316L material [113].	72
Figure 3.2: Optical microscopy of ME SS 316L microstructure (after sintering) and SLM SS 316L microstructure along the growth direction [114].	73
Figure 3.3: Schematic of different layer direction (W-, T-, L-specimens) [115].	74
Figure 3.4: Optical microscopy of microstructure in ME 316L part [116].	74
Figure 3.5: Linear shrinkage trends as a function of different layer orientation and layer thickness [115].	75
Figure 3.6: The effects of the oriented binder domain on the shrinkage and the generation of voids [115].	75
Figure 3.7: Relative part density (right) and shrinkage behaviour (left) varying theoretical infill levels [117].	76
Figure 3.8: Evaluation of porosity for different sintering temperatures and times. [Black squares indicate measured porosities of sintered samples after thermal debinding at a	

heating rate of 0.3 °C/min. Red dots indicate measured sintered porosities after debinding at 0.2 °C/min] [104].	77
Figure 3.9: 3D porosity: front view of H-L (a) and H-P(b); top view of H-L (c) and H-P (d); CT slice of H-L sample (e)and H-P samples (f); histogram for overall porosity of H-L samples (g) and H-P samples (h) [118].	79
Figure 3.10: Optical micrographs of the microstructure of the sintered samples with different build orientations after uniaxial tensile stretching [119].	80
Figure 3.11: Ultimate strength (left) and strain at break (right) of the sintered parts printed in various layer directions and thicknesses [115].	81
Figure 3.12: SEM micrographs of fracture surfaces after tensile tests of W-specimen (a), T-specimen (b) and L-specimen (c) printed in a layer thicknesses in 0.1 mm [115].	81
Figure 3.13: Compressive stress and strain varying infill levels [117].	82
Figure 3.14: Micro CT porosity analysis (a) As-built green part, (b) Ordinary sintered part, and (c) HIP sintered part [120].	83
Figure 3.15: Engineering stress – strain curves for sintering and HIP sintering samples with fractography [120].	83
Figure 3.16: Aging time versus Vickers hardness for various temperatures [122].	85
Figure 3.17: Different aging solution and aging treatment and the resulting mechanical characteristics [123].	86
Figure 3.18: Macrograph of sintered tensile specimens printed in the flat layout (top), the side layout (middle) and the vertical layout (bottom) [124].	87
Figure 3.19: Optical macrographs of sintered specimens in the flat layout (a), the side layout (b), the vertical layout (c); SEM micrographs, focusing on the voids between perimeter wall area of sintered tensile specimens printed in the flat layout (d), the side layout (e), and the vertical layout (f) [124].	88
Figure 3.20: Linear shrinkage of the sintered specimens printed in various layer directions [125].	89
Figure 3.21: SEM micrographs of cross-sections of the as-sintered specimens observed perpendicular to the thicknesses of the L-specimen [125].	90
Figure 3.22: Relative densities of the sintered and aged specimens printed in various layer directions [125].	90

Figure 3.23: SEM image of AISI 630 sintered (top), quenched (middle) and aged (bottom) specimens [126].	91
Figure 3.24: Axial strain field data for different loading conditions [128].	92
Figure 3.25: Flexural stress – strain curves varying build orientations (a); average flexural strength and strain to failure varying build orientations (b) [129].	93
Figure 3.26: Fracture surface of sintered samples at low magnification with flat (a) and on-edge (b) orientations; high magnification of the fracture surface with flat (d) and on-edge (e) orientations corresponding to the red-dashed boxes [129].	94
Figure 3.27: Tensile stress at maximum load, tensile stress at yield and elongation at break histograms as a function of different printing angles [131].	95
Figure 3.28: Cross section view of the fracture surface without undergoing tensile test at 0° (a) and 90° (j) printing angles [131].	96
Figure 3.29: Ultimate strength and strain at break of the sintered and aged specimens printed in various layer directions [125].	97
Figure 3.30: Roughness profiles and corresponding arithmetic mean roughness (R_a) of sintered and H900 treated samples [133].	97
Figure 3.31: Schematic of SMAT set-up [134].	98
Figure 3.32: Net section stress – engineering strain curves of sintered and SMAT specimens [134].	99
Figure 4.1: Details about process and methodology and different aspects of samples printed with different set of process parameters (in particular layer thickness).	108
Figure 4.2: Boxplot for shrinkages and bulk density outliers identification.	111
Figure 4.3: Errorbar of bulk density and shrinkages.	112
Figure 4.4: Main effects plot for bulk density (a) and aggregate data (b) as a function of process parameters.	115
Figure 4.5: Aggregate data of shrinkage along X-axis (a) and Y-axis (b) and Z-axis (c) as a function of process parameters.	116
Figure 4.6: Pie-chart of ratio between percentages of AISI 316, op and cp volume.	117
Figure 5.1: Dimensions of Charpy impact samples.	122
Figure 5.2: U-bend sample.	123
Figure 5.3: Tensile stress-strain curves (a); fracture positions of the samples (b).	125
Figure 5.4: Compressive stress–stroke curves.	126

Figure 5.5: Bending stress-stroke curves.	127
Figure 5.6: Samples with complete fracture (a), samples with partial fracture (b).	128
Figure 5.7: XRD patterns of the ME 316L stainless steel.	129
Figure 5.8: Rockwell B Hardness (left) and Vickers hardness (right) values in their relative positions within the sample.	130
Figure 6.1: Cross section of the filament: 1000X (a), 2500X (b).	134
Figure 6.2: Boxplot for shrinkages and apparent density outliers identification.	140
Figure 6.3: Average values of apparent density as a function of the process parameters combination.	142
Figure 6.4: Average values of dimensional shrinkages as a function of the process parameters combination.	143
Figure 6.5: Main effects plots for density (a), planar shrinkage (b) and Z shrinkage (c).	144
Figure 6.6: Residuals versus fits plots for apparent density, planar shrinkage and Z shrinkage.	144
Figure 6.7: Cross section XY plan X100 (left), Cross section YZ plan X100 (right).	145
Figure 6.8: Digital-microscope micrographs of the cross-sections along building directions of samples AS-IS (a,b), H900 (c) and H1150 (d).	147
Figure 6.9: Tensile properties of AISI 630 ME samples	148
Figure 6.10: Deviation of tensile properties of ME samples in the different conditions from the relative monolithic material	148
Figure 6.11: Optical and SEM analysis of fracture surfaces at different magnifications: (a,b) 40 X, (c) 100 X, (d,e) 500 X, (f) 1500 X.	150
Figure 6.12: Compressive stress-stroke curves.	151
Figure 6.13: Bending curves.	153
Figure 6.14: Bending test phases for the H1150 specimen.	153
Figure 6.15: Vickers hardness values.	154
Figure 7.1: Flow chart of the recycling methodology.	160
Figure 7.2: TGA curves for commercial (blue line) and recycled (orange dashed line) filaments.	164
Figure 7.3: Cross sectional micrographs of commercial (a) and recycled (b) filaments; SEM micrographs of commercial (c) and recycled (d) filaments.	166

Figure 7.4: Optical micrographs of the Top view of primary (a) and secondary (b) green parts; optical micrographs of the Side view of primary (c) and secondary (d) green parts.

167

Figure 7.5: Digital-microscope micrographs of etched cross-section of primary (a) and secondary (b) sintered samples along building directions of samples.

169

● ***List of tables***

Table 1.1: AM process families, example processes and processable materials.	11
Table 4.1: Design of experiments: sample identification and process parameters combinations.	108
Table 4.2: ANOVA p-values.	113
Table 5.1: Optimized process parameters combination.	121
Table 5.2. Tensile properties of 316L AM samples.	124
Table 5.3: Comparison of tensile properties among 316L specimens fabricated by means of ME technique.	124
Table 5.4: Absorbed energy values of samples.	128
Table 6.1: Ramps of the sintering cycle.	135
Table 6.2: Levels of the process parameters	135
Table 6.3: Taguchi Design of experiments: sample identification and process parameters combinations.	136
Table 6.4: Solution and aging treatments.	139
Table 6.5: ANOVA p-values.	141
Table 6.6: Tensile and compressive yield strength values.	152
Table 6.7: Coefficients of variation of AS IS, H900 and H1150 samples for each mechanical tests.	155
Table 7.1: Process parameters of filament extruder and spooler.	161
Table 7.2: Ramps of the sintering cycle.	162
Table 7.3: Cycle for thermogravimetric analysis.	162
Table 7.4: Particle size distribution of commercial and recycled filaments.	166
Table 7.5: Comparison of apparent density among 316L specimens fabricated by means of the MME technique.	168
Table 7.6: Comparison of Vickers hardness values among 316L specimens fabricated by means of the MME technique.	170